UNIVERSITE DE LIMOGES ET UNIVERSITE LIBANAISE

ED n° 521 Sciences et Ingénierie pour l'Information, Mathématiques
FACULTE DES SCIENCES ET TECHNIQUES
XLIM – Département Système RF

Ecole Doctorale des Sciences et de Technologie
FACULTE DES SCIENCES
GRIT – Département Groupe de Recherche en Informatique et Télécommunications

THESE

pour obtenir le grade de
DOCTEUR DE L'UNIVERSITÉ DE LIMOGES
Discipline / Spécialité : Electronique des Hautes Fréquences, Photonique et Systèmes
DOCTEUR DE L'UNIVERSITÉ LIBANAISE
Discipline / Spécialité : Télécommunication et réseau

Présentée et soutenue le 27 Octobre 2017 par

ALI SIBLINI

Optimisation des antennes MARPEM (Matrice agile rayonnantes a pixel élaborés en Meta-matériaux) par l'utilisation de formes d'ondes spécifiques pour application RFID et RADAR

Thèse en cotutelle dirigée par Mr. Bernard JECKO et Mr. Mohamed RAMMAL

JURY:

T. MONEDIERE	Président	*Professeur, université de Limoges*
A. SHARAHIA	Rapporteur	*Professeur, université de Rennes*
J. RIBERO	Rapporteur	*Professeur, université Nice- SOPHIA ANTIPOLIS*
A. ALAEDDINE	Examinateur	*Professeur, université Libanaise*
A. BEILLON	Examinateur	*Docteur / Ingénieur antennes, CNES Toulouse*
B. JECKO	Examinateur	*Professeur émérite, université de Limoges*
M. RAMMAL	Examinateur	*Professeur, université Libanaise*
C. MENUDIER	Examinateur	*Professeur, université de Limoges*
J. JOMAA	Invité	*Professeur, université Libanaise*

The most beautiful feeling in the world is when we whisper at the ear of the earth ... and GOD hears us.

To the great reformer, the savior of humanity,
Al Imam Al Mahdi…

Acknowledgments

Acknowledgments

First of all thanks for my God that gave me the abilities of all the good things I achieved and support me by the all the resources in my life ***"And for those who fear Allah, He (ever) prepares a way out and He provides for him from sources he never could imagine. And if any one puts his trust in Allah, sufficient is (Allah) for him for Allah will surely accomplish his purpose: verily, for all things has Allah appointed a due proportion"***.

Great thanks for my parents that work hardly for tens of years to make success for me. Thanks for my wife and children that were the lovely valuable gift from God, they are the real happiness and this work is a gift for them.

This thesis work was carried out in the laboratory XLIM "Systèmes RF" and in collaboration with the GRIT laboratory (Department of Research in Computer Science and Telecommunications) in the framework of a joint thesis between the Limoges University and the Lebanese University. On this occasion, I would like to thank Mr. Bernard JARRY, director of the Doctoral School Limoges University, Mr. Alain Célérier president of Limoges University, Mr. Thierry MONEDIERE director of the RF-Systems department in XLIM. Also I would like to thank Mr. Fouad AYOUB the president of the Lebanese University and Mr. Fawaz Al OMAR the Doyen of the Doctoral School of Sciences and Technology in the Lebanese University.

Thanks for M. Patricia LEROY (Secretary at XLIM Systèmes RF), M. Zeinab IBRAHIM and M. Fatima HASAN (Secretaries at Lebanese University EDST) for their availability in all the administrative procedures in Limoges University and the Lebanese University respectively.

Thanks for Eric ARNAUD "Engineer in XLIM Systèmes RF" for his work in the fabrication and measurements during my thesis. Thanks for the CNES comity, especially for Mr. Anthony BELLION for the financial and technical support in the work done in this thesis.

Great thanks for my supervisor ***Bernard JECKO*** *(Professor Emirate at XLIM Limoges University) for his valuable guidance and support during the thesis for three years and during the defense of my thesis. It was a period that we developed together a big work and I learn a lot from this expert professor in the research and development skills. Thanks for Mr.* ***Mohammad RAMMAL*** *and* ***Mr. Ali ALAEDDIN*** *(Professors at Lebanese University) the Director and the Co-director of my thesis, they supported me with the necessary skills and advices during my thesis.*

Especially great valuable thanks for my real friend ***Dr. Hussein ABOU TAAM*** *that was very helpful in technical and scientific part,* ***"A FRIEND INDEED IS A FRIEND IN NEED"****.*

Thanks for Mr. Mohammad Ali SIBLINI my family relative for his kind support during the thesis period I stayed in Lebanon.

In the Lebanese comity in Limoges I would like to thank all the friends that we share together a very nice time, especially thanks for my brother in law **Karim YAZBECK**, **Jamil FOUANY**, **Amel MAATI**, Yaakoub DIA, Ahmad HAIDAR, Ousama MORTADA….

General Introduction

The radio systems field is rapidly evolving and used in applications such as terrestrial telecommunications, space applications, telecommunications, satellites, RFID (Radio Frequency Identification), civilian radars, military applications concerning the radars of fighter planes, electronic warfare and others. The technical and economic development of these systems is now strongly conditioned by their abilities to improve flexibility, multitask to support the huge requirements that appear after the rapid telecommunication evolution. At the same time, the complexity of radio contributes relatively quickly to the increase in development costs. Also, optimization of each component of the complete system can be enough interesting. Optimization can occur relatively, such as the search for efficiency, the improvement of the design, reducing complexities, introducing instrumental concepts innovations and this is where agility comes in.

Antennas are an important link in the wireless telecommunication chain. It is responsible for the transmission and reception of the signal radiated in the free space. Depending on the radiation objectives to be achieved, the antennas are distinguished and classified. There are directional antennas capable of concentrating energy in a particular direction, the sector antennas which serve to cover a zone or sector with significant gain, omnidirectional antennas whose type of coverage is uniform in a given azimuth plane and the radiated energy is thus equal in the space surrounding the antenna (360°). There are also antennas that are agile in radiation which can change their radiation characteristics (direction of pointing, lobe shape, etc.) using an active control system and can group the same radiation functions cited previously in a single antenna. The antenna system developed within the framework of this thesis belongs to the category of antennas with radiation agility.

In the last 10 years, the term "radiation agility antennas" is an interest for the wireless telecommunications market. It is a real challenge research and development (R & D) in every corner of the world to adopt this technological advance in order to obtain antennas with high performance but also with solutions at the lowest cost and with the least possible complexity. Therefore, antenna systems with radiation agility must be capable of performing reconfiguration, beam forming, pointing functions and spatial electronic beams in different applications. More specifically:

In space telecommunications which is the subject of the work done during this thesis, first of all, the ground antennas pointing to the satellite scrolling which is widely studied. Concerning the satellite antennas, the most important radiation targets are adaptive terrestrial coverage, surveillance of areas and so on. Space applications at large, medium and low height orbits act at different bands especially in the range 1-40 GHz from the L-band up to the ka-band. Such applications insure several services such as global positioning systems, cellular communications, direct broadcasting, marine communications and other applications. Various antennas used in the space stations such as parabolic and helical. However the increase in technology leads to a wide range of services and applications that require more specialized specifications. Specifications are mainly the small size for the development of Nano and Micro satellites and the agility of beam forming. Agility in beam forming requires antennas that function with different patterns such as directive beam, multi directive beams and large angle beam that is widely known as isoflux. Also space communication has forced the use of Circular polarization. The fundamental advantage of circular polarization is that it solves the problems of polarization changes due to the reflections that occur during signal travelling from space station to land stations. Therefore we can avoid fading and flutter when circular polarization is used at each end of the link. In the context of this thesis we studied such a solution that is suitable for the small satellites that require antenna system small in size, low weight, agile in terms of beam forming abilities, and circularly polarized radiating beam.

On the civilian applications, manufacturers and operators of networks are increasingly calling for agile antennas, beam forming, high gain, broadband or multi-band and especially low-cost. For example, in terrestrial telecommunications, the reconfiguration of diagrams according to the density of the subscribers, tracking mobile users and others are subjects to many researches. Currently, the market for particularly long-range RFID requires agile large gain and wide coverage antennas to reach few dozen or even a few hundreds of devices and tags at distinct distances.

In terms of military applications and military radars, electronic microwave war systems and directed-energy microwave weapons, radiant systems are evolving towards the spatial agility that can detect and cover. Radiating systems have the challenge of optimizing the electromagnetic contributions of each route which should favor a chosen direction and not spread too much of the energy in space (secondary lobes, array lobes, ambiguity, blindness, coupling, rear radiation, etc.). These optimizations are made to track and detect securely and discreetly mobile targets, to monitor prohibited areas (terrestrial borders, military base stations ...), to identify friend-enemy and finally to destroy or disrupt the electronics of opposing systems (use of microwave weapons and jammers in directed energy).

In general, the design of beam forming and high gain antennas is based on two main approaches to obtain agile radiation patterns, either on the arrays or on the approach of equivalent radiating surfaces, the corn antennas for example. To introduce agility into these radiation patterns, the most of the antennas with radiation agility are constructed from arrays of elementary antennas. Applications are evolving inexorably towards an all-electronic agility for problems of performance, speed, range and clutter. The first antennas with electronics agility were born for purely military applications (e.g. in the radars of planes fighter).

In this context, **XLIM RF-Systems** department, an antenna system called **MARPEM** (Agile Matrix Radiating with Pixels Elaborated in Meta-materials, **ARMA** in English stands for Agile Radiating Matrix Antenna) whose principle is the subject of a patent CNRS (National Center for Scientific Research) which has already been accepted. This antenna system must perform functions such as radiation pattern, circular polarization, spatial electronic sweeps and very high gain patterns using a number of elements of a matrix antenna.

The electromagnetic approach **ARMA** was studied in past thesis done at **XLIM RF-Systems**. Several antennas were realized to validate the performances of this concept, during the thesis done by Hussein AbouTaam. These realizations include linearly polarized antennas designed for radar and some terrestrial applications and show high performances in comparison with the other agile antennas. We aim in this thesis to introduce this agility to the applications that request circular polarization electromagnetic radiation, mainly space systems and support the new advance in this domain with the flexibility to have multi radiation abilities with circular polarization.

This thesis presents first in **Chapter I** the needs of agility in beam forming in several domain and applications. Then the state of the art of the electronically agile system AESA for beam forming will be presented, with a brief description of the theoretical sampling procedure. Then the limitations of AESA are listed and the introduction to our new approach is explained in theoretically. The conception of the **ARMA** sampling procedure is discussed giving arises to the special EBG antenna called pixel. The concept of linearly polarized pixel is explained and the design architecture beginning from the classical EBG antenna and the low profile EBG antenna to the final pixel structure. At the end of **Chapter I** there are the advantages of **ARMA** approach in comparison with AESA in linear polarization with a summary of the past work done on **ARMA** in linear polarization. Comparisons with AESA are referenced by the published papers that illustrate all the performances of **ARMA**.

In **Chapter II** there is the design of the circularly polarized pixel with different feeding configurations. Then the pixel pattern symmetry in terms of the number of feeds gives an introduction to the design of the circularly polarized pixel. Pixels with different configuration with circular polarization will be shown in Chapter II. Then the design of the circular polarization circuits is presented. Pixel connected to the polarization circuit is studied and the results of the bandwidth, gain and axial ratio are shown. This chapter end by the choice of the best circularly polarized pixel to be used in the next chapters.

Chapter II is dedicated to show the performances of **ARMA** in circular polarization. Performances are compared with the classical AESA solution also circularly polarized. Comparison with AESA will be done concerning the bandwidth, the axial ratio of the scanning beams and the wide beam well-known as Isoflux. 1D and 2D solutions of **ARMA** will be designed and their results will be presented in different beam forming applications.

Chapter IV is for the CNES project. The explanation of the objectives of the CNES and the specifications of the desired antenna for the Nano-Satellite applications is presented first. Then there is the design of the 2D circularly polarized **ARMA** solution with the different feeding laws for two different beam modes. The beam modes specified by the CNES are studied and the resulted gain and axial ratio patterns are shown. Several optimizations are done regarding the feeding law to enhance the Isoflux pattern homogeneity in the different azimuthal planes. Also the design of the power divider for Isoflux and the realization of the whole antenna system are done and measurements are compared to the simulation results.

Chapter V explains some problem in the conception of the power divider and gives solutions with new power divider design. Also some limitations in the antenna study and design and in the geometrical structure and the power divider connectivity are discussed giving arise to the perspectives and future work.

Finally the general conclusion illustrates the work achieved and the limitations that will introduce new work and designs in the future work and open new challenges in the design of the **ARMA** circularly polarized system.

Chapter I
Agile Beam Antenna
State of the ART
ARMA and AESA Comparison

Table of Contents

I. Introduction

This chapter is divided into two parts. First part will present the agile antenna systems in the literature used for electromagnetic beam steering and beam forming. Then highlight on the principle of the electronically agile antenna AESA, beam forming and beam steering agility needs and interests, limitations of AESA. The second part is devoted to present the new agile system **ARMA** and its performances (in linear polarization) in comparison with AESA. Remind that **ARMA** approach is based on a patent done by XLIM RF-Systems department **[I-1]**. Notice that in this chapter and the entire thesis we consider the electronically agile system, since there are also the mechanical agile systems which are not included in our study.

II. Beam steering and beam forming

II-1 General definition

Beam forming means transmitting or receiving electromagnetic beams preferentially in some directions over others using the RF antenna front end. In transmission for example some applications need to cover a specific geographical area that means the electromagnetic beam should be radiated in a specific pattern to achieve the area coverage specifications. This gives arise to the formation of the electromagnetic beam pattern. Beam steering means scanning beams in different directions while maintaining, for example, directive pointing each time in a desired predefined azimuth and elevation angles.

Beam forming and beam steering are extensively used where several applications need radiation pattern reconfiguration such as the formation of multi-sectorial beams, wide beams, directive beams and beam scanning. These applications demand the agile reconfiguration of the beam using the same antenna; in this case the antenna should be agile. Beam forming and beam steering agile antennas are antennas that have the ability to change its beam form to several specific radiation patterns.

Several techniques were used to perform agile beam forming and beam steering such as mechanical and electronically agile antennas, we are working in this thesis on the electronically agile antennas only. From several years the direction of beam steering and in general beam forming is going toward the electronically solution where the beams are formed and radiated in a given predefined patterns by controlling antenna arrays. This solution (electronically) is well known as AESA (Active electronically scanned antenna arrays). Where the antenna is a set of elementary antennas periodically arranged and the feeding low of the array elements is controlled by means of beam forming network (BFN).

II-2 Agile antennas requirements and interests

The aim and the interest of these antennas is to make more flexible communication systems for various applications, such as terrestrial and space telecommunications mainly for satellites, RFID, radars and electronic warfare. Such a desired communication system is able to serve different applications that require different beam specifications. So, building agile antenna gives the communication devices an RF front end to be used for different objectives.

II-2.1 Applications

II-2.1.1 Satellites for space telecommunication

One of the most important applications is the satellites; the purpose of satellites is to provide a multitude of services in the field of telephony, multimedia and determining geographical locations. A few are presented in **Figure I-1**. They also complement the terrestrial and submarine infrastructures where they exist and provide access to services in areas where infrastructure does not provide the establishment of a terrestrial network, due to inadequate topography, or the low population density.

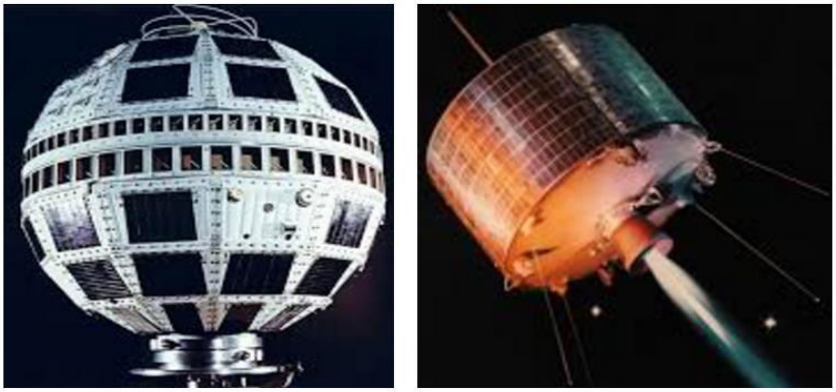

Figure I-1. First telecommunication satellites (Telestar and Syncom).

Nowadays the existent technology introduces many new requirements in the domain of satellites. Special satellites now include mainly the small size (Nano and micro satellites) for the aim of low lunching costs. These space stations serve a lot of civilian and military applications. What is very important is the low weight and multitask. For the reason of multitask the RF front end should be agile and the bandwidth is an important factor, also the solutions for the antennas must be small in size and light in weight.

The number of the Nano satellites (1-10 kg) launched into the orbits has grown twice just within the half year of 2013. These satellites are commercialized rapidly and used in earth observation, collection of distributed sensor data of internet of things all around the world. Currently these satellites are going to be very small for example the Cube-Sat is a type of miniaturized satellite for space research that usually has a volume of exactly one liter (10 cm cube) and has a mass of no more than 1.33 kilograms. This evolution requires very small and low weight agile antennas to fit the requirements of the small satellites and the multi-tasks to be served by these systems. **Figure I-2** shows some examples of the Cube-Sat.

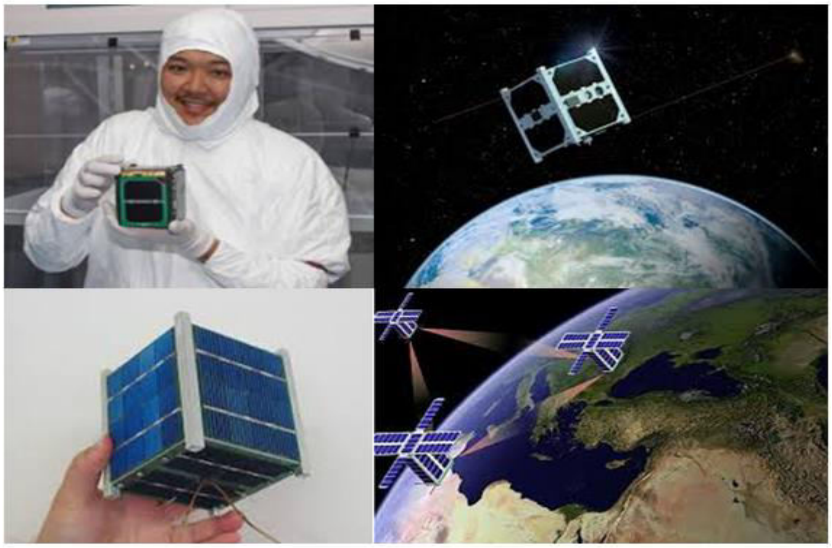

Figure I-2. Cube-Sat examples.

II-2.1.2 Terrestrial telecommunication

Communication systems are ubiquitous around us and more important in a world where the internet and telecommunications become access doors to the whole world, whether to communicate, to exchange files, watch movies on demand, buy products on the other side of the planet, and so on. This evolution requires the need to remain connected in any geographical location by benefiting from the same conditions of use, as a broadband connection for example of ADSL wired type (response time, throughput, connection stability ...).

The radio systems perform wireless communications, cellular networks with an affordable cost, but they have a cost still very high to achieve high flow rates. The technical and economic development of these radio systems is today very strongly conditioned by their capacities to a significant improvement or an increase in the services provided to the users. To satisfy the potential response increasingly envisaged by industrialists and telecommunications operators, is to implement type: array of active agile antennas.

One of the terrestrial applications is the radio frequency identification (RFID), this technology that incorporates the use of electromagnetic wave to detect the tags and uniquely identify an object, animal, or person. RFID is coming into increasing use in industry as an alternative to the bar code. The advantage of RFID is that it does not require direct contact. An RFID system consists of three components: an antenna and transceiver and a transponder (the tag). The antenna uses radio frequency waves to transmit a signal that activates the transponder. When activated, the tag transmits data back to the antenna. The data is used to notify a programmable logic controller that an action should occur. The action could be as simple as raising an access gate or as complicated as interfacing with a database to carry out a monetary transaction. Some applications require the use of long range RFID and wake up some transceivers in different locations, meaning that different far tags are located in some defined or undefined locations are under the action being waked at a manner to start working and detect the tags. These applications gives arise to be supported by agile antennas. In the other hand the tags may be in different orientation with respect to the transceiver meaning that circular polarization is more efficient, mainly for the long range detections. For that the agility will make the antenna serve in different manners and support the RFID with a solution to reconfigure the beam, moreover circularly polarized agile antenna is now a requirement that will improve their performances and in addition give long range usability of the RFID systems.

II-2.1.3 Electronic warfare

Electronic Warfare (EW) is the operation of radio of an adversary and, conversely, to prevent it from doing so. This means that all operations to acquire control of the electromagnetic spectrum, to intercept and/or interference in orders or information circulating in the communications systems of the opponent. The EW is subdivided into three branches: attack, support and protect. Electronic attack is to prevent the opponent from using the spectrum; it is therefore essentially a matter of interference emissions and luring or intrusion measures.

- **The electronic attack** includes the use of directed energy weapons, intended to destroy or damage the adverse electronic systems.
- **Electronic support** brings together all the “passive means” of war, its objective is the “control of the radio spectrum”.
- **Electronic protection** includes all devices and procedures to combat electronic attacks and the means of information of the adversary.

II-2.1.4 Radars

Large efforts are currently underway to develop scanning antennas completely electronic. At the moment, these efforts are only reflected in the military applications, particularly in the radars of fighter planes. For this, a new field of antennas applications with radiation agility is shown in the following paragraph.

II-2.1.4.1 Principle and operation definition

Radar is a system that uses radio waves to detect the presence of targets from the received echoes, determine the position of the target in distance and in angular coordinates with respect to the emitter and calculating the radial velocity of the target. The principle of functioning of radar has evolved to give rise to other systems such as anti-collision radars, cross-wall vision radar, SAR (synthesized aperture-radar) radars used to produce 2D images of the detected scene, etc. The radar system consists of a transmitter and receiver connected to an antenna which must be sufficiently agile in radiation.

II-2.1.4.2 Frequency bands and applications

The working frequency bands of the radar systems are imposed according to the application type. These frequencies correspond to the carrier frequency of the transmitted signal. **Table I-1** shows the corresponding frequency bands for different applications.

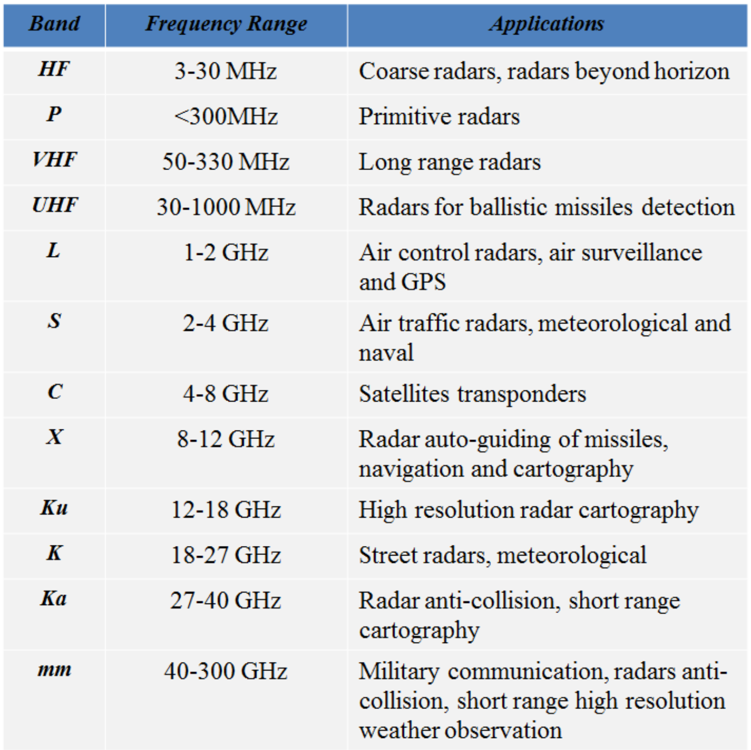

Band	***Frequency Range***	***Applications***
HF	3-30 MHz	Coarse radars, radars beyond horizon
P	<300MHz	Primitive radars
VHF	50-330 MHz	Long range radars
UHF	30-1000 MHz	Radars for ballistic missiles detection
L	1-2 GHz	Air control radars, air surveillance and GPS
S	2-4 GHz	Air traffic radars, meteorological and naval
C	4-8 GHz	Satellites transponders
X	8-12 GHz	Radar auto-guiding of missiles, navigation and cartography
Ku	12-18 GHz	High resolution radar cartography
K	18-27 GHz	Street radars, meteorological
Ka	27-40 GHz	Radar anti-collision, short range cartography
mm	40-300 GHz	Military communication, radars anti-collision, short range high resolution weather observation

Table I-1. Allocated frequency bands and related radar applications.

II-2.1.4.3 Radar evolution: from mechanics to electronics

Since the Second World War, radars have continued to integrate new features, often dealt with simultaneously: targeting and targeting multiple aircrafts, ground attack, communication and aids to navigation, guidance and avoidance of obstacles for low-level penetration, etc. This change in needs, over the last thirty years, require the development of active scanning **[I-2]** **(Figure I-3.a)**, the detriment of the scanning antennas **(Figure I-3.b)** technologically mastered and much less expensive.

Figure I-3. (a) French radar designed to detect satellites orbiting between 400 and 1000 km, (b) primary mechanical scanning radar for an airport.

III. Agile radiating surface

From the theory given by Maxwell equations and the green function, the radiating surface of any antenna is related to the radiated beam at any point in the space. This is the basic concept of the radiating aperture where the radiated field at a point P of the space is deduced from the radiation surface field of the antenna using a spatial Fourier transform (SFT). **[Eq.1.1]** and **[Eq.1.2]** illustrates the concept and transform the near field distribution $E_s(x,y)$ to the radiating beam $E(\varphi,\theta)$ **(Figure I-4)**. Then changing the radiated electric field requires controlling the radiating surface of the antenna.

Agile antennas are based on agile radiating surface, which is a surface that is controlled to give several radiation patterns. The concept is based on generating a radiating surface for any desired shape. Agile antennas should have the ability to give several radiation patterns that means the radiating surface should be controlled (by sampling procedure) each time to give a predefined pattern. In the literature this agility is obtained by antenna arrays AESA where the radiating surface is sampled using the Dirac function.

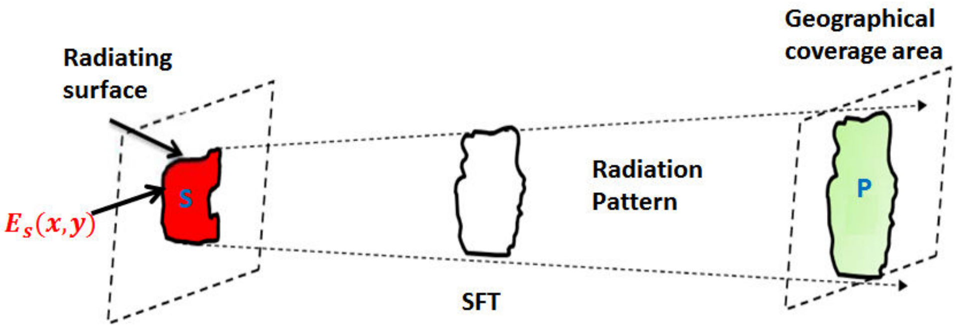

Figure I-4. Schematic representation of the radiating aperture antenna working principle.

$$E(P) = \frac{jk}{4\pi}\psi(R)(1+\mathrm{Cos}\,\theta)\left(\mathrm{Sin}\,\varphi\,\overrightarrow{e_\theta} - \mathrm{Sin}\,\varphi\,\overrightarrow{e_\varphi}\right)SFT. \quad \textbf{[Eq.I.1]}$$

$$SFT = \oiint E_s(x,y)\,e^{j(k_x x\,\mathrm{Sin}\,\theta\,\mathrm{Cos}\,\varphi + k_y y\,\mathrm{Sin}\,\theta\,\mathrm{Sin}\,\varphi)}ds. \quad \textbf{[Eq.I.2]}$$

Where: $\psi(R) = \frac{e^{jkR}}{R}$.

IV. Radiation surface sampling

A moving radiation pattern is obtained by changing the electric field law (magnitude and phase) on the radiating surface as shown in **Figure I-5**. To perform that, the $E_s(x,y)$ field must be sampled.

Experimentally there is only one method in the literature to do such sampling, the AESA solution. In AESA the sampling depends on the Dirac Comb function and is done using antenna arrays. **ARMA** introduces new sampling method that is to build a smaller radiating surfaces uniform in magnitude and phase. When the sampling is done then each sample will be weighted using a predefined law in magnitude and phase and then the radiating electric field is the contribution of all the weighted radiating surfaces according to the integral given in **[Eq.I.2]**. Recall that the radiation pattern of any antenna is obtained by using Maxwell Equations; equations of propagation in free space; free space Green function, and applying the equivalent principle on a radiating surface surrounding the antenna.

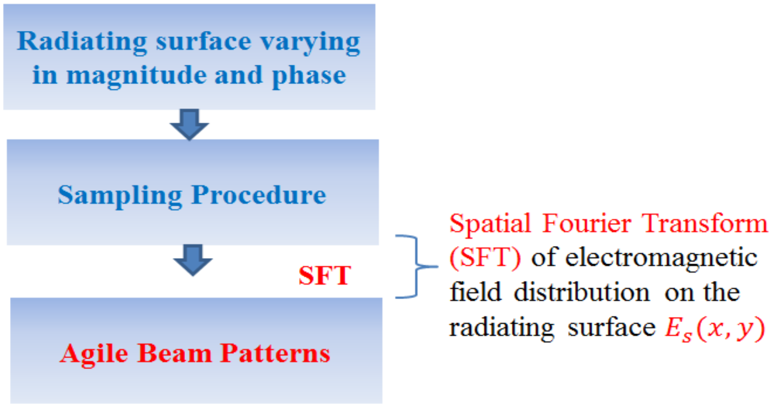

Figure I-5. Agile beam patterns related to radiating surface.

IV-1 Sampling using Dirac Comb

This well-known procedure **[I-21]** multiplies the $E_s(x, y)$ by a two dimensional Dirac Comb to obtain the sampled field following the form in **[Eq.I.3]**:

$$\widetilde{E_s}(x, y) = \sum_i \sum_j E_s(x_i, y_j)\delta_{x_i,y_j}(x, y). \qquad \textbf{[Eq.I.3]}$$

Where δ is the two dimensional Dirac function characterized by **[Eq.I.4]**:

$$f(y_i, y_j) = \int f(x, y)\delta_{x_i,y_j} dxdy. \qquad \textbf{[Eq.I.4]}$$

The $\widetilde{E_s}(x, y)$ sampled field is introduced in **[Eq.I.3]** and the property of the Dirac function is applied to obtain **[Eq.I.5]** and **[Eq.I.6]**:

$$E(P) = k \iint_S \sum_i \sum_j E_s(x_i, y_j)\delta_{x_i,y_j}(x, y)e^{j(k_x x \operatorname{Sin}\theta \operatorname{Cos}\varphi + k_y y \operatorname{Sin}\theta \operatorname{Sin}\varphi)}\, dxdy. \qquad \textbf{[Eq.I.5]}$$

$$E(P) = k \sum_i \sum_j \iint_S E_s(x_i, y_j)\delta_{x_i,y_j}(x, y)e^{j(k_x x \operatorname{Sin}\theta \operatorname{Cos}\varphi + k_y y \operatorname{Sin}\theta \operatorname{Sin}\varphi)}\, dxdy. \qquad \textbf{[Eq.I.6]}$$

Then the electric radiated field appears as a sum of contributions of punctual elementary antennas periodically distributed on the surface *S*. That is the Array Approach.

IV-2 New sampling using a Rectangular function (Quantification)

If the radiating surface S is sampled into small connected pieces $s_{i,j}$ called pixels, the radiated electric field is the sum of all these uniform surface fields contributions, the concept is explained theoretically with the equations **[Eq.I.7]**, **[Eq.I.8]** and **[Eq.I.9]**.

$$E(P) = k \iint_S E_S(x, y)e^{j(k_x x \operatorname{Sin}\theta \operatorname{Cos}\varphi + k_y y \operatorname{Sin}\theta \operatorname{Sin}\varphi)}\, ds. \qquad \textbf{[Eq.I.7]}$$

$$E(P) = k \sum_i \sum_j \iint_{Si,j} E_{i,j}(x, y)e^{j(k_x x \operatorname{Sin}\theta \operatorname{Cos}\varphi + k_y y \operatorname{Sin}\theta \operatorname{Sin}\varphi)}\, ds. \qquad \textbf{[Eq.I.8]}$$

Then:

$$E(P) = k \sum_i \sum_j \iint_{Si,j} A_{i,j}\, e_{i,j}(x, y)e^{j(k_x x \operatorname{Sin}\theta \operatorname{Cos}\varphi + k_y y \operatorname{Sin}\theta \operatorname{Sin}\varphi)}\, ds =$$
$$\sum_i \sum_j A_{i,j} \iint_{Si,j} e_{i,j}(x, y)e^{j(k_x x \operatorname{Sin}\theta \operatorname{Cos}\varphi + k_y y \operatorname{Sin}\theta \operatorname{Sin}\varphi)}\, ds. \qquad \textbf{[Eq.I.9]}$$

Where $\boldsymbol{e_{i,j}}$ and $\boldsymbol{A_{i,j}}$ are respectively the field on the small surface considered as a constant field and the weight applied on each normalized pixel surface field ($\boldsymbol{e_{i,j}}$).

This new sampling suggests that the whole structure can be considered as a matrix of (M x N) pixels, each able to generate a given contribution to the building of the whole field ($E(P)$). In the most general cases, there is no restriction on the surface S, and the pixels can have any shape, but must be connected together. Like for the arrays, the pixels must be fed by a beam forming network (BFN) to apply appropriate weights in order to obtain the expected radiation pattern.

In conclusion, the two approaches introduce different spatial Fourier transform due to the different sampling procedures of the radiating surface. The uniform electric field of the new sampling procedure is the main concept introduced to the agile antennas that is **ARMA** and will be explained later during this chapter.

V. AESA solution

V-1 Definition

An active electronically scanned array (AESA) is a type of phased array antenna that is, electronically-controlled array antenna in which the EM beams of radio waves can be electronically steered in different directions without moving the antenna. In general beam forming is achieved using this agile system. In the AESA, each antenna element is connected to a small transmit/receive module (TRM) under the control of a computer, which performs the functions of a transmitter and/or receiver for the antenna. Elements in the array are fed by specific weighting law of magnitudes and phases using the beam forming network. This is the concept of sampling the radiating surface where each element when weighted represents one sample. **Figure I-6** shows the general structure of AESA system.

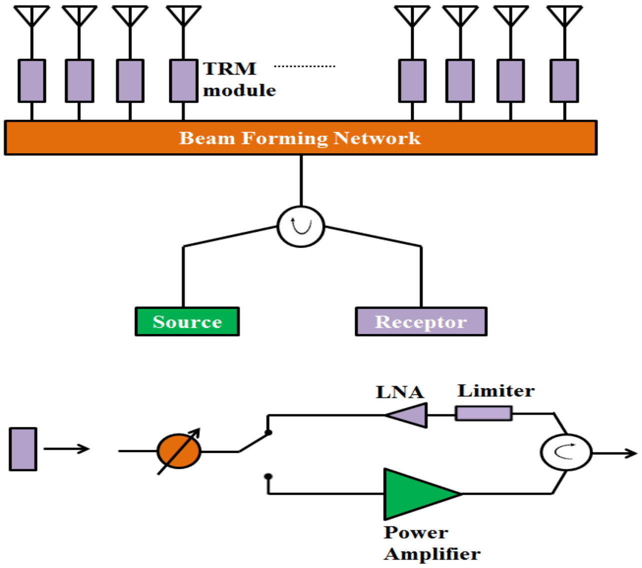

Figure I-6. General structure of AESA.

V-2 Elementary antenna

In AESA the elements of the array could have any pattern type such as omnidirectional, directional, sectorial etc. According to the antenna type the most used are the planar antennas mainly the patch antenna due to its simple form, less complexity in fabrication, small weight and its low cost. Elementary antennas are used to design the array where the periodicity between elements plays an important role in the AESA performances. Performances like the coupling between the elements of the array, side lobes and the undesired grating lobes that appear during steering the beam. In the next paragraph the limitations of these classical antenna arrays are listed giving arise to introduce the new approach **ARMA** that overcomes these limitation.

V-3 Limitations of AESA

The approach of elementary antenna arrays remains the most used solution to make radiant systems with agility in radiation. This solution limitations arising mainly from the concept of arrays and the radiating elements constitute them. Among these limitations:

- The low surface efficiency obtained by the antenna arrays.
- The spacing between elementary radiating sources which must be less than 0.8λ to prevent the occurrence of unwanted grating lobes when the main lobe is in the axial direction.
- The spacing between elementary radiating sources which must be less than 0.5λ in order to ensure good steering of the radiation lobe.
- Far steering angles limited to values between ±50° linked essentially to the coupling between elements and to the appearance of the grating lobes.
- In order to ensure high gains, the number of elements must be large due to the small spacing between elements, which increases the cost of manufacturing and also complicates the experimentation.
- The installation of protections (insulators, circulators ...) to reduce the strong effect of the mutual coupling between radiating elements, which is very expensive.
- The bandwidth is limited by the bandwidth of the elementary antenna.

VI. Beam forming network

Beam forming network (BFN) is used in transmission and reception in AESA. The aim in transmission is to distribute the power to the elements of the antenna array according to a predefined low of magnitudes and phases. In transmission BFN allows the formation of the beam in a desired pattern or simply scan the beam to a specific azimuth and elevation angles. In the reception the BFN works as a combiner that gives a signal that is the contribution of the received signal from all the elements of the array. Remark that the BFN used in AESA is the same used in **ARMA**.

VI-1 General beam forming network architecture

Several architectures are available in the literature from the simple to the most complicated designs. But in general we can consider the BFN shown in **Figure I-7**. In **Figure I-7** the TRM (Transmit/Receive Module) **[I-3]** is placed upstream of each radiating element. This module is responsible for generating high power for transmission, low-noise amplification in reception and also the phase control. So using the TRMs we are able to insure the power distribution law necessary for the beam forming. The sensitivity of antenna systems is improved through low-noise amplification and generation of the high power at the input of the radiating elements. In addition, TRMs offer amplitude and phase flexibility for both channels (up and down). By the arrival of low-cost AsGa MMICs, automated assembly of microwave components and the continued growth of digital processor clock speeds, these architectures will be ideal for systems requiring rapid space scanning and thus, a low probability of being intercepted, especially for the use in the adaptive antennas (Smart Antenna), digital antenna arrays, etc.

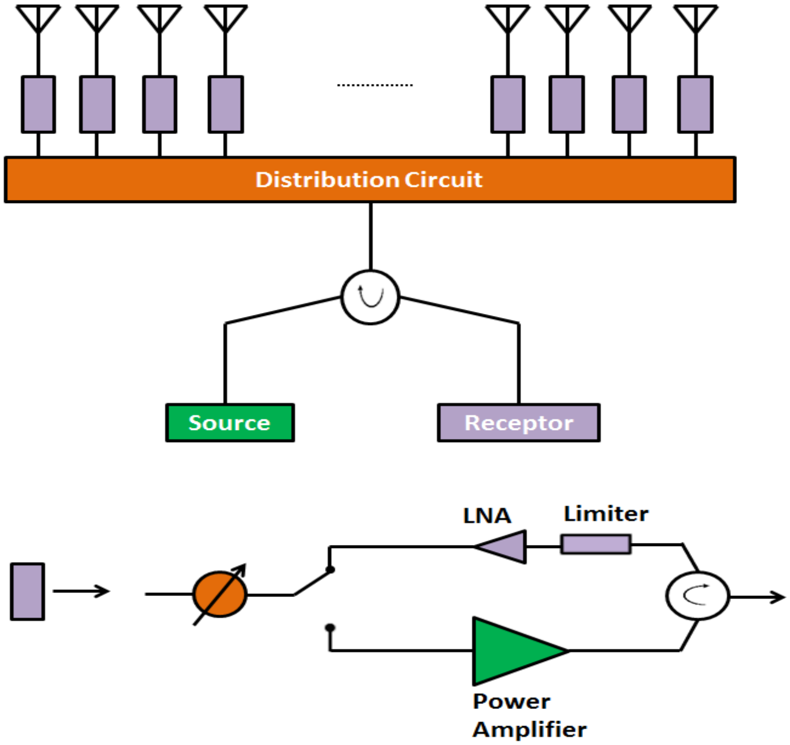

Figure I-7. General BFN architecture for beam steering and beam forming.

VII. ARMA concept

Since AESA main limitations are due to the Dirac Comb sampling procedure, we intended to introduce our solution that depends on the new sampling (discussed in **paragraph IV-2**). The concept of **ARMA** is based on this new sampling approach of the radiating surface. Agility is obtained by sampling the surface into smaller connected radiation surfaces where each is uniform in magnitude and phase. This in contrary with the classical sampling procedure used in AESA shows high performances that will be shown during this chapter.

ARMA is an agile antenna system that is based on the new agile radiation surface, developed to meet high gain needs with agility in radiation. This antenna system must perform all the agility functions (reconfiguration and electronic beam forming) with good performances while avoiding, as much as possible, limitations of conventional antenna arrays. The next paragraph is devoted to present the operating principle of **ARMA** which consists of reconfigurable radiant surfaces from elementary electromagnetic sources specific and original "pixels".

VII-1 Functioning principle

The operating principle of **ARMA** is based on the theory of radiating aperture. As a reminder, the radiation pattern is obtained practically by a Spatial Fourier Transform (TFS) of the electromagnetic field distribution on the radiating surface $E_s(x,y)$ of the antenna according to **[Eq.I.1]** and **[Eq.I.2]**. This concept was shown and illustrated in **Figure I-4**.

VII-2 Concept of pixels radiating surface in linear polarization

The concept of **ARMA** is based on the creation of a radiant field surface EM spatially varying in amplitude and in phase generated from small surfaces radiating elements. These connected surfaces are constructed using electromagnetic "Pixels". Pixel is responsible for the generation of a radiating surface original element with special electromagnetic properties with homogeneity of fields just on the surface of the structure of the pixel. To do that, these pixels consist of radiating elements with electromagnetic band-gap materials (EBG materials) (deduced from the EBG antennas **[I-4]**, **[I-5]**, **[I-6]** and **[I-7]**). Then, the radiating surface of the pixel must be uniform in magnitude and phase and never exceeds the boundaries of this pixel.

Finally, **ARMA** is formed of N x M matrix of connected pixels; the global matrix must be capable of generating radiating surfaces of particular shapes, associating all the elementary surfaces, according to the state of the pixels controlled in amplitude and in phase to produce a formed, reconfigurable and agile beam.

To build the radiating surface plate illustrated in **Figure I-8** or any surface shapes, this surface **(Figure I-8a)** will, in the first step, be pixelated (sampled) by introducing a planar matrix composed of N×M connected pixels (M can be not equal to N) (this sampling is explained in **paragraph VIII**), **(Figure I-8.b)**. In the second step, the desired surface is generated by operating the pixels corresponding to the matrix **(Figure I-8.c)**.

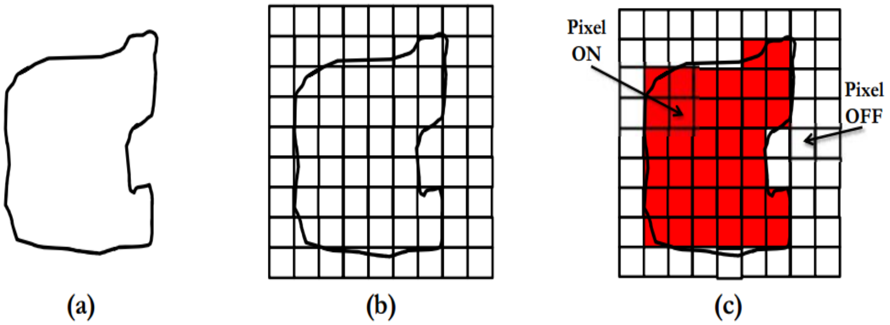

Figure I-8. Radiating surface: (a), desired surface: (b), surface generated by actuating the corresponding pixels: (c).

VII-3 Linearly polarized pixel design

The method to construct the elementary uniform radiating surface of **ARMA** was deducted from the large size low profile EBG antenna. To understand the concept we have to remind a little bit about the EBG antenna and the low profile EBG antenna then introduce the design of the pixel; the details will be presented in the **[Appendix I]**.

VII-3.1 EBG structure and EBG antenna

A long time the EBG materials and the well-known EBG antenna were studied. EBG materials composed of a periodic assembly of dielectric or metallic elements in one, two or even three directions. These EBG structures have a transmission coefficient that show a band gap centered at the frequency of its design. The characteristics of EBG structure become particularly important when a defect is inserted in its periodicity. **[I-8]** and **[I-9]** show that insertion of a break (defect) in the periodicity of the EBG material, makes it possible to modify its electromagnetic behavior by creating pass band within the band gap enabling the waves to pass through. **Figure I-9** shows an EBG structure with and without the defect in periodicity and the corresponding transmission coefficient.

EBG antenna constitutes of a periodic EBG material structure (with a defect in its periodicity) and an electromagnetic source (in the middle of the defect), it has a bidirectional directive radiation pattern and two modes in function of frequency (radial leaky-type wave mode and evanescent mode with a cut-off frequency f_0). When the lower part is replaced by a ground plane (according to the image theory) the radiation pattern is then omnidirectional and the whole structure has the same spatial frequency characteristics.

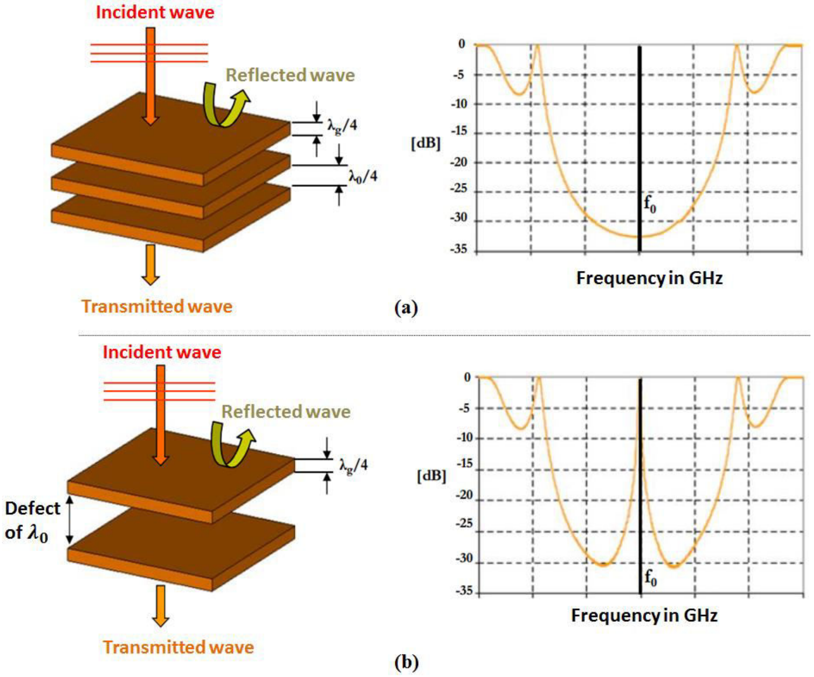

Figure I-9. EBG structure and the corresponding transmission coefficient: (a) without defect, (b) with defect.

VII-3.2 Low profile EBG antenna

The height of a classical EBG antenna (the distance from the ground plane to the EBG structure) operating around a frequency f_0 is given according to **[Eq.I.10]**. Where R_{sup}, R_{inf}, $\emptyset_{sup}$ and $\emptyset_{inf}$ are respectively the magnitudes and phases of the reflection coefficients of the upper wall (EBG structure) and the lower walls (ground plane). So normally this height is around $\lambda_0/2$ **(Figure I-10)** because the reflection phase of the EBG material usually tends to π and the reflection phase of the totally reflected surface ($\emptyset_{inf}$ of the ground plane) equals π.

$$h = \frac{\lambda_0}{2}\left(\frac{\phi_{SUP}+\phi_{INF}}{2\pi}\right). \qquad \textbf{[Eq.I.10]}$$

Indeed, the characteristics of the latter strongly affect the antenna performance (high directivity and operating bandwidth less than 10%). Thus, to reduce this congestion also the height of the resonator, it is necessary to resonate at the working frequency of the antenna structure between the ground plane and the FSS with negative reflectivity ($\emptyset_{inf}$<0). Recent work done by the **XLIM RF-Systems** laboratory and others are possible to considerably reduce the height of the antenna using EBG materials or FSS that possess a negative phase of reflection tending to -π **[I-10]** to **[I-11]**.

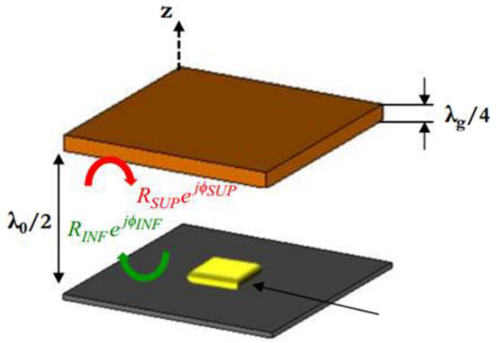

Figure I-10. Classical EBG antenna example.

This new EBG antenna called “Low Profile” EBG antenna, due to its strong compactness (≈λ / 20) is characterized by a wide band in operation (sometimes greater than 50%) caused by the negative phase of the EBG which induces a low quality factor of the resonator (according to **[Eq.I.11]**). In the “Low Profile” EBG antenna the directivity increased to 11dB. Although the performance between the classical and “Low Profile” are different, the operating principle (radial evanescence of modes, frequency evolution of the directivity between two zones of operation, etc.) remains always the same. An explanation of the basic principle of the EBG antennas is now possible to present the pixel which will be the most important part to build **ARMA**.

$$Q = \frac{\sqrt{R_{SUP}}}{1-R_{SUP}}\left(\frac{\phi_{SUP}+\phi_{INF}}{2}\right). \qquad \textbf{[Eq.I.11]}$$

VII-3.3 High gain EBG antenna

The idea for designing the EBG pixel consists of a large gain EBG antenna and therefore large dimensions. It acts as a resonant cavity formed between a metallic ground plane (lower wall) and a frequency selective surface in FSS (upper wall) in z direction. The excitation system is constituted of a patch printed above a dielectric substrate and placed at the center of the cavity of the EBG antenna **(Figure I-11)**.

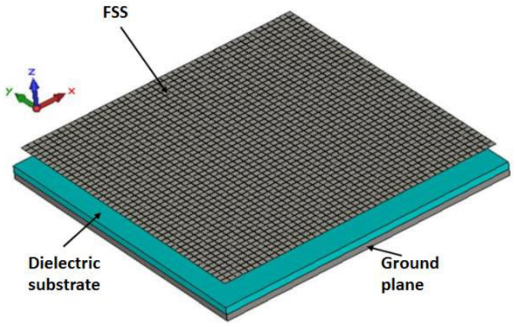

Figure I-11. Structure of high gain EBG antenna.

The cartography of the E-field in such an antenna **(Figure I-12)** shows that it works well on the principle of a 1D z-resonator with an evanescent transversely variation of fields. These fields decrease exponentially radially around the source **(Figure I-12a)**. This leads, on the top of the antenna, to a large circular radiating surface with a field distribution that varies in amplitude and decreases in exponential manner from the axis of symmetry of the structure **(Figure I-12.b)**. This distribution, the radiating surface of the antenna, leads according to the spatial Fourier transform to a directional and symmetrical radiation patterns.

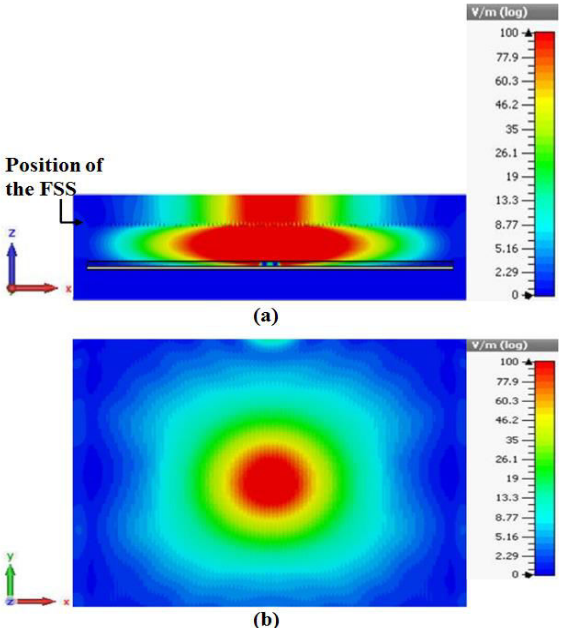

Figure I-12. Cartography of the electric field (a) cut plane in the middle along y-axis, (b) top view.

VII-3.4 Introduce the metallic walls

Due to the transverse evanescence of the fields we avoid undesirable radial resonances. Then the idea is to build the pixel from the large EBG antenna to obtain special electromagnetic radiating surface uniform in magnitude and phase **[I-12]** and **[I-13]**. This is attained by inserting metallic walls inside the large EBG antenna **(Figure I-13)**, so that the radiating surface shape follows the shape of the inserted walls and doesn't exceed its dimensions. In **Figure I-14** there is an example of square metallic walls used and the corresponding square radiating surface. The final pixel structure to be used for **ARMA** is described in the next paragraph.

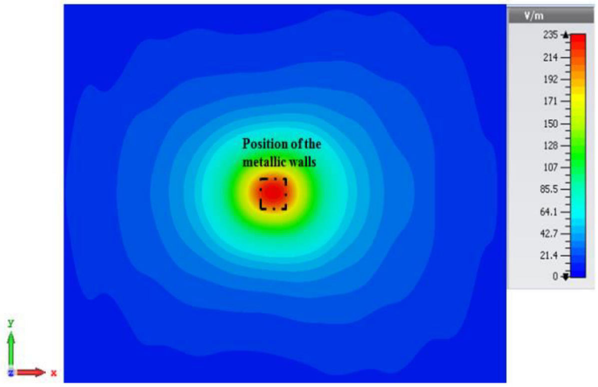

Figure I-13. The place of insertion of 4 metallic walls to change the shape geometry of the circular radiating surface.

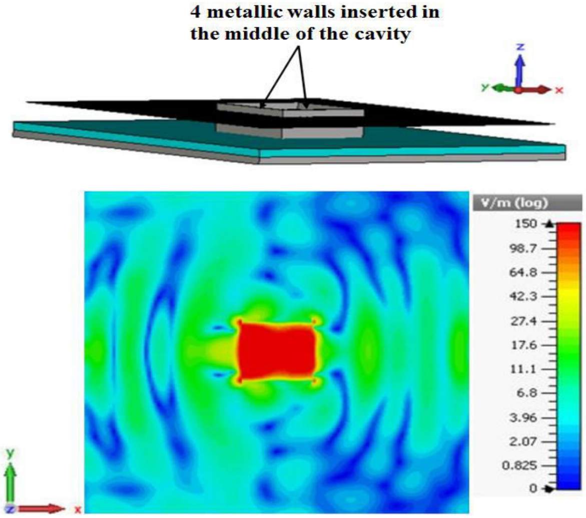

Figure I-14. Structure of the large gain EBG antenna with square metallic walls inserted and the corresponding radiating field cartography.

VII-3.5 Final pixel structure

The final pixel **(Figure I-15)** is therefore formed by:

1. A ground plane presenting the lower face of the structure.
2. Semi reflected surface on the top that could be a dielectric, Meta-material, or FSS (that is the case in this thesis).
3. Cavity between the ground plane and the semi-reflected surface.
4. A wall enclosure formed by four metal walls surrounding the cavity (can have any shape).
5. Excitation source that transform the electric energy to electromagnetic energy that excite the whole structure. In our work the excitation source is a patch printed on a dielectric substrate, in general it could be a dipole, monopole, etc. **[I-14]**.

Indeed, in the example of **Figure I-15**, the FSS is formed of an arrangement of small square metallic pieces, which give rise to a negative phase of reflection which tends to -π. This negative phase results in a very compact cavity in the order of λ/10 given by **[Eq.I.10]**. The proposed pixel is therefore a “Low Profile” antenna. It is necessary to note that the pixel operating principle is also valid for other types of FSS exhibiting properties of different reflectivity.

The walls are extension in the direction orthogonal to the ground plane and surrounding the excitation system, the cavity and the FSS. On the upper surface of the pixel a radiating surface of predefined shape and limited by its contour, while the EBG antennas without a walls generates radiating surface with circular geometry **(Figure I-12.b)**. The cartography of **(Figure I-15.b)** shows a square-shaped radiating surface with a distribution of the uniform field over the entire pixel which doesn’t exceed the pixel structure.

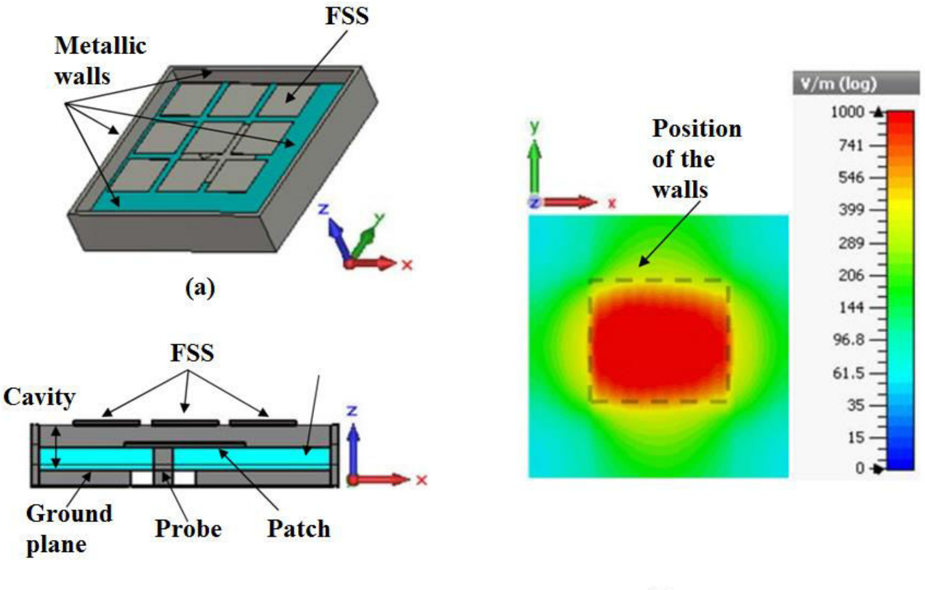

(a) (b)

Figure I-15. Pixel simple structure, perspective view (a), cut view along x-axis (b), cartography of the radiating surface top view (c).

VIII. ARMA AESA principles comparison in linear polarization

In what follows an illustration of the main performances of **ARMA** compared to AESA in linear polarization. For more details refer to the references for each where the theoretical and experimental prototypes of **ARMA** are presented. Remind that the two approaches depend on different procedures for sampling the radiating surface (AESA Dirac Comb and **ARMA** connected uniform radiating surfaces using pixels). For the aim of comparison consider the two kinds of antennas with 1D structure **[I-15]**, **[I-16]** and **[I-17]** and with the same planar surfaces, the same number of elements (number of elementary array antennas equal to the number of pixels) and the same law for the feeding network.

VIII-1 Radiating surface efficiency in the axial direction

The result of the comparison of the surface efficiencies is the same as comparing a phased array and an aperture antenna (horn antenna for example). In the phased array, the surface efficiency is usually less than 65% and in the horn antenna it is more than 75%. These results are approximately the same with AESA and **ARMA** respectively. That means a difference in axial gain of 0.6 dB in our example which is not very significant. It is more significant (2dB) for larger surfaces **[I-18]**.

VIII-2 Coupling between two adjacent elements

The coupling effect between two adjacent pixels in **ARMA** is lower (at least 4 dB) than that between adjacent elements in the array antenna. This property is due to the radially vanishing mode of the EBG antenna used to build the pixel **[I-19]** and not due to the presence of the walls **[I-17]**.

VIII-3 Maximum gain as a function of the elevation angle θ

The maximum gain curve (for the steering beam) must follow the law of $1 + \text{Cos}\,\theta$ that is approximately the case for the **ARMA** solution but not the case for the patch array for $\theta \geq 55°$ **[I-16]**. This result is confirmed in **[I-20]** where the maximum of the gain for the 70° direction is 4 dB higher in **ARMA** than AESA. This result can be generalized for any **ARMA** antenna used for beam-forming **[I-21]** or beam-steering with any beam shape.

VIII-4 Side lobes and Grating lobes compared to pixel lobes

As it was shown in the first part, the radiated field is approximately the spatial Fourier transform of the sampled surface field and the sampling procedures are different for the **ARMA** and AESA approaches. Since in **ARMA** procedure the sampled surface field is smoother (uniform sampled surfaces), the spatial Fourier transform introduces lower side lobes **[I-18]**, the grating lobes for the array and pixel lobes for **ARMA** appear at the same angles (Fourier transforms with the same periodicity) but not at the same level. This result was tested also for larger design size (1.2λ is the dimension of each pixel and also of each patch antenna), the grating lobes obtained with **ARMA** is 11dB lower than that of AESA with a better gain for the main lobe **[I-18]**.

VIII-5 High axial gain solutions

In the same way, **ARMA** and AESA approaches are good choices to obtain high gain (>30dB) with low profile structures. Unfortunately high gain means a large number of elements which increases dramatically the BFN losses and the cost. But, as it is shown in the previous paragraph, **ARMA** is the good candidate to minimize the number of elements of the BFN because the dimensions of the pixels can be increased without significant side lobes effects for maximum radiation around the axial direction **[I-17]**. For example, to obtain a 25 dB gain using an array solution with inter-element steps of 0.6λ, 100 elements need to be used. In the **ARMA** solution, if the pixel surface of 0.6λx0.6λ is chosen to keep the same periodicity, the **ARMA** solution needs the same number of elements. But, it is possible to obtain the same results with 1.2λx1.2λ pixels, corresponding to the same radiating surface and the same gain obtained using 25 elements instead of 100 without significant degradation of the pattern. To verify this property, a 5x5 pixels **ARMA** antenna was studied; the expected directivity (25dB) was obtained with an equal amplitudes and equal phases feeding procedure.

VIII-6 Frequency dependence

The pixel of the **ARMA** solution is derived from a low profile EBG Antenna (**[I-19]** and **[I-22]**) which presents a very stable behavior as a function of the frequency more than the patch antenna. Consequently the pixel and then the whole **ARMA** antenna have the same frequency stability as shown in the maximum directivity as a function of the frequency in **[I-22]**.

IX. Conclusion

This chapter shows the agile beam forming and beam steering antenna AESA and explain briefly the concept of the new agile antenna **ARMA** and its advantages in comparison with AESA in linear polarization. First the two electromagnetic principles were compared showing fundamental differences. These performances illustrates the interest of the new approach (in linear polarization), but the manufacturing of **ARMA** is a little bit more complicate. However the cost is not significantly larger, because for such an antenna that is the BFN that set the price high or low cost and in both antennas the same kind of BFN is used (sometimes with a lower number of elements for the **ARMA** solution). The performances show that **ARMA** overcome AESA in the lower couplings between the elementary antennas, lower side lobes and grating lobes for the scanned beams, higher maximum directivity in function of frequency, high gain with less number of elements, the ability to use larger periodicity without significant changes in the pattern and with low accepted grating lobes.

All the study on **ARMA** for now includes linearly polarized antennas in the theoretical study, design and realization. However, the need for circularly polarized agile antennas still a need in many applications such as, space applications, Nano-satellites, RF-ID, CNES space studies and satellites. Moreover it’s a need in all the applications that require high reception performance and efficiency regardless of the geometrical location and movement of the transceivers. For that in the content of this thesis we aim to build a circularly polarized **ARMA**. The study of **ARMA** with circular polarization starts by building a pixel with circular polarization having a uniform radiating surface (the basic theoretical approach of the electric field sampling in **ARMA**).

In the next **(Chapter II)** the pixel with circular polarization will be shown, and then the design of the circularly polarized pixels with the feeding polarization circuits are presented. This study will be the first step to build the whole antenna **ARMA** for the circular polarization patterns needs.

X. Bibliography of Chapter I

[I-1] Patent: JECKO, B.; HAJJ, M.; CHANTALAT, R.; SALAH TOUBET, «Antenne élémentaire et antenne réseau mono ou bidimensionnelle correspondante» PCT Patent: PCT/EP2012/076509; French Patent: FR 11 62141.

[I-2] Colin, J.-M., "Phased array radars in France: present and future," Phased Array Systems and Technology, 1996. IEEE International Symposium, vol. no. pp.458, 462, 15-18 Oct. 1996.

[I-3] Kopp, B.A.; Borkowski, M.; Jerinic, G., "Transmit/receive modules" Microwave Theory and Techniques, IEEE Transactions on, vol.50, no.3, pp.827, 834, Mar 2002.

[I-4] N. G. Alexopoulos and D. R. Jackson, "Fundamental superstrate effects on printed circuit antennas" IEEE Trans. Antennas Propag., vol. 32, pp. 807–816, Aug. 1984.

[I-5] Y. J. Lee, J. Yeo, R. Mittra, and W. S. Park, "Design of a Frequency Selective Surface (FSS) type superstrate for dual band directivity enhancement of microstrip patch antennas" in Proceedings of the IEEE Antennas and Propagation Society International Symposium and USNC/URSI Meeting, pp. 2–5, Washington, DC, USA, July 2005.

[I-6] D. R. Jackson, A. A. Oliner, and A. Ip, "Leaky-wave propagation and radiation for a narrow-beam multiple-layer dielectric structure" IEEE Trans. Antennas Propag., vol. 41, no. 3, pp. 344–348, Mar. 1993.

[I-7] Thevenot, M., C. Cheype, A. Reineix, and B. Jecko, « Directive photonic band gap antennas », IEEE, Transaction on Microwave Theory and Techniques, Vol. 47, No. 11, 2115–2122, Nov. 1999.

[I-8] M. THEVENOT, **"Analyse comportementale et conception des matériaux diélectriques à bande interdite photonique. Application à l'étude et à la conception d'un nouveau type d'antenne"**. Université de Limoges thèse n°34-1999, octobre1999.

[I-9] M. THEVENOT – C. CHEYPE – A. REINEIX – B. JECKO, **"Directive photonic band-gap antennas"**, IEEE Transactions on Microwave Theory and techniques, Vol 47 n°11, November 1999, Page(s): 2115–2121.

[I-10] F. Yang and Y. Rahmat-Samii, **"Microstrip antennas integrated with electromagnetic band-gap (EBG) structures: a low mutual coupling design for array applications"**, *IEEE Transactions on Antennas and Propagation*, vol. 51, no. 10, pp.2936–2946, 2003.

[I-11] R. Chantalat, L. Moustafa, M. Thevenot, T. Monédière and B. Jecko, **"Low Profile EBG Resonator Antennas"**, *Hindawi Publishing Corporation, International Journal of Antennas and Propagation*, Volume 2009, Article ID 394801, 7 pages.

[I-12] HAJJ HAJJ Mohamad, CHREIM Hassan, RODES Emmanuel, ARNAUD Eric, SERHAL Dina and JECKO Bernard, **"Rectangular M-PRS Structure for Sectorial Base Station Antenna with Vertical Polarization"**, *Microwave and Optical Technology Letters*, MOTL, Vol 52, Issue 4, start page 990, 2010.

[I-13] HAJJ Mohamad, RODES Emmanuel, SERHAL Dina, JECKO Bernard, **"Metallic EBG Sectorial Antennas with different polarizations"**, AUTOMATIKA, Journal for Control, Measurement, Electronics, Computing and Communications, Vol. 49 No. 3-4 November 2008.

[I-14] M. SALAH TOUBET, **"Etude d'antennes BIE planaires de hauteur très inférieure à la longueur d'onde dite: The ULP EBG Antennes"**. Thèse de doctorat – n°92-2011, Université de Limoges, 21 décembre 2011.

[I-15] H. ABOU TAAM, G. ZAKKA EL NASHEF, M. SALAH TOUBET, E.ARNAUD, B. JECKO, T.MONEDIERE and M. RAMMAL, «Scan Performance And Re-configurability Of Agile Radiating Matrix Antenna Prototype» International Journal of Antennas and Propagation IJAP Vol. 2015 Article ID169303 8 pages. DOI : 10.1155:2015:169303.

[I-16] Hussein ABOU TAAM, Moustapha SALAH TOUBET, Thierry Monedière, Bernard JECKO, Mohamed RAMMAL, «A New Agile Radiating System Called Electromagnetic Band Gap Matrix Antenna» Journal: International Journal of Antennas and Propagation, vol. 2014, Article ID 342518, 7 pages, 2014.

[I-17] Hussein ABOU TAAM, Moustapha SALAH TOUBET, Thierry MONEDIERE, Bernard JECKO, Mohamed RAMMAL «Interests of a 1D EBG Matrix compared to a patch array in terms of mutual coupling and grating lobe» IEEE, 7th European Conference on Antennas and Propagation EuCAP, 8-12 April 2013, Sweden.

[I-18] L. SCHWARTZ « Méthode mathématiques pour les sciences physiques» Collection Enseignement des Sciences – Hermann – Oct. 1997.

[I-19] C. MENUDIER, M. THEVENOT, T. MONEDIERE, B. JECKO «EBG Resonator Antennas: State of Art and Prospects» 6th International Conference on Antenna Theory and Techniques ICATT'07, Sevastopol, the Crimea, Ukraine, September 17-21, 2007.

[I-20] Hussein ABOU TAAM, Georges ZAKKA EL NASHEF, Moustapha SALAH TOUBET, Eric ARNAUD, Bernard JECKO, Mohamed RAMMAL. «Feeding technique for the experimental validation of EBG matrix antenna» Journal: Microwave and Optical Technology Letters, Vol.57, n°3, March 2015, Article ID MOP-14 0936.

[I-21] Ali SIBLINI, Bernard JECKO, Hussein ABOU TAAM, Mohamed RAMMAL «New Circularly Polarized Matrix Antenna for Space Applications» WTS 2016 - London – 18/04/2016 au 20/04/2016.

[I-22] Toubet, M.S.; Hajj, M.; Chantalat, R.; Arnaud, E.; Jecko, B.; Monediere, T.; Hongjiang Zhang; Diot, J., «Wide Bandwidth, High-Gain, and Low- Profile EBG Prototype for High Power Applications» Antennas and Wireless Propagation Letters, IEEE , vol.10, no., pp.1362,1365, 201.

List of Figures

List of Tables

Chapter II
Circularly Polarized Pixel

Table of Contents

I. Introduction

ARMA approach shows big advantages to be used in comparison with the classical antenna arrays in linear polarization; this made it possible to a major axis of research around antennas with radiation agility with circular polarization. Remind that the pixel design is the first step to do that. Then, the choice of the elementary source for circularly polarized **ARMA** system will be the main point to build such agile antennas. This chapter will present the study done to design the circularly polarized pixel using the circularly polarized patch as a source antenna to feed the EBG cavity. The patch is considered because of its interesting low weight, low cost, compactness and many characteristics. This pixel must have a uniformly radiating surface (as described in **Chapter I**) with circular polarization. Then the design of circuits for circular polarization will be presented and the results of pixel connected to the polarization circuit will be shown.

The performances of the pixel alone are not the objectives in my study, but to show these performances we consider the pixel alone in this chapter. However, these performances mainly the frequency dependence of the pixel is very important later to study the circularly polarized **ARMA**.

The work done in this chapter will be the main step to build **ARMA** antennas with circularly polarized field for different applications and it is a part of a big project for the **CNES** (National Center for Space Studies, France) that recommended the use of **ARMA** circularly polarized; they are building Nano and Micro satellites which will serve different applications that need circularly polarized field patterns.

II. Circular polarization

II-1 Polarization and axial ratio

When a wave is travelling in space the property that describes its electric field rotation at a fixed point as a function of time is called wave polarization. Since the electric and magnetic field vectors are always related according to Maxwell equations, it is enough to specify the polarization of one of them. And generally it is specified by the electric field **[II-1]**, **[II-2]** and **[II-3]**. The polarization plane is the plane containing the electric and magnetic field vectors and it is always perpendicular to the plane of propagation. The contour drawn by the tip of the electric field vector describes the wave polarization which could be an ellipse, circle or a line **(Figure II-1) [II-1]**. **Figure II-2** shows the plane wave with the electric field components, the major axes and the minor axes. Theoretically for circular polarization the two magnitudes of these axes should be equal but also we consider the electric field circularly polarized if the ratio of the magnitudes varies between 1 and 2 (in linear scale) or 0-3dB in logarithmic scale.

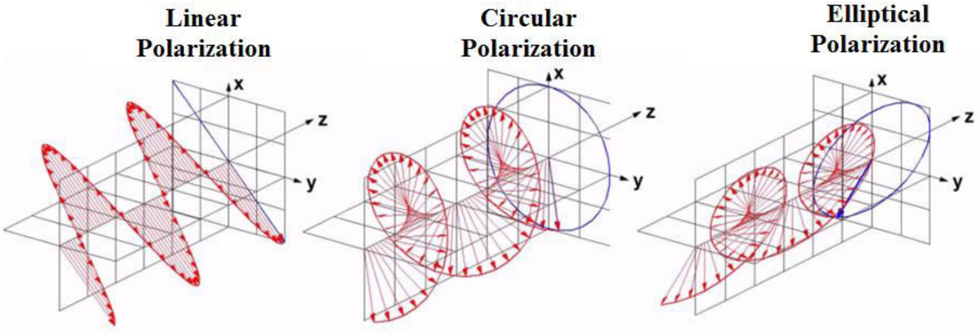

Figure II-1. Polarization types of the electromagnetic wave.

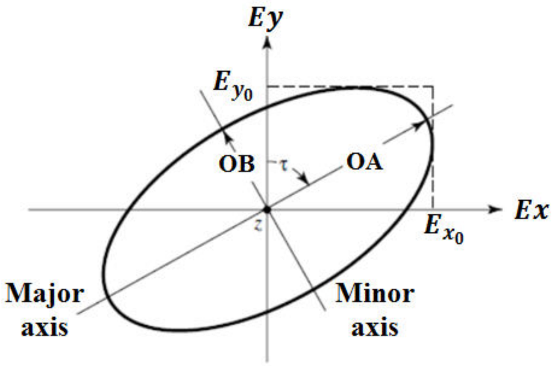

Figure II-2. Plane wave and its polarization.

II-2 Advantages of circular polarization

Polarization is a very important factor in wave propagation between the transmitting and receiver antennas. Having the same kind of polarization is important so that the receiving antenna can extract the signal from the transmitted wave **[II-4]**. Maximum power transfer will take place when the receiving antenna has the same direction and polarization, otherwise there will be polarization mismatch. If polarization mismatch occurs it will add more losses **[II-1]**, **[II-5]** and **[II-6]**. Polarization is very important when considering wave reflection **[II-2]**. In general circular polarization is better according to the following:

- Reflectivity: Radio signals are reflected or absorbed depending on the material they come in contact with. Because linear polarized antennas are able to “attack” the problem in only one plane, if the reflecting surface does not reflect the signal precisely in the same plane, the signal strength will be lost. Since circular polarized antennas send and receive in all planes, the signal strength is not lost, but is transferred to a different plane.

- Received energy: Electromagnetic signals can be absorbed by the antenna depending on the polarization of the designed antenna. As a result, circular polarized antennas give a higher probability of a successful link because it is transmitting on all planes and the receiver antenna circularly polarized detect and absorb the energy in all the planes.

- In circular polarization the antenna sends double the energy in comparison with the linear polarized antenna (more by 3dB).

- Multi-path: Multi-path is caused when the primary signal and the reflected signal reach a receiver at nearly the same time. This creates an “out of phase” problem. The receiving radio must spend its resources to distinguish, sort out, and process the proper signal, thus degrading performance and speed. Linear Polarized antennas are more susceptible to multi-path due to increased possibility of reflection. Out of phase radios can cause dead-spots, decreased throughput, distance issues and reduce overall performance.

- Inclement weather: Rain and snow cause some of the conditions explained above (i.e. reflectivity, absorption, phasing, multi-path and line of sight). Circular polarization is more resistant to signal degradation due to inclement weather conditions for all the reason stated above.

- Line-of-Sight: When there is no line-of-sight path due to the presence of obstructions (i.e. buildings), circular polarization is much more effective than linear polarization for establishing and maintaining communication links.

III. Circularly polarized patch antenna techniques overview

Patch antenna consists of conducting patch on a ground plane separated by dielectric substrate. The conducting patch can take any shape (triangular, circular, rectangular, elliptical etc…) but rectangular and circular configurations are the most commonly used. The main characteristics of the patch antenna (Gain, resonance frequency, bandwidth and the input impedance) are affected by the patch size, dielectric thickness and the feeding procedure. A lot of feeding techniques available in the literature the microstrip line feed, coaxial feed and aperture coupled feed which are not in the objective of study in this chapter. What make it interesting to use patch antenna in our thesis to build the circularly polarized pixel are the advantages listed below:

- Light weight and low volume.
- Low profile planar configuration which can be easily made conformal to host surface.
- Low fabrication cost.
- Supports both, linear as well as circular polarization.
- Can be easily integrated with microwave integrated circuits (MICs).
- Mechanically robust when mounted on rigid surfaces.

In my study I want to feed the pixel by circularly polarized patch since it is very easy to apply several feeding ports (one, two and four). Several techniques were the subject of many researches regarding the design of circularly polarized patch, in what follows a small overview for common used techniques and their performances, mainly the adapted bandwidth and circular polarization bandwidth.

III-1 Single feed circularly polarized patch antenna

Truncated edges patch with a single feed can generate circular polarization radiation. Typical configurations are shown in **Figure II-3**. These structures are desirable in the antennas where for some reasons we cannot use power divider circuits to generate phase shifted sources for dual feed of the patch (will be shown in next paragraph). However the most disadvantages of these structures are the narrow adapted bandwidth (around 2%) and the narrow circularly polarized patch **[II-7]** (taking the axial ratio limit 3dB). Also in terms of the elevation angles, the axial ratio is below 3dB for narrow angles around the axial direction.

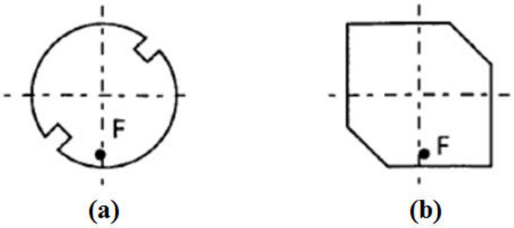

Figure II-3. Single feed truncated edge patches for circular polarization.

III-2 Dual feed circularly polarized patch antenna

The dual-orthogonal feeds **(Figure II-4)** excite two orthogonal modes with equal amplitude but with 90° phase shifts, this feeding is generated by power divider circuit like the Wilkinson power divider, hybrid coupler or simply a splitter with two microstrip lines as shown in **Figure II-4**. In general the adapted bandwidth attains 5% to 10% depending on the dielectric substrate thickness and the circular polarization bandwidth is mostly 5% **[II-8] [II-9] [II-10]**. The most disadvantages of these structures is that the axial ratio is strongly affected by the dielectric thickness, then improving the axial ratio in terms of bandwidth and elevation angles requires lower dielectric thickness. This means that the adapted bandwidth will go lower. Also the dissymmetry in the feeding structure makes the axial ratio and radiation patterns not symmetrical **[II-8] [II-9] [II-10]**, which is not favorable when used to build the antenna array.

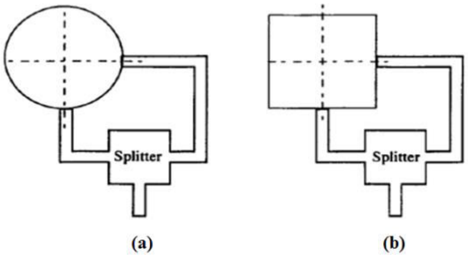

Figure II-4. Dual feed patch with power divider circuit.

III-3 Quad feed circularly polarized patch antenna

Circularly polarized patch antenna could be attained also by feeding the patch with four ports **[II-11]** with sequential phases of 0°, 90°, 180° and 270° these phase shifted feeds are attained by a divider circuit. **Figure II-5** shows an example of a patch antenna with four ports. The adapted bandwidth and the circular polarization bandwidth of this configuration reach 5%; several techniques are available in the literature to increase the bandwidth mainly the stacked patch antenna that could reach a bandwidth up to 20% **[II-11]**. The gain and the axial ratio pattern are symmetrical meaning that if we consider any azimuth plane the pattern in terms of the elevation angles is symmetrical with respect to the axial direction describing zero azimuth and zero elevation angles **[II-11]**.

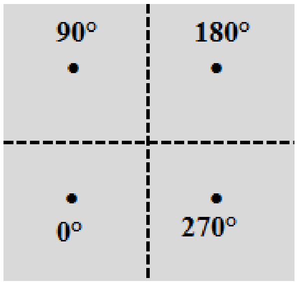

Figure II-5. Quad feed circularly polarized patch antenna.

III-4 Slotted circularly polarized patch antenna

Slotted patch is useful to make a more compact design where the slot could have many shapes, diagonal, cross, circular, rectangular, flower slot **[I-12]** or square. But the adapted bandwidth is very small (around 1.5% to 3%) and the circular polarization bandwidth is mostly 1% **[I-12] [I-13] [I-14]**. **Figure II-6** shows some examples of the patch with slots.

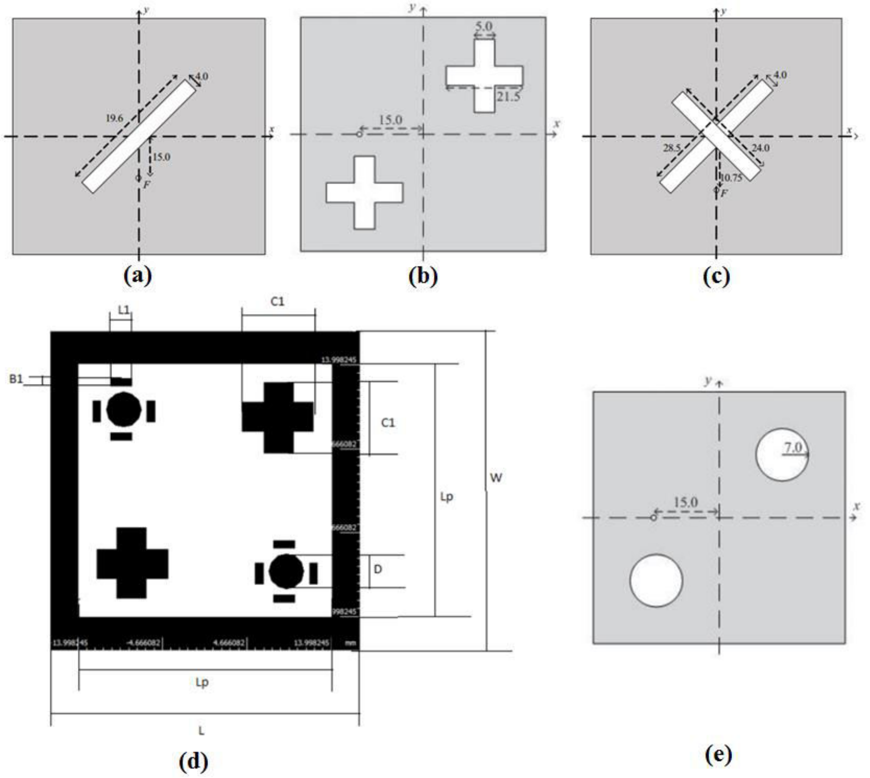

Figure II-6. Patch with slots, (a) rectangular along the diagonal, (b) two crosses symmetrical along diagonal, (c) cross at middle, (d) flower, (e) two circles symmetrical along diagonal.

III-5 Circular polarization from linearly polarized patch antennas

Two linearly polarized patch antennas can be orthogonally arranged as shown in **Figure II-7.a**, with one of the patches being fed 90° out of phase can generate circular polarization pattern. Also the same if four linearly polarized patches arranged orthogonally with different possibilities for the phase shifts for the feeding of the patches as shown in

Figure II-7.b and **II-7.c**. The disadvantages of these configurations are the larger space requirements and rapid degradation of circular polarization with elevation angle around the axial direction.

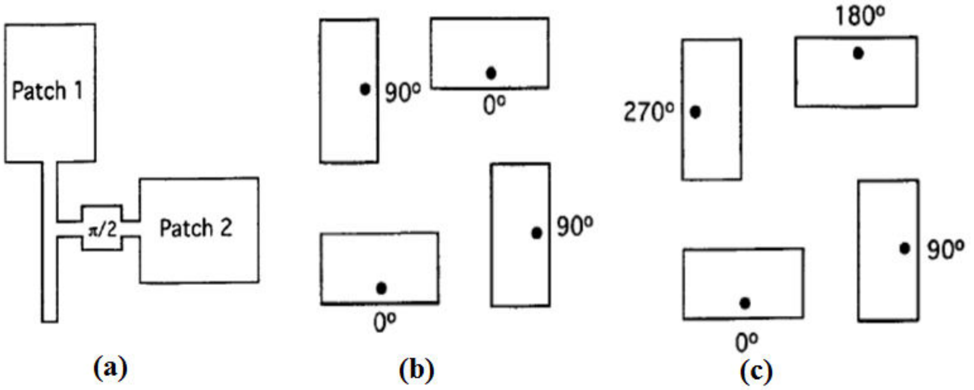

Figure II-7. Circular polarization from linearly polarized patches, (a) two patches with 90° phase shift, (b) four patches with two 90° phase shifts, (c) four patches with 0°, 90°, 180° and 270° phase shifts.

IV. Circularly polarized pixel

Remind that the pixel is derived from the low profile EBG antenna **[II-15]** as described in **Chapter I**. The feeding of the EBG cavity is done using patch antenna circularly polarized to benefit from the interesting advantages of the patch antenna structures mentioned above. The main constraint in our pixel design is the size of the pixel which is 0.5 λx0.5 λ, so the EM source inside the pixel must fit the dimensions restrictions. The circularly polarized patch is a good candidate for such a solution and we can use only one patch inside the cavity. Also later we will see that each circularly polarized patch inside the pixel cavity will be fed by a polarization circuit that means the circuit should be small enough to be printed behind the pixel of small dimensions. The used configurations are the dual feeding and the quad feeding circularly polarized patches with the coaxial feeding procedure. In this chapter and the entire chapters the perfect feeding procedure means the coaxial cables are with the waveguide port of the CST software, however the un-perfect feed (real case) is the pixel fed by the polarization circuit designed in the Momentum software and taken to CST as touchstone file. The following parameters are common for all the studied pixels in this chapter:

- Patch and FSS substrates RO6002 of ε=2.94 and thickness 1.5mm.
- Pixel size of 0.5 λ x0.5λ.
- Height λ/8.
- Central frequency 8.2 GHz.

VI-1 Pixel study in terms of number of feeding ports in linear polarization

This paragraph presents the behavior of the linearly polarized pixel when the patch used is fed by several ports. The aim of this study is to show the gain pattern and bandwidth and make an introduction for the choice of the circularly polarized pixel design.

IV-1.1 Pixel with patch fed by one port in linear polarization

Figure II-8 shows the dimensions and architecture of the pixel with one feeding port. The bandwidth (779 MHz, 9.5%) and gain pattern are shown in **Figure II-9**. The important point to be observed is the dissymmetry in the gain pattern in the elevation angles in the same azimuth plane φ=0° **(Figure II-9.b)**. What is more favorable is to have symmetrical pattern for the aim of synthesis in the 1D and 2D **ARMA**.

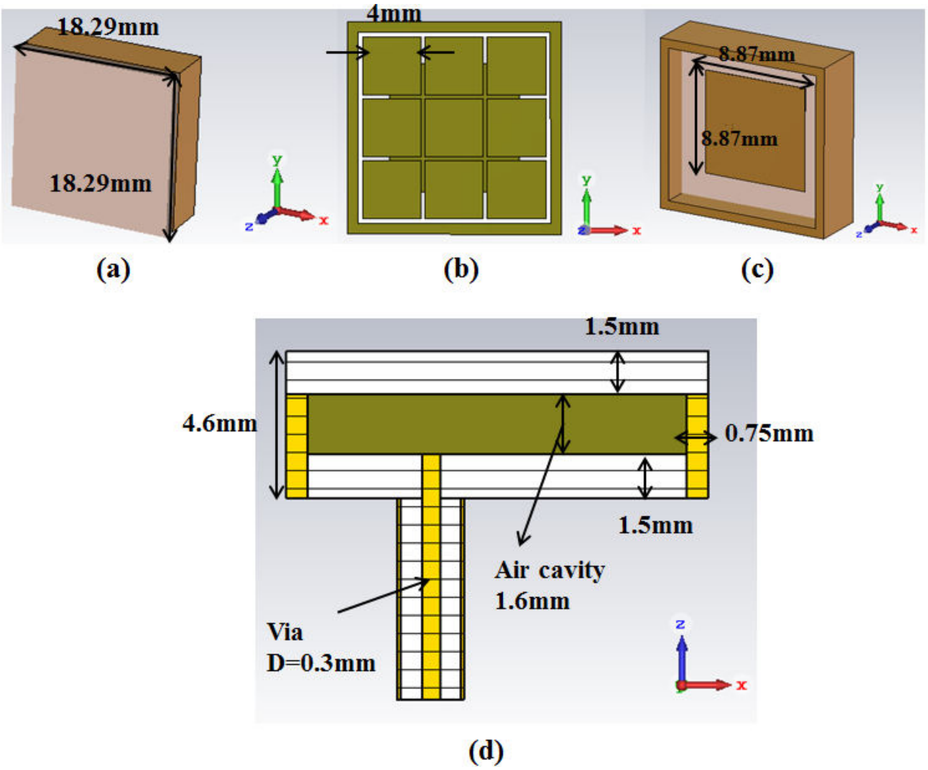

Figure II-8. Pixel with one feeding port (0.5λx0.5λ) (f_0=8.2GHz), (a) perspective view, (b) FSS dimensions, (c) without FSS, (d) cut view along “y”.

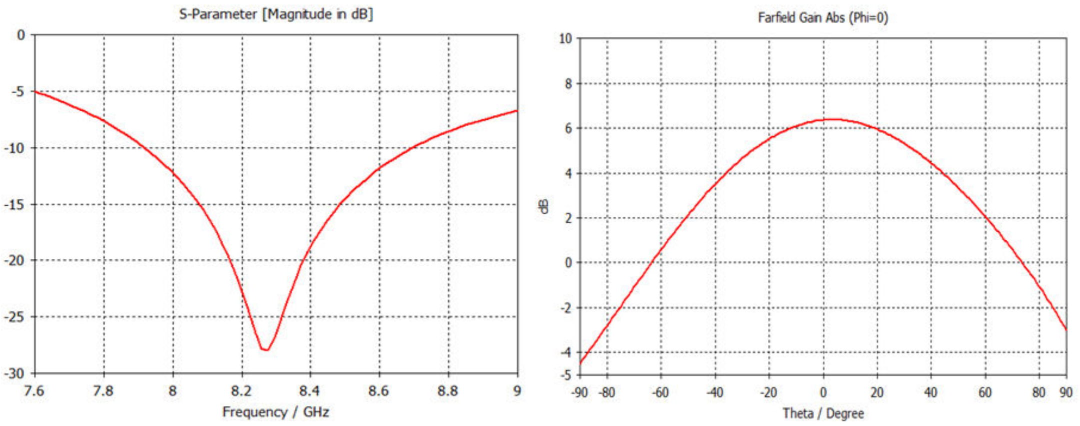

(a) **(b)**

Figure II-9. Pixel with one feeding port: (a) Return loss, (b) gain pattern (f=8.2GHz).

Many techniques could be applied on the patch (with one feeding probe) exciting the FSS cavity to make circular polarization **([II-16] [II-17])**. However these techniques give a narrow axial ratio below 3dB in terms of elevation angles, also a narrow circularly polarized bandwidth **([II-16] [II-17])** that is undesired as a solution to be used for multitasks with different beam forms (wide like isoflux and directive beams).

IV-1.2 Dissymmetry compensation of the one feeding port technique in linear polarization

To insure symmetry in E and H planes in terms of elevation angles with respect to the axial direction representing (φ=0° and θ=0°), two feeding ports in opposite sides phase shifted by 180° are used **(Figure II-10)** (new feeding port symmetrical to the port in **Figure II-9** is added to the design). This procedure gives a bandwidth of 985 MHz (12%), **(Figure II-11.a)** and pattern that is the contribution of two patterns opposite oriented to compensate the dissymmetry of the one port pixel geometry. But this geometrical and electromagnetic configuration doesn't give symmetry for the E in comparison with H plane **(Figure II-11.b)**.

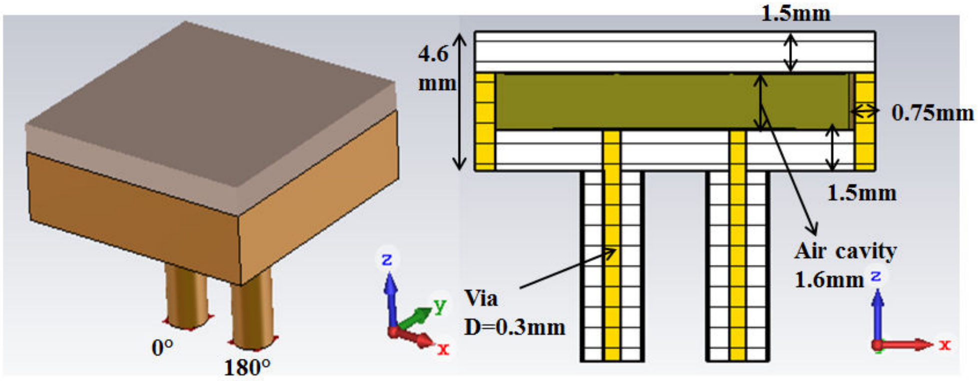

Figure II-10. Pixel with one two feeding ports (0.5λx0.5λ) (f=8.2GHz).

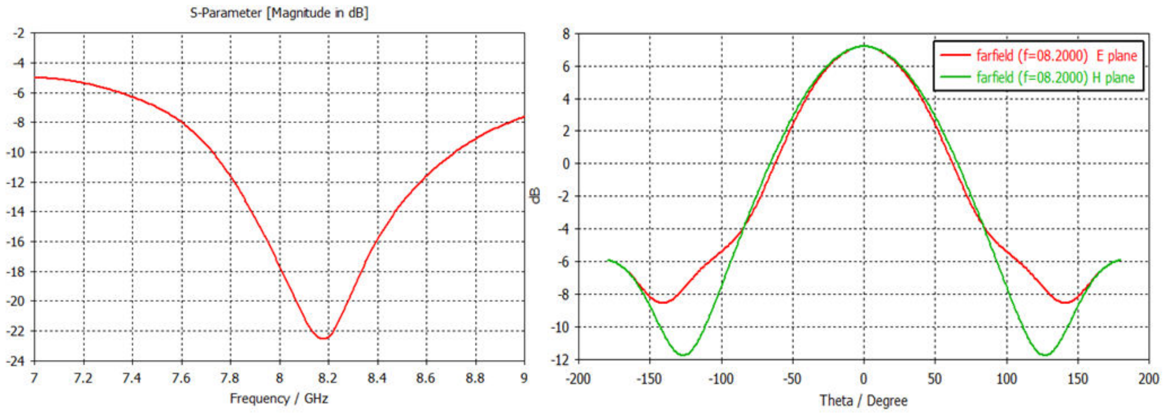

(a) (b)

Figure II-11. Pixel with two feeding port: (a) Return loss, (b) gain pattern (f=8.2GHz).

That is why it's recommended for good symmetrical pattern to use the four feeding ports procedure to design the circularly polarized pixel.

IV-2 Circularly polarized pixel with patch fed by two ports 90° phase shifted

A pixel with patch fed by two feeding ports 90° phase shifted give a circularly polarized field. **Figure II-12** shows the pixel with dual fed patch inside the EBG cavity, the excitation coaxial cables, the FSS printed on the dielectric (all specifications and dimensions as mentioned in above and in **Figure II-8**).

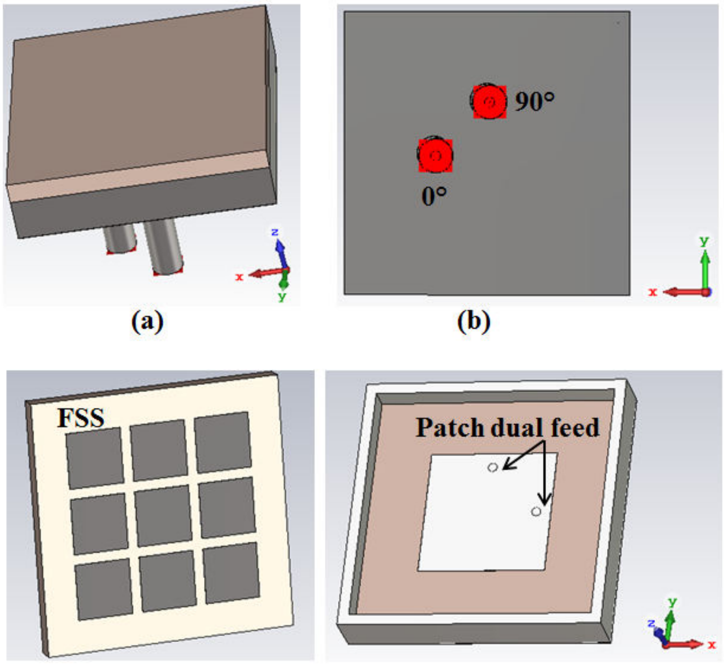

(a) (b)

(c) (d)

Figure II-12. Pixel, (a) perspective view, (b) Bottom view, (c) FSS printed on RO6002 substrate, (d) dual fed patch inside the cavity.

The most important characteristics of the pixel is the uniform radiating surface as explained in **Chapter I** should be uniform and limited to the dimensions of the pixel. The magnitude of the radiating surface is shown in Figure **II-13.a**. Also current at the surface of the patch is shown in **Figure II-13**. The current is rotating as seen taken at different time giving arise to a circularly polarized electric field.

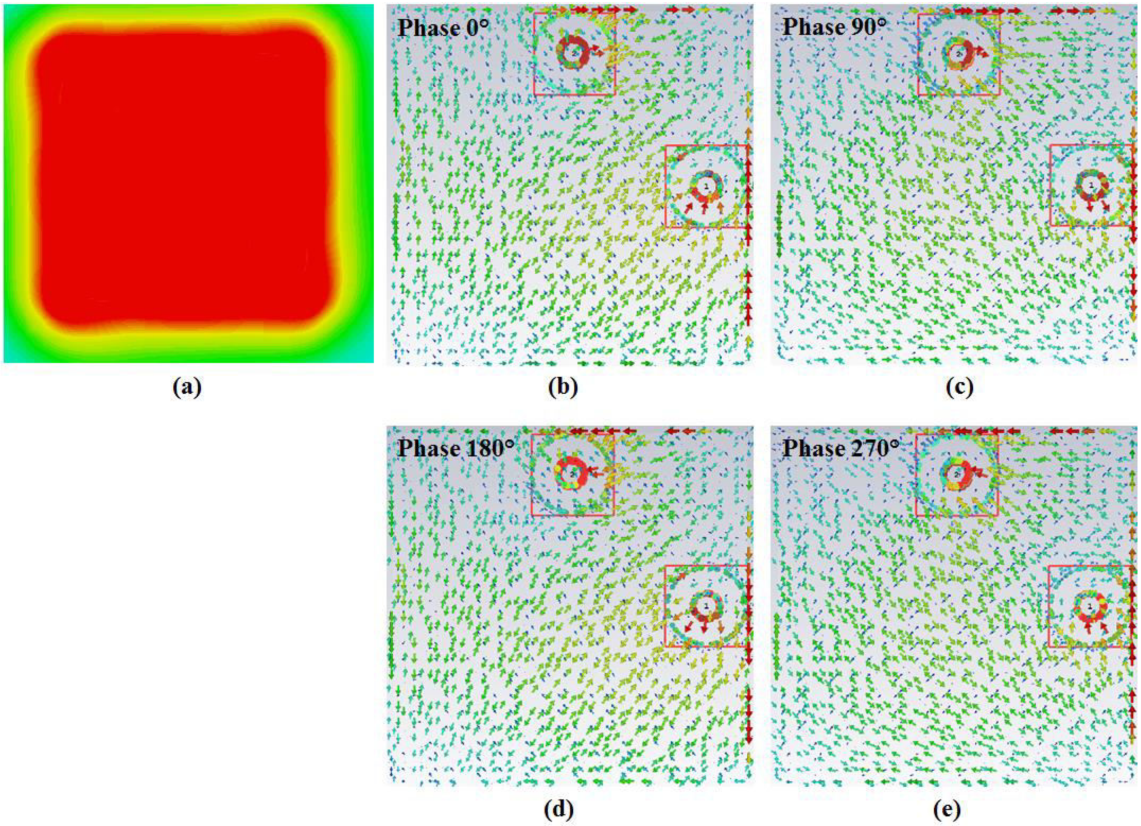

Figure II-13. (a) Uniform radiating surface (magnitude), (b, c, d and e) surface current at different phases.

The gain and axial ratio patterns are not symmetrical as you can see in **Figure II-14** also the axial ratio is not wide enough (θ between ±47° for azimuth plane φ=30°) under the 3dB constraint, that is favorable is to be wider in order to be used for different reconfigurations for the beam that could be wide or directive.

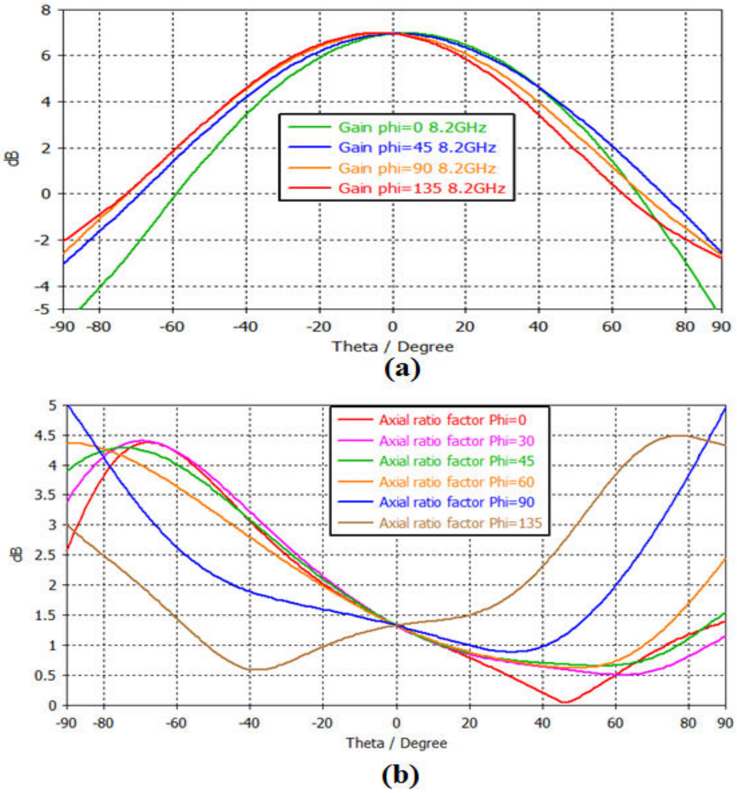

(a)

(b)

Figure II-14. Pixel with patch fed by two feeding port, (a) gain pattern, (b) axial ratio pattern.

IV-2.1 Axial ratio enhancement

Parametric study on the patch substrate of the patch inside the pixel was done to improve the axial ratio. Experimentally as we decrease the substrate thickness of the patch the axial ratio becomes better. But normally we are losing the high bandwidth. **Figure II-15** shows the axial ratio for the plane φ=0° and the bandwidth for different substrate thicknesses (h=1.5mm, 0.8mm, 0.4mm). For h=0.4mm the axial ratio is below 3dB for wide elevation angles (±90°) but the bandwidth is 317 MHz, however the bandwidth is 764 MHz for h=1.5mm.

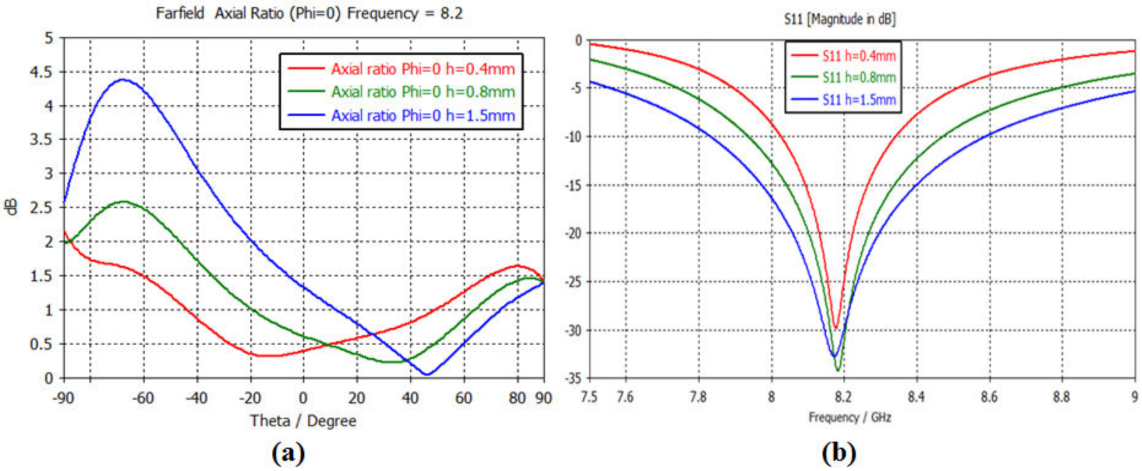

Figure II-15. Pixel with two feeding port substrate height parametric study: (a) axial ratio pattern, (b) bandwidth.

As a conclusion the pixel with the patch of two ports could be used for generating circularly polarized pattern for the applications that meet the resulted performances in terms of bandwidth, axial ratio and gain pattern. However we are looking for a solution with higher bandwidth and better axial ratio to be used later in the whole **ARMA** antenna.

IV-3 Circularly polarized pixel with patch fed by four ports

Looking for better solution we build a pixel with a patch fed by four ports with phase shifts of 0°, 90°, 180° and 270° **(Figure II-16)**. The magnitude of the uniform radiating surface and the surface current at the patch level are shown in **Figure II-17**. This architecture gives a totally symmetrical pattern for the gain and the axial ratio **(Figure II-18.a** and **Figure II-18.b)** also the axial ratio is below 3dB in all the azimuth planes for wide elevation angle (±90°). What is interesting also is the bandwidth of this low profile pixel which is shown in **Figure II-19**, the bandwidth is 950 MHz (11.5%).

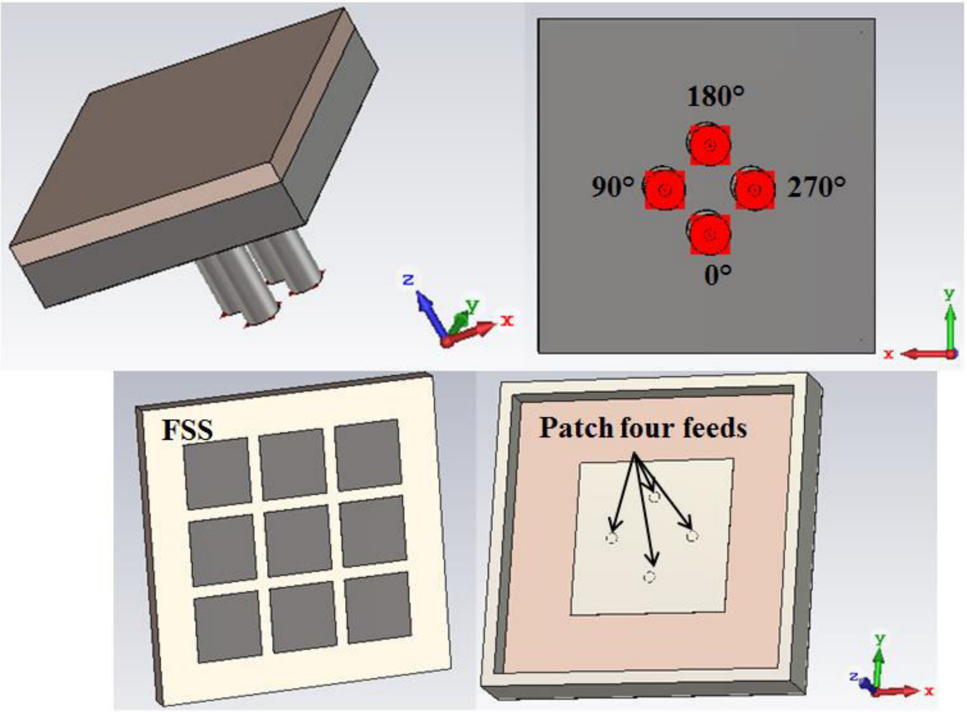

Figure II-16. Pixel with patch fed by four feeding port, (a) perspective view, (b) bottom view.

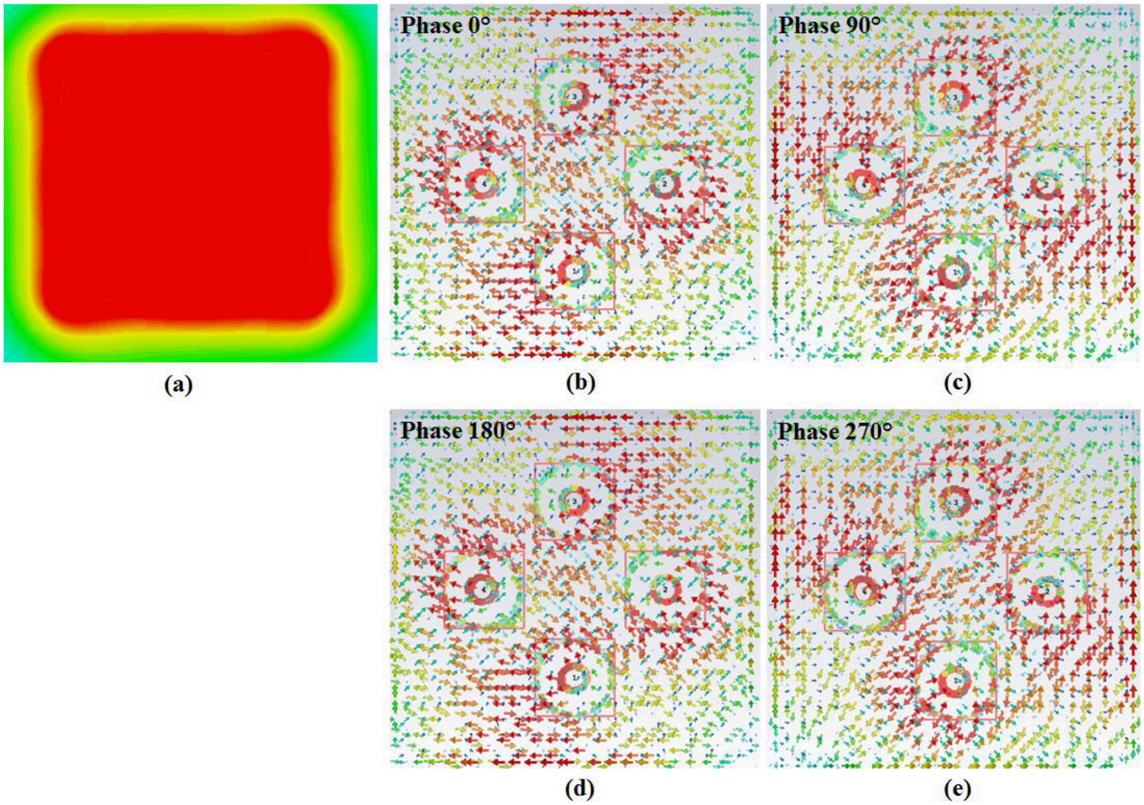

Figure II-17. (a) Uniform radiating surface (magnitude), (b, c, d and e) surface current at different phases.

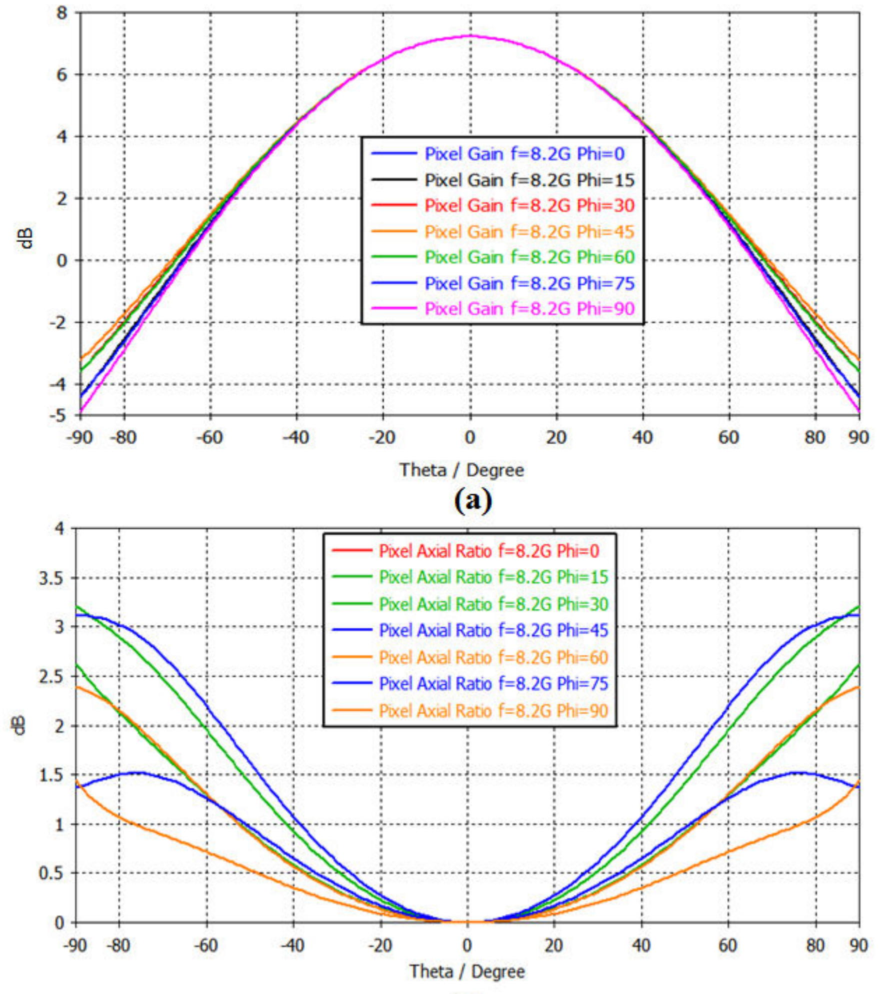

(a)

(b)

Figure II-18. Pixel with patch fed by four ports, (a) gain pattern, (b) axial ratio pattern.

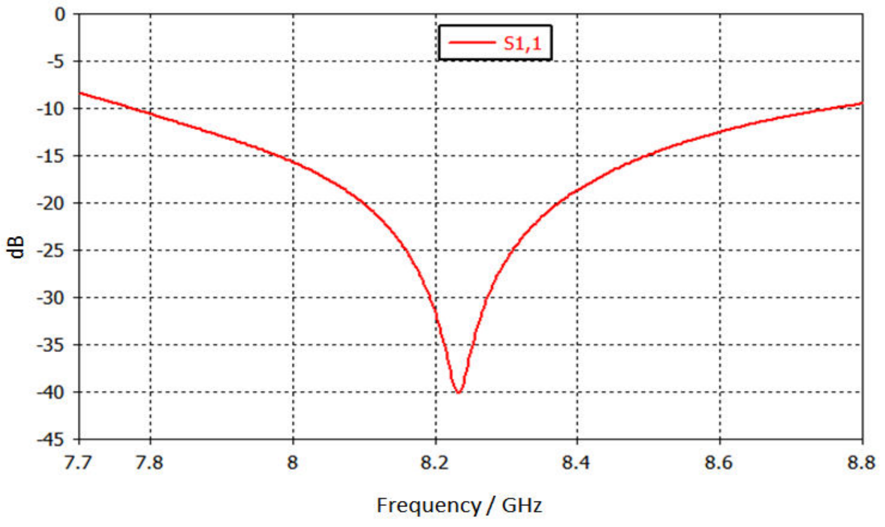

Figure II-19. Pixel with patch fed by four ports return loss.

IV-4 Pixel fed by polarization circuit

Circularly polarized pixels with patch fed by two or four ports need to be fed with a phase shifted sources taking as a phase reference one of the ports. In the above study the phase shifts are introduced in CST software simulation settings as an ideal phases (0° and 90° for the two ports and 0°, 90°, 180° and 270° for the four ports). However realization of the circular polarization in this case requires circuits that have an RF-input and phase shifted RF-outputs. Several architectures were studied with two and four outputs, the most important constraints for these circuits are the degree of stability of the outputs magnitudes and phases, magnitudes theoretically considered equal and phases as mentioned above. These outputs vary with frequency and the errors start to be worst as going far from the central frequency of the designed circuit. Bandwidth of the circuit is taken as the range of frequencies where the errors in magnitudes and phases connected to the pixel give a good axial ratio that met the constraints specified by the application. In this way we can define the circular polarization bandwidth where it should be inside the adapted bandwidth of the pixel with the perfect ideal feeding procedure given by CST.

In **ARMA** antenna each pixel will be fed by a polarization circuit, the circuit should be with an enough small dimension to fit the dimensions of the pixel (jointed pixels). Insuring small dimensions for the circuit the substrate used is the TMM13i with high permittivity ε=12.2 and thickness equals to 0.381mm with dielectric loss of 0.0019. **Figure II-20** shows the area allowed to print the circuit behind the pixel with dimensions 0.5λx0.5λ.

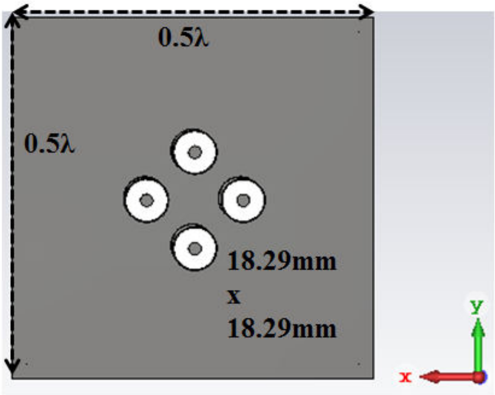

Figure II-20. Pixel bottom view showing the area allowed for the polarization circuit.

IV-4.1 Circuits with two feeding outputs

Two circuits were designed one of microstrip lines and the second with a 90° hybrid coupler. The hybrid coupler insures a high stability in the amplitude and phase balance over a large frequency band in comparison with the classical microstrip transmission lines technique also the input and output impedance (Z_0) is 50Ω **[II-18]**. **Figure II-21** shows the two circuits designed in Momentum software. The dimensions of these circuits are small enough to be printed behind the pixel area.

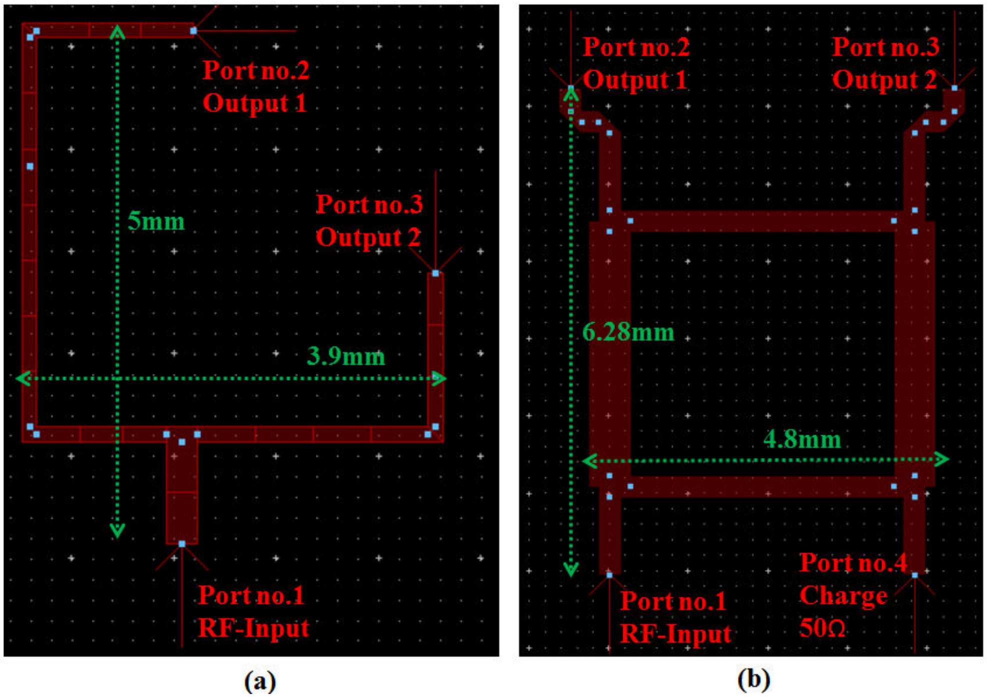

Figure II-21. Two output ports circuits, (a) microstrip lines, (b) 90° hybrid coupler.

Figure II-22 shows the evolution of the magnitudes and phases of the hybrid coupler circuit in terms of frequency, where the maximum magnitude error (mag (out1) - mag (out2) theoretically must be zero) is 0.464dB at frequency of 7.6GHz and the error at the central frequency (8.2GHz) is 0.066dB **(Figure II-22.a)**. The phase shift that should be 90° has an error that is maximum (1.391°) at 7.6GHz and equals to 0.149° at the 8.2GHz **(Figure II-22.b)**.

The adaptation at the input of hybrid coupler and the isolation of the two outputs are given in **Figure II-23** that shows the return loss adapted at a wide band (18%) enough greater than the bandwidth of the pixel presented in **Figure II-15**. Also the output ports are totally isolated over a wideband.

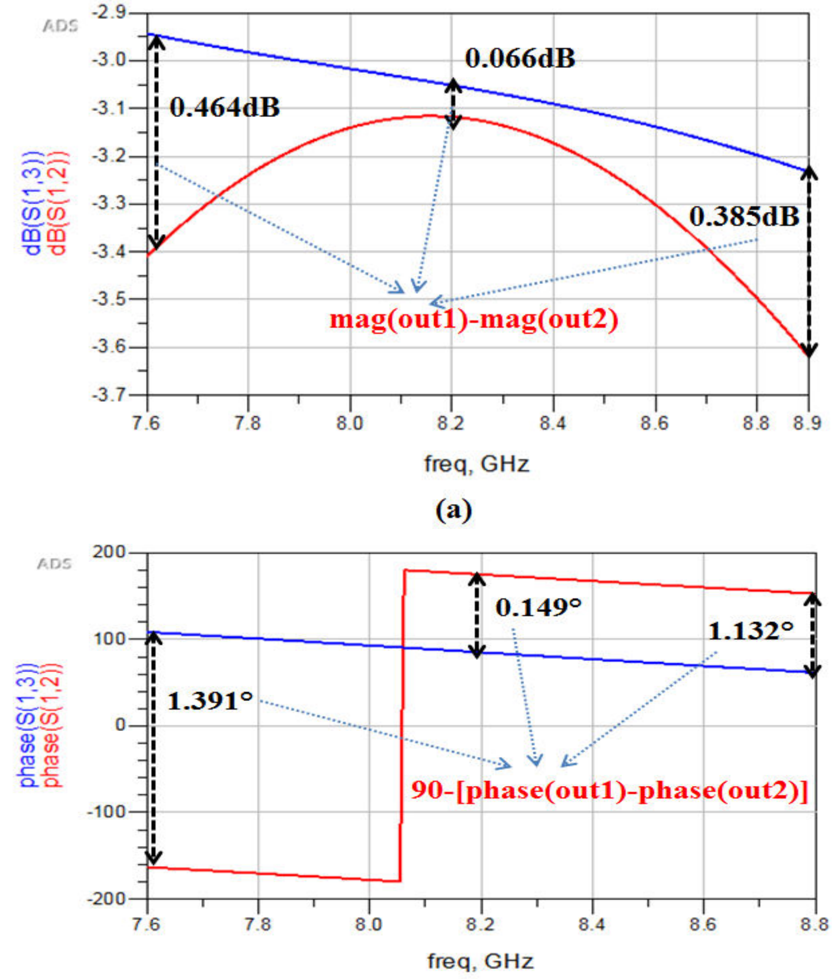

(a)

(b)

Figure II-22. Evolution of the magnitudes and phases of the hybrid coupler outputs in terms of frequency.

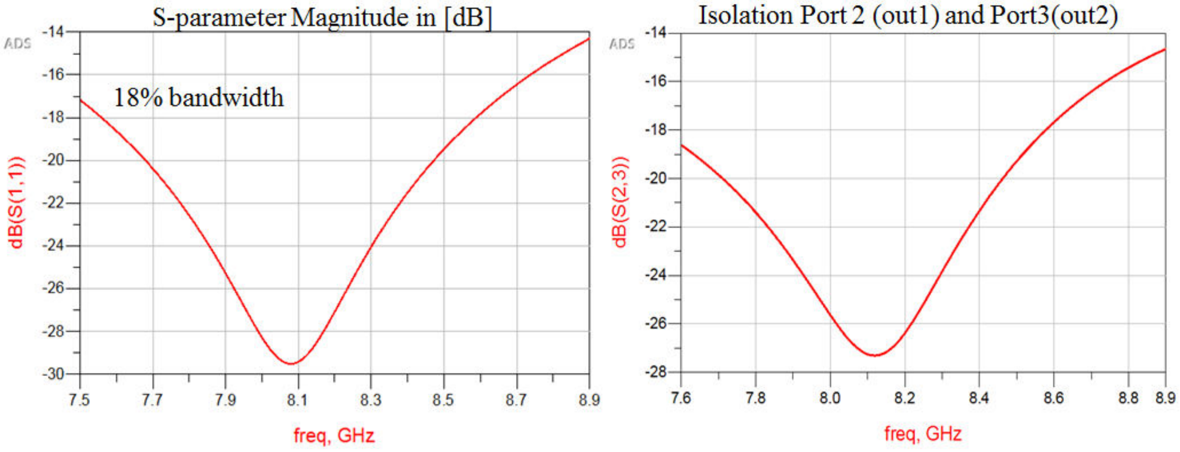

(a) (b)

Figure II-23. (a) S-parameter at the input of the hybrid coupler, (b) isolation of the outputs.

The hybrid coupler results are stable in a wideband, that is why will be used to feed the pixel with patch fed by two ports later in this chapter. However the results of the circuit with microstrip lines at 7.6GHz are worst (1.121dB for magnitude and 15° for the phase) and at 8.2GHz the magnitude and phase errors are 0.2dB and 1° respectively.

IV-4.2 Circuit with four feeding outputs

Several architectures also were tested (microstrip transmission lines, microstrip lines with hybrid coupler, combination of hybrid couplers) the best circuit among will be presented which corresponds for the circuit of three hybrid couplers **(Figure II-24)**. At the input (port no.1) matching impendence is attained by a single stub impendence transformer and the outputs are measured at the ports 2, 3, 4 and 5. The total size of the circuit is 17.3mmx15.8mm that is smaller than the pixel area.

Figure II-25 and **Figure II-26** show the output magnitudes and phases evolution as function of frequency [7.6GHz 8.6GHz], remind that theoretically magnitudes should be all equal to -6dB and the phases should be sequentially shifted from the port no.1 (considered the zero reference) by 90°, 180° and 270°. In **Figure II-25** the maximum error in magnitude is attained at 7.6GHz which is 0.47dB and the error at 8.2GHz is 0.19dB. The label error1, error2 and error3 in **Figure II-26** correspond for the error in phase shift of output ports (3, 4 and 5) with respect to port2.

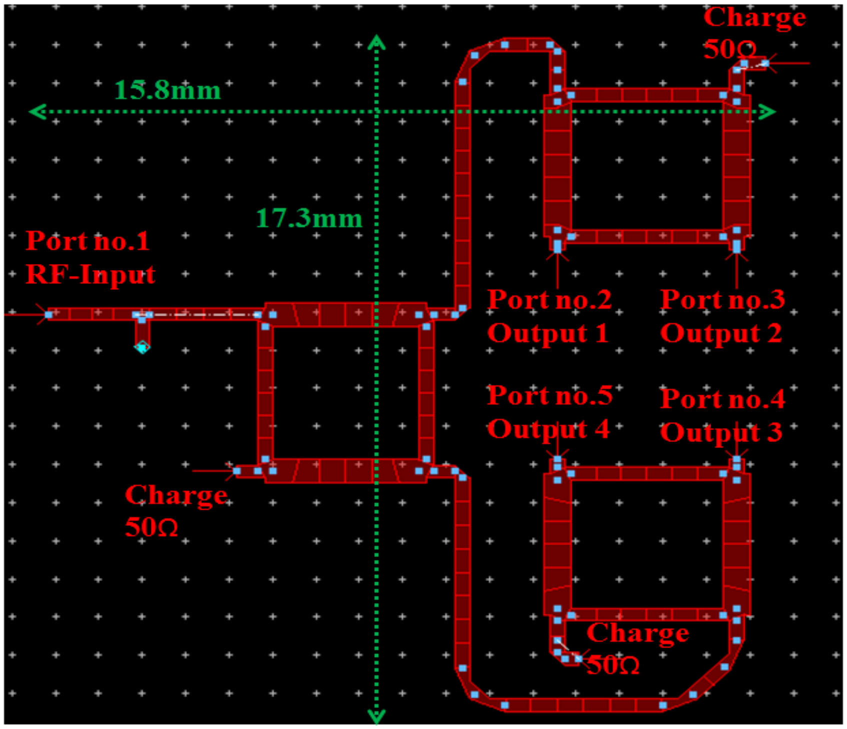

Figure II-24. Circuit with three hybrid couplers to fed the pixel with four ports.

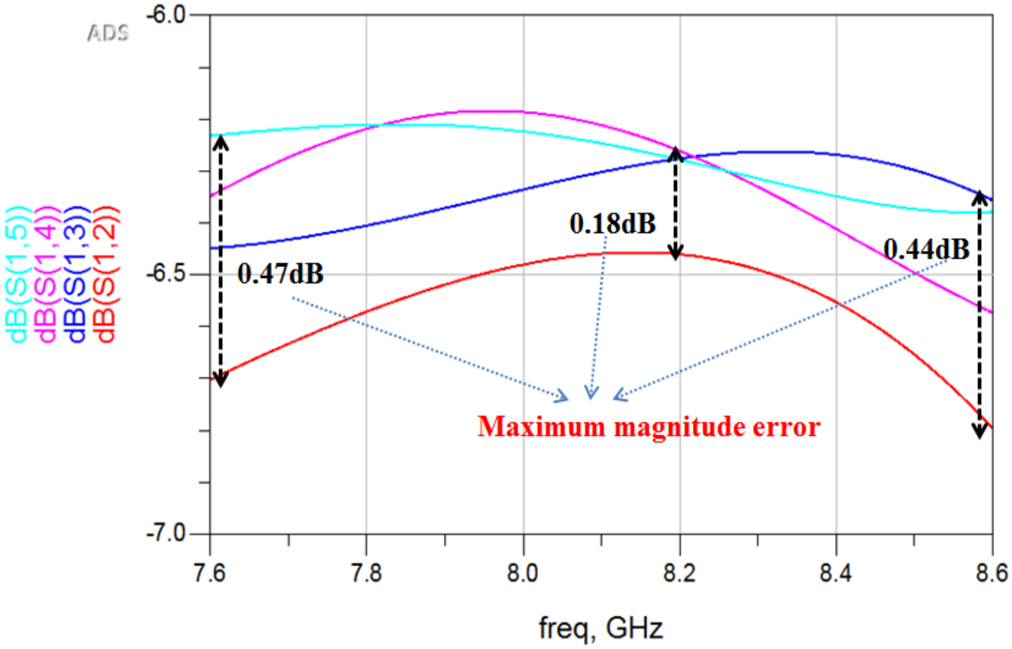

Figure II-25. The output magnitudes of the ports 3, 4 and 5 of the three hybrid couplers circuit.

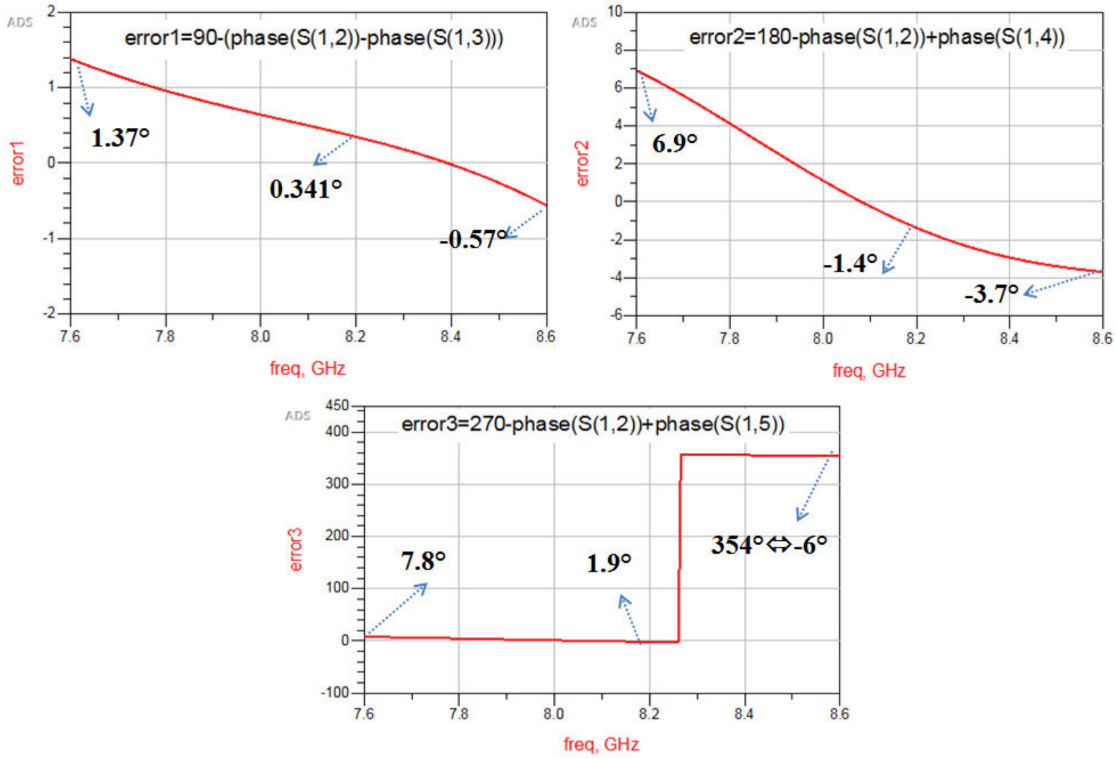

Figure II-26. Phase shift errors of the output ports 3, 4 and 5 of the three hybrid couplers circuit.

Adaptation at the input of the circuit (20%) and the isolation of the output ports are shown in **Figure II-27**. The input is adapted below -14dB for a bandwidth of 1GHz and the ports are well isolated.

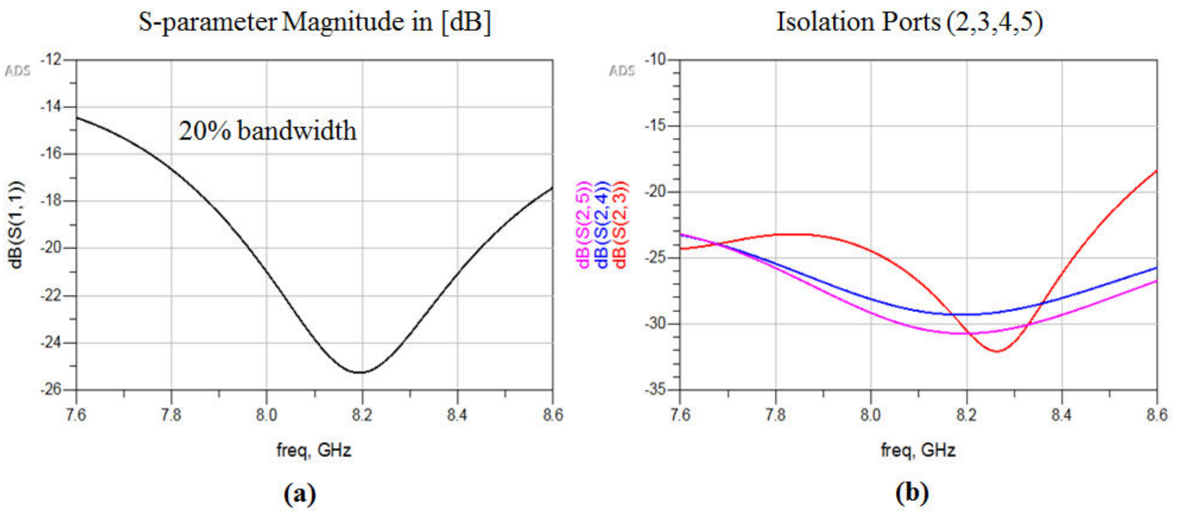

Figure II-27. S-parameters, (a) adaptation at input port1, (b) isolation between of output ports (2, 3, 4 and 5).

IV-4.3 Pixel with patch fed by two ports connected to polarization circuit

Pixel with patch fed by two ports **(Figure II-12)** is connected to the polarization circuit (hybrid coupler **Figure II-21.b**), the circuit results file is taken from Momentum to CST and the schematic is shown in **Figure II-28** with the connectivity of the ports. The adaptation at the input port is given in **Figure II-29** shows a bandwidth of 11%.

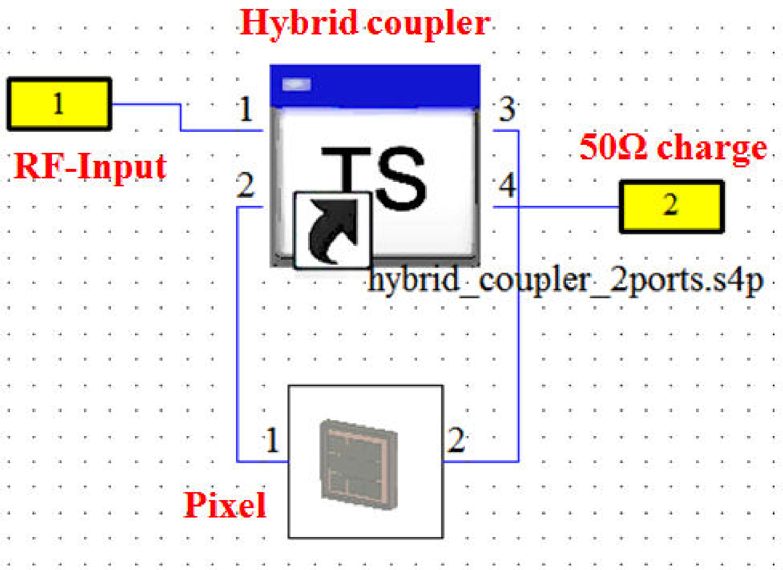

Figure II-28. Pixel and hybrid coupler schematic.

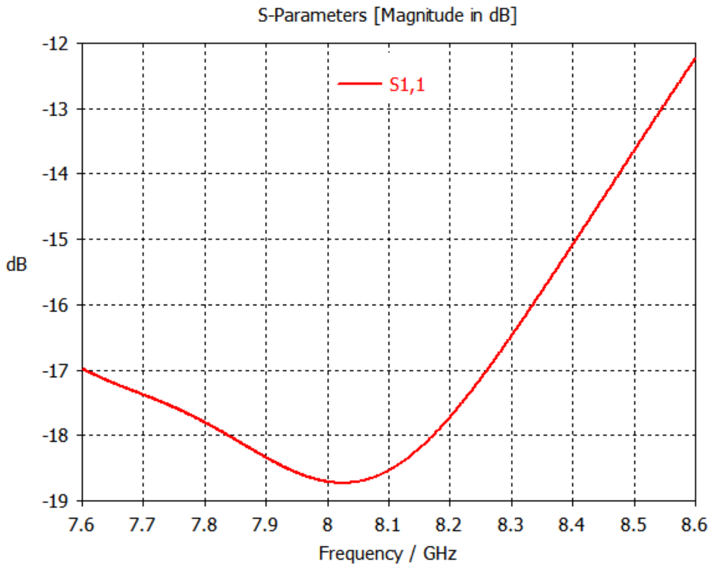

Figure II-29. Adaptation at input of the circuit (hybrid coupler) connected to the pixel (two ports).

The evolution of the gain (in the axial direction) in terms of frequency [7.6-8.6] GHz is given in **FigureII-30**, where the gain varies from 6.2dB to 7.1dB showing the evanescent mode of the pixel. The pixel in the next chapters will not be used alone because this is not the aim of our study, so this result is not exactly the same when the pixel is inside the whole **ARMA** antenna. Gain pattern at different frequencies is given in **Figure II-31**.

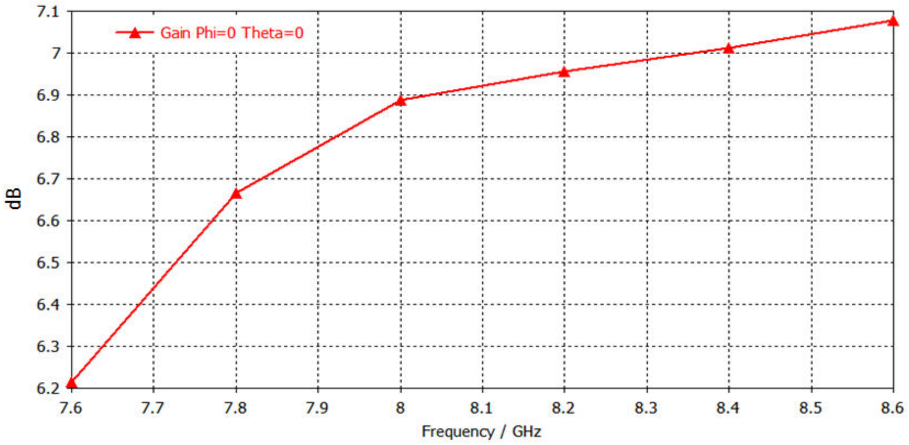

Figure II-30. Gain evolution in terms of frequency of two ports pixel connected to hybrid coupler.

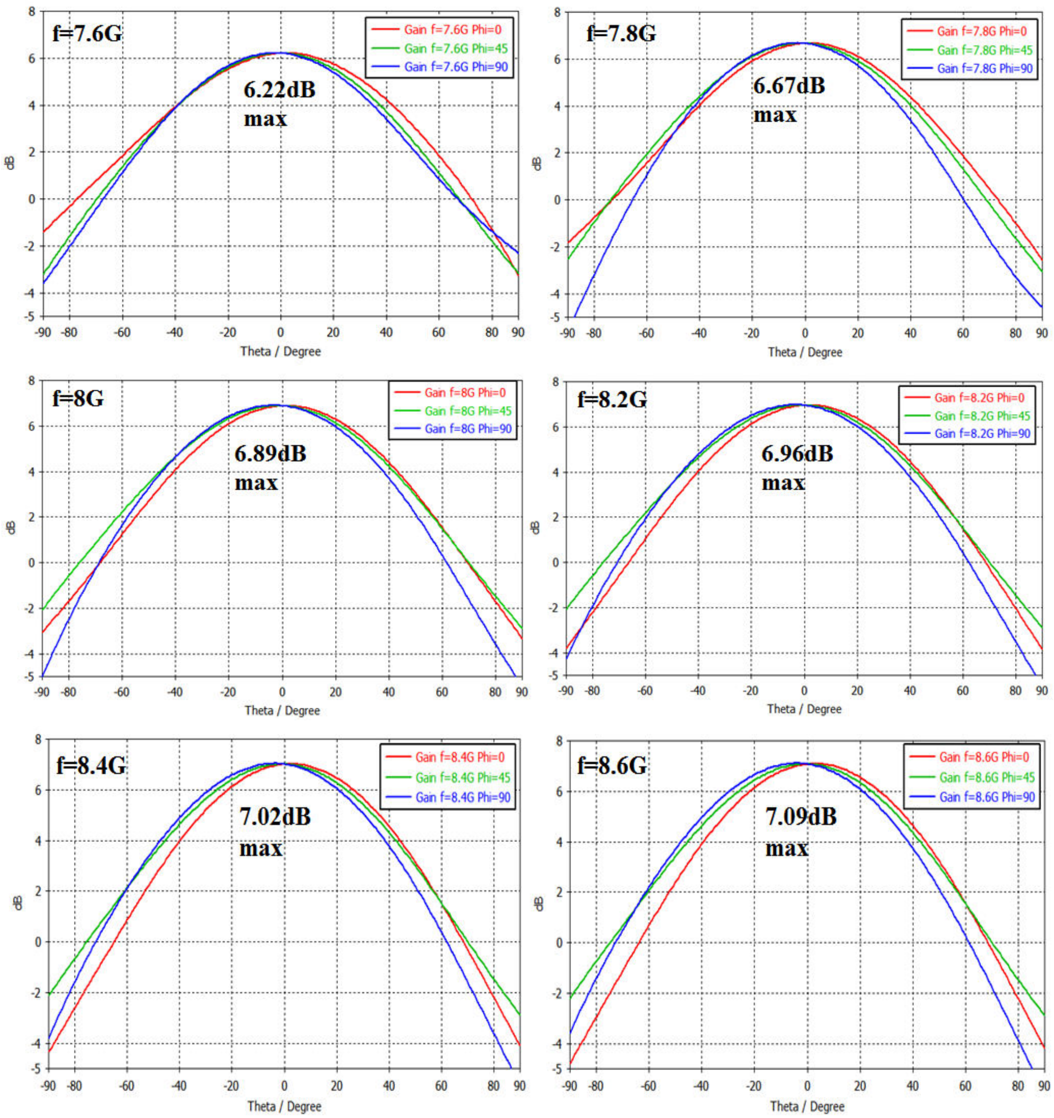

Figure II-31. Gain pattern of two ports pixel with hybrid coupler at different frequencies.

The axial ratio as a function of frequency is given in **Figure II-32**, the choice of the azimuth plane φ=30° and elevation angle θ =47° because it is the worst case for the axial ratio given previously in **Figure II-14.b**, then the azimuth plane φ=0° is taken with different elevation angles (θ=0°, 45° and 60°).

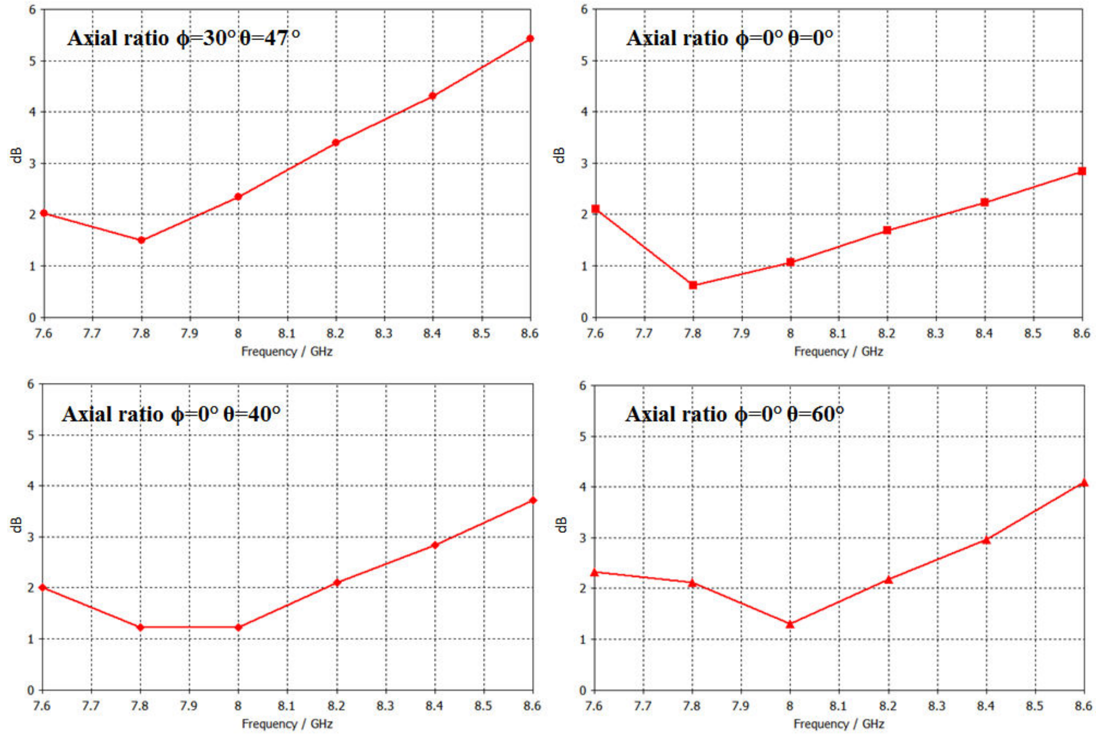

Figure II-32. Evolution of the axial ration with frequency for two ports pixel with hybrid coupler.

IV-4.4 Pixel with patch fed by four ports connected to polarization circuit

Pixel with patch fed by four feeding ports is connected to the polarization circuit (three hybrid couplers **Figure II-24**), the circuit results file is taken from Momentum to CST and the schematic is shown in **Figure II-33** with the connectivity of the ports.

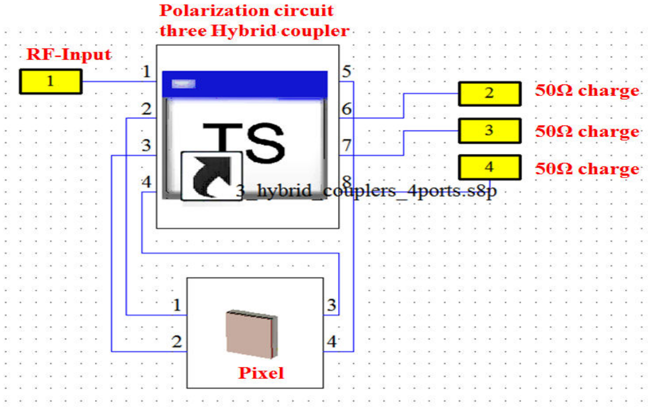

Figure II-33. Pixel four ports and polarization circuit schematic.

The adaptation at the input port is given in **Figure II-34**. The adapted bandwidth is very large (12%) (Greater than 1GHz below the -10 dB, in **Figure II-34** [7.8-8.6] GHz below -17dB) but we have to look for the circular polarization bandwidth that is the bandwidth where the axial ratio remains under the constraint of 3dB. Gain pattern of the pixel connected to the polarization circuit as a function of frequency is shown in **Figure II-35** the gain varies from 6dB to 7.2dB.

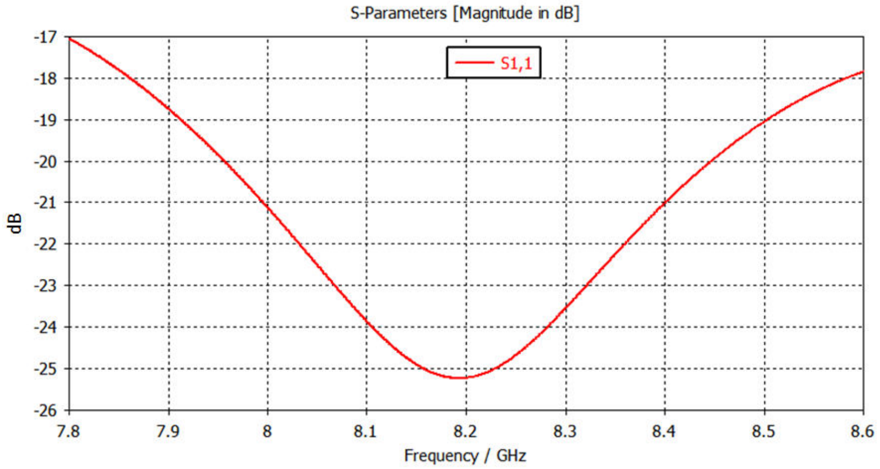

Figure II-34. Adaptation at the input of the circuit connected to the pixel (four ports).

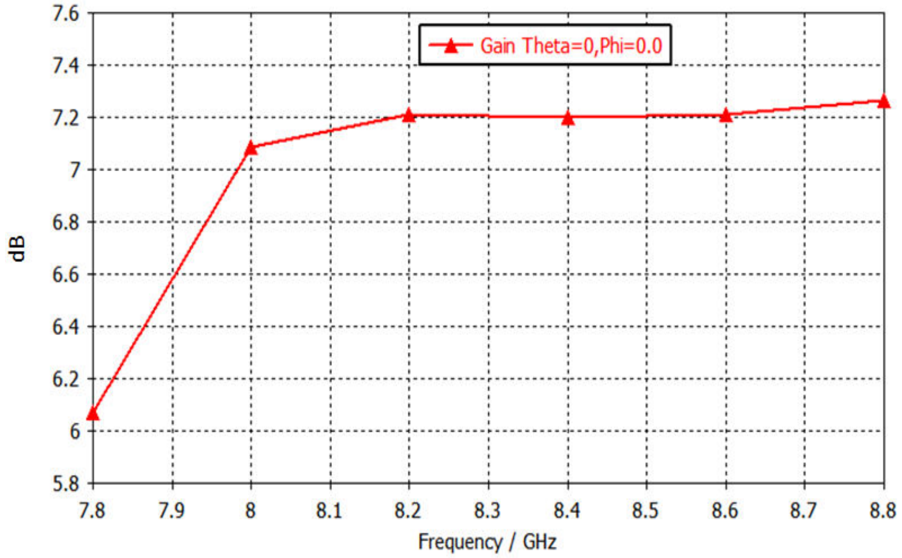

Figure II-35. Gain evolution in terms of frequency four ports pixel connected to polarization circuit.

The gain evolution shown in **Figure II-35** shows that the gain within the bandwidth considered is decreased by 1.2dB from the maximum gain attained in this band. So, the minimum gain is approximately 6dB for the frequency 7.8GHz, 7.25dB at 8.8GHz and 7.2dB at the central frequency (8.2GHz). That is to say that this pixel is characterized by good gain stability over a bandwidth of 1GHz.

Gain patterns in the frequency band [7.8-8.8] GHz with a step of 200MHz are shown in **Figure II-36**, at each frequency the azimuth planes considered are φ=0°, 45° and 90°.

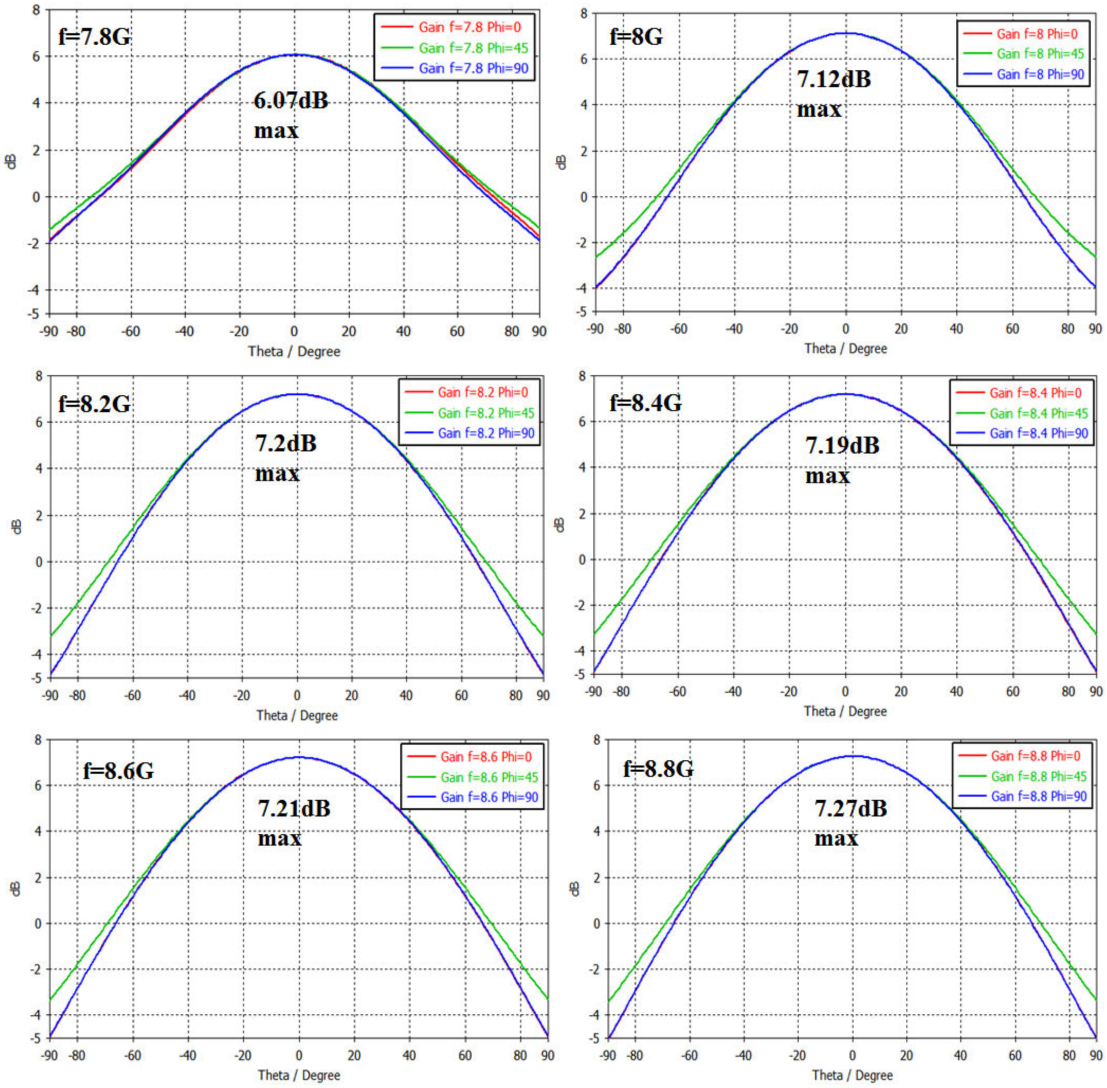

Figure II-36. Gain pattern of two ports pixel with hybrid coupler at different frequencies.

The axial ratio as a function of frequency is given in **Figure II-37** where the azimuth plane is φ=0° and elevation angles vary from θ =0° to θ =65°. The axial ratio is below 3dB for a wideband from 7.8GHz to 8.8GHz for elevation angles between ±65°, this gives a circularly polarized bandwidth of 10%. Then in **Figure II-38** the axial ratio pattern at different frequencies are shown taking the azimuth planes is φ=0°, φ=0° and φ=90°.

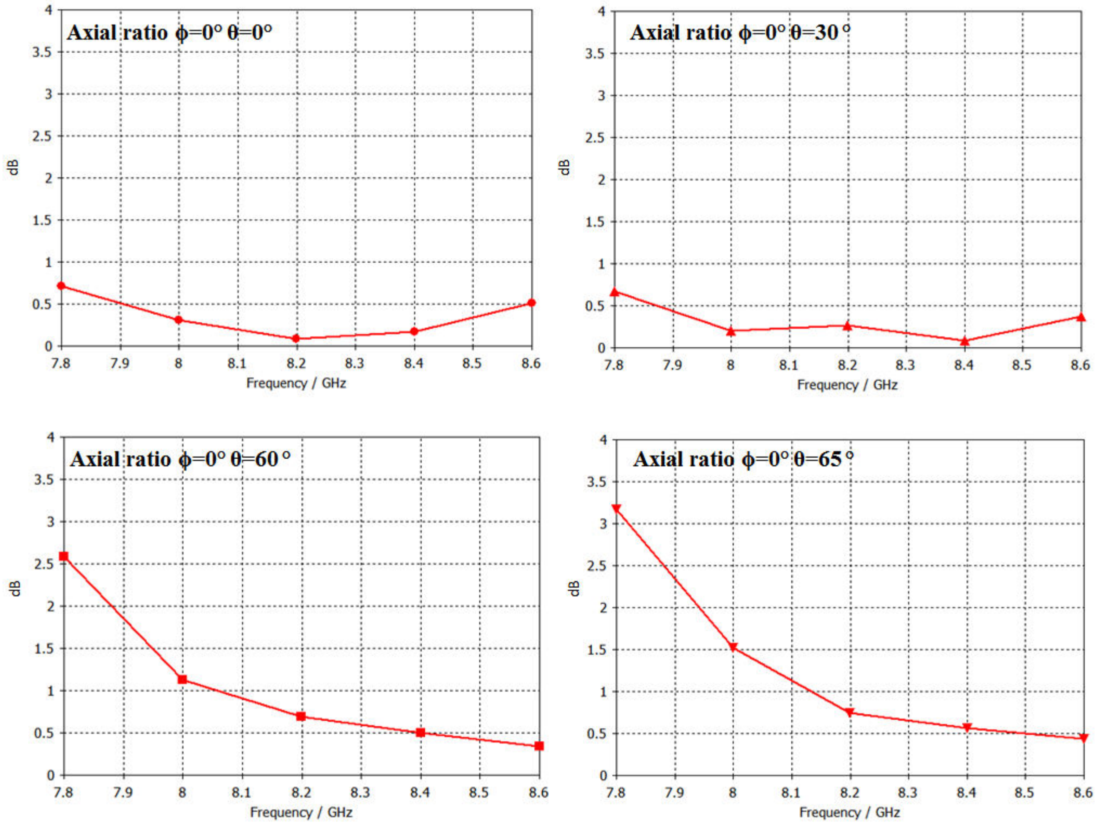

Figure II-37. Evolution of axial ration with frequency for four ports pixel with polarization circuit.

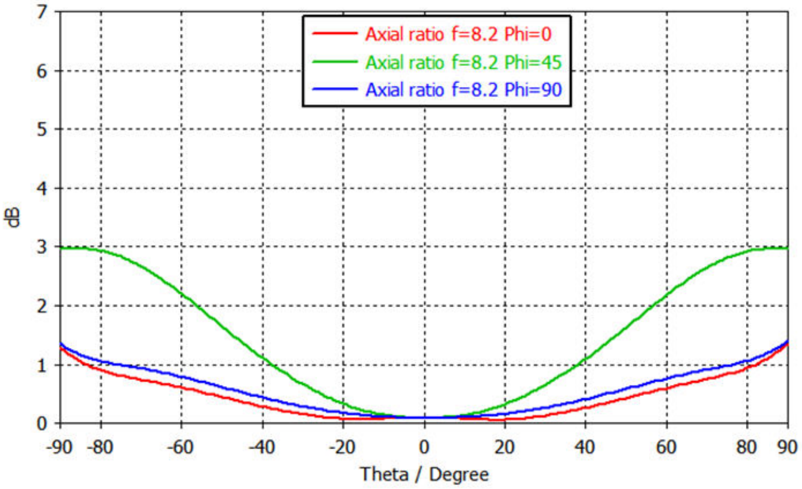

Figure II-38. Axial ratio at 8.2GHz, pixel four ports with polarization circuit.

V. Conclusion

In this chapter the axial ratio and circular polarization were defined and the common used techniques for circularly polarized patch. The pixel derived from the low profile EBG antenna **[II-15]** was fed by a circularly polarized patch (remind that the pixel has uniform radiating surface after the insertion of the metallic walls in the appropriate region), where two techniques were discussed briefly (two and four ports). The circularly polarized pixel in the two cases shows good performances in terms of the gain, axial ratio and bandwidth. However, the pixel with the patch fed by four ports gives a better circularly polarized bandwidth and symmetrical desirable pattern. The polarization circuits using the hybrid couple is the best choice to feed the patch inside the EBG cavity, it shows a high stability in magnitudes and phases for a large band. This gives arise to choose the best solution to be used for circularly polarized **ARMA** that is the pixel with the patch fed by four ports connected to the polarization circuit of three hybrid couplers. This solution shows high adapted bandwidth (12%), high circular polarization bandwidth (10%), good gain stability at wideband and symmetrical radiation and axial ratio patterns. The solution with the two ports and the hybrid coupler could be used for **ARMA** but it depends on the required performances and the application.

Then the circularly polarized pixel studied will not be used alone in this thesis, but to build the whole circularly polarized **ARMA** antenna. However, these circularly polarized pixels could be used alone as an antenna for some applications with the interesting performances mainly the bandwidth and the axial ratio.

In the next **(Chapter III) ARMA** with circular polarization will be shown, presenting the agility in beam forming and a comparison with the classical AESA solution in circular polarization.

VI. Bibliography of Chapter II

[II-1] John L. Volakis, Antenna Engineering Handbook 4th edition, McGraw-Hill, 2007.

[II-2] William, H. Hayt, Jr. John A. Buck, Engineering Electromagnetic 6th edition, McGraw-Hill, 2001.

[II-3] Samuel Silver, Microwave Antenna Theory and Design, McGraw-Hill 1949.

[II-4] Herbert P. Neff Jr., Introductory Electromagnetic, John Wiley & Son, Inc.1991.

[II-5] D. M. Pozar, Microwave and RF Design of Wireless Systems, John Wiley & Son, Inc, 2001.

[II-6] C. A. Balanis, Antenna Theory Analysis and Design 3rd edition, John Wiley & Sons, Inc., 2005.

[II-7] "Corners Truncated Microstrip Patch Antenna", Taha Imeci, Anil Saral Department of Electronics and Communication Engineering Halic University, Istanbul, TURKEY.

[II-8] Dual-Feed Circularly Polarized Microstrip Antenna for S-band Transmitter of Synthetic Aperture Radar (SAR) System. Anggit Dwi Novella, Heroe Wijant, Agus Dwi Prasety, School of Electrical Engineering, Telkom University, Indonesia.

[II-9] A NOVEL DESIGN OF DUAL CIRCULARLY POLARIZED ANTENNA FED BY L-STRIP. G.-L. Wu, W. Mu, G. Zhao, and Y.-C. Jiao National Laboratory of Antennas and Microwave Technology Xidian University, China.

[II-10] Dual circularly-polarized patch antenna using even and odd feed-line modes. Adam Narbudowicz, Student Member, IEEE, Xiulong Bao, Senior Member, IEEE, and Max J. Ammann, Senior Member, IEEE. AP1211-1588.R1.

[II-11] Terrance J. Hawkins, Frank Butscher, Lockheed Martin Space Systems Company Sunnyvale, CA. Sunnyvale, CA. "Frequency Scalable, Low Profile, Broadband Quad Fed Patch Element/Array". 28th AIAA International Communications Satellite Systems Conference (ICSSC-2010) 30 August - 2 September 2010, Anaheim, California.

[II-12] Flower Shaped Slotted Microstrip Patch Antenna for Circular Polarization. Vikrant Kaim, Amit Birwal, R. K. Jaiswal, K. R. Ranjan, Kamlesh Pate, IOSR Journal of Electrical and Electronics Engineering (IOSR-JEEE), Volume 11, Jan – Feb. 2016.

[II-13] Slotted Microstrip Antennas for Circular Polarization with Compact Size. Nasimuddin, Zhi Ning Chen, and Xianming Qing, Institute for Infocomm Research Singapore.

[II-14] Circularly Polarized Slotted/Slit-Microstrip Patch Antennas. Nasimuddin, Zhi-Ning Chen and Xianming Qing Institute for Infocomm Research Singapore.

[II-15] R. Chantalat, L. Moustafa, M. Thevenot, T. Monédière and B. Jecko, **“Low Profile EBG Resonator Antennas”**, Hindawi Publishing Corporation, International Journal of Antennas and Propagation, Volume 2009, Article ID 394801, 7 pages.

[II-16] Marwa Shakeeb, **“Circularly Polarized Microstrip Antenna”**, thesis in the Department of Electrical and Computer Engineering Concordia University.

[II-17] Akshay Goyal, Aastha Gupta, Lavi Agarwal, **“A Review Paper on Circularly Polarized Microstrip Patch Antenna”**, **International** Journal of New Technology and Research (IJNTR) ISSN:2454-4116, Volume-2, Issue-3, March 2016.

[II-18] Design of Hybrid Coupler. International Journal of Advanced Research in Electrical, Electronics and Instrumentation Engineering. T.Jayachitra, V.K Pandey and Anshuman Singh, Noida Institute of Engineering and Technology, Greater Noida, UP, India.

List of Figures

Chapter III
Circularly Polarized ARMA Performances

Table of Contents

I. Introduction

Chapter I illustrates the performances of **ARMA** that overcome AESA limitations in linear polarization (radiation surface efficiency, gain as a function of elevation angle, couplings, high axial gain etc…). Then in **Chapter II** the circularly polarized pixel was studied to be used in the circularly polarized **ARMA**. Then in this chapter the objectives are as follows:

- Firstly, comparison of the pixel and patch antenna in circular polarization. Normally the pixel is not used alone (**ARMA** is formed by jointed pixels each has a uniformly radiating surface), but for the aim of comparison with the circularly polarized patch antenna with a given ground plane we consider the pixel alone with the same dimensions.
- Secondly, the beam steering of the two approaches will be compared by considering 1D architecture for each of the same parameters and dimensions. The main parameters to be considered in comparison are the axial ratio, axial ratio as a function of steering angles and bandwidth.
- Thirdly, beam forming comparison taking an example, the well-known “Isoflux” beam. Definition of the isoflux radiation pattern used by satellites at low earth orbits will be described and considered. So, the AESA **ARMA** comparison in beam forming will be done by taking this example of 1D isoflux radiation pattern. The main comparison will be shown regarding the maximum gain, the position of the elevation angles of this maximum gain and the axial ratio.
- Finally, 2D **ARMA** will be used for the aim of beam forming; the example of the 1D Isoflux beam forming with circular polarization will be extended to 2D Isoflux using 2D square **ARMA**.

II. Circularly polarized pixel performances comparison with patch antenna

Consider the pixel and patch antenna located on the ground plane with same dimensions (0.5λx0.5λ) fed by four ports with sequential phase shifts of 0°, 90°, 180° and 270°. Both designed to work in the X-band at the central frequency 8.2GHz. Architectures are shown in **Figure III-1** and **Figure III-2**.The parameters of the designs of both antennas are as follows:

- Central frequency 8.2GHz.
- Patch antenna and feeding patch inside the EBG cavity substrate: RO6002 with permittivity 2.94 and tangent loss of 0.002.
- FSS substrate RO6002 for the pixel.
- Substrate of patch antenna, substrate of feeding patch inside the EBG cavity, FSS substrate, same height 1.524mm.

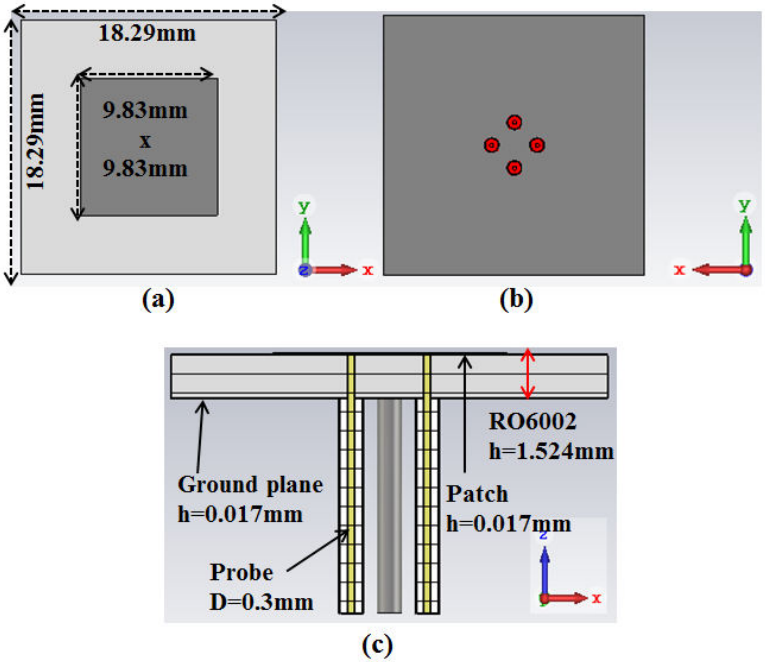

Figure III-1. Patch antenna, (a) top view, (b) bottom view, (c) cut view along y.

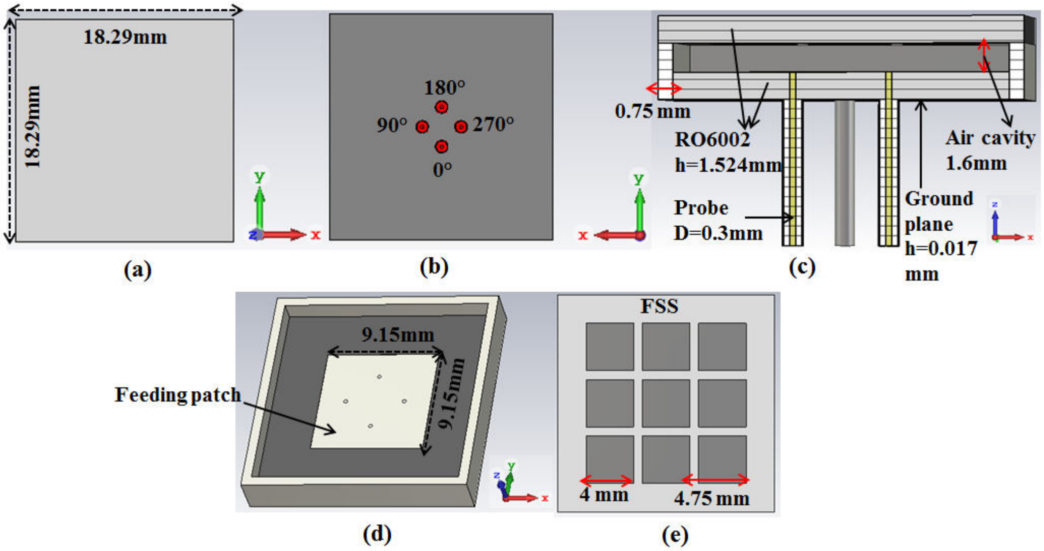

Figure III-2. Pixel, (a) top view, (b) bottom view, (c) cut view along y, (d) feeding patch inside EBG cavity, (e) FSS dimensions.

In what follows a comparison of the results is achieved using the two architectures of **Figure III-1** and **Figure III-2**. Comparison will be done on the radiating surfaces, bandwidth, gain, angular aperture, axial ratio and frequency dependence.

II-1 Radiating surface

The pixel and patch antenna radiating surfaces are compared in **Figure III-3** where the magnitude of the electric field on the surface of the patch attains its maximum at the patch edges and is zero at the center of the patch, however the pixel has a uniform radiating surface inside the area limited by the metallic walls. This uniformity, as described in **Chapter I** is used in the new sampling procedure of **ARMA**, is the same now but will be used to generate circular polarization field.

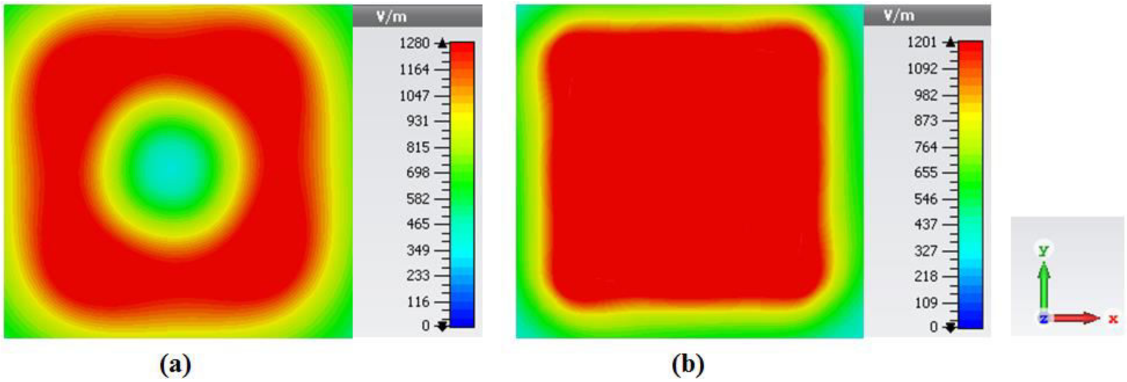

Figure III-3. Radiating surfaces circular polarization, (a) patch antenna, (b) pixel.

II-2 Bandwidth

Return loss parameter at one of the ports is compared in **Figure III-4**; it shows an improvement of the bandwidth for the pixel in comparison with the patch. Pixel bandwidth is 985MHz (12%) and patch bandwidth is 423MHz (5.1%), this high bandwidth of the pixel is due to the low profile EBG cavity **[III-1]**.

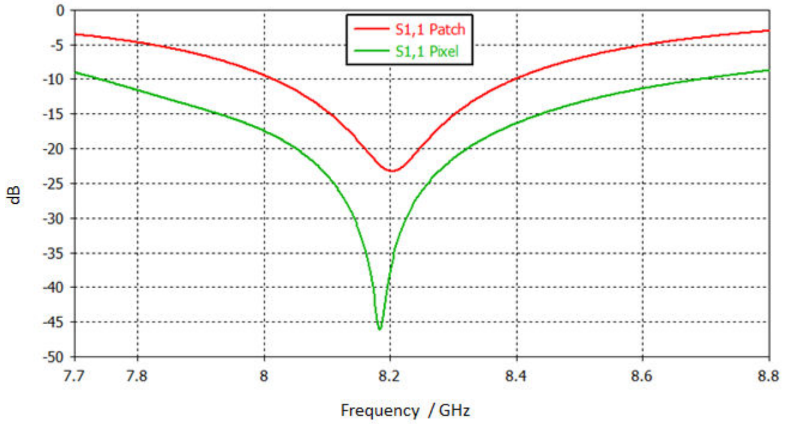

Figure III-4. Adapted bandwidth, (green curve) pixel, (red curve) patch antenna.

II-3 Radiation pattern

The frequency evolution of the maximum gain given in **Figure III-5** shows a higher gain for the pixel compared to the patch antenna in a wideband around the central frequency 8.2GHz. The gain of the pixel is higher by 0.5dB at 8.2GHz and 1.7dB at 8.6GHz. This gives a higher gain balance for the pixel in comparison with the patch antenna. Then the gain at 8.2GHz for the azimuth plane φ=0° is given in **Figure III-6**, the pixel gain is 7.19dB with an angular aperture 82° however the patch antenna gain is 6.69dB with an angular aperture 90°.

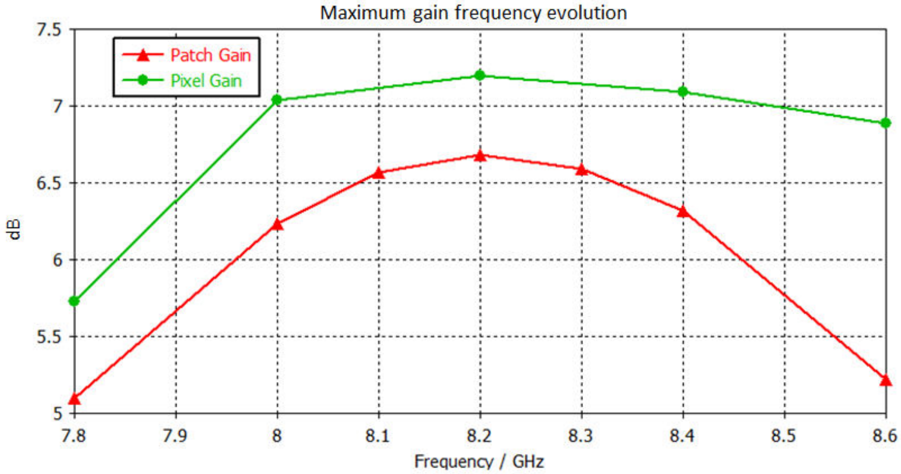

Figure III-5. Maximum gain evolutions function of frequency, (green curve) pixel, (red curve) patch antenna.

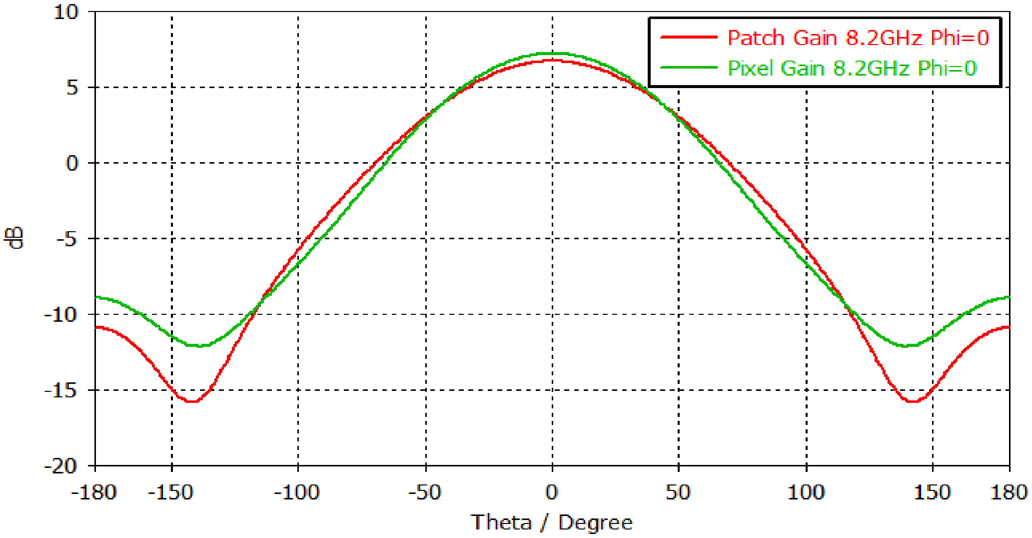

Figure III- 6 Gain at 8.2GHz for azimuth plane φ=0°, (green curve) pixel, (red curve) patch antenna.

II-4 Axial ratio

The axial ratio of the pixel and patch antenna is given at different frequencies 8GHz, 8.2GHz and 8.4GHz for different azimuth planes φ=0°, φ=30°, φ=45° and φ=60° in **Figure III-7**. The pixel shows better axial ratio that is below 3dB for the elevation angles between θ=±90° in the entire considered band. However the patch antenna axial ratio is higher than 3dB for some azimuth planes. These results are not very significant if we consider the pixel alone since for the far elevation angles outside the angular apertures (given in the paragraph II-3) the gain is not high meaning that the pixel and the patch antenna radiation gain is low. But the pixel better axial ratio will prove in this chapter its importance when used in the whole circularly polarized **ARMA** antenna for the aim of agility in beam steering and beam forming.

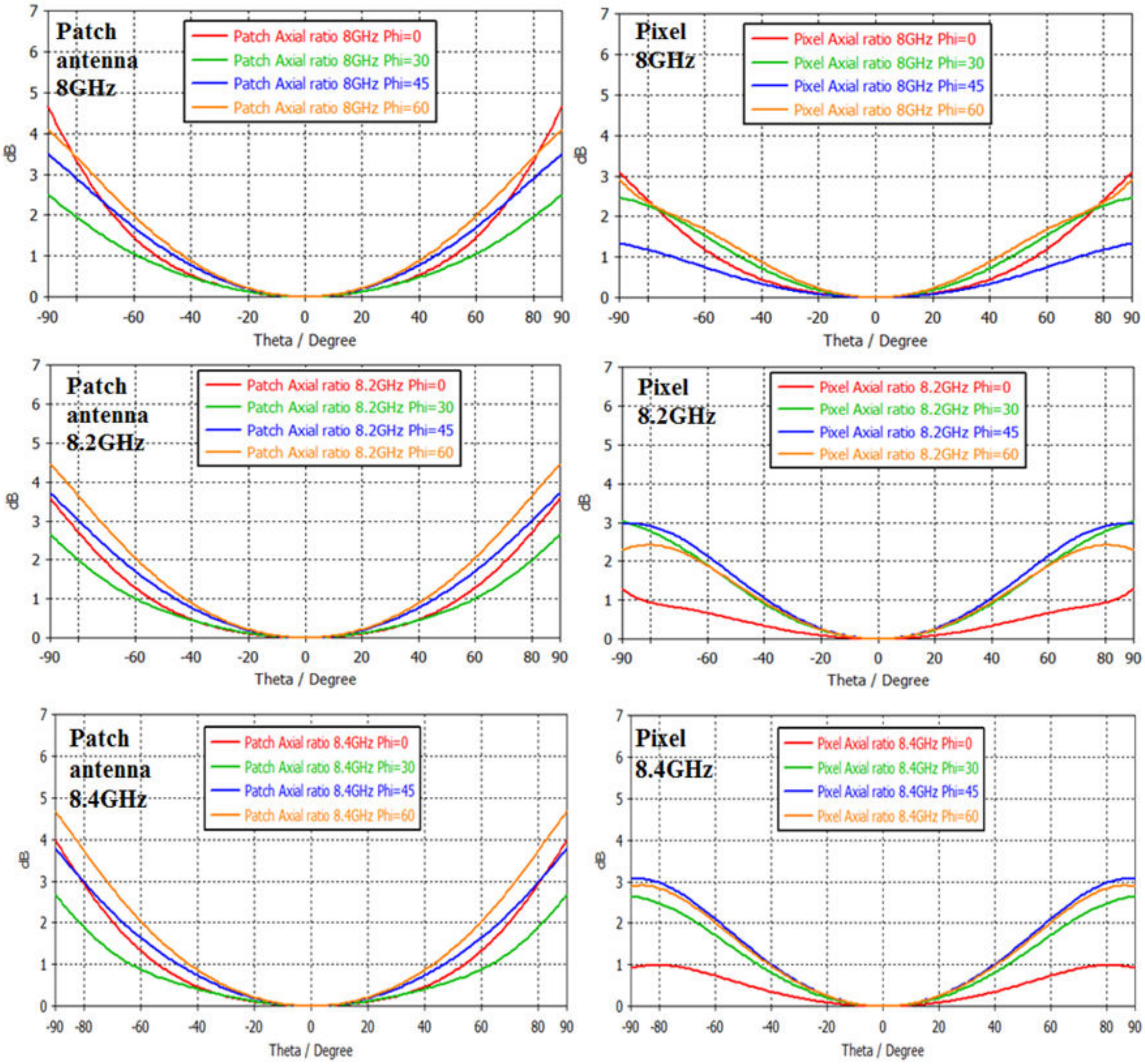

Figure III-7. Axial ratio comparison of the pixel and patch antenna.

II-5 Coupling of the adjacent elements

To compare the coupling of the adjacent elements in **ARMA** and AESA, 1x5 **ARMA** and AESA of the same dimensions (0.5λ spacing with central functioning frequency at 8.2GHz) are used both with circular polarization attained by the four ports for each element. **Figure III-8** shows the two antennas from bottom view, the label of the ports and the comparison of the couplings (adjacent ports are considered for comparison). Couplings effect of **ARMA** is lower by 2dB than AESA.

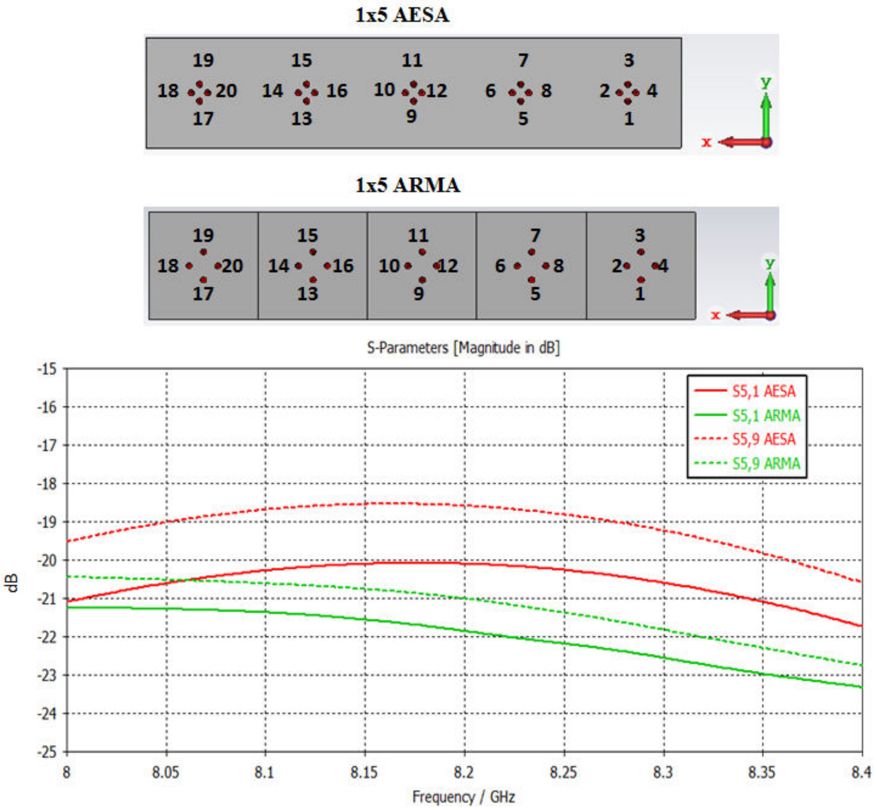

Figure III-8. 1D ARMA and AESA bottom view with ports labeling and couplings comparison, (solid curves) AESA, (dashed curves) ARMA.

III. Circularly polarized ARMA and AESA performances comparison in beam steering

III-1 Circularly polarized ARMA and AESA designs

For the aim of beam steering, one dimensional **ARMA** and AESA antennas are considered with large number of elements, 1x17 patches antenna for AESA 1x17 pixels for **ARMA**. The used patch antenna and pixel dimensions (0.5λx0.5λ) and parameters are as described previously in **paragraph II** (working in the X-band at the central frequency 8.2GHz), these designs with the four feeding ports gives circular polarization radiation patterns. The architectures of the **ARMA** and AESA are shown in **Figure III-9** and **Figure III-10** will be used for the aim of beam steering. The patches printed on the substrate in AESA **(Figure III-10.a)** have not exactly the same dimensions as in **ARMA (Figure III-9.c)** but both the pixel (inside **ARMA**) and patch antenna (inside AESA) works at the same frequency 8.2GH. The patch inside the pixel is used as an electromagnetic source to feed the EBG cavity (we can have another type of source antennas like dipole, etc.). Comparison of these two approaches will be presented regarding the adapted bandwidth, couplings, steering beams and axial ratio.

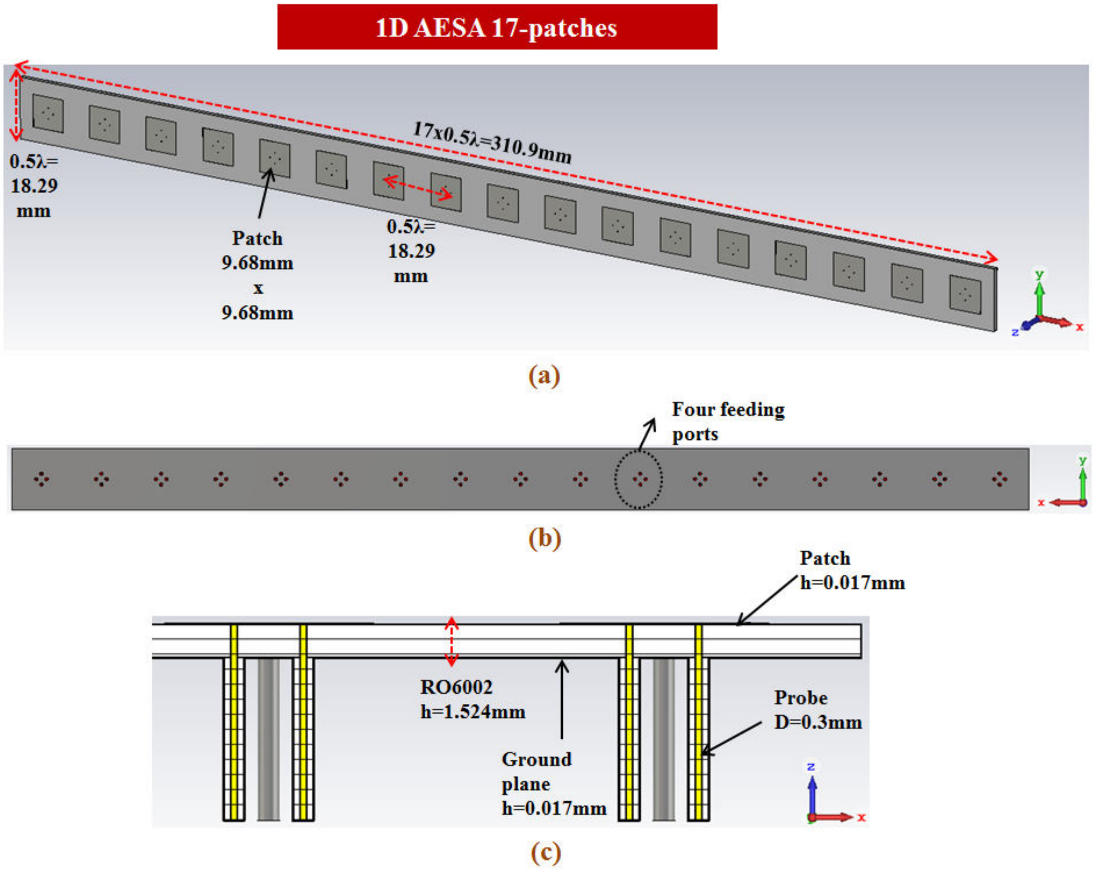

Figure III-9. 1D AESA 17-patches, (a) Perspective view, (b) Bottom view, (c) cut view along y.

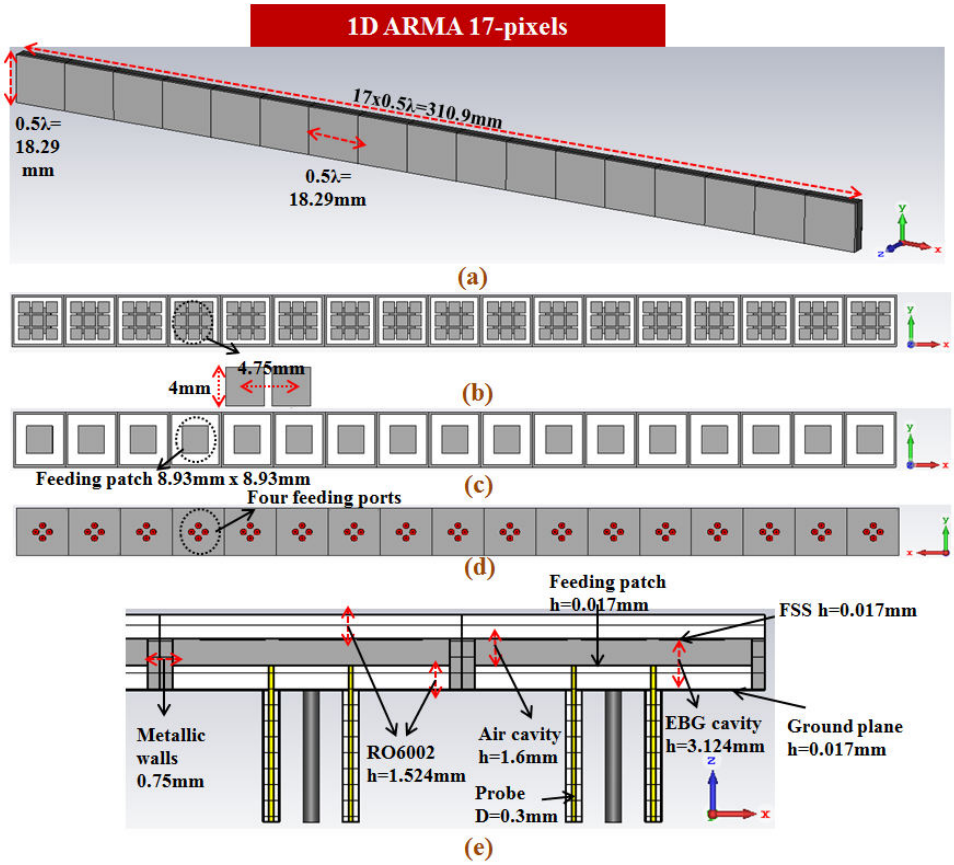

Figure III-10. 1D ARMA 17-pixels, (a) perspective view, (b) top view show FSS, (c) top view show feeding patch inside the EBG cavity, (d) cut view along y.

III-2 Bandwidth

The bandwidth of **ARMA** and AESA are shown in **Figure III-11**. The return loss parameter at the central pixel and the central patch antenna inside the matrices were considered, where the S-parameter is taken at one of the four ports in each. The **ARMA** bandwidth is 893MHz (10.8%) where in AESA the bandwidth is 320MHz (3.9%). Remind that the high bandwidth in **ARMA** is due to the low profile EBG cavity **(**λ/12**) (Figure III-10.e** EBG cavity height is 3.124mm**) [III-1]**.

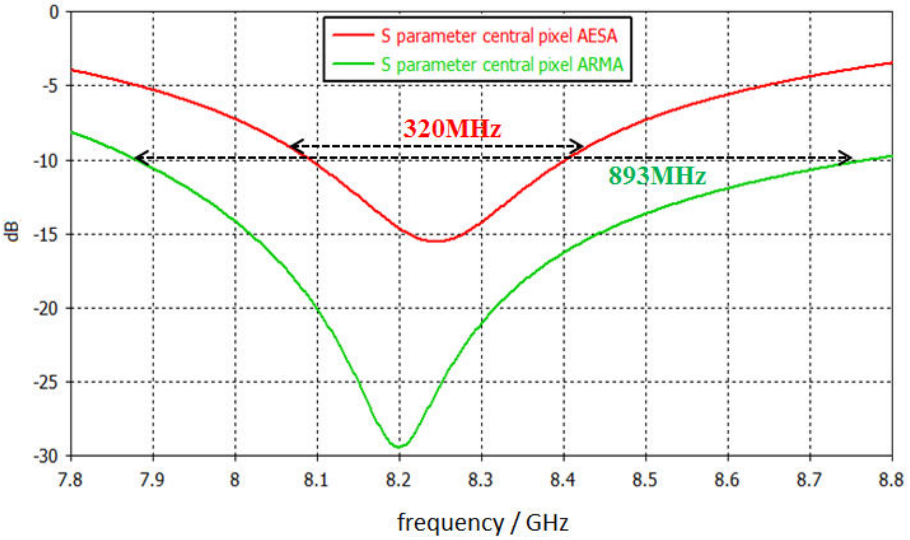

Figure III-11. S-parameter central element, (green curve) ARMA (10.8% bandwidth), (red curve) AESA (3.9% bandwidth).

III-3 Radiating surface

Radiating surface of AESA contains dis-continuities, where the magnitude of the electric field is zero between the elementary patch antennas as shown in **Figure III-12.a**, also the electric field magnitude at the center of each patch antenna is zero and tends to its maximum at the patch edges. In **ARMA** the magnitude of the electric field is uniform all over the antenna, remind that **ARMA** is formed by connected pixels where each has uniform radiating surface. Then the **Figure III-12.b** follows the new sampling procedure described briefly in **Chapter I (paragraph IV-2)**, but now this radiating surface will generate circularly polarized patterns. The electric field of **ARMA** is slightly lower than that of AESA but have uniform shape, that is why the gain in **ARMA** is not very high than that of AESA (shown in the next paragraphs)

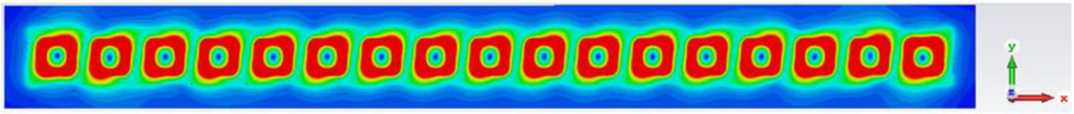

(a)

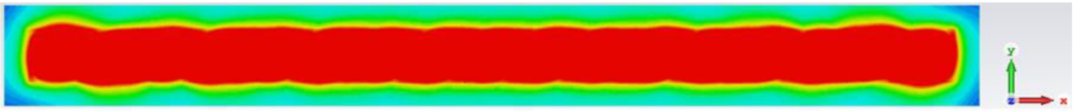

(b)

Figure III- 12. Radiating surface electric field magnitude, (a) AESA, (b) ARMA.

III-4 Steering beams and axial ratio

ARMA solution in this thesis is used for circular polarization beam steering and beam forming. The well-known AESA solution does the same; in this paragraph the two solutions are compared with respect to circularly polarized steering beams where the axial ratio as a function of the steering angles is the main objective in this comparison. For the aim of beam steering pixels are fed by equally amplitudes phase shifted weights. The first pixel is considered the zero reference for the phase and the rest are fed according to the law in **Table III-1**. The phase shift "α" in **Table III-1** is calculated according to **[Eq.III-1]** where θ_s is the elevation steering angle. For AESA the same feeding law is used as **ARMA**.

$$\alpha = -180 \sin \theta_s. \qquad \textbf{[Eq.III-1]}$$

	Pixel no.1	Pixel no.2	Pixel no.3	Pixel no.4	Pixel no.5	Pixel no.6	Pixel no.7	Pixel no.8
Magnitude	1	1	1	1	1	1	1	1
Phase	0	α	2α	3α	4α	5α	6α	7α
	Pixel no.9	Pixel no.10	Pixel no.11	Pixel no.12	Pixel no.13	Pixel no.14	Pixel no.15	Pixel no.16
Magnitude	1	1	1	1	1	1	1	1
Phase	8α	9α	10α	11α	12α	13α	14α	15α
	Pixel no.17							
Magnitude	1							
Phase	16α							

Table III-1. Feeding law for the ARMA and AESA steering angles.

Figure III-13 shows the gain and axial ratio patterns for the steered beams obtained by **ARMA** and AESA antennas (described in **Figure III-9** and **Figure III-10**). The steering angles considered for θ_s are 0° **(Figure III-13.a)**, -30° **(Figure III-13.b)**, -50° **(Figure III-13.c)** and -70° **(Figure III-13.d)**. These results are obtained at 8.2GHz for the azimuth plane φ=0° where for each steered beam the axial ratio is shown inside the interesting zone which is the angular aperture of the steered beam. The gain evolution is the same for **ARMA** and AESA as a function of steering angle in circular polarization, however with **ARMA** the axial ratio is always better where for AESA it becomes worst especially for the far steering angles higher than ±50°. Notice that, for the steering angle at -70° **(Figure III-13.d)** we start having significant grating lobes for AESA and pixel lobes for **ARMA** at the elevation angle +84°, in **ARMA** the pixel lobes is lower than the AESA grating lobes by 4dB.

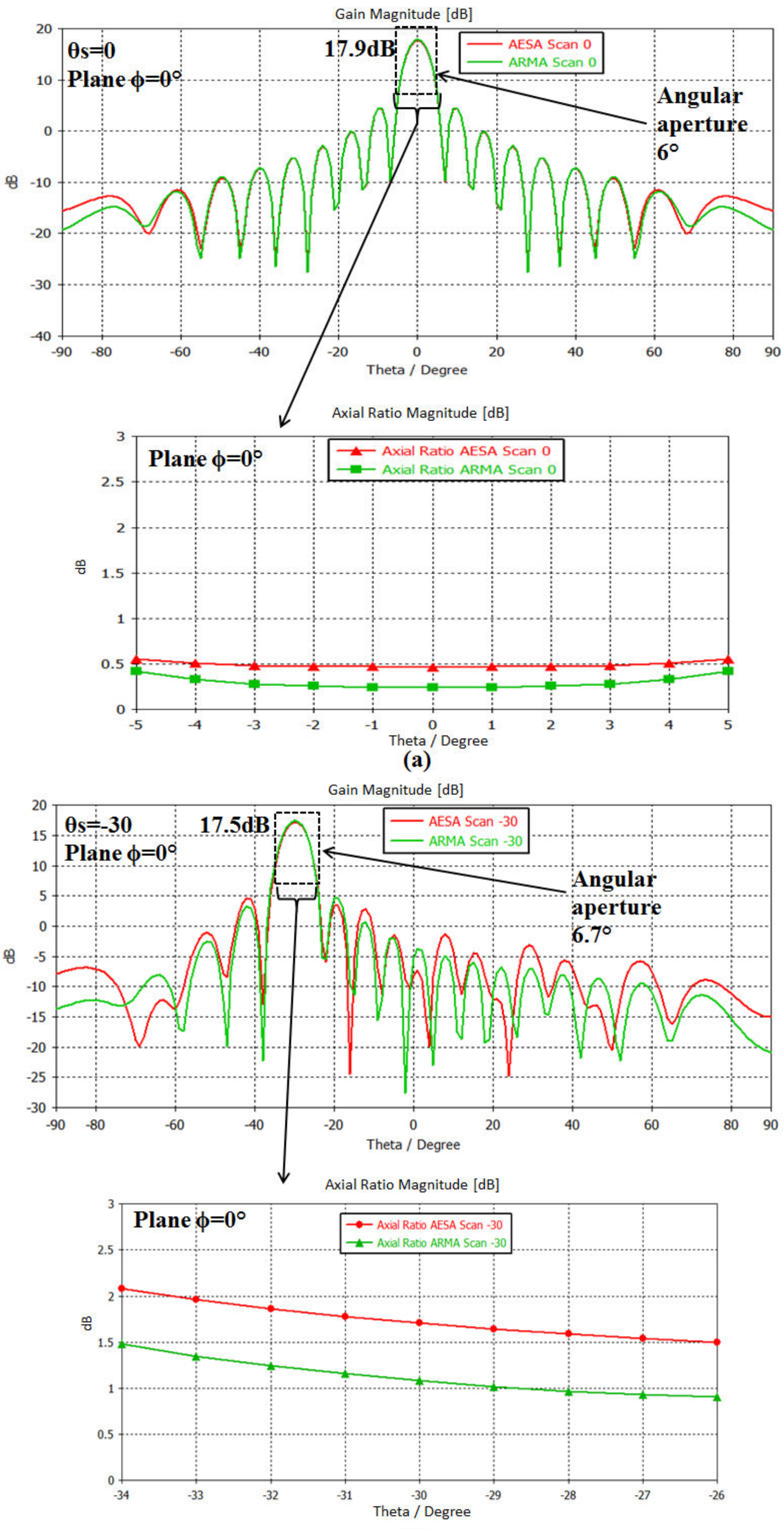
Gain Magnitude [dB]
θs=0
Plane ϕ=0°
17.9dB
AESA Scan 0
ARMA Scan 0
Angular aperture 6°
dB
Theta / Degree
Axial Ratio Magnitude [dB]
Plane ϕ=0°
Axial Ratio AESA Scan 0
Axial Ratio ARMA Scan 0
dB
Theta / Degree
Gain Magnitude [dB]
θs=-30
Plane ϕ=0°
17.5dB
AESA Scan -30
ARMA Scan -30
Angular aperture 6.7°
dB
Theta / Degree
Axial Ratio Magnitude [dB]
Plane ϕ=0°
Axial Ratio AESA Scan -30
Axial Ratio ARMA Scan -30
dB
Theta / Degree

(a)

(b)

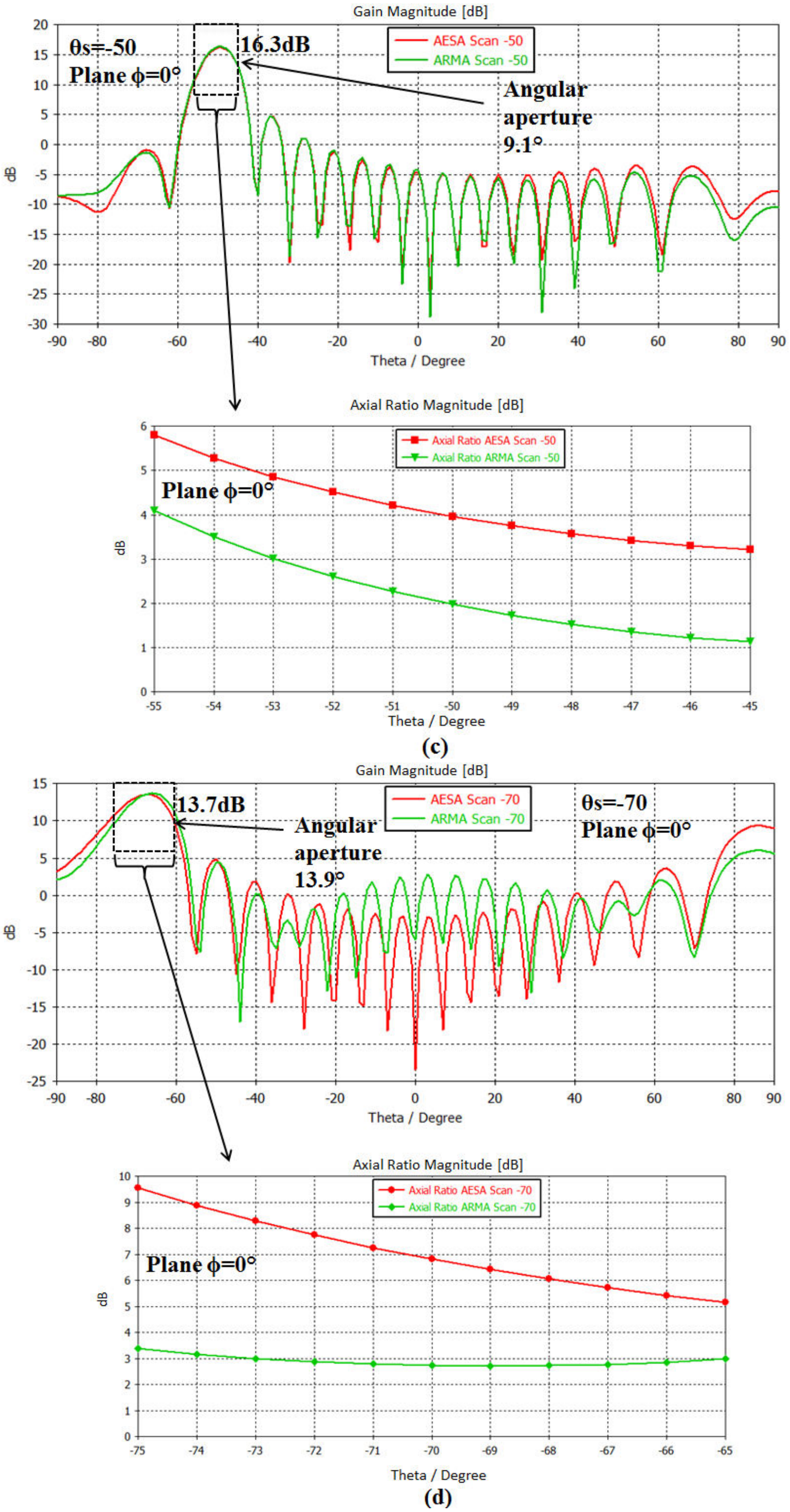

Figure III-13. Steering beams and axial ratio ARMA (green curves) and AESA (red curves), (a) $\boldsymbol{\theta s}$=0°, (b) $\boldsymbol{\theta s}$=-30°, (c) $\boldsymbol{\theta s}$=-50°, (d) $\boldsymbol{\theta s}$=-70°.

IV. Circularly polarized ARMA and AESA performances comparison in beam forming

IV-1 1D ARMA and AESA for Isoflux beam forming

In this paragraph the two antennas **ARMA** and AESA will be used for beam forming, the beam considered is well-known as “Isoflux” **([III-2] [III-3] [III-4])**. This type of radiation pattern is essential in many space applications for the earth observation and telecommunication between terrestrial and satellites data links. If we consider a satellite in the low earth orbit (LEO) far 800km from the earth, then the gain pattern “Isoflux” must follow special conditions with maximum radiation at far elevation angles ±60° and minimum in the axial direction, such that the power under the effect of many losses mainly the path loss, is received at the earth data links with equal power **(Figure III-14.a)**. Then the gain pattern follows the template given in **Figure III-14.b** with minimum and maximum gain masks.

Main constraint in the space application is the circular polarization, it is essential to insure good connection for the end to end links since the signal travelling in the space will be subjected to many orientations. Thus circularly polarized antennas at the satellites and at the earth stations can overcome this problem. For that circularly polarized **ARMA** is a good candidate for circularly polarized beam forming in space applications.

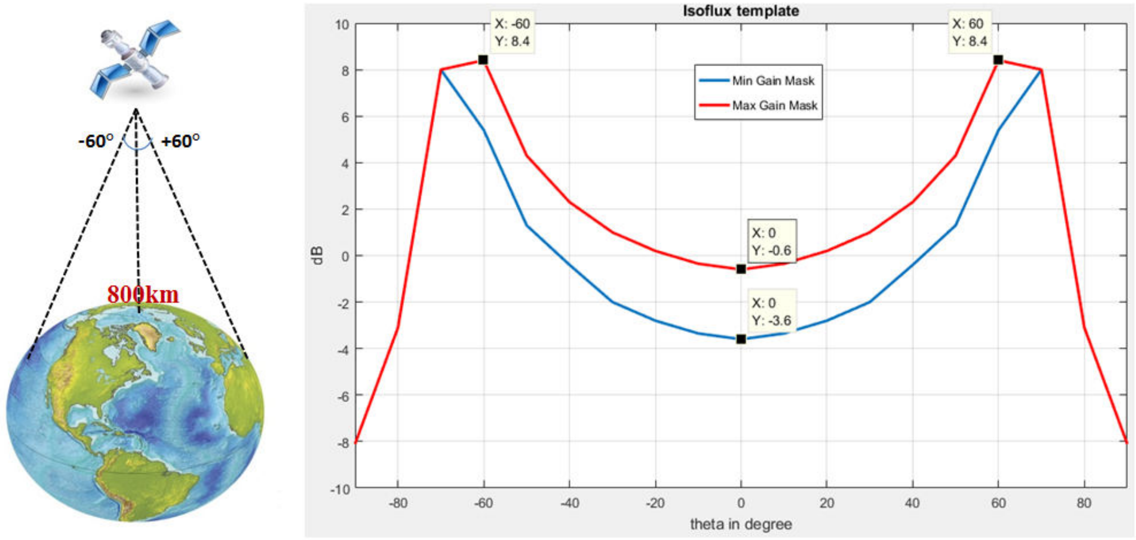

(a) **(b)**

Figure III-14. (a) Earth observation from low earth orbit 800km, (b) corresponding radiation pattern specifications with minimum and maximum masks.

IV-2 Antennas architectures

For the aim of 1D Isoflux beam forming, 1D circularly polarized **ARMA** and AESA designs were considered with five elements each (using the designs for the patch antenna and the pixel described in **Figure III-1** and **Figure III-2**). Then the antennas architectures are 1x5 AESA and 1x5 **ARMA** given in **Figure III-15**.

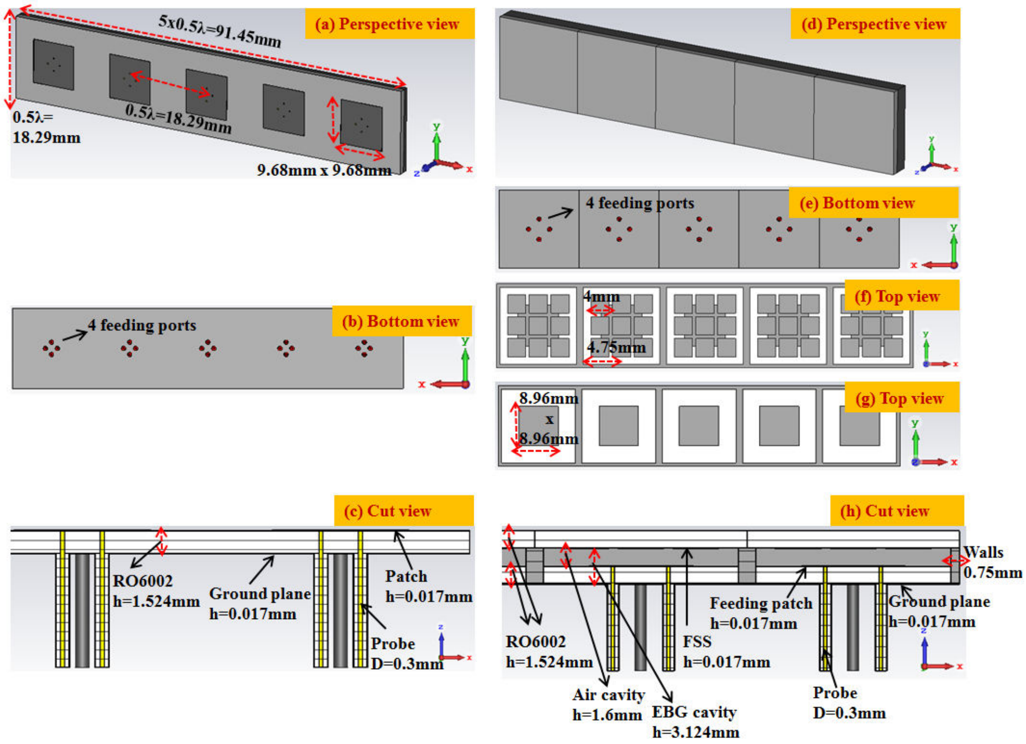

Figure III-15. AESA architecture (left): (a) perspective view, (b) bottom view, (c) cut view along y. ARMA architecture (right): (d) perspective view, (e) bottom view, (f, g) top view, (h) cut view along y.

IV-3 Feeding law

Formation of the 1D isoflux beam requires feeding AESA and **ARMA** with special law following the concept of the SFT that relates the radiation surface to the radiated far-field **(Chapter I paragraph IV)**. To obtain the isoflux pattern an approximation was done, using the Sinc-shape for the radiating surface we obtain theoretically the rectangular radiation pattern, and then with the effects of the antenna edges, the reflection with the rectangular shape will give an isoflux pattern **(Figure III-14.b)**. So, the radiation surfaces of both **ARMA** and AESA are chosen to have “Sinc” shape, the Sinc is sampled and five samples are distributed as weights for the antennas **(Figure III-16)**.

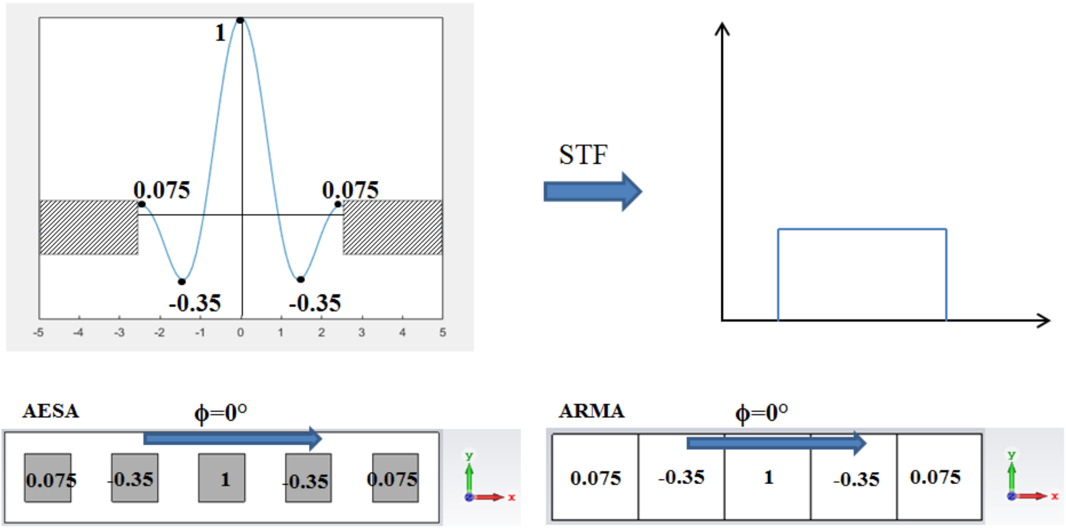

Figure III-16. Sinc sampled five samples distributed on ARMA and AESA elements.

IV-4 1D Isoflux gain and axial ratio ARMA and AESA comparison

The results of the gain and axial ratio patterns of the two antennas **ARMA** and AESA are compared in **Figure III-17**. These results are for the azimuth plane φ=0° at 8.2GHz. Both results of the gain follow the template given by **Figure III-14.b**, but the gain of AESA is slightly higher (0.3dB not very significant); however the position of the maximum gain for the Isoflux in **ARMA** is better according to the template. In **ARMA** maximum gain is 7.4dB at the elevation angles ±61° and in AESA the maximum gain is 7.7dB at ±50°. Also the axial ratio for of the circularly polarized **ARMA** is better (lower by 1dB to 1.8dB), especially in the regions where the Isoflux starts to have maximum gain ([-30° -70°] and [30° 70°]).

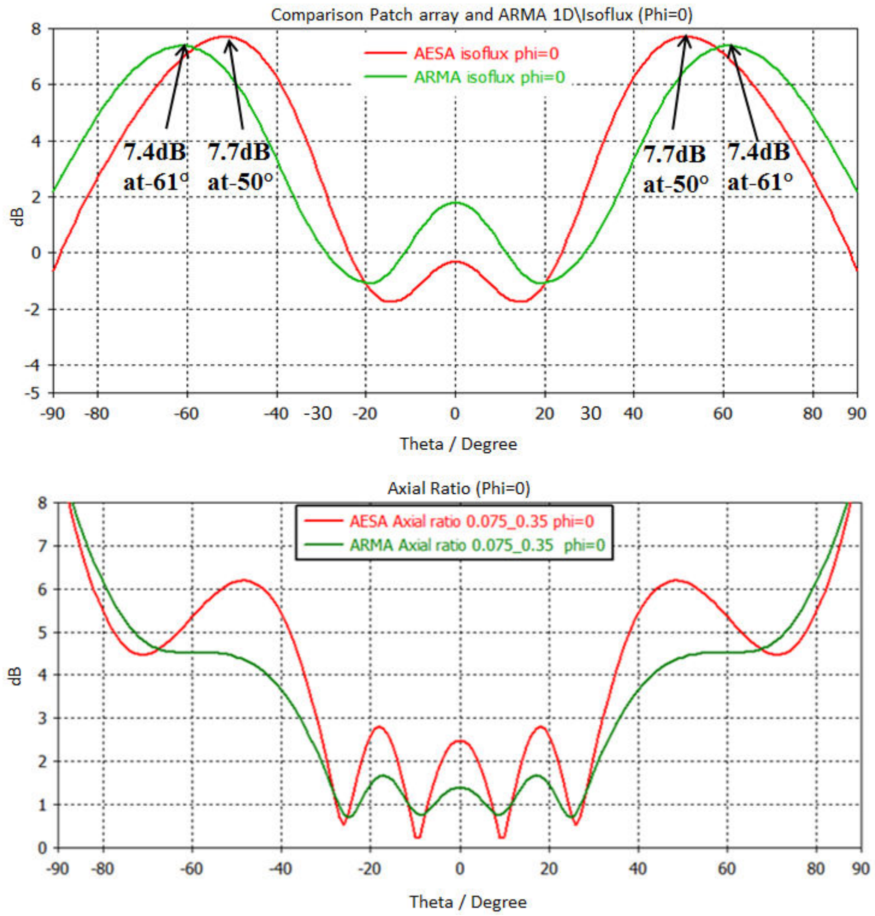

Figure III-17. Isoflux gain and axial ratio comparison, (green curves) ARMA, (red curves) AESA.

Looking for **ARMA** Isoflux in **Figure III-17** the gain in the axial direction is approximately 2dB that is a little bit higher than in the template **(Figure III-14)**. So, an optimization is possible to decrease this axial gain by increasing the value of the weights having 180° phases (negative values **Figure III-16)** from 0.35 to 0.4 (for both **ARMA** and AESA). Then after this optimization the Isoflux gain and axial ratio patterns are compared in **Figure III-18**.

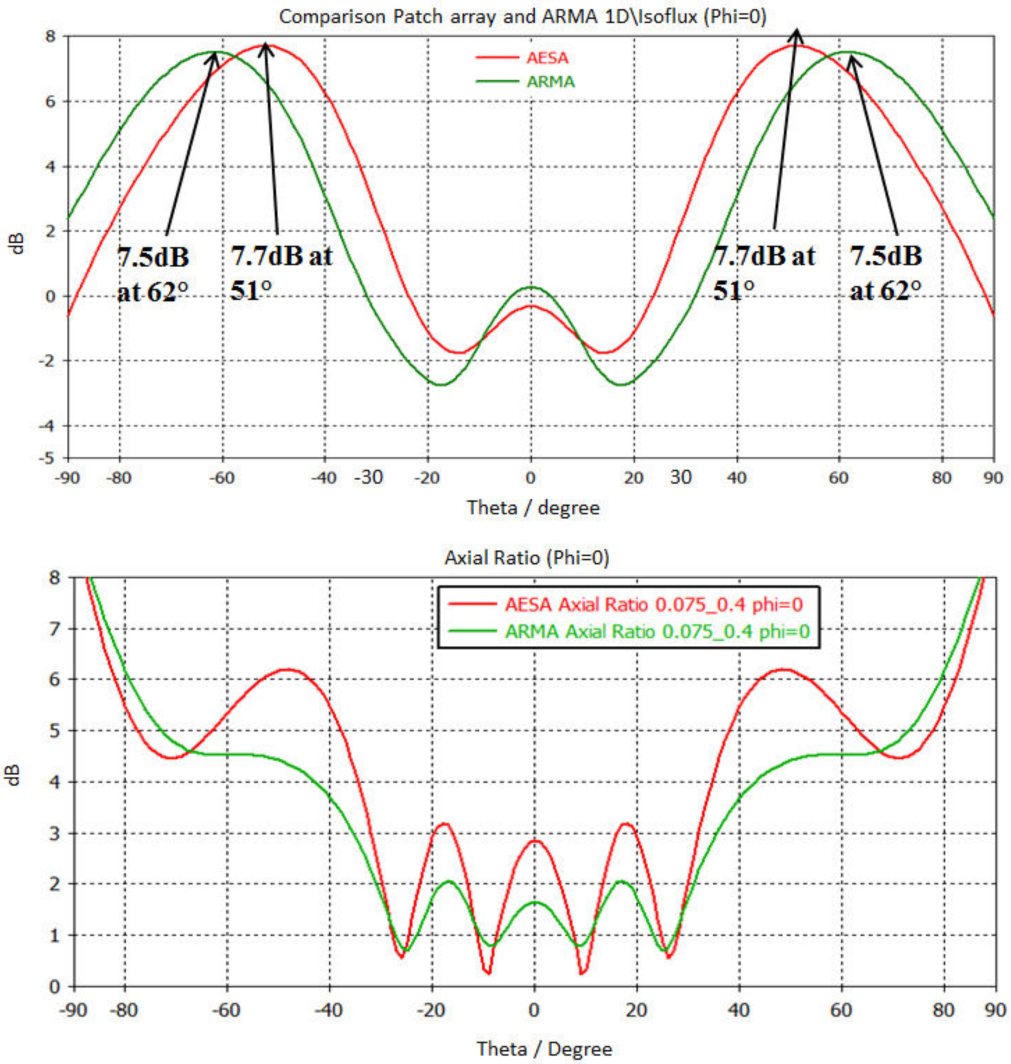

Figure III-18. **Isoflux optimization and axial ratio, (green curves) ARMA, (red curves) AESA.**

V. 2D ARMA solution for the 2D Isoflux beam forming

V-1 2D ARMA architecture 5x5 matrix

The 1D isoflux obtained will be extended now using the 2D matrix to generate the two dimensional Isoflux pattern. For that 5x5 **ARMA** is considered (25 pixels), the pixel architecture used is the one described previously in **Figure III-2**. Then the 2D **ARMA** architecture is shown in **Figure III-19**.

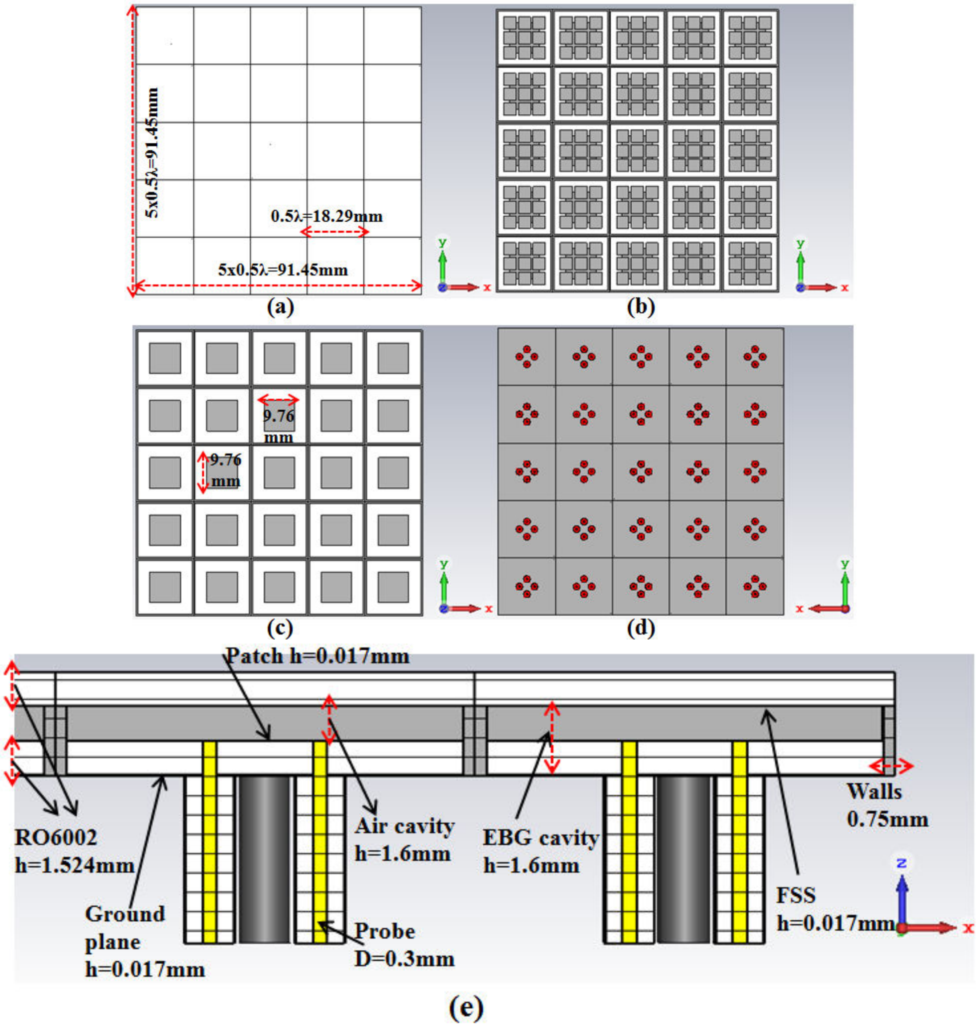

Figure III- 19. 2D ARMA, (a) top view, (b) top view showing FSS, (c) top view showing patch inside cavity, (d) bottom view, (e) cut view along y.

V-2 From 1D isoflux to 2D using Butler matrix technique

Going from 1D to 2D matrix could be done using the Butler method, where the weights of the 1D matrix is distributed as a line and column **(Figure III-20)** and the weights of the matrix is obtained by multiplying the weights ($A_i e^{j\varphi_i}$) from the line and column one by one to obtain the magnitudes $A_{i,j}$ and phases $\varphi_{i,j}$ of the 5x5 matrix.

The results of the Isoflux gain and the axial ratio patterns at 8.2GHz are shown in **Figure III-21**. The considered azimuth planes are φ=0°, 22.5°, 45°, 67.5° and 90°. Results show that the maximum Isoflux gain is 4.72dB at θ=52° and the minimum gain is 3.3dB at θ=40° (for the isoflux pattern in the two azimuth planes), this dissymmetry in the pattern is due to the reflections from the antenna edges that is not the same in all the directions **(Figure III-20)**. The axial ratio is below 3dB with some oscillations above 3dB at some elevation angles, this is due to the surface current that makes reflections at the edges of the antenna

(**[III-5] [III-6]**) and has its maximum effect at this specific elevation angles giving arise to higher axial ratio.

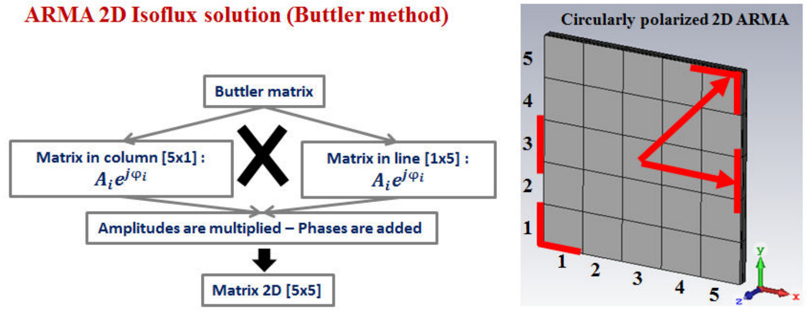

Table of amplitudes $A_{i,j}$					
	1	2	3	4	5
1	0	0,002	0,01	0.002	0
2	0.002	0.03	0.18	0.03	0,002
3	0.01	0.18	1	0.18	0.01
4	0,002	0.03	0.18	0.03	0,002
5	0	0.002	0.01	0.002	0

Table of $\varphi_{i,j}$					
	1	2	3	4	5
1	0°	180°	0°	180°	0°
2	180°	0°	180°	0°	180°
3	0°	180°	0°	180°	0°
4	180°	0°	180°	0°	180°
5	0°	180°	0°	180°	0°

Figure III-20. Butler method from 1D to 2D matrix for Isoflux beam forming.

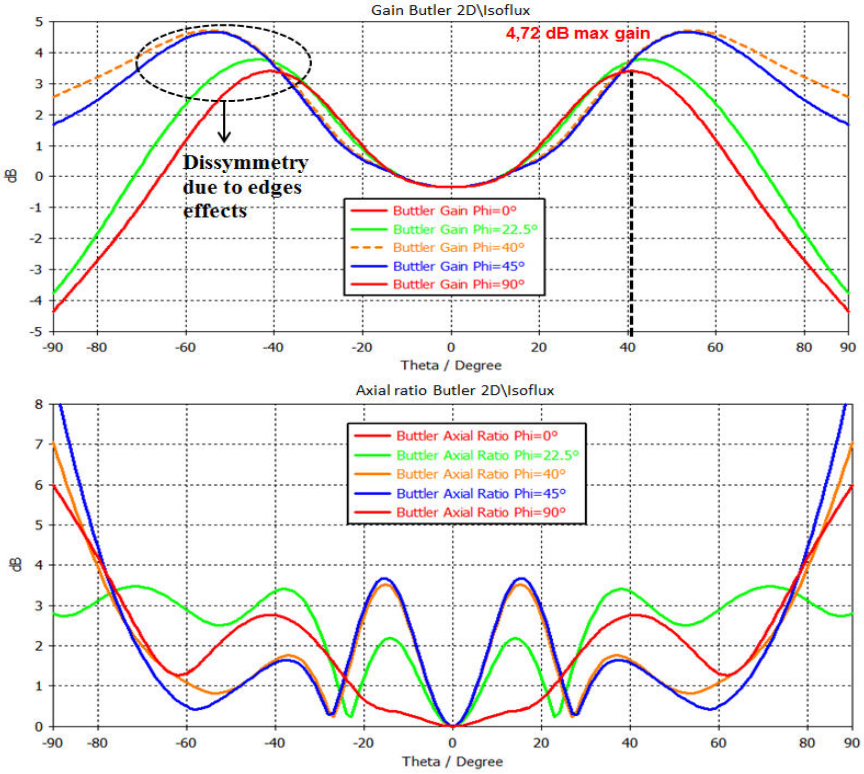

Figure III-21. 2D isoflux and axial ratio obtained by Butler matrix.

V-3 Sinc-circular solution

The feeding law of the two dimensional **ARMA** (for 2D Isoflux beam forming) in this paragraph is calculated using synthesis algorithm. This synthesis algorithm depends on Min-Max search of the weights by several iterations to find the optimal solution using the template given for the algorithm (template given in **Figure III-14.b**). This algorithm was developed in Limoges University during a past thesis (**[III-7] [III-8])** to give solutions for the planar antenna arrays for beam forming. The weights resulted from this solution have a Sinc shape in all the directions of the antenna, that is why it is called Sinc-circular. Feeding law distributed on the 5x5 **ARMA** is shown in **Figure III-22**.

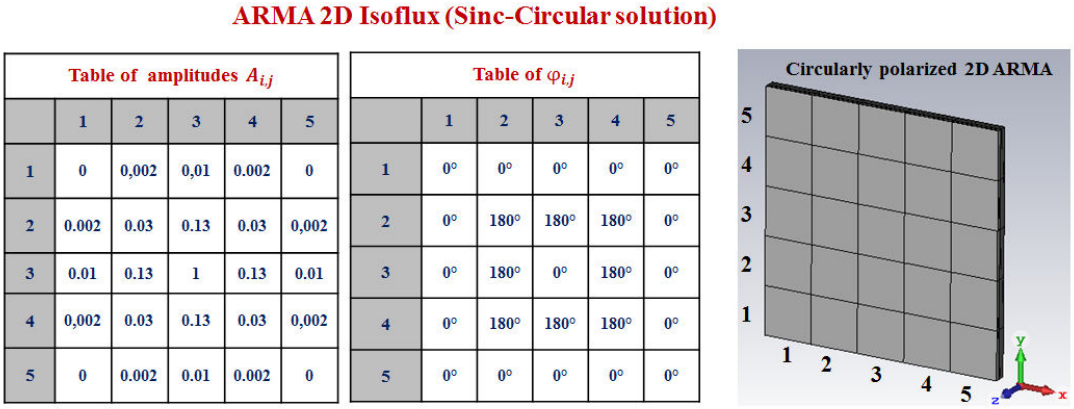

ARMA 2D Isoflux (Sinc-Circular solution)

Table of amplitudes $A_{i,j}$

	1	2	3	4	5
1	0	0,002	0,01	0.002	0
2	0.002	0.03	0.13	0.03	0,002
3	0.01	0.13	1	0.13	0.01
4	0,002	0.03	0.13	0.03	0,002
5	0	0.002	0.01	0.002	0

Table of $\varphi_{i,j}$

	1	2	3	4	5
1	0°	0°	0°	0°	0°
2	0°	180°	180°	180°	0°
3	0°	180°	0°	180°	0°
4	0°	180°	180°	180°	0°
5	0°	0°	0°	0°	0°

Figure III-22. Sinc-Circular feeding law for 2D isoflux.

Compared to the Butler solution the Sinc-Circular is slightly better regarding the Isoflux maximum gain positions, its wider by 3° **(Figure III-23)**. Also the axial ratio of the Sinc-circular solution is better especially at the far elevation angles [-90° to -40°] and [40° to 90°] **(Figure III-23)**. Then the Sin-Circular solution will be considered and will be optimized later in **Chapter IV** that will be dedicated for the CNES project.

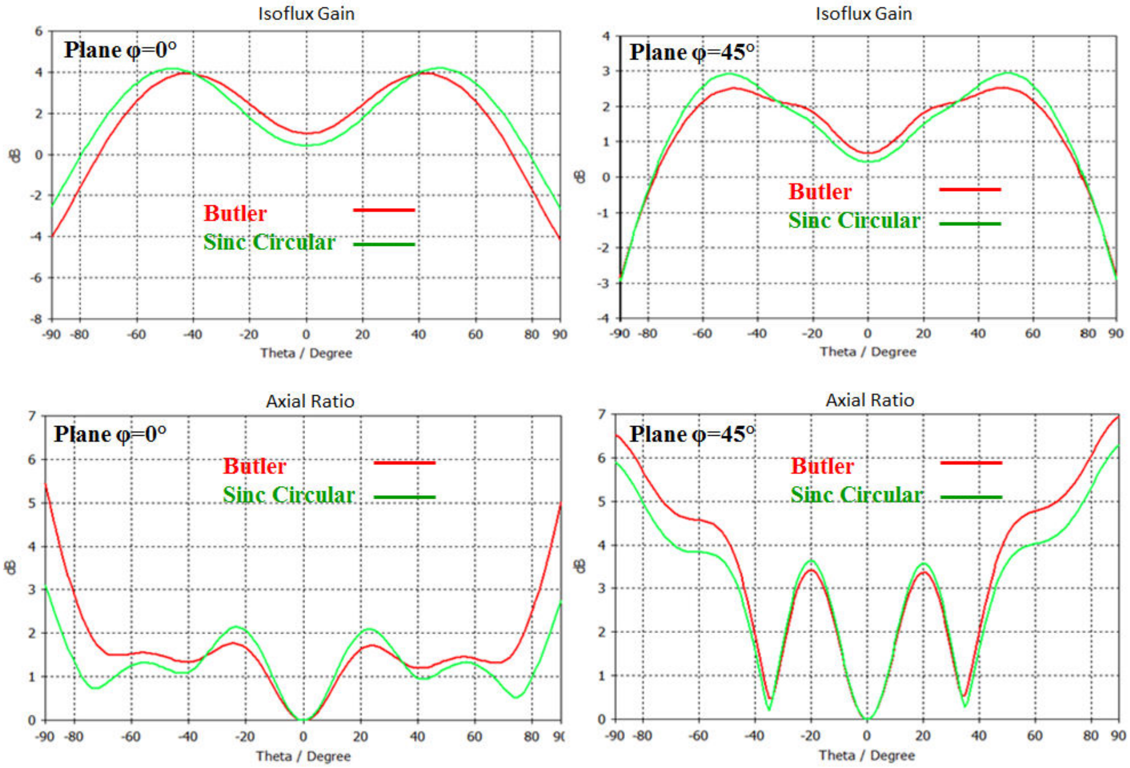

Figure III- 23. Butler and Sinc-Circular comparison for 2D Isoflux beam forming.

V-4 Sinc-circular with zeros weights at the edges of ARMA

The weights of the pixels at the edges of the 5x5 **ARMA** in the Sinc-Circular solution are very small compared to the other pixels inside the matrix. An idea to try zero weights at these pixels can be used **(Figure III-24)**, this will make it easier to design the power divider to feed the matrix; instead of using a power divider of one input and 25 outputs we need to design a power divider of one input and 9 outputs. Also with the zero weights at the edges pixels we will have only nine polarization circuits **(Chapter II)** instead of 25. Comparison of the Sinc-Circular solution and the Sinc-Circular solution with zero weights (pixels at the edges of the 5x5 matrix) shows that there is no big significant difference in the Isoflux gain and the axial ratio patterns **(Figure III-25)**.

ARMA 2D Isoflux (Sinc-Circular solution zero edges)

Table of amplitudes $A_{i,j}$

	1	2	3	4	5
1	0	0	0	0	0
2	0	0.03	0.13	0.03	0
3	0	0.13	1	0.13	0
4	0	0.03	0.13	0.03	0
5	0	0	0	0	0

Table of $\varphi_{i,j}$

	1	2	3	4	5
1	0°	0°	0°	0°	0°
2	0°	180°	180°	180°	0°
3	0°	180°	0°	180°	0°
4	0°	180°	180°	180°	0°
5	0°	0°	0°	0°	0°

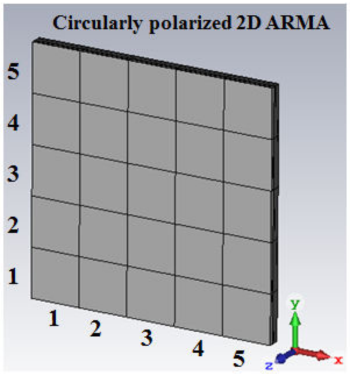

Figure III-24. Sinc-Circular solution with zero edges.

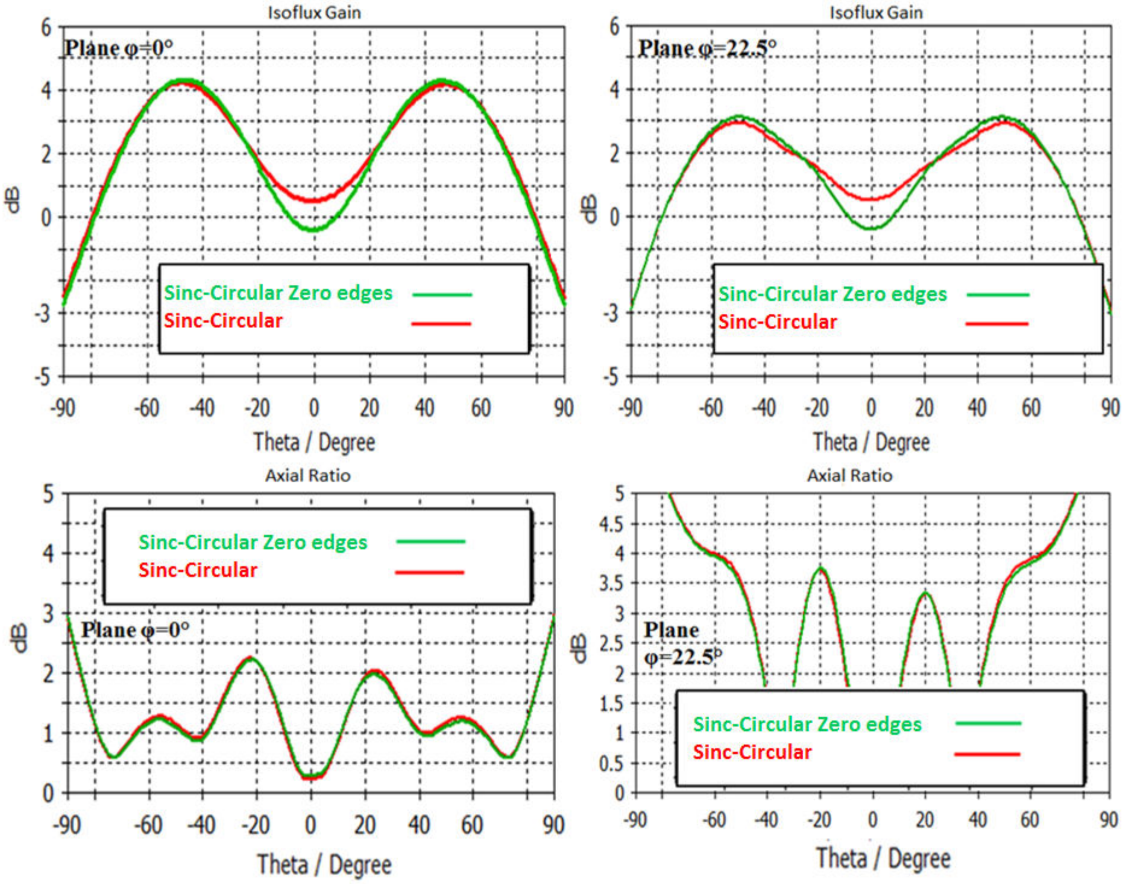

Figure III-25. Comparison of Sinc-Circular solution and Sinc-Circular solution with zero edges.

V-5 Elimination of pixels with zero weights 3x3 ARMA solution

Having zero weights for the pixels at the edges of the 5x5 matrix could give a question of why we do not eliminate these pixels with zero weights (not fed). In fact eliminating these pixels meaning that the surface current at the edges will be higher and the reflections from the peripherals of the matrix will disturb more the pattern of the antenna mainly the axial ratio.

Figure III-26 shows the 3x3 matrix of **ARMA** (after eliminating the pixels at the edges which are 16 pixels). Then **Figure III-27** shows the axial ratio after eliminating these pixels, the axial ratio is higher by 5dB at some elevation angles due to the edges reflections. The result is that having the pixels not fed at the edges is not the same as eliminating these pixels but better.

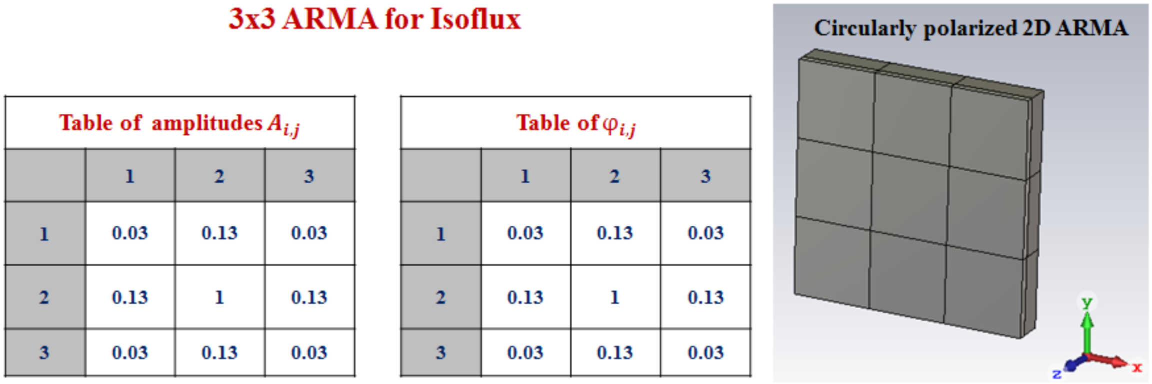

Table of amplitudes $A_{i,j}$	1	2	3
1	0.03	0.13	0.03
2	0.13	1	0.13
3	0.03	0.13	0.03

Table of $\varphi_{i,j}$	1	2	3
1	0.03	0.13	0.03
2	0.13	1	0.13
3	0.03	0.13	0.03

Figure III-26. Eliminating the pixels at edges of the 5x5 ARMA to get 3x3 ARMA.

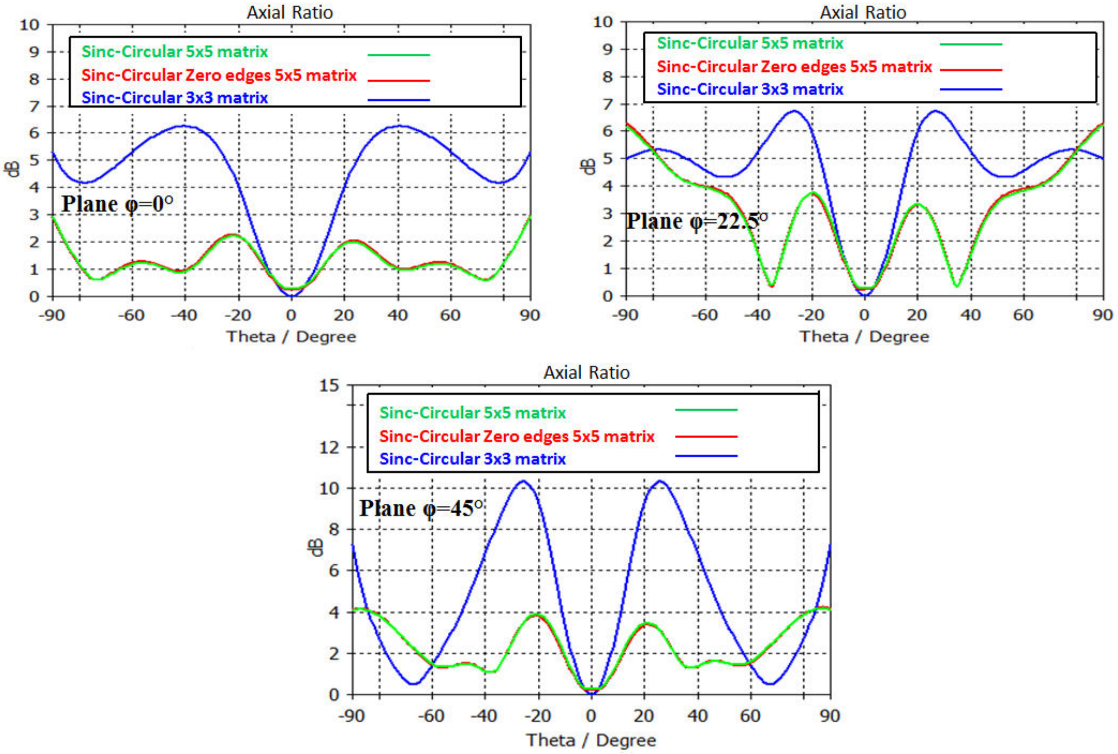

Figure III-27. Axial ratio comparison, Sinc-Circular Sinc-Circular with zero edges and the 3x3 matrix solutions.

VI. Conclusion

This chapter shows that **ARMA** has several advantages against AESA in circular polarization. Comparison of the pixel and patch antenna show higher bandwidth, higher gain as a function of frequency, better axial ratio for the pixel. Then the axial ratio as a function of the elevation steering angles in 1D **ARMA** is better especially for the far steering angles where AESA has the worst axial ratio. Also, regarding the other type of beams “wide beam” the example considered of the 1D isoflux proves that **ARMA** is better regarding the axial ratio and the wider positions of the Isoflux maximums.

Then an example of 2D beam forming was studied using the method of Butler and the Min-Max synthesis algorithm to find the feeding law of the 5x5 **ARMA**. Results shows that the solution resulted from the synthesis algorithm (Sinc-Circular) gives better results, and then this solution was extended to the solution of the Sinc-Circular with zero weights at the edges pixels of the matrix. Having these un-fed pixels has no big effect on the antenna gain and axial ratio patterns, but makes easier for the power divider to be designed in the next chapters.

The next chapter will be dedicated for the CNES project; the solutions of the 2D isoflux studied in this chapter will be extended and optimized using different feeding laws to achieve the requirements of the CNES Isoflux specifications.

VII. Bibliography of Chapter III

[III-1] R. Chantalat, L. Moustafa, M. Thevenot, T. Monédière and B. Jecko, "Low Profile EBG Resonator Antennas", Hindawi Publishing Corporation, International Journal of Antennas and Propagation, Volume 2009, Article ID 394801, 7 pages.

[III-2] A Meta-surface antenna for space application, G. Minatti, S. Maci, P. De Vita, A. Ferni, M Sabbadini. Proceeding of ISAP2012 Japan.

[III-3] L-band compact printed quadrifilar helix antenna with 'Iso-Flux' radiating pattern for stratospheric balloons telemetry. Nelson Fonseca, Sami Hebib, Herv´e Aubert. HAL Id: hal-00432239.

[III-4] X-band compact dual circularly polarized isoflux antenna for Nano-satellite applications, Eric Arnaud, Cyrille Menudier, J Fouany, T Monediere, M Thevenot, International journal of microwave and wireless technologies, 2017, pp.1 – 8, <10.1017/S1759078716001410>, <hal-01431624>.

[III-5] "On The Use Of Metal Gratings To Reduce Diffraction From A Finite Ground Plane In Circularly-Polarized Microstrip Arrays", Adrianus B. Smolders, Rob M. C. Mestrom, Abolghasem Zamanifekri, and Ad C. F. Reniers, , Progress In Electromagnetics Research Letters, Vol. 42, 65-78, 2013.

[III-6] "Axial ratio improvement in aperture antennas using high-impedance ground plane", ARTICLE in ELECTRONICS LETTERS · DECEMBER 2002.

[III-7] Contribution of study and synthesis of the printed antenna arrays, Application on the conception of array beam forming. Thesis at Limoges University, Mohammad Rammal, 29 January 1993.

[III-8] N. Fadlallah, M. Rammal, H. Rammal, P. Vaudon, R. Ghayoula and A. Gharsallah, "A general synthesis method for linear phased antenna array", IET Microwaves, Antennas and Propagation, vol. 2, no. 4, pp. 338–342, 2008.

List of figures

List of tables

Chapter IV

CNES Project

Table of Contents

I. Introduction

This chapter is dedicated to solve the problem of the CNES project where two different electromagnetic modes are required for space applications, “beam forming using circularly polarized **ARMA** antenna”. CNES is working on a big project regarding the Nano-satellite that will be launched into low earth orbit (LEO) at 800km height to serve for different applications for the space-earth communication and they (CNES community) recommended the use of **ARMA** concept to achieve the desired circularly polarized beam forming. These applications need two different beam patterns; wide Isoflux beam for wide earth coverage and high gain axial beam for high data rates communications. In this chapter the two modes will be studied and the different feeding laws for the beam forming will be presented. The Isoflux beam will be studied and realized however the axial high gain beam is a subject for design and study only. Remind that circular polarization is achieved by feeding the EBG cavity in **ARMA** by circularly polarized patch antenna connected to the circuit of three hybrid couplers **(Chapter II, paragraphs II-7.3, II-8.2 and II-8.4)**.

Isoflux beam forming is done by optimizing of the feeding law of the square circularly polarized **ARMA** antenna focusing on the homogeneity of the Isoflux pattern in the different azimuth planes and the position of the maximums of the Isoflux (specified at elevation angles $\theta=\pm60°$). Also the axial ratio (for the aim of circular polarization) must be below 3dB at the elevation angles where the Isoflux gain attains its maximum. The axial high gain beam will be studied also using the square circularly polarized **ARMA** antenna where the maximum gain of this mode required 13dB. Switching between the modes (Isoflux and axial beams) is considered also at the elevation angles $\theta=\pm30°$. The solutions to be considered (for beam forming) are all with zero weights at the edges of **ARMA**, remind that the weights at the edges have no big effect in the gain and the axial ratio pattern **(Chapter III paragraph V-4)**.

So, in this chapter there are: explanation of the CNES project and specifications required, the beam forming procedure for the two modes, the design of the antenna, and the design of the power divider for Isoflux beam forming, the realization of the **ARMA** antenna with the polarization circuits and the power divider and finally simulation-measurements comparison. One of the limitations in study of the problem is the small area reserved for the antenna on the top of the Nano-satellite which limits the size of the antenna. The specified area for the antenna allows the use of 5x5 **ARMA** (this area is pixelated or sampled using maximum 25 pixels with a periodicity of 0.5λ).

II. State the problem of the CNES

II-1 Nano-Satellites

Nano-Satellites are very small platforms whose mass does not exceed 10Kg (**Table IV-1**). They are intended to be used for services which are not desirable to have a large payload. They can also be used to carry out preparatory missions for other more ambitious missions. The goal is for example to validate technologies by reducing risk taking. But the future lies probably in the deployment of 20 to 50 Nano-satellite constellations for distributed measures.

Type	Weight (Kg)	Cost ($ US)	Development time
Classical satellite	>1000	0.1-2 B	>5 years
Medium satellite	500-1000	50-100 M	4 years
Mini satellite	100-500	10-50 M	3 years
Micro satellite	10-100	2-10 M	1 year
Nano satellite	1-10	0.2-2 M	1 year
Pico satellite	<1	20-200 K	<1 year

Table IV-1. Classifications of satellites according to their weights, costs and development time.

Small satellites are under the research and development in many universities and space agencies for example NASA develops projects of military missions. The major advantage of this platform is that it allows rapid to space: the development times are relatively short and the costs could be considerably lowered to 20K€/Kg against 100k€/Kg today with the arrival of new launcher manufacturers.

Another driving force behind the development of space technologies is the creation of the Nano-satellite standard "Cube-Sat", the first prototypes of which have been deployed in space since 2003. This standard is a modular format consisting of cubes of 10 cm of edge (format "1U") (**Figure IV-1**); Each of these cubes contains its own solar panels, weighs less than 1Kg and can be assembled in clusters of 2, 3, 6 or 12 to compose larger satellites and more powerful, respectively "2U", "3U", "6U" and "12U" (**Table IV-2**). These Nano-satellites fly in low orbit, between 200 km and 700 km and their short life is about 2 years.

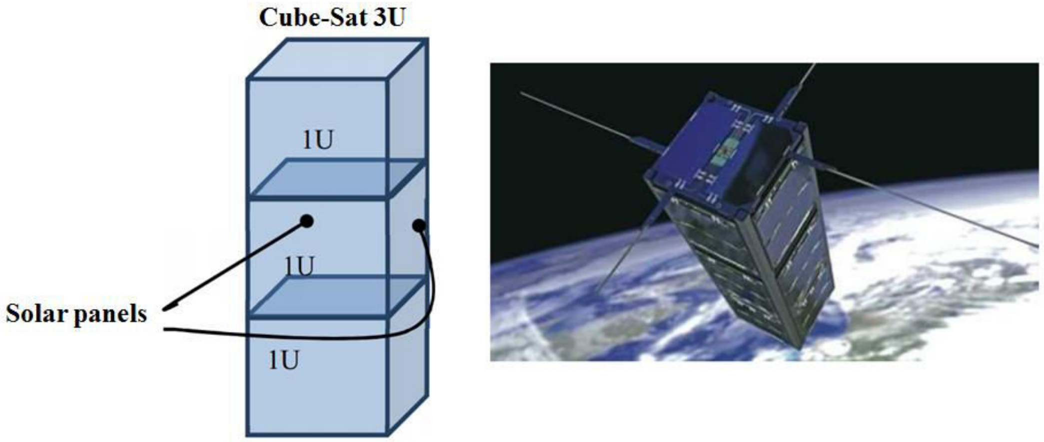

Figure IV-1. A representative model of a 3U-type platform (left), model of a Nano-Satellite with an assembly of 3 cube-Sat with deployable solar panels (at right).

Cube-Sat architecture	Dimensions	Weight (Kg)
1U Cube	10cmx10cmx10cm	1Kg
2U Cube	10cmx10cmx20cm	2Kg
3U Cube	10cmx10cmx30cm	3Kg
6U Cube	10cmx20cmx30cm	6Kg

Table IV-2. Cube-Sat modular format.

II-2 Presentation of the CNES objectives

The speeds offered by UHF / VHF links that were previously used by the platforms Nano-Satellites "Cube-Sat" limit the volumes of data that can be exchanged with the ground. Power and surfaces available on Nano-Satellites platforms prohibit indeed embarking the strong antennas gain which made it possible to establish high Speed links. To meet the challenge it is envisaged to carry out the X-band link with ground stations a few meters in diameter. To do this, the satellite must have circular polarization antenna, with an Isoflux diagram to optimize the gain during scrolling associated with the low orbit. The development of such an antenna is a key to make the link. This antenna must be integrated on the available area of the platform Cube-Sat (10cmx10cm). The size of the antenna should use the least space possible inside the Cube-Sat volume.

The CNES call for a project concerns the Nano-satellite. The XLIM (RF-Systems department) have established a partnership respond to the call for project and start working to resolve the problem using circularly polarized **ARMA** technology as recommended by the CNES. The essential points of the specifications are in the next paragraph.

II-3 Project specifications

The study consists of designing an antenna operating in the X band [8-8.4] GHz to function with two different beams. First is an Isoflux pattern and second the axial high gain pattern, both with circular polarization for Nano-type satellite platforms Cube-Sat 3U and 6U. The bandwidth is set at 400 MHz around 8.2 GHz. The polarization must be circular on the same band, so axial ratio must be less than 3 dB in the cone θ = ± 60°. Throughout the study phase, the platforms considered is 3U-type as shown in **Figure IV-2** (This platform is a parallelepiped of 10cm x 10cm x 30cm).

The performance of the antenna developed to fulfill the specifications must be impacted as little as possible by the platform and must be optimized with the perturbations generated by the platform. The area reserved for the antenna is a square of 90mm of edges and the antenna must not protrude beyond the platform.

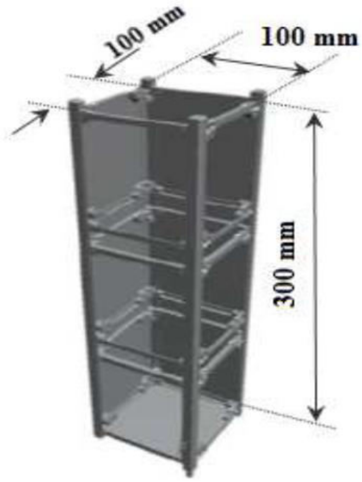

Figure IV-2. Cube-sat 3U platform.

II-3.1 Beam modes specifications

In this chapter, there is the design of the two beam patterns and the testing done in the presence of the Cube-Sat support. The realizations and measurements will be done regarding the Isoflux part whereas the axial high gain beam is under the study and simulation only. Remind that we are going to use the circularly polarized **ARMA** antenna that has the agility to give different beams when it’s feeding law is reconfigured using the control techniques of the BFN.

The first mode is the wide beam (Isoflux); the Isoflux pattern is used for wide area coverage of the earth from the space where the antenna must radiate power equally for the earth meaning, that the receivers at different distances of the earth should receive the same power as in **Figure IV-3**. This can explain the fact that the maximum gain should be at far elevation angles, considered at θ=±60° for the satellite at orbit far 800km from the earth. Then the constraints for this wide beam are as follows:

- Position of the gain maxima for the Isoflux are at elevation angles θ = ± 60°.
- 3dB gain at θ=±30°.
- The interesting zone for the Isoflux is bounded by [θ>30°] and [θ<-30°].
- Axial gain for the wide beam is not important, low gain in the axial direction considered between [-30° 30°] elevation angles.
- Axial ratio less than 3dB in the regions of maximum Isoflux gain.

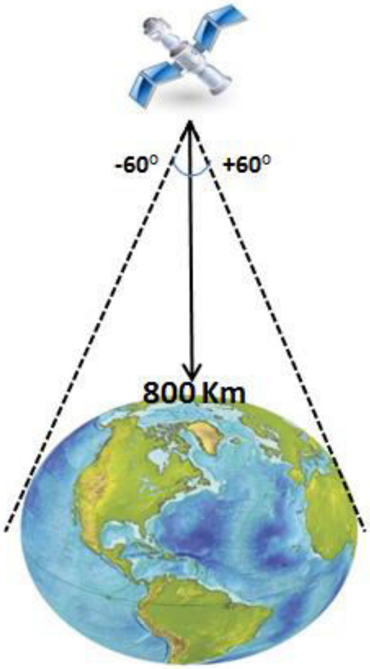

Figure IV-3. Isoflux beam wide range coverage.

The second mode has 13dB gain in the axial direction and the gain at θ=±30° must be greater than 3dB. From the two beams the switching elevation angles between the two modes are at θ=±30°, the template for the two modes is shown in **Figure IV-4**. Then the antenna will switch between the two modes according to the different CNES applications required, the switching angle is considered according the coverage area of each beam during the satellite-earth base stations communication. So, for the gain at this switching elevation angles in the two modes we have chosen to be 3dB to avoid blind regions.

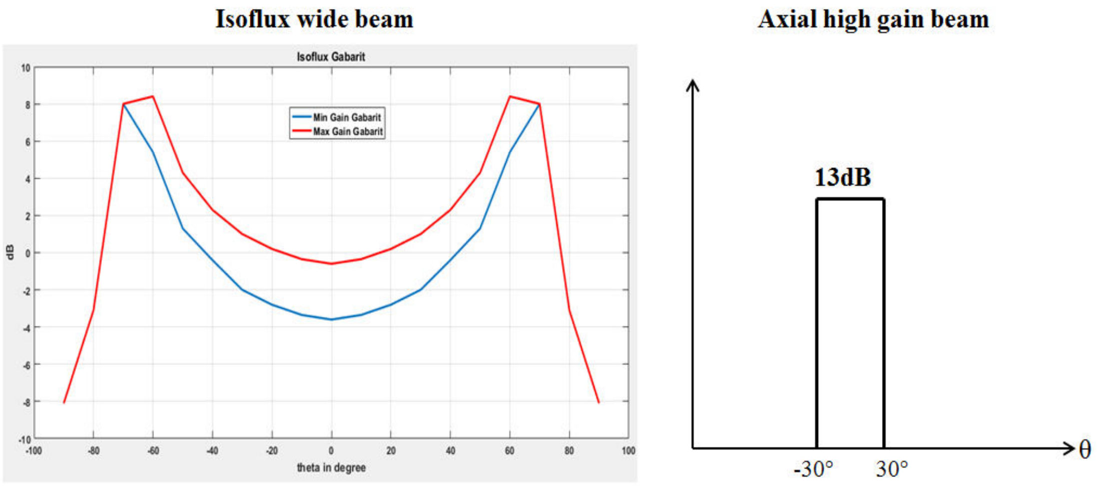
Isoflux wide beam

Axial high gain beam

Figure IV-4. Two beams Isoflux and high gain axial modes.

III. 5x5 square ARMA feeding law optimization for Isoflux

Having accomplished the 1D Isoflux and the two dimensional solutions (Butler matrix technique, the Sin-Circular and the Sinc-Circular with zero edges in **Chapter III**), in this paragraph the aim is to optimize the Sinc-Circular solution with zero edges (analysis using CST software) to fit the CNES desired Isoflux beam. The feeding law of the 5x5 square **ARMA** antenna (architecture described in **Chapter 3 Figure III-9**) is parameterized in this study using the CST software according to **Figure IV-5**, where "C" and "M" corresponds for the corner and middle pixels of the 3x3 active part inside the 5x5 matrix (remind that the pixels at the edges are not fed, zero weights). The two parameters "C" and "M" are tuned in CST and the analysis of the Isoflux beam is done taking in account the Isoflux specifications mentioned above and the homogeneity of the Isoflux pattern in the different azimuth planes.

Table of amplitudes $A_{i,j}$

	1	2	3	4	5
1	0	0	0	0	0
2	0	C	M	C	0
3	0	M	1	M	0
4	0	C	M	C	0
5	0	0	0	0	0

Table of phases $\varphi_{i,j}$

	1	2	3	4	5
1	0°	0°	0°	0°	0°
2	0°	180°	180°	180°	0°
3	0°	180°	0°	180°	0°
4	0°	180°	180°	180°	0°
5	0°	0°	0°	0°	0°

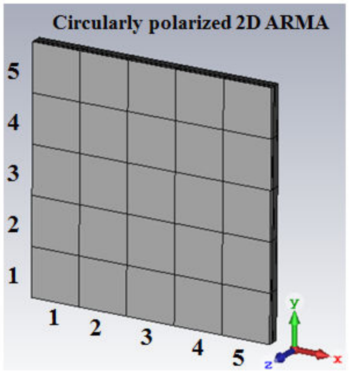
Circularly polarized 2D ARMA

Figure IV-5. CST Parameterization for Sinc-Circular solution with zero edges.

III-1 Sinc-Circular zero edges symmetrical solution

To increase the maximum gain of the isoflux, the gain in the axial direction must be decreased by giving higher weights for the pixels of 180° phase. Solution used is called the symmetrical solution, where “C” and “M” parameters are given equal values with (C=M). An advantage of this solution is that the power divider to be designed to distribute the power (according the symmetrical solution) will have nine outputs with eight of them are equal in magnitudes and phases. Using this configuration (increase C and M equally) the contribution of the corresponding pixels gives lower gain in the axial direction, and then a higher gain at the maximums of the isoflux pattern. The best to be considered with this solution must have as wide as possible the position (elevation angles) of the maximum gain (near ±60°) and axial ratio less than 3dB in the same regions where the Isoflux gain attains its maximum.

Figure IV-6 shows the gain and axial ratio patterns for different symmetrical cases (C=M=0.08 and C=M=0.2). Analysis shows that when “C” and “M” is higher the maximum gain of the Isoflux is increased and the position of the maximum gain is attained at wider elevation angles. For example taking the azimuth plane $\varphi=0°$, the maximum gain for C=M=0.08 is 5.8dB at $\theta=\pm47°$ **(Figure IV-6.a)** and for C=M=0.2 the maximum gain is 6.6dB at $\theta=\pm51°$ **(Figure IV-6.b)**. And for the azimuth plane $\varphi=60°$, the maximum gain for C=M=0.08 is 4.2dB at $\theta=\pm40°$ **(Figure IV-6.a)** and for C=M=0.2 the maximum gain is 3.4dB at $\theta=\pm50°$ **(Figure IV-6.b)**. But another point must be taken in account is that when increasing “C” and “M” the axial gain is going higher near 0dB (for C=M=0.2), this explains the fact that the maximum Isoflux gain is decreased in some planes (from 4.2dB at $\varphi=60°$ for C=M=0.08 to 3.4dB at $\varphi=60°$ for C=M=0.15). Also when increasing the value of “C” and “M” the gain at $\theta=\pm30°$ is decreased ([3 to 3.6] dB for C=M=0.08 and [-1.6 to 0] dB for C=M=0.2).

Regarding the circular polarization, the axial ratio in **Figure IV-6.b** starts to be higher than 3dB in some azimuth planes inside the Isoflux interesting regions for C=M=0.2. When we increase the weights with 180° phase the field at the elevation angles around $\theta=\pm20°$ tends to be very small approximately zero. So, the bad axial ratio that tends to infinity is due to that no field in these regions. That is not the case in the **Figure IV-6.a**.

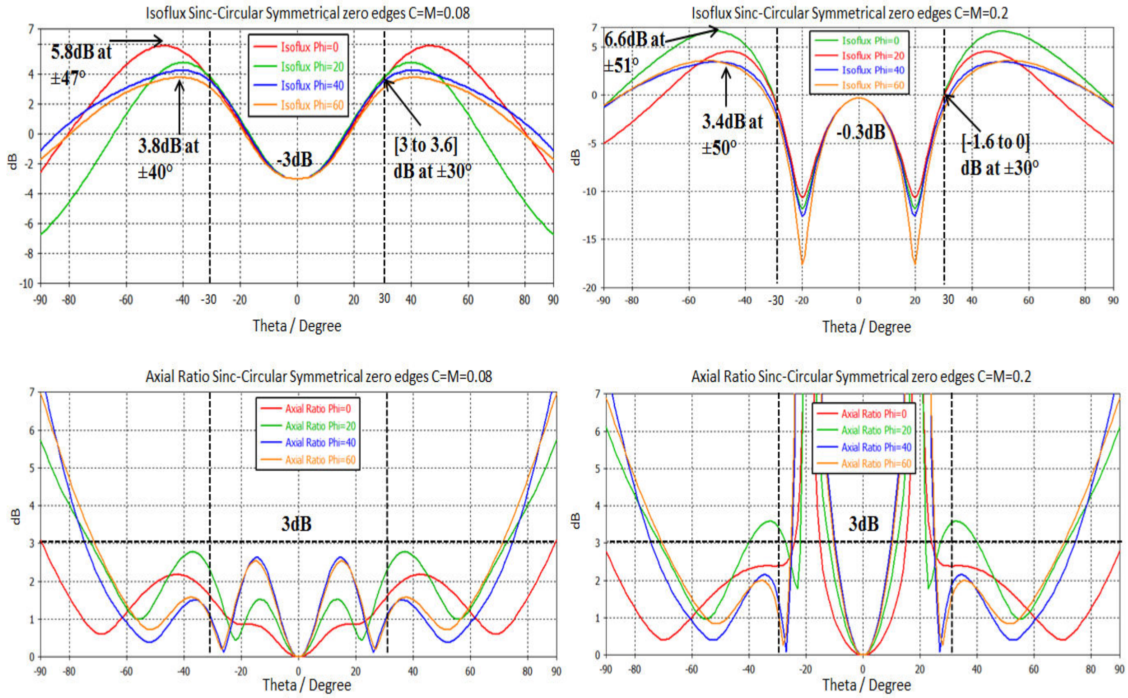

(a) (b)

Figure IV-6. Sinc-Circular zero edges symmetrical solutions.

Then in the symmetrical solution the best value (using CST analysis) to be considered with the three conditions for the Isoflux beam (increasing position of the maximum gain toward θ=±60°, decreasing the axial gain and the 3dB gain at θ=±30°) and the condition of the axial ratio below 3dB is shown in **Figure IV-7**. The greyed zone in **Figure IV-7** is the axial non-interesting zone for the Isoflux mode. This solution is for C=M=0.15 where the maximum gain is 6.4dB at θ=±50° for the azimuth plane φ=0° and the minimum gain is 3.7dB at θ=±51° for the azimuth plane φ=60°. The 3dB gain of the switching modes angles is achieved at θ=±33° (near θ=±30°). The axial ratio is below 3dB in the entire interesting region for the Isoflux beam meaning that circular polarization is well achieved for this beam.

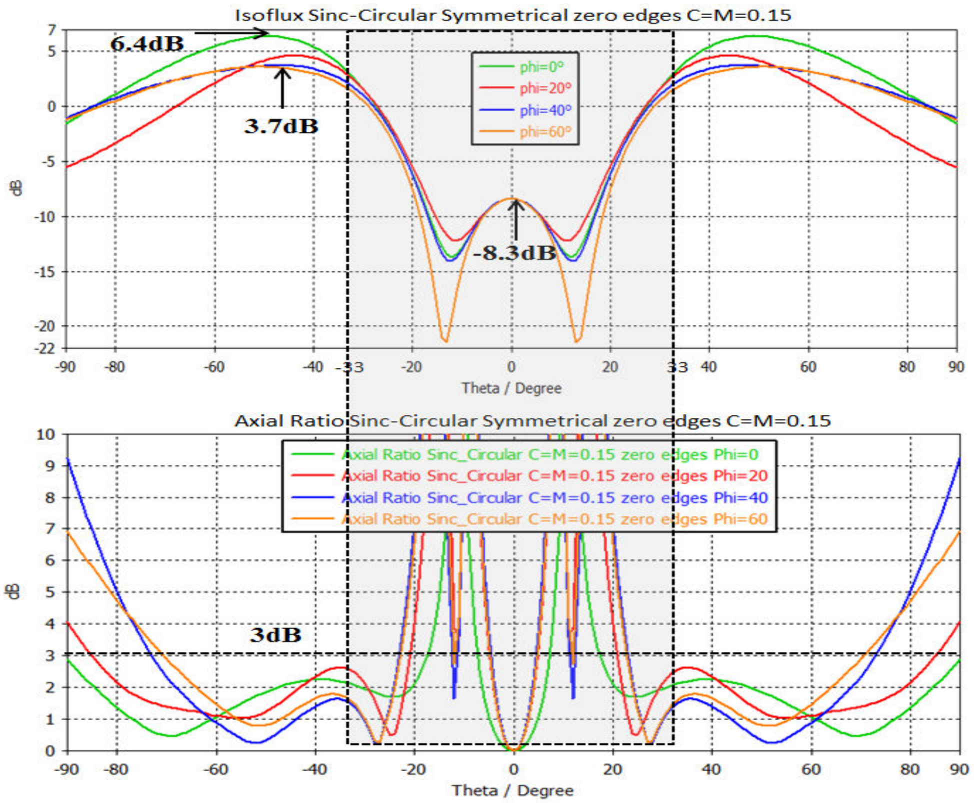

Figure IV-7. Best of the symmetrical solutions (C=M=0.15) with the corresponding axial ratio.

As a conclusion the analysis shows that the symmetrical Sinc-Circular solution (zero edges and C=M=0.15) gives results that are good according to the CNES specifications. The position of the maximum gain is not attained at θ=±60°, but the gain at these angles (θ=±60°) is decreased no more than 1dB from the maximum gain in each azimuth plane considered in the curves of **Figure IV-7**. The 3dB switching gain position is at θ=±33° and not θ=±30° but this is not very significant according to the CNES applications requirements. The axial ratio is very good lower than 3dB and fits the CNES specifications.

III-2 Enhancement of the Isoflux homogeneity in the different azimuth planes

The solutions given in the previous paragraph give non-uniform Isoflux pattern; there is gain difference between the different azimuth planes **(Figure IV-6 and Figure IV-7**). For example in **Figure IV-7** (C=M=0.15) the maximum isoflux gain in planes φ=0° and φ=60° are 6.4dB and 3.7dB respectively, meaning that a difference of 6.4-3.7=2.7dB. This is normal since the square matrix physical structure is not symmetrical; the distance from the center of the matrix to the edges in different directions is not the same. This gives different contributions for the reflections of the electric field at the edges on the pattern of the antenna in the different azimuth planes. The solution for that is to compensate the difference by the feeding law. The parameters “C” and “M” are changed (using the analysis procedure in CST software) to get minimum difference for the gain in the different planes. Different cases were studied; **Figure IV-8** shows the best results obtained for the minimization of the gain difference where the results are obtained for the couples (C=0.09, M=0.15) and (C=0.07, M=0.15) both with zero edges. In **Figure IV-8** the azimuth planes considered are φ=0° (plane with maximum Isoflux gain), φ=45° (plane with minimum isoflux gain) and φ=30°.

For (C=0.07, M=0.15) the gain difference is minimized from 2.7dB (C=M=0.15 **Figure IV-7**) to 1.1dB, the maximum gain equals to 5dB (θ=±50°, φ=0°) and the minimum gain is 3.9dB (θ=±51°, φ=45°). The 3dB gain (switching between the two modes) is attained at θ=±33° (near θ=±30°). The axial ratio is below 3dB inside the interesting Isoflux regions (for both cases in **Figure IV-8**). Also using this solution not only the homogeneity is improved but also we don’t have the problems of the very high axial ratio that appear previously in **Figure IV-6.b** and **Figure IV-7**.

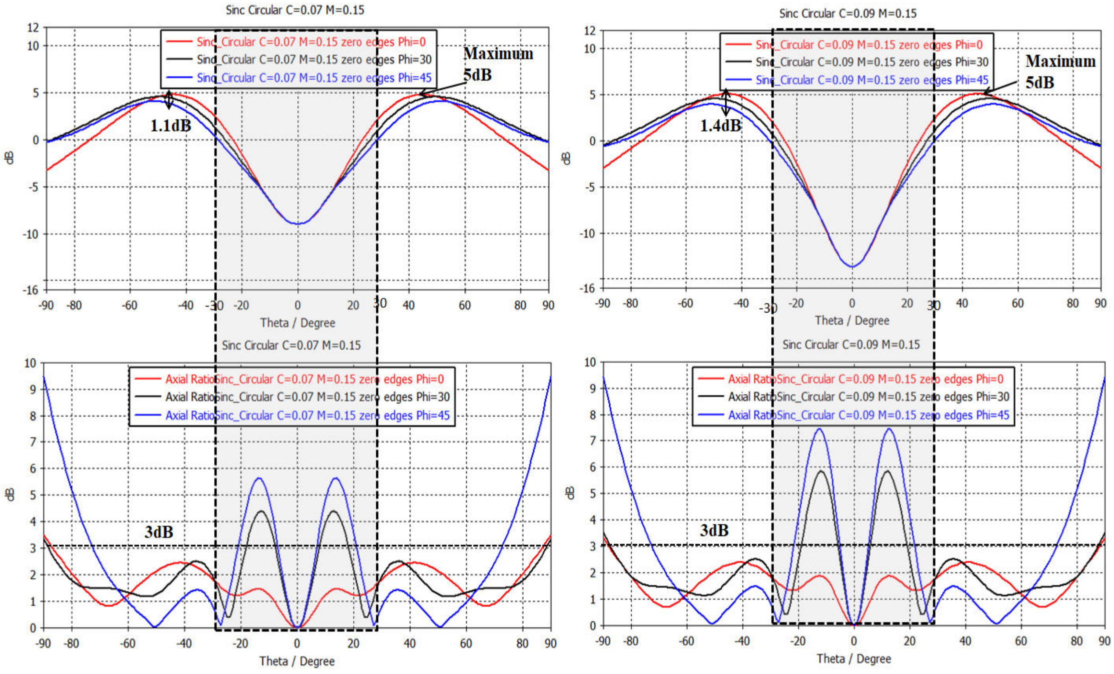

Figure IV-8. Compensation of the dissymmetry of the Isoflux in different azimuth planes.

III-3 Conclusion

The feeding laws presented in the previous two paragraphs give two solutions; the first is a symmetrical solution that maximizes the Isoflux gain and the elevation angles positions of the maximum gain. The second (non-symmetrical) minimizes the gain difference in the isoflux pattern in the different azimuth planes to insure the uniformity of the Isoflux pattern. **Table IV-3** illustrates the main results obtained by the non-symmetrical solution (C=0.07, M=0.15 **Figure IV-8**) and the symmetrical solution (C=M=0.15 **Figure IV-7**).

In **Table IV-3** the gain difference of the Isoflux in the non-symmetrical solution is reduced from 2.7dB to 1.1dB, but the maximum gain is reduced (from 6.4dB to 5dB) due to the smaller values given for the pixels corresponds to the parameter “C”. Also in the non-symmetrical solution the gain at θ=±30° is [0 to 2] dB (for different azimuth planes) but for the symmetrical solution its [1.5 to 2.6] dB. Regarding the position of the maximum Isoflux gain in the symmetrical solution it’s between θ=±49° and θ=±51° in the different azimuth planes, but in the non-symmetrical it’s between θ=±45° and θ=±51°. One more interesting advantage of the symmetrical solution also is the easier power divider design that will have eight outputs with equal amplitudes and equal phases.

Then the feeding law that will be considered (Isoflux beam forming) for the 5x5 square **ARMA** antenna is the Sinc-Circular zero edges symmetrical solution with C=M=0.15. Where the position of the maximum gain is not attained at θ=±60° (according to CNES specifications), but the gain at these angles is smaller from the maximum gain at most by 1dB. Also the axial ratio is below 3dB and the circular polarization is achieved according to the CNES specifications, with the axial ratio tend to be very high but in the non-interesting regions where there is no field (no radiation).

	Symmetrical solution	Non-Symmetrical solution
Gain at θ=±30°	Between 1.5 and 2.6 dB	Between 0 and 2.6 dB
Maximum Isoflux Gain	6.4dB at θ=±51°	5dB at θ=±51°
Minimum Gain	3.7dB at θ=±49°	3.9dB at θ=±45°
Power divider	1 to 9 with eight equal-amplitudes equal-phases outputs	1 to 9

Table IV-3. Symmetrical and non-symmetrical solutions comparison.

III-4 Power divider specifications

Beam forming is achieved by means of the power divider that distributes the input power on the pixels of the matrix antenna according to certain law of magnitudes and phases. Isoflux beam forming is obtained using the symmetrical Sinc-Circular (C=M=0.15) solution with zero edges (9 pixels are fed). The central pixel in the matrix is considered the reference for the feeding law (magnitude=1 and phase=0), the other eight pixels are fed by the weights of 0.15 magnitudes and 180° phases (with respect to the central pixel in the matrix). Then the desired power divider must have nine outputs, **Figure IV-9** shows the input output ports labeling (Input: RF_in and outputs: P1 to P9) and the desired weights at the outputs of the power divider.

	Electric field weight	Power weight	Corresponding Si,i parameter (linear mag)
P1	0.15 / 180°	0.0225	0.138
P2	0.15 / 180°	0.0225	0.138
P3	0.15 / 180°	0.0225	0.138
P4	0.15 / 180°	0.0225	0.138
P5	1 / 0°	1	0.92
P6	0.15 / 180°	0.0225	0.138
P7	0.15 / 180°	0.0225	0.138
P8	0.15 / 180°	0.0225	0.138
P9	0.15 / 180°	0.0225	0.138

Figure IV-9. 1 to 9 power divider weights.

IV. Two modes diagram

The antenna required must have two different modes (wide Isoflux and the axial high gain modes) the first was presented in the previous paragraphs. The two beams for the CNES will be presented together in this paragraph. For the Isoflux beam the results of the symmetrical solution will be considered (C=M=0.15 zero edges).

IV-1 Axial beam forming

The axial beam requested by the CNES must have a maximum gain of 13dB, to do that nine pixels of the matrix are fed by equal weights (magnitudes and phases) with zeros at the matrix edges (**Figure IV-10.a**). The maximum gain obtained by this configuration is 14.2dB with a gain 3dB at the elevation angles θ=±33° and the axial ratio is below 3dB is the entire interesting axial zone θ= [-30°, 30°] **(Figure IV-11)**. The antenna can give a higher gain 19dB, this high gain is not requested in the CNES specifications but it’s presented to show the maximum gain the antenna can give. The 19dB gain is achieved by feeding all the pixels of the 5x5 matrix as shown in **Figure IV-10.b** with the axial ratio also below 3dB shown in the aperture angle of the 19dB beam (**Figure IV-11**).

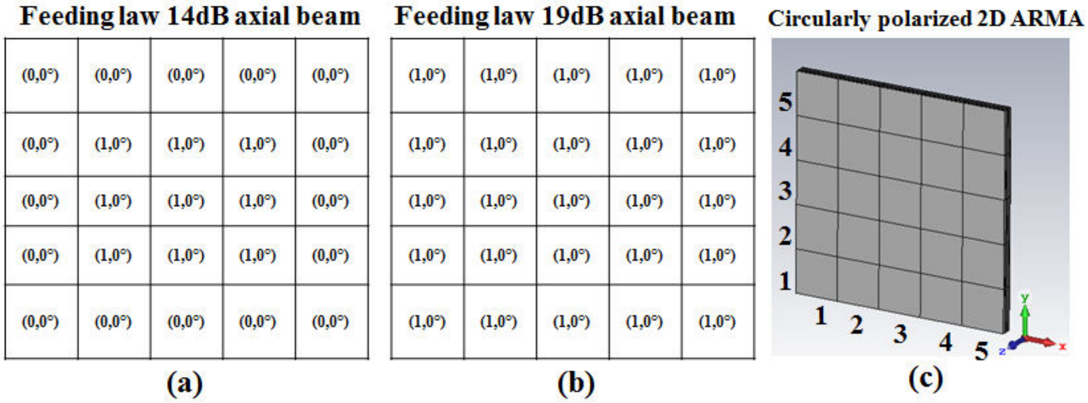

Feeding law 14dB axial beam

(0,0°)	(0,0°)	(0,0°)	(0,0°)	(0,0°)
(0,0°)	(1,0°)	(1,0°)	(1,0°)	(0,0°)
(0,0°)	(1,0°)	(1,0°)	(1,0°)	(0,0°)
(0,0°)	(1,0°)	(1,0°)	(1,0°)	(0,0°)
(0,0°)	(0,0°)	(0,0°)	(0,0°)	(0,0°)

(a)

Feeding law 19dB axial beam

(1,0°)	(1,0°)	(1,0°)	(1,0°)	(1,0°)
(1,0°)	(1,0°)	(1,0°)	(1,0°)	(1,0°)
(1,0°)	(1,0°)	(1,0°)	(1,0°)	(1,0°)
(1,0°)	(1,0°)	(1,0°)	(1,0°)	(1,0°)
(1,0°)	(1,0°)	(1,0°)	(1,0°)	(1,0°)

(b)

(c)

Figure IV-10. Feeding law for the high gain axial beams, (a) 14dB gain, (b) 19dB gain, (c) 5x5 circularly polarized ARMA.

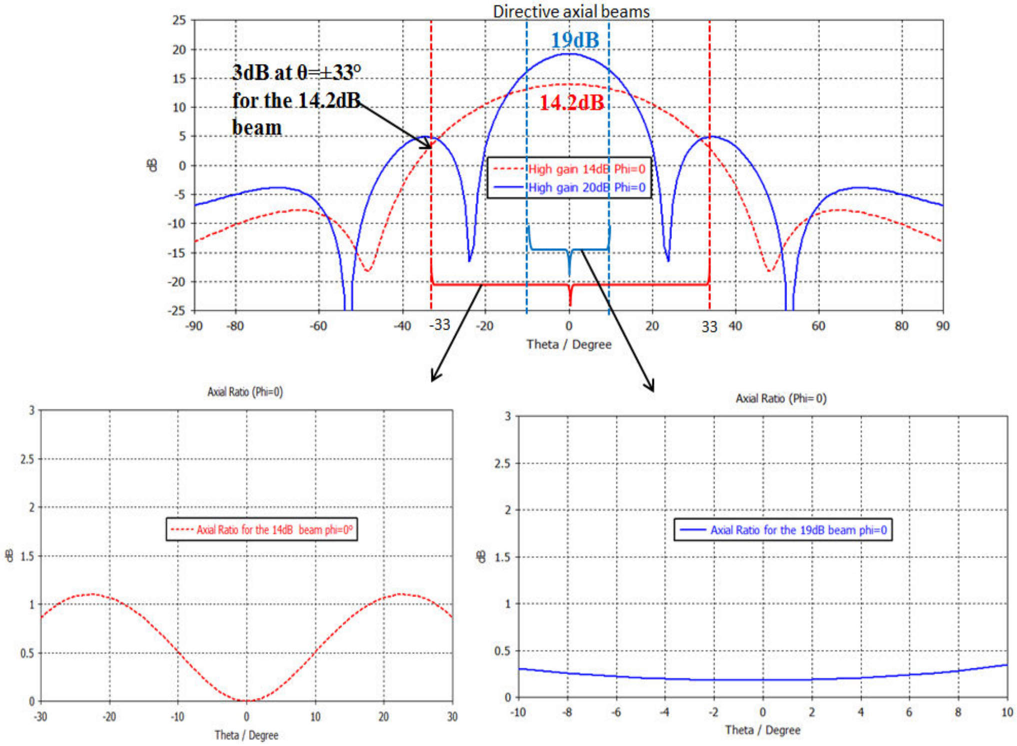

Figure IV-11. Directive axial beams, (dashed red) 14.2dB requested by CNES, (blue) 19dB gain.

Beam forming in the axial direction also is done to support new patterns for different applications, two cases are studied to have axial patterns with sectorial and isoflux types with the corresponding feeding laws given in **Figure IV-12**. The sectorial

(Figure IV-13.a) beam has a maximum 11.4dB which is smaller than the 13dB constraint, but maintained equally in the elevation angles range θ= [-20°, 20°] and decreases to 7dB at θ=±30°. The Isoflux axial beam **(Figure IV-13.b)** have the maximum gain of 11dB at θ=±20°, 6dB gain in the axial direction and 3dB at θ=±36°. This isoflux axial beam can be used for the same objective of the wide isoflux beam studied before but in the elevation angles near the axial direction, the aim is to compensate for power reception differences at the distant terrestrial base stations (equal received power).

Feeding law Isoflux axial beam

(0.3, 180°)	(0.3, 180°)	(0.3, 180°)	(0.3, 180°)	(0.3, 180°)
(0.3, 180°)	(1,0°)	(1,0°)	(1,0°)	(0.3, 180°)
(0.3, 180°)	(1,0°)	(1,0°)	(1,0°)	(0.3, 180°)
(0.3, 180°)	(1,0°)	(1,0°)	(1,0°)	(0.3, 180°)
(0.3, 180°)	(0.3, 180°)	(0.3, 180°)	(0.3, 180°)	(0.3, 180°)

Feeding law sectorial axial beam

(0.15, 180°)	(0.15, 180°)	(0.15, 180°)	(0.15, 180°)	(0.15, 180°)
(0.15, 180°)	(1,0°)	(1,0°)	(1,0°)	(0.15, 180°)
(0.15, 0°)	(1,0°)	(1,0°)	(1,0°)	(0.15, 180°)
(0.15, 180°)	(1,0°)	(1,0°)	(1,0°)	(0.15, 180°)
(0.15, 180°)	((0.15, 180°)	(0.15, 180°)	(0.15, 180°)	(0.15, 180°)

Circularly polarized 2D ARMA

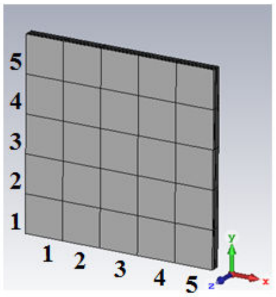

Figure IV-12. Feeding laws for the sectorial and Isoflux axial beams.

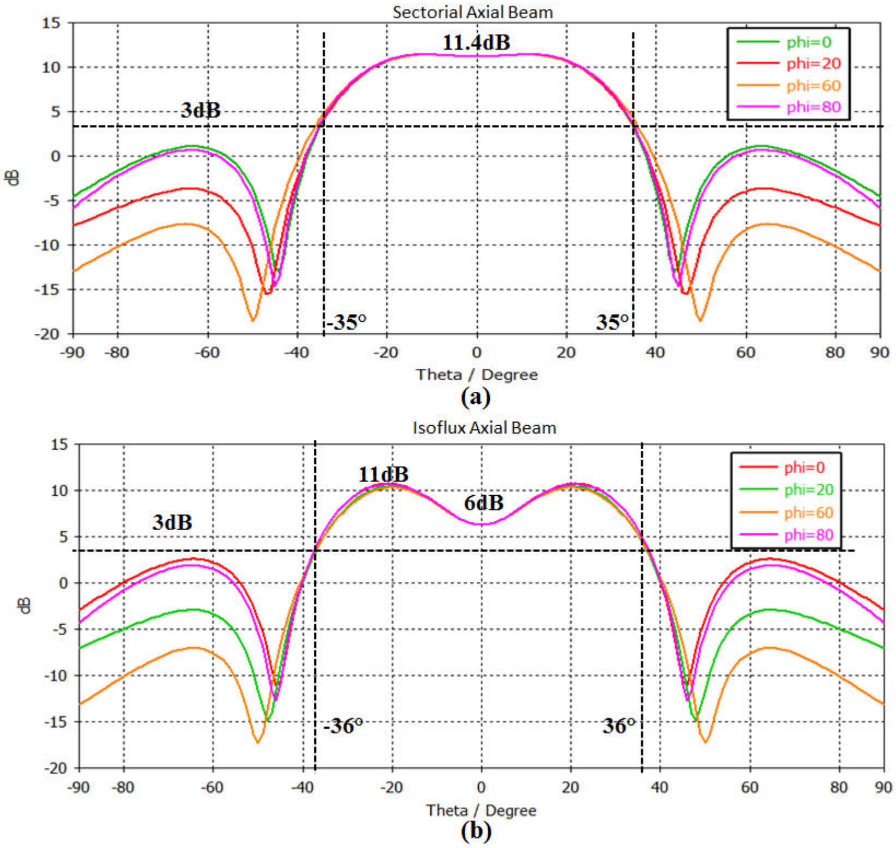

Figure IV-13. Axial beams: (a) Sectorial axial beam, (b) Isoflux axial beam.

IV-2 CNES two modes patterns

Figure III-14, show the two different patterns where the blue color and the grey color cover the interesting zones of the axial and wide Isoflux beams respectively. The wide Isoflux beam corresponds for the symmetrical Sinc-Circular solution (C=M=0.15 zero edges) studied previously and the directive 14.2dB beam. The curves show the two gain patterns with the corresponding axial ratio for each zone and the switching elevation angles between the two radiating modes which is maintained at θ=±30°.

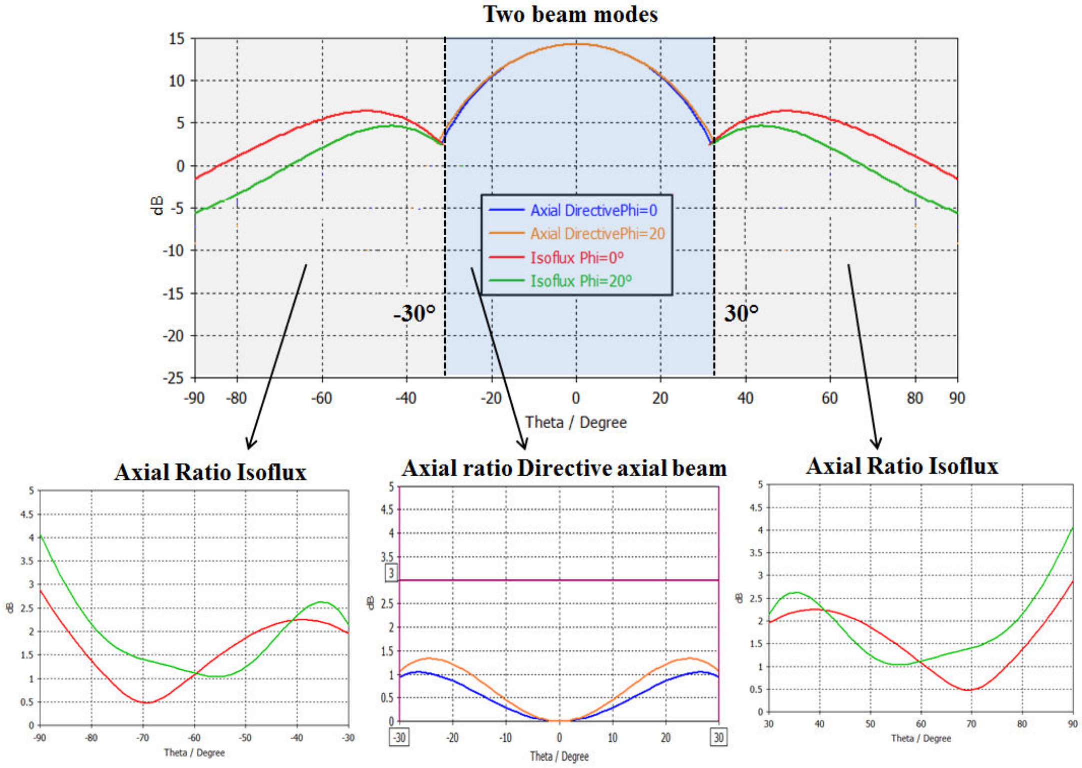

Figure IV-14. Two modes, Sinc-Circular symmetrical C=M=0.15 and axial directive beams.

V. Antenna realization

V-1 Power divider design and realization

The power divider (with specifications in **paragraph III-4**) is build using the microstrip lines parallel architecture printed on a substrate that is located above a ground plane. **Figure IV-15.a** shows the design on ADS software (schematic) and **Figure IV-15.b** shows the Momentum design after optimizations. Design parameters of the power divider are as follows:

- Substrate: Rogers RO6002 (εr=2.94, tanδ=0.0012) with 0.762mm thickness.
- Distance between (output ports) ≥ 13mm, to put the connectors.
- Output ports aligned on the same side (more convenient for coaxial cables).
- Length of divider circuit ≤ 13cm.
- Metallic thickness 0.017mm for the ground plane and microstrip lines.

The dimensions of the power divider shown in **Figure IV-15.b** fit the conditions mentioned above where the length of the power divider is 11.2cm < 13cm, the output ports are aligned on the same side and the distance between the output ports is greater than 13mm. Simulation results at f=8.2GHz of the output magnitudes ($S_{i,10}$ linear scale) and phases ($S_{i,10}$ in degrees) at the ports "P1" to "P9" **(Figure IV-15.b)** are illustrated in **Table IV-4**. Fabricated design of the power divider is given in **Figure IV-16** where it's packaged in a metallic box. Then the simulations and measurements comparison are shown in **Figure IV-17** (adaptation at the power divider input "P10"), **Figure IV-18** (S-parameters magnitudes at the outputs of the power divider) and **Figure IV-19** (S-parameters phases at the outputs of the power divider).

There is a big difference between the measured and the simulated S-parameter at power divider input port "P10" **(Figure IV-17)** this is due to the conception of the power divider that have some problems; problems that change the matching impedance. But the measured S-parameter at "P10" is still adapted below -10dB (-12.5dB). The measured output magnitudes and phases are in good agreements near the simulated results; magnitudes presented in linear scale **(Figure IV-18** and **Figure IV-19)**.

Port number	P1	P2	P3	P4	P5	P6	P7	P8	P9
Si,10 simulation magnitude	0.130	0.128	0.130	0.122	0.921	0.122	0.130	0.128	0.130
Si,10 simulation phase	176°	174°	174°	176°	0°	176°	174°	174°	174°

Table IV-4. Power divider theoretical required and simulation results at 8.2GHz.

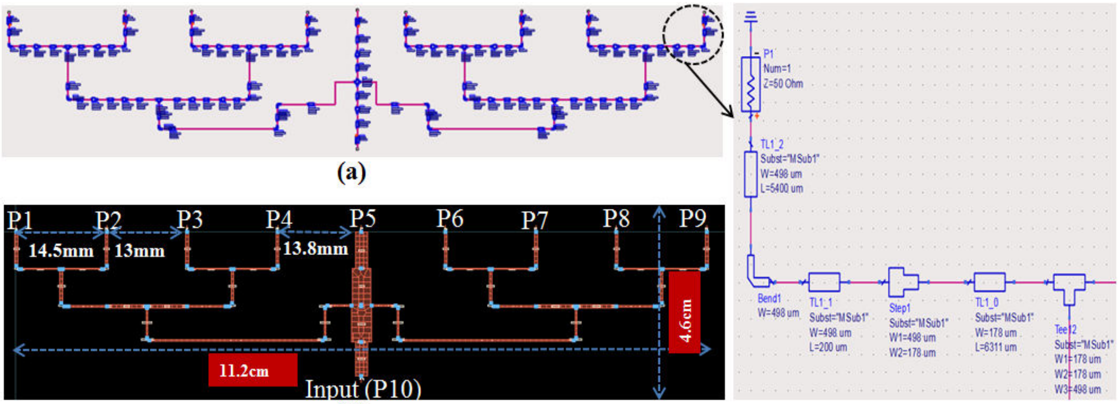

(a)

(b)

Figure IV-15. Power divider design: (a) ADS design, (b) optimized design in Momentum.

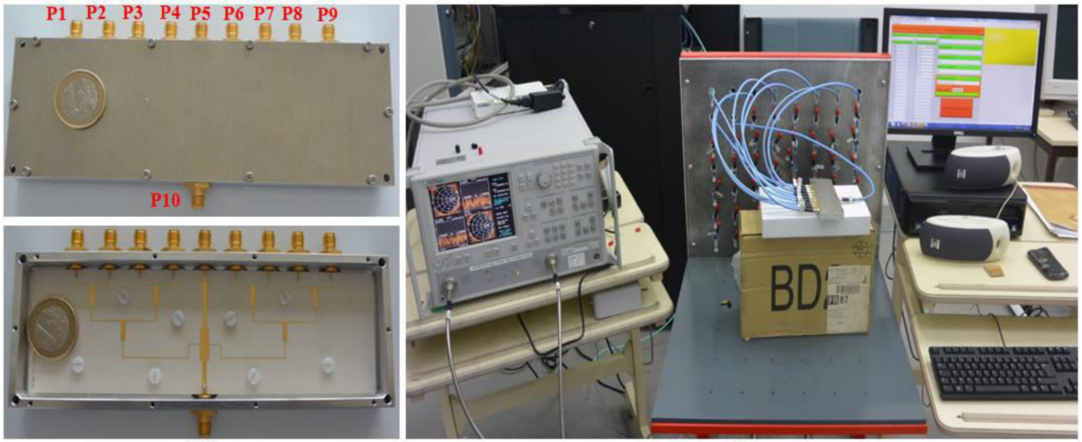

(a)

(b)

Figure IV-16. (a) Fabricated power divider, (b) measurements in the laboratory.

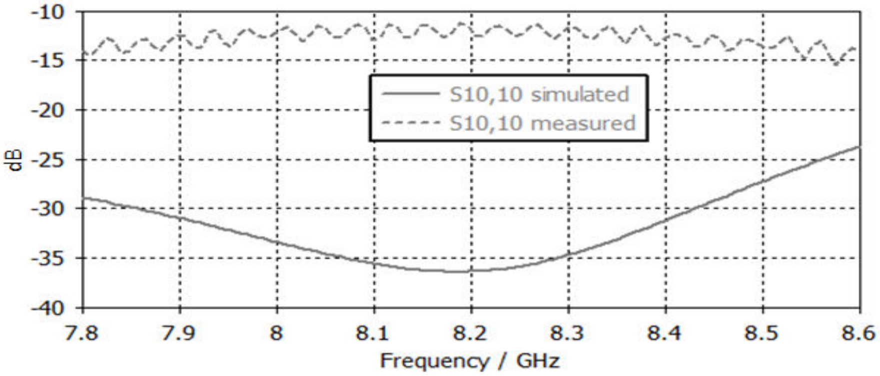

Figure IV-17. Simulation-measurement comparison, S-parameter at the input of the power divider.

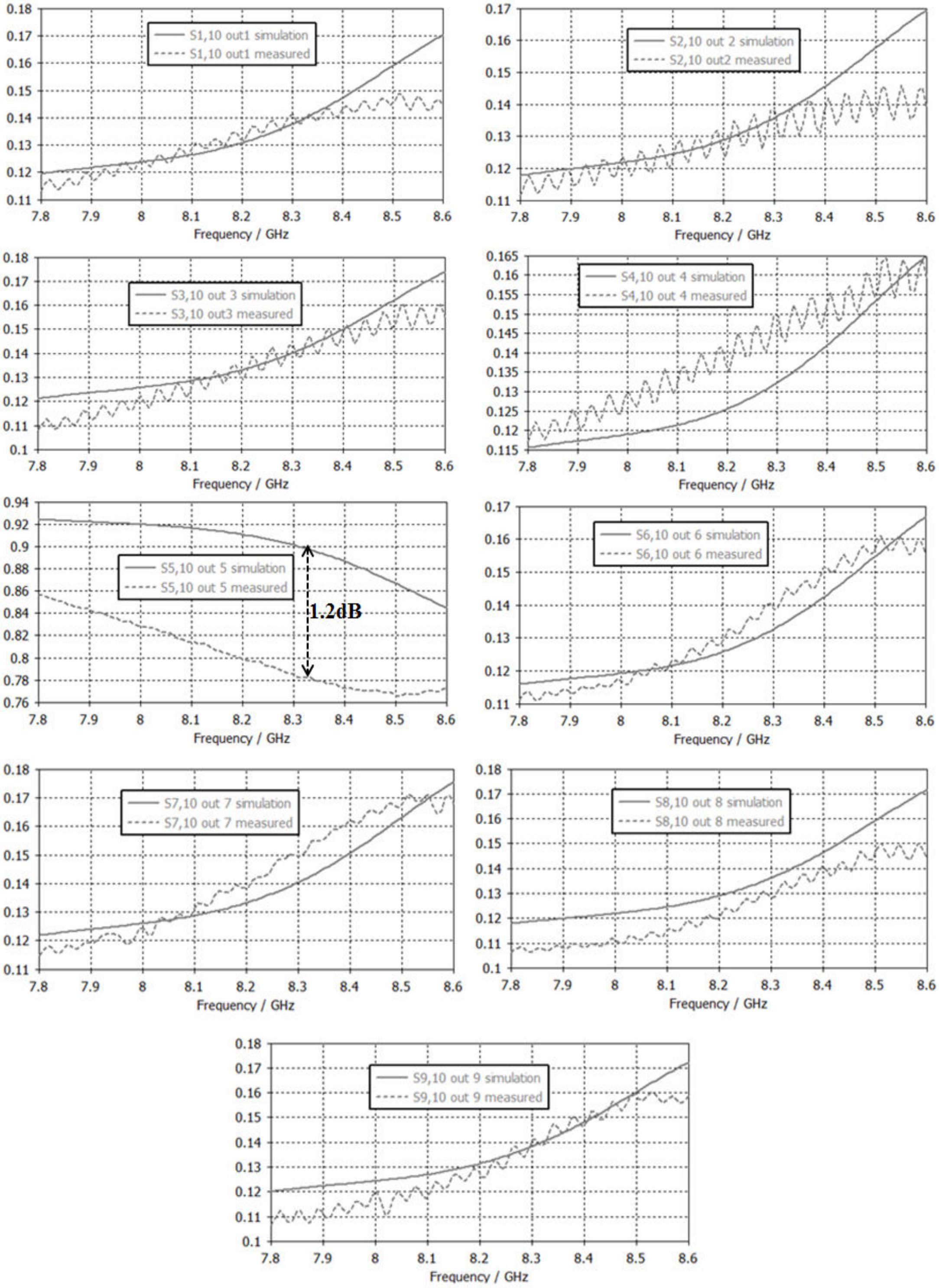

Figure IV-18. Simulation-measurement comparison, S-parameter magnitudes (linear scale) at power divider outputs.

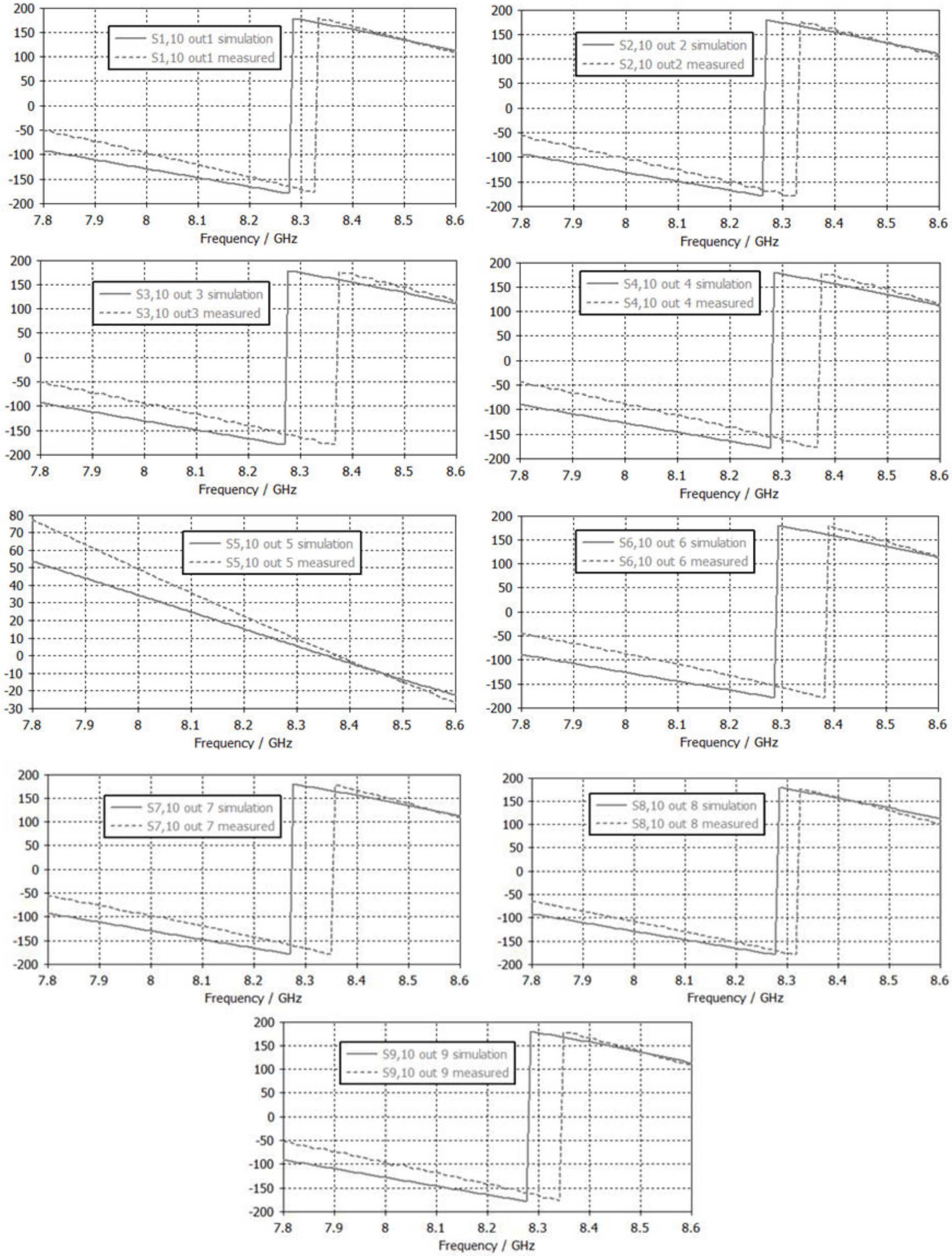

Figure IV-19. Simulation-measurement comparison, S-parameter phase (in degrees) at power divider outputs.

V-2 ARMA architecture and realization

In what follows the design architecture of the antenna in CST (ARMA fed by the polarization circuits) and the fabricated prototype. The design is an ARMA of 5x5 jointed pixels with the following parameters:

- 5x5 ARMA: 25 jointed pixels with 0.5λ spacing.
- Central frequency: $f_0 = 8.2\text{GHz}$.
- Patch and FSS substrates: Rogers, RO6002 of (εr=2.94, tanδ=0.0012), 1.524mm heights.
- Metallic walls: 2mm height, 1.5mm thickness.
- Polarization circuits substrate: TMM10i (εr=9.8, tanδ=0.002), 0.381mm height.
- Patches, FSS and ground plane: 0.017mm thickness.

The antenna consists of three layers **(Figure IV-20)**: the FSS layer, the patch layer and the polarization circuit layer; details will next be shown with the layers connectivity. The rigid plastic screws (blue color **Figure IV-20**) are used to fix the different layers together.

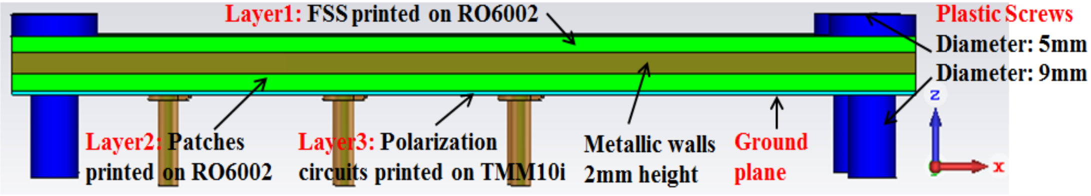

Figure IV-20. ARMA different layers, side view.

V-2.1 Polarization circuits realization: Layer3 in Figure IV-20

The polarization circuit **(Figure IV-21.a)** printed on the TMM10i substrate is designed to generate the phase shifts (theoretically 0°, 90°, 180° and 270°) needed to feed the patch inside the EBG cavity **(Chapter II paragraph II-8.2)**. The main challenge in the circuit design **(Figure IV-21.a)** is the small area reserved behind the pixel (0.5λx0.5λ=18.29mmx18.29mm) that must be enough for: three hybrid couplers, three resistors pads and a connector pad. Each of the three hybrid couplers have one port connected to a resistor of 50Ω (**ATC 504L** given by ATC Company) that needs a pad to be grounded; these pads are designed and optimized alone to have very small dimensions. The input connector of the circuit used, has high performances and small size (4.2mm diameter **R222.508.000** given by Radiall Company), the connector pad for grounding and the microstrip line to solder the circuit-connector pin was also optimized to have small size **[Appendix II]**.

Figure IV-21.b shows all the circuits in the design and **Figure IV-21.c** shows the fabricated circuits with the connectors and resistors. Remind that we need nine circuits for nine fed pixels and the pixels at the peripherals of the matrix are connected to 50Ω impedances (not fed). The holes at the corners of **Figure IV-21.b** are made to allow the pass of the screws **(Figure IV-20)**.

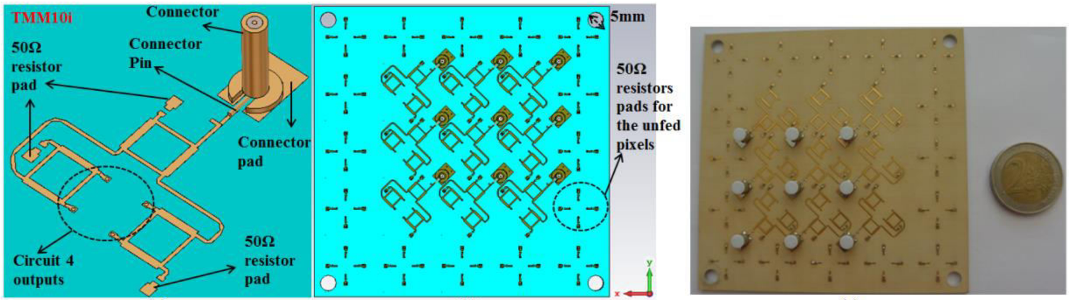

(a) (b) (c)

Figure IV-21. (a) Polarization circuit, (b) nine circuits, (c) fabrication.

V-2.2 FSS realization: Layer1 in Figure IV-20

Layer1 is the FSS printed on the RO6002 substrate. **Figure IV-22** shows the designed and fabricated layer with the FSS dimensions. The holes at the corners of this layer are for the screws.

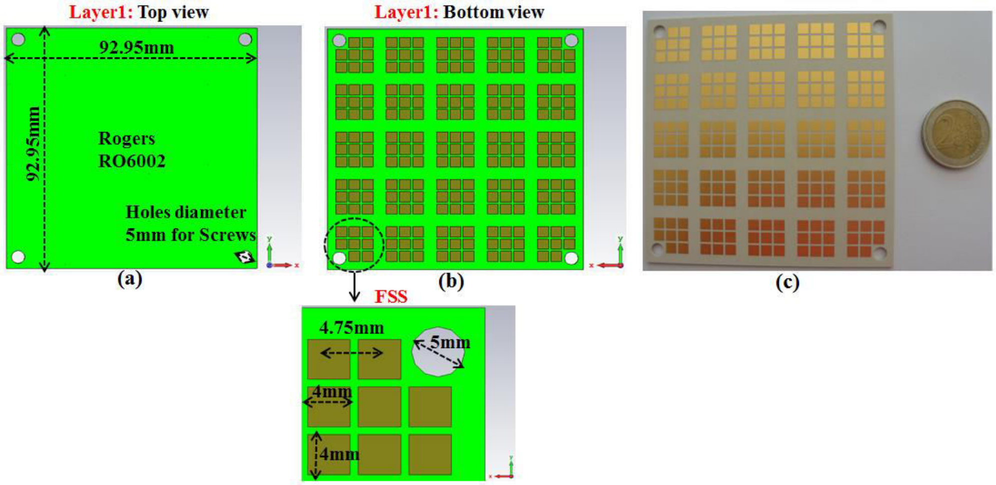

(a) (b) (c)

Figure IV-22. Layer1 FSS printed on RO6002, (a) top view, (b) bottom view, (c) fabrication.

V-2.3 Metallic walls realization

The metallic walls (2mm height) design and fabrication are shown in **Figure IV-23**. The height of these walls is 2mm and the thickness is 1.5mm. More details about the metallic walls connection with the ground plane will be shown next.

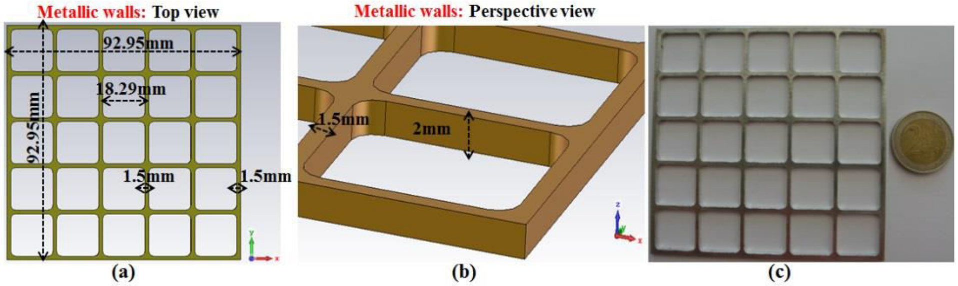

Figure IV-23. Metallic walls, (a) top view, (b) perspective view, (c) fabrication.

V-2.4 Antenna layers connectivity: Layers 1, 2, 3 in Figure IV-20

The layer3 is the feeding patches printed on the RO6002 substrate, with metallic plates (described next), **Figure IV-24** shows the designed and fabricated layer and **Figure IV-25** shows the different fabricated layers. The description and connectivity between layers are explained in the next paragraph. The screws are inserted inside the pixels located at the corners of the matrix, for that the patches at the corners (un-fed) are truncated from their edges a little bit **(Figure IV-24.a)** to allow the pass of the plastic screws (this will make no sense or perturbations since these pixels are not fed. By this way we avoid the use of an extra support (that may lead to perturbations) at the edges of the matrix to fix the different layers.

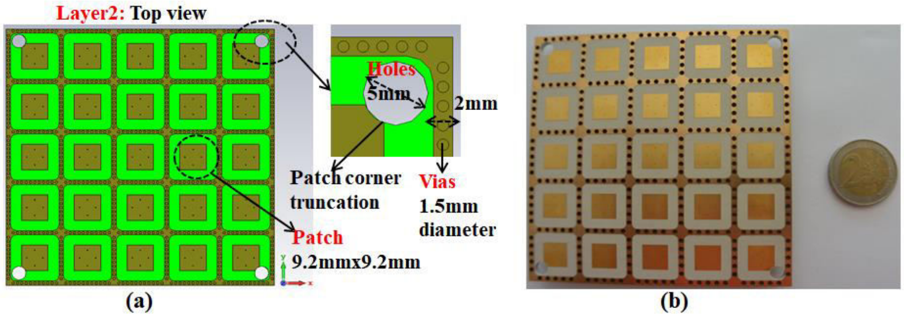

Figure IV-24. Layer2, patches and metallic plates: (a) top view, (b) fabrication.

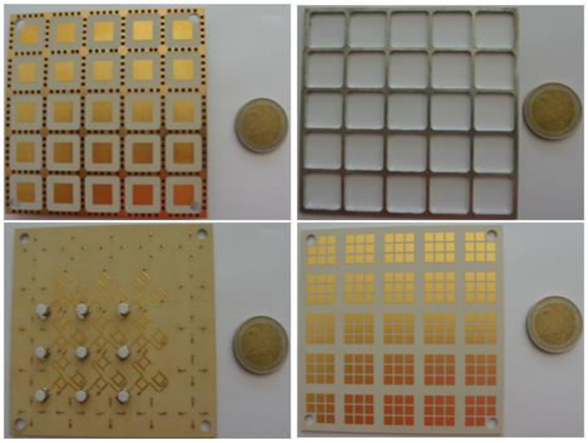

Figure IV-25. Fabricated layers (Layer1, Layer2 and Layer3) and the metallic walls.

The antenna top, bottom and side views are shown in **Figure IV-26.a** and **Figure IV-26.b**. Notice that the metallic walls are from the top of patches substrate to the bottom of the FSS substrate **(Figure IV-26.e)**. Normally the metallic walls are connected to the ground plane as described in the whole thesis (closed cavity), but for some manufacturing difficulties it was recommended by the manufacturers not to have this kind of connectivity:

The ground plane is common **(Figure IV-26.c)** for both the feeding patch substrate (RO6002) and the polarization circuit substrate (TMM10i). To make the metallic walls and ground planes directly connected, the patch substrate must be dig to insert the metallic walls inside, but the ground plane is very thin (0.017mm) and it is not possible to do that. The thin layer for the ground plane is necessary to make the different vias inside it. So we insure this connectivity using another solution **(Figure IV-26.e)**: On the layer of the patches (Layer3) we use metallic plates (0.017mm thickness) and we make vias (Vias1 in **Figure IV-26.e**, 1.6mm diameter) from these metallic plates to the ground plane, so that the metallic walls placed on the top of theses plates is connected to the ground plane by means of these vias. A study was done to optimize the vias diameter and the periodicity between vias to have the same results for the antenna as if the metallic walls were connected to the ground plane **[Appendix II]**. The patches are connected to the outputs of the polarization circuits **(Figure IV-21)** by vias (Vias2 in **Figure IV-26.e**, 0.3mm diameter). The resistors pads of the hybrid couplers **(Figure IV-21.a)**, the resistor pads of the un-fed pixels **(Figure IV-21.b)** and the connectors pads **(Figure IV-21.a)** are connected with the ground plane by vias (Vias3 in **Figure IV-26.e**, 0.3mm diameter).

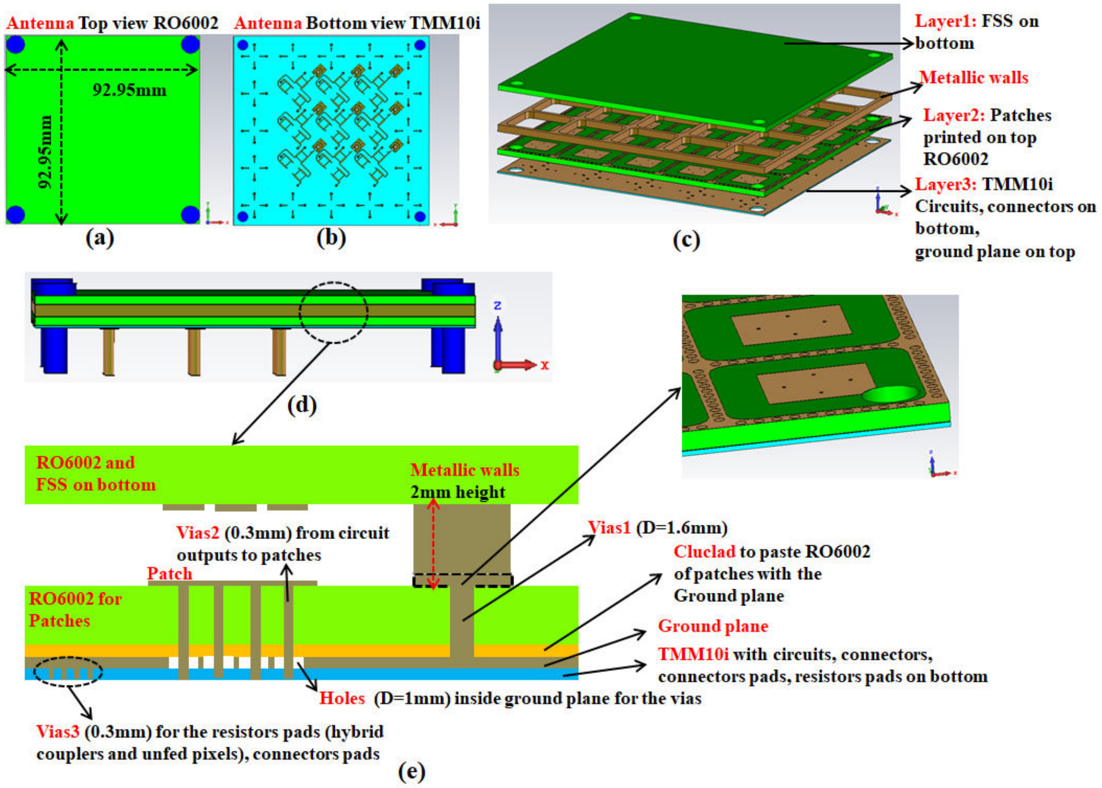

Figure IV-26. Matrix antenna, (a) top view, (b) bottom view, (c) side view, (d) side view showing.

VI. Simulation measurements comparison

The antenna is put on a support in the CST design **(Figure IV-27.a)** and tested then the results obtained are compared with measurements. The different fabricated **(Figure IV-25)** layers are assembled, connected by the screws and connected to the power divider by the cables (R201.508.000 from Radiall Company) **(Figure IV-27.c)**. The antenna is encased from all the sides by aluminum metallic support **(Figure IV-27.b)** like the Cube-Sat support and measured in the anechoic chamber. Then in the next paragraphs there are the simulation and measurements comparison of the realized gain, axial ratio and the bandwidth.

(a) (b) (c)

Figure IV-27. Antenna, (a) with metallic support in CST, (b) fabricated layers, (c) fabricated with aluminum support, (d) in the anechoic chamber.

VI-1 Bandwidth at the input of the polarization circuits

Figure IV-28.a shows: the schematic in CST for the matrix antenna connected to the polarization circuits (touchstone files taken from Momentum software), the corresponding 50Ω charges (for the hybrid couplers and the unfed pixels) and the labeling of the inputs of the polarization circuits. **Figure IV-28.b** shows the corresponding ports labeling in the antenna fabricated.

The S-parameters ($S_{i,i}$) shown in **Figure IV-29** show a bandwidth of greater than 800MHz in both simulation and measurements. But the measured bandwidth is shifted approximately by 400MHz from the simulated one. The study of the possibilities of this shift shows that: the permittivity of the RO6002 of the patches layer and the permittivity of the TMM10i of the circuit have real values a little bit different from the values in the CST design. The measured couplings shown in **Figure IV-30** are good even if they are not exactly equal to the simulation results, but all the measured couplings are below -24dB. Remark that the measured couplings are better than the simulated ones; this is due to the fact that the realized design shows losses and couplings effects inside the TMM10i and at the polarization circuit inputs better than the simulation with the given design parameters.

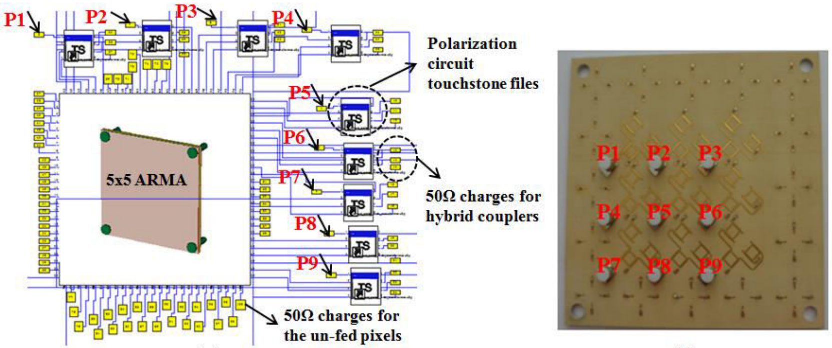

(a) (b)

Figure IV-28. (a) Ports labeling of matrix connected to polarization circuits, (b) corresponding ports in fabrication.

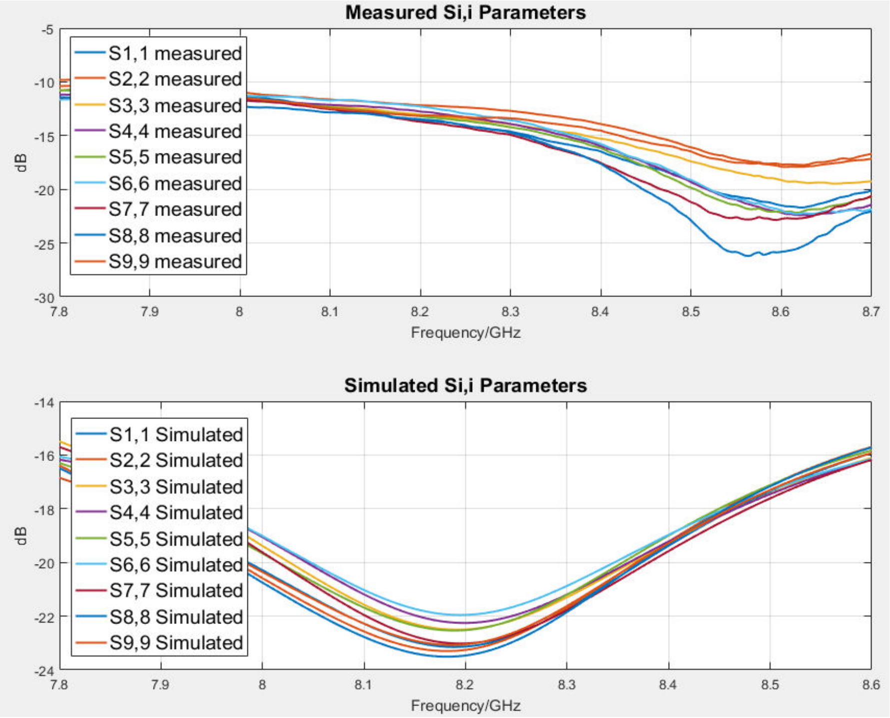

Figure IV-29. S-parameter at “P1” to “P9” (upper curves) measured, (lower curves) simulation.

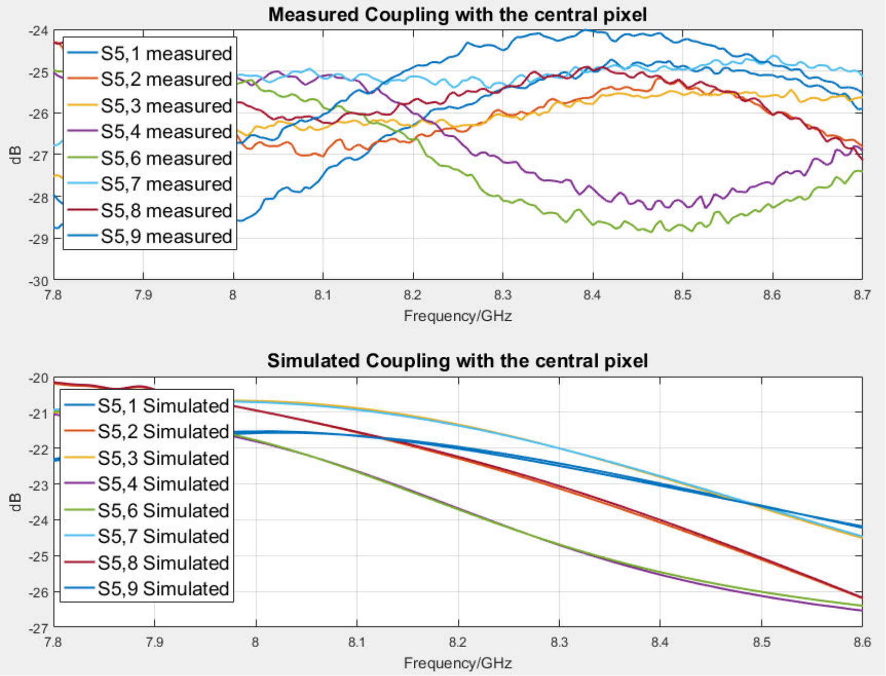

Figure IV-30. Couplings of the ports with “P5”, (upper curves) measured (lower curves) simulation.

VI-2 Bandwidth of the whole structure at the input of the power divider

Figure IV-31.a shows: the matrix antenna connected to the polarization circuits and power divider (touchstone files taken from Momentum software). **Figure IV-31.b** the input of the power divider for the fabricated antenna. The simulation-measurement S-parameters at the power divider input are shown in **Figure IV-32**. The measured S-parameter is a little bit higher than the simulated one; this is due to the un-perfect matching at the input of the power divider.

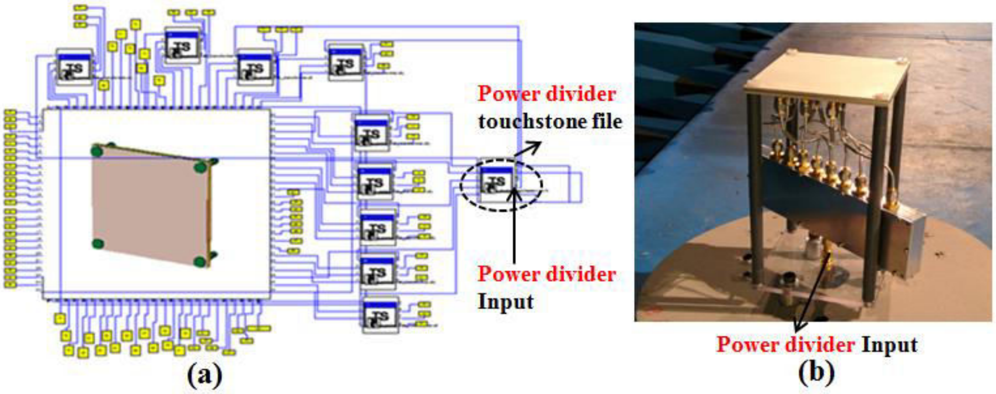

Figure IV-31. Input port for the whole structure, (a) CST schematic, (b) in fabrication.

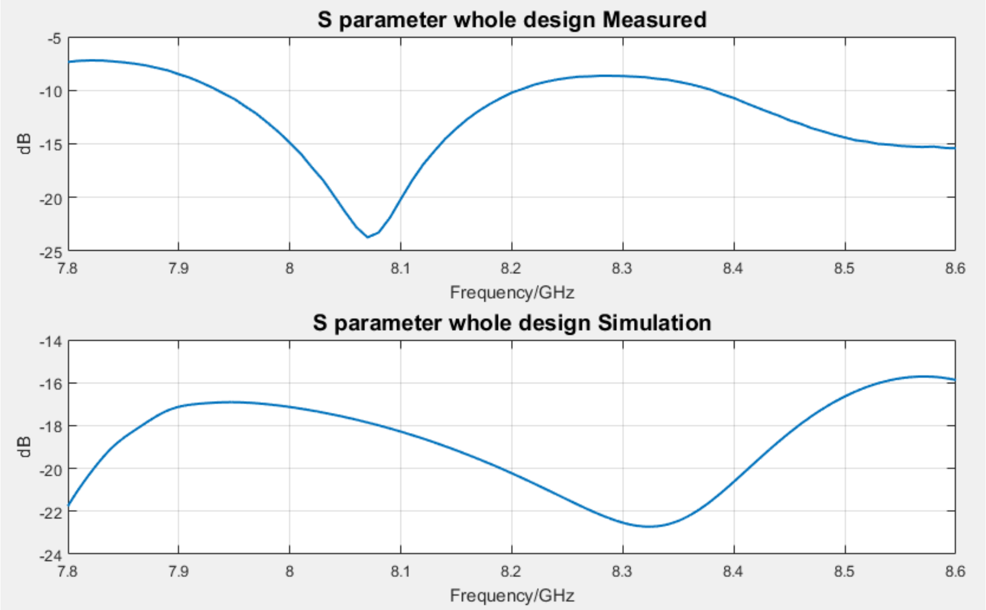

Figure IV-32. S-parameter whole structure, (upper) measured, (lower) simulation.

VI-3 Realized gain and axial ratio

In what follows in this paragraph there are the realized gain and the axial ratio simulations and measurements comparison. Comparison is done at frequencies 8GHz (**Figure IV-33** and **Figure IV-34**), 8.2GHz (**Figure IV-35** and **Figure IV-36**) and 8.4GHz (**Figure IV-37** and **Figure IV-38**). At each frequency the realized gain and axial ratio patterns are given in the azimuth planes φ=0°, 15°, 30° and 45°. Then at the end of this paragraph there are the comments on these results. In this entire paragraph the solid curves are related to the simulation results and the dashed curves are related to the measurements.

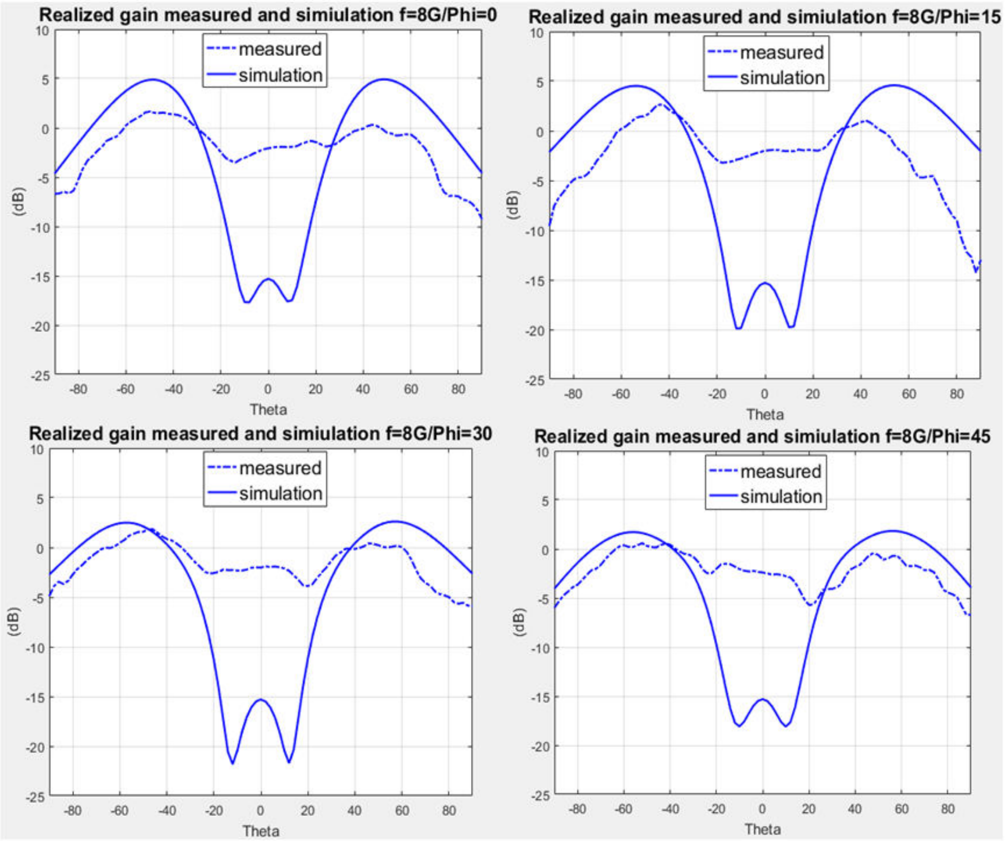

Figure IV-33. Realized gain f=8GHz, (solid) simulation, (dashed) measured.

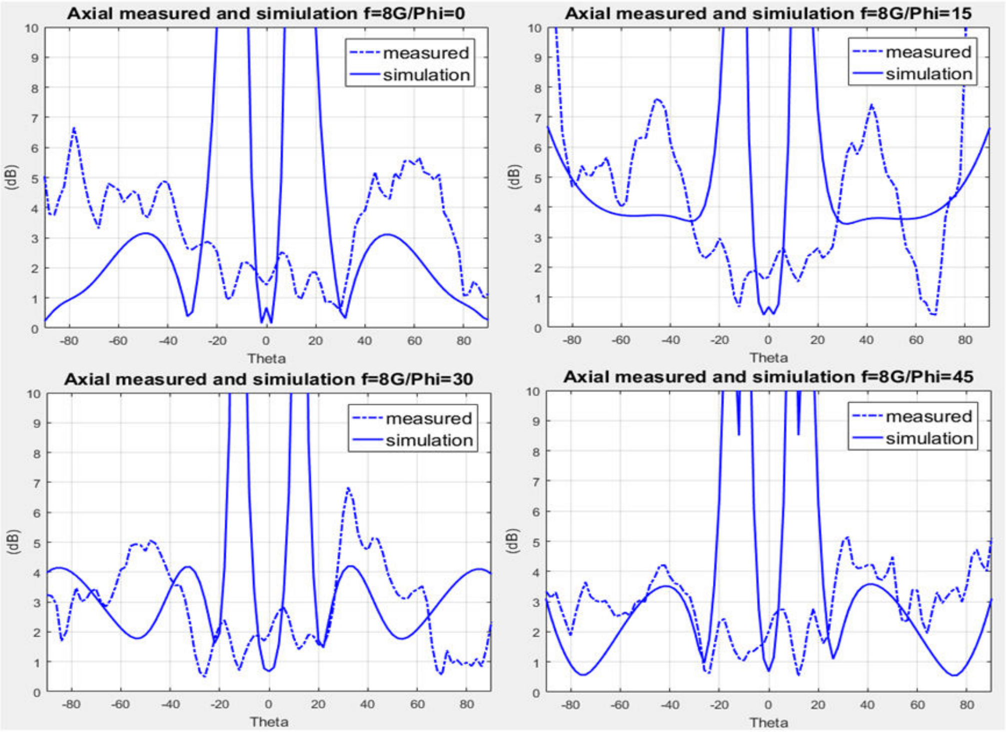

Figure IV-34. Axial ratio f=8GHz, (solid) simulation, (dashed) measured.

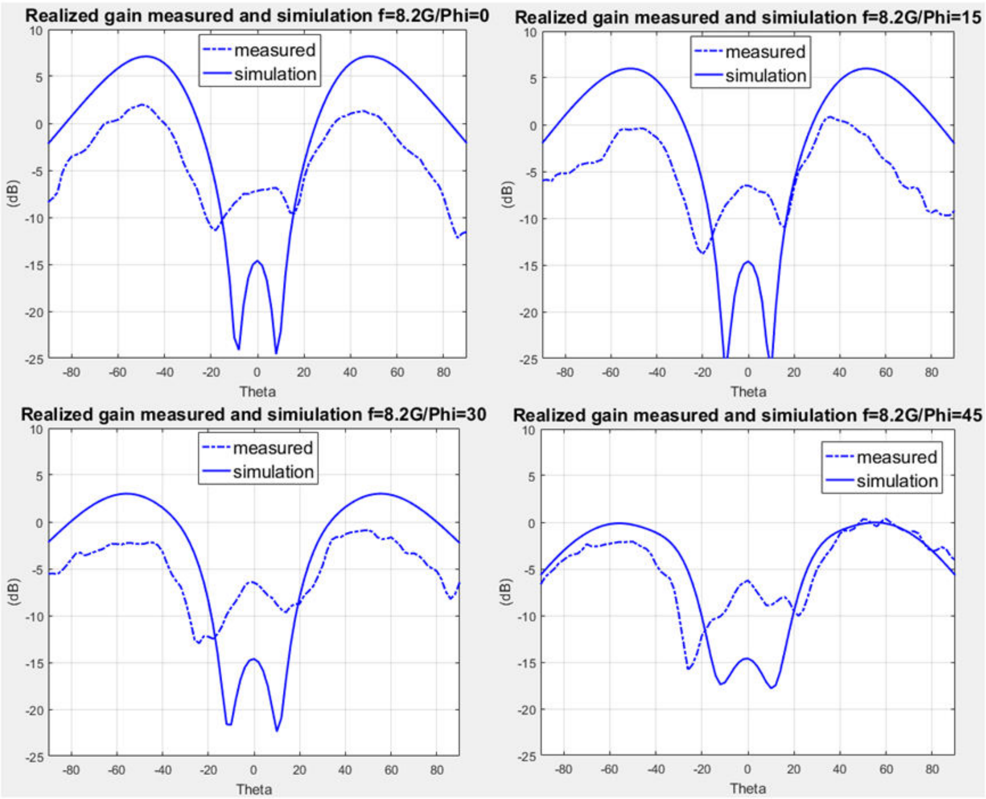

Figure IV-35. Realized gain f=8.2GHz, (solid) simulation, (dashed) measured.

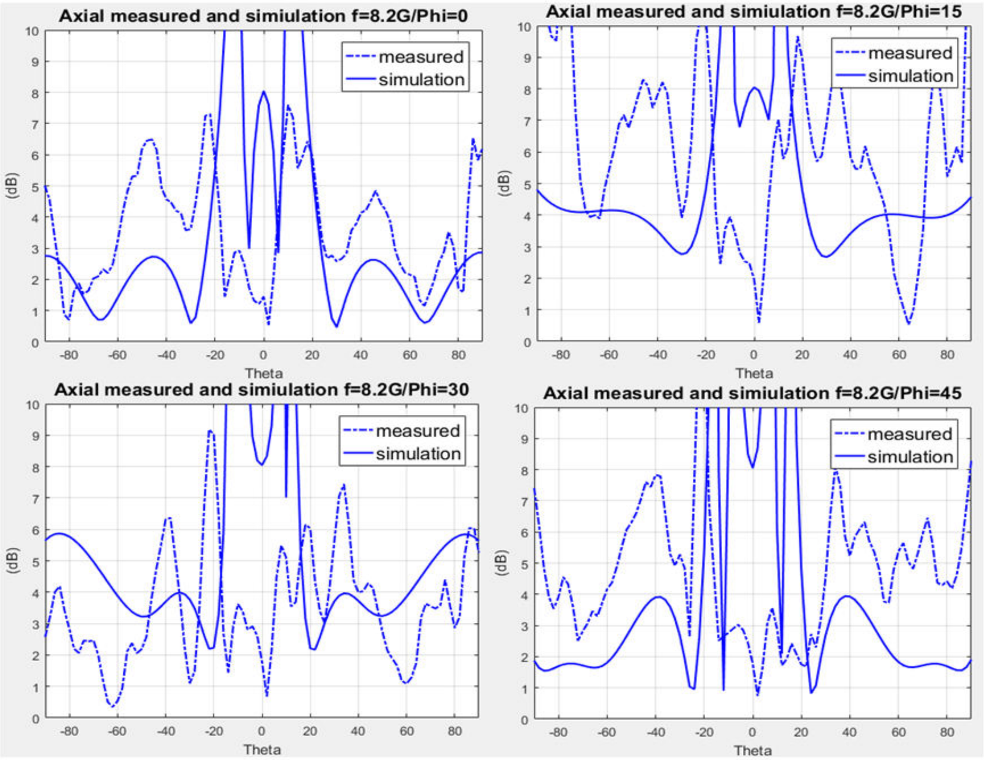

Figure IV-36. Axial ratio f=8.2GHz, (solid) simulation, (dashed) measured.

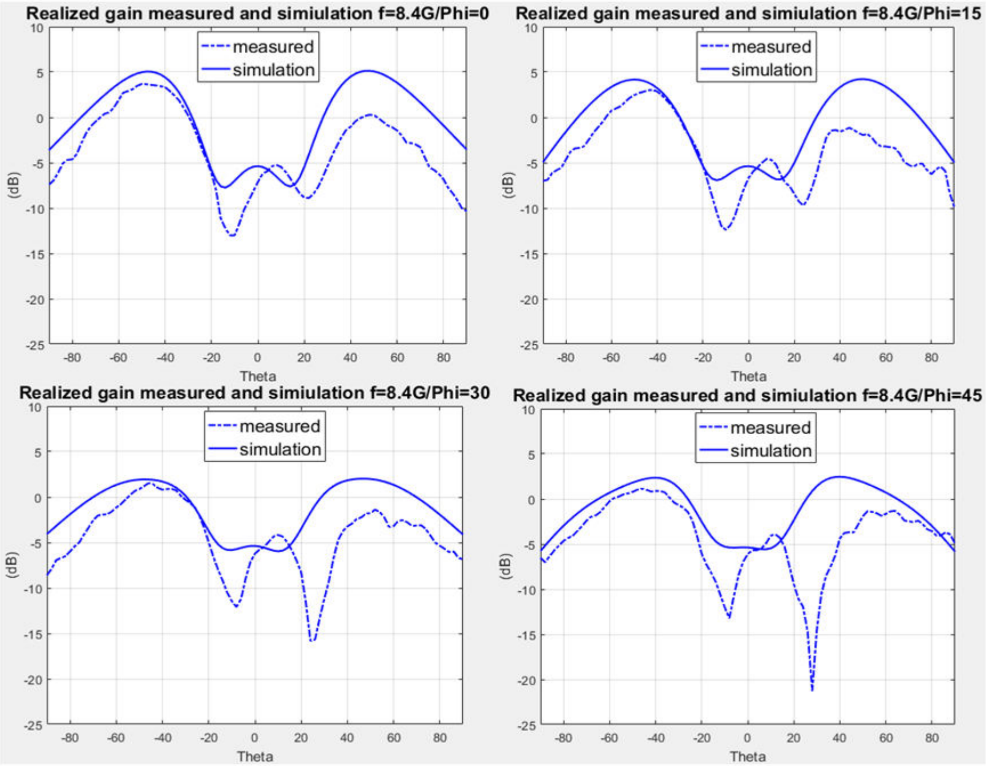

Figure IV-37. Realized gain f=8.4GHz, (solid) simulation, (dashed) measured.

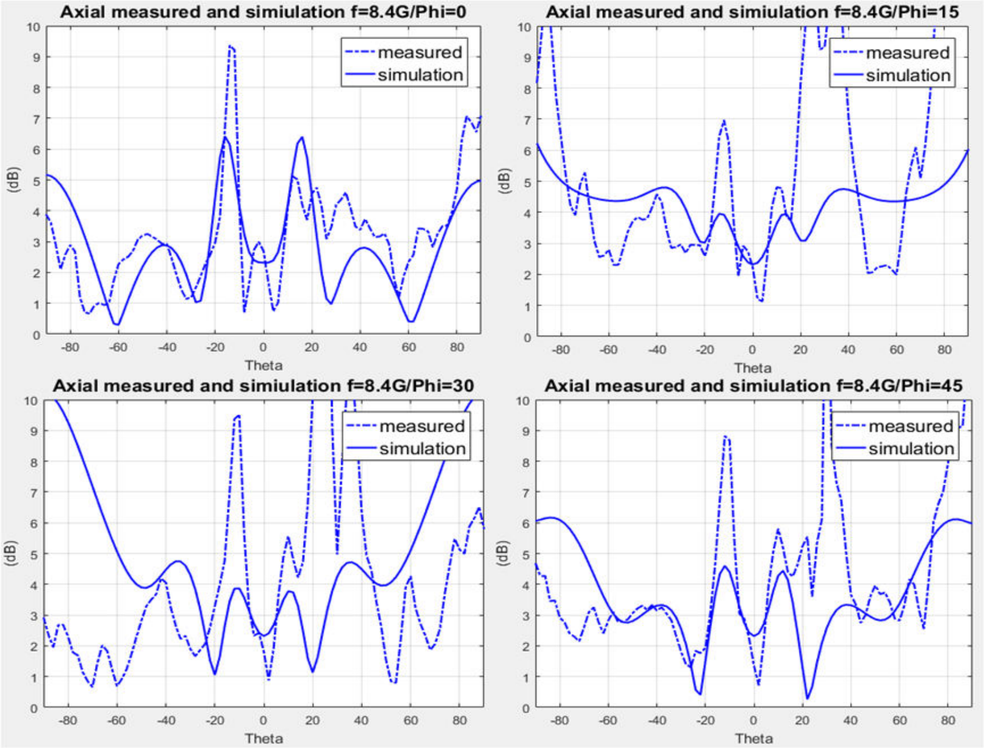

Figure IV-38. Axial ratio f=8.4GHz, (solid) simulation, (dashed) measured.

The measurements show some inconvenient results in some cases. After the first measurements were done, we had some problems with the antenna. The connectors between the power divider and the antenna were destroyed and some parts of the antenna were damaged then and we were not able to make new measurements.

VII. Conclusion and future work

In this chapter the CNES project specifications were presented giving arise to the requirements of the matrix antenna dimensions, bandwidth, two beam modes and axial ratio.

In the theoretical and design parts: The Isoflux beam was studied and the feeding law optimizations give gain and axial ratio patterns with good agreements with the specifications. Different feeding laws were studied; the symmetrical Sinc-Circular and the non-symmetrical where these solutions solve the problems of the maximum gain positions and the dissymmetry of the Isoflux pattern in the different azimuth planes. The bandwidth of the antenna was greater enough (>800MHz) than the specified bandwidth (400MHz). Then the axial high gain mode was studied using three different patterns directive (14.2dB beam and 19dB beam), sectorial (maintain 11dB gain around the axial direction) and the isoflux axial beam. The two modes patterns were presented with their corresponding axial ratio that was below 3dB in the corresponding interesting zones for each mode. The feeding law of the Isoflux beam was attained by the power divider design that was with good agreements with the dimension and outputs results specified theoretically, but with some problems in the connectivity with the polarization circuits.

In the realization part, the polarization circuit was realized with very small dimensions, where all the components were optimized to have small dimensions; hybrid couplers, resistors and connectors pads. The power divider was realized and tested alone, the measurements of the power divider alone show good agreement with the simulation, but also show a problem in the matching impedance at the input. The different layers of the antenna were fabricated and the measurements in the anechoic chamber were done. The measured bandwidth was 800MHz. The measured results presented include some problems: Frequency shift at the input of the polarization circuits **(Figure IV-29)**, mismatching at the input of the power divider **(Figure IV-32)** and perturbation on the gain and axial ratio patterns (results in **paragraph VI-3**). Many cases were tested regarding the possible fabrication problems that show no significant effects **[Appendix II]**. However testing shows two reasons for these measured problems:

1. The real values of the substrates permittivity used (RO6002 and TMM10i), that cause the frequency shift measured at the inputs of the polarization circuit and the whole structure.
2. The power divider conception: We didn’t use the same architecture at for the power divider as the polarization circuit, to avoid the power losses inside the 50Ω impedance used in the hybrid coupler. The polarization circuit’s inputs are matched to have 50Ω impedances; however this is not the case for the power divider output

ports. The architecture used to build the power divider lead (in theory and design) to microstrip lines at the outputs with high impedance, so when connected with polarization circuit by the cables the mismatching impedance causes the output magnitudes and phases of the divider to change their values; we didn't master that at the beginning. Then this lead to some perturbations in the feeding law that was expected to be the symmetrical Sinc-Circular "C=M=0.15", and makes the measured patterns to be in some cases with bad agreements with the simulated results. Also an important reason that leads also to perturbations in power divider outputs is the isolation of the output ports (power divider). The outputs of the power divider (magnitudes and phases) shown in **paragraph V-1** are related to the power divider tested alone and not connected with the antenna polarization circuits; that is why these results were with good agreement with the simulations. Then this problem is illustrated by the following:

- The mismatched connection at the input of the power divider causes the un-perfect adaptation for the global S-parameter of the antenna.
- The high impedance at the outputs of the power divider that causes: the mismatching impedance of the connectivity between the power divider and the polarization circuits and the bad isolation of the power divider outputs. These result in gain losses and perturbations of the feeding law expected by the power divider.

In the next **(Chapter-V)** these problems will be explained more in details and the corresponding solutions will be presented. Also the future work and perspectives regarding the Isoflux and the antenna architecture will be shown.

List of Figures

List of Tables

Chapter V

Fabrication Problems and Solutions

Table of Contents

I. Introduction

In **Chapter IV** the conception and design of the circularly polarized **ARMA** for the bi-mode beams was presented including the 5x5 pixels matrix, the polarization circuit and the power divider. Also the feeding law optimization was done giving the solution with better possible, using the squared shape matrix, Isoflux maximums gain positions and pattern homogeneity. However measurements after realization show some problems of frequency shift (at the input of the polarization circuit connected to the antenna), miss-matching impedance (at the input of the power divider) and perturbations of the Isoflux and axial ratio patterns in some cases. In this chapter the reasons of these problems will be discussed and the solutions will be given. Also in this chapter the limitations due to the structural geometry of the antenna will be more stated in details and the effect of the cube-sat support on the antenna patterns will be studied. The perspectives and future work will show more solutions for the power divider and whole antenna architecture and also new geometrical structures.

The two main conception problems to be studied are:

1. The permittivity of the substrates related to the frequency shift.
2. The conception of the power divider that is the reason for the mismatching impedance, the feeding law perturbations and the Isoflux and axial ratio patterns deformations.

II. Frequency shift problem and solution

II-1 TMM10i and RO6002 characterization

The frequency shift results from the difference in the permittivity the RO6002 and TMM10i (laminates given by the Rogers Company). We were not able to make characterizations for these substrates before the antenna manufacturing due to financial problems. Good characterization of a stacked design with different dielectric constant substrates requires several realizations; more information about the procedure is presented in **[1]** (**[1]** is a thesis at XLIM RF-systems 2015 **Chapter IV**). In our case the cost is related to the TMM10i laminate cost and fabrication price. TMM10i is of Ceramic type that is rigid, and we were not able to make many circuits fabrications in the laboratory at XLIM. Even if there are many equipment but the vias to do inside this material were very small (0.3mm diameter) and need special equipment. Only "Cibel Company" was able to do this manufacturing and the cost was high.

II-2 Study of permittivity value shift effect

RO6002 is used in the antenna to print the FSS on the top and the feeding patches inside the pixel cavity. The design permittivity is $\varepsilon_r = 2.94$ and the real permittivity in realization may differ by ±5% error in the worst case. This error changes the impedance of the feeding patch inside the EBG cavity that requires a little shift in the feeding probes positions; to adapt the feeding point of the feeding patch with the input impedance of the coaxial cable to 50Ω which if not adapted results in resonance frequency shift. Circularly polarized pixel with four ports designed to work at the central frequency 8.2GHz with 0.5λx0.5λ ground plane is shown in **Figure V-1.a**. The RO6002 dielectric constant is tested with three different values and the frequency shift for each is shown in **Figure V-1.b**. The return loss parameters in **Figure V-1.b** are taken at one of the four ports of the pixel where the results show: Frequency shift +195MHz for $\varepsilon_r = 2.78$ (corresponds for error of -5%) and frequency shift -177MHz for $\varepsilon_r = 3.08$ (corresponds for error +5%). These results (frequency shift) are the same if we consider the pixel inside the matrix antenna (5x5 pixels **ARMA**).

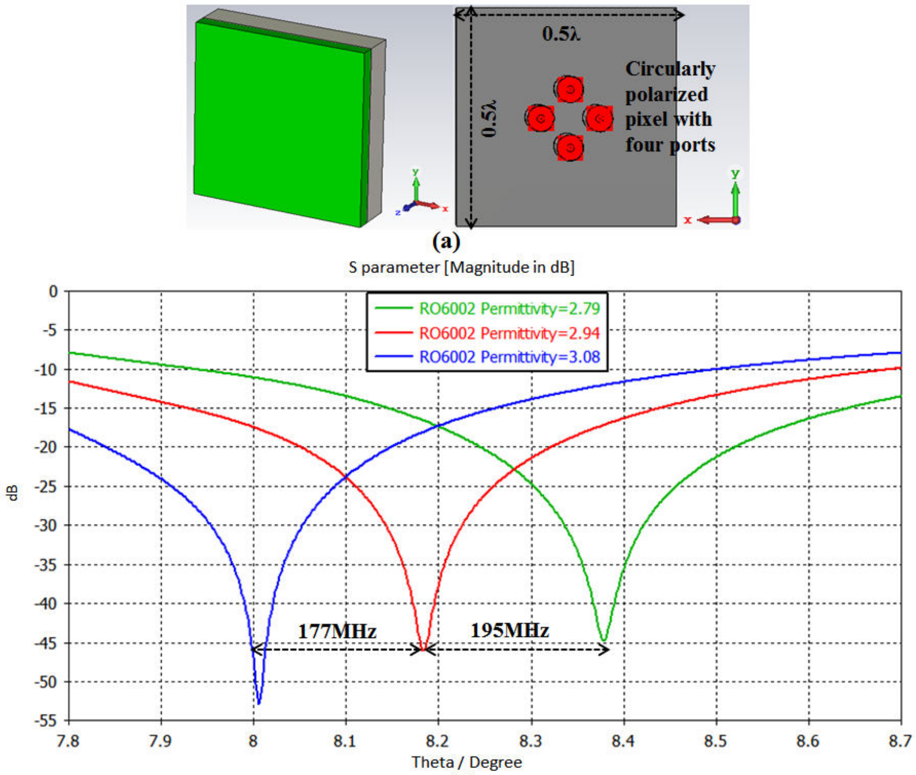

(a)

(b)

Figure V-1. (a) Circularly polarized pixel, (b) RO6002 ε_r error and the corresponding frequency shift, (red) $\varepsilon_r = \mathbf{2.94}$, (blue) $\varepsilon_r = \mathbf{3.08}$, (green) $\varepsilon_r = \mathbf{2.78}$.

TMM10i with given permittivity $\varepsilon_r = 10.35$ is used to print the polarization circuit behind the pixel. **Figure V-2.a** shows the schematic in the CST for the pixel with four ports **(Figure V-1.a)** connected to the polarization circuit touchstone file taken from Momentum software. Three touchstone files was generated and connected to the pixel, each with different permittivity for the TMM10i substrate. **Figure V-2.b** shows the frequency shift in the return loss simulated at the input of the circuit connected to the pixel. For $\varepsilon_r = 10.35$ the return loss parameter is centered at 8.2GHz, however for $\varepsilon_r = 9.83$ (corresponds for error -5%) the return loss parameter is shifted +188MHz and for $\varepsilon_r = 10.87$ the return loss parameter is shifted +165MHz.

The results of **Figure V-1.b** and **Figure V-2.b** shows that the combination of -5% error in RO6002 permittivity and -5% error in TMM10i permittivity results in frequency shift of 195+188=338MHz. Several errors combinations are possible, to get the good permittivity for each substrate, these combinations of errors must be included in CST and the corresponding designs should be manufactured and measured. In this way a comparison between the simulation and measurements give the accurate values for the realized substrates. But as mentioned above we were not able to do that due to financial reasons.

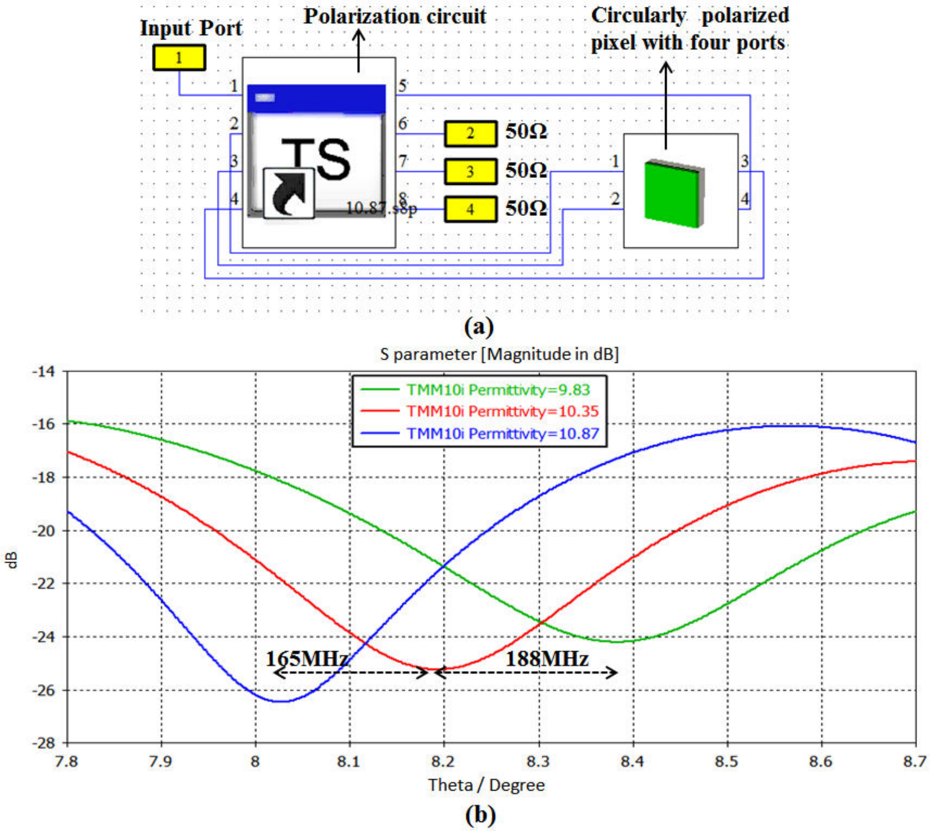

Figure V-2. (a) CST schematic of circularly polarized pixel connected to polarization circuit, (b) TMM10i ε_r error and the corresponding frequency shift, (red) $\varepsilon_r = \mathbf{10.35}$, (blue) $\varepsilon_r = \mathbf{10.87}$, (green) $\varepsilon_r = \mathbf{9.83}$.

II-3 Problem solutions

Frequency shift resulted from the permittivity shift of the used substrates (RO6002 and TMM10i). Two possible solutions: First the same design could be manufactured again with adapting the feeding patches dimensions inside the pixels cavities; multiplying the dimensions by a correction coefficient to resonate at the desired frequency 8.2GHz. Second solution is to make the permittivity characterization **[1]** for the substrates as mentioned above in **paragraph II-1**. This problem could be simply resolved for new fabrication; new fabrication was not done mainly to financial problem.

III. Power divider conception problems

In this section the problems of the perturbations and dissymmetry in the measured Isoflux patterns will be discussed. First, the problems are stated then the procedure followed to discover the reasons for the problems will be presented. Giving arise to the solutions suggested and studied.

III-1 Gain and axial ratio pattern perturbations

The measured gain shows some perturbations, examples given in **Figure V-3** include three main problems: The dissymmetry with respect to the elevation angles, the big difference in the isoflux gain (simulation-measurement) and the high gain in the axial direction that is expected to be much lower. In fact the last two are related to each other and could be considered on problem.

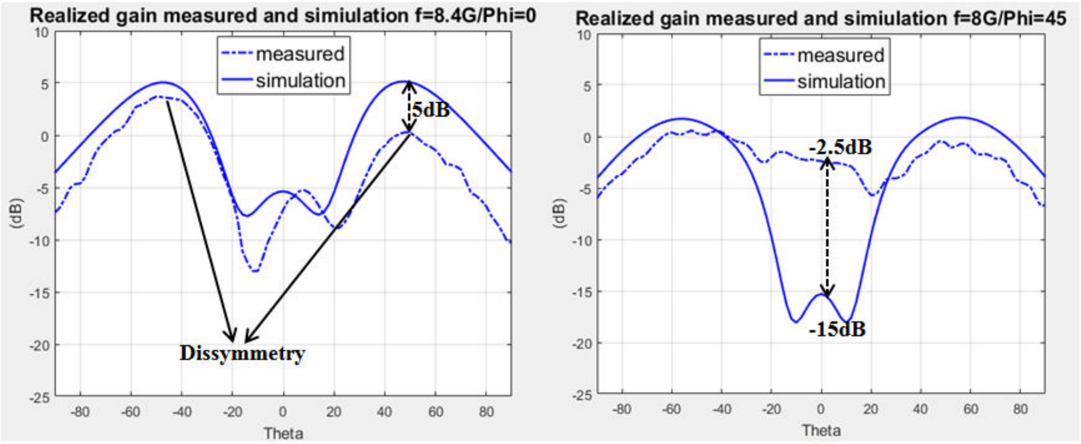

(a) **(b)**

Figure V-3. Examples of measured gain pattern problems, (a) f=8.4GHz φ=0°, (b) f=8GHz φ=45°.

The procedure followed to discover the problem is to do several testing on the antenna (5x5 pixels **ARMA**) using the feeding law of symmetrical Sync-Circular solution; theoretically C=M= (0.15, 180°). During testing Isoflux realized gain is considered at the frequency f=8.2GHz in the azimuthal planes φ=0°, φ=45° and φ=90°. The gain pattern in the two azimuth planes φ=0° and φ=90° must be symmetrical. And the maximum gain difference is between the two azimuth planes φ=0° and φ=45°. Then testing procedure is illustrated as follows:

Case1: Antenna with the perfect feeding procedure (coaxial cables) with "C=M= (0.15, 180°)" **(Figure V-4)**. In **Figure V-5.a** the realized gain pattern in the azimuth planes φ=0°and φ=90° are completely symmetrical, this is obvious since the physical structure in these two planes is symmetrical and the feeding law is ideal symmetrical with no errors. **Figure V-5.b** shows the realized maximum gain difference which occur in between the azimuth planes φ=0°and φ=45° (2.5dB). These results are the best could be obtained using the square geometrical form **ARMA** and the considered feeding law.

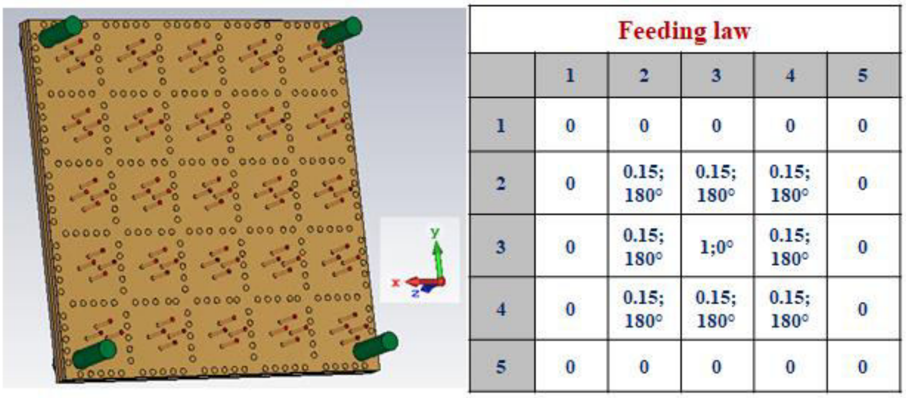

Feeding law

	1	2	3	4	5
1	0	0	0	0	0
2	0	0.15; 180°	0.15; 180°	0.15; 180°	0
3	0	0.15; 180°	1;0°	0.15; 180°	0
4	0	0.15; 180°	0.15; 180°	0.15; 180°	0
5	0	0	0	0	0

Figure V-4. "Case1" ARMA antenna with perfect feeding procedure and the feeding law.

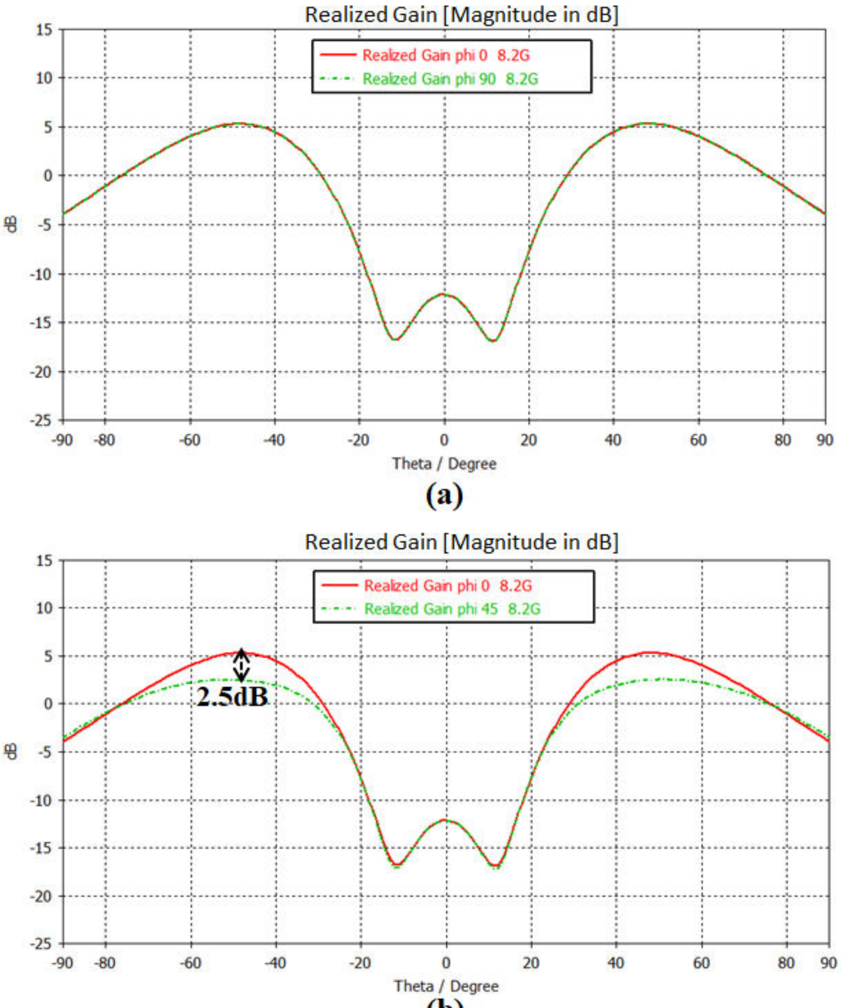

Figure V-5. "Case1" Realized gain f=8.2GHz, (a) symmetrical planes φ=0°and φ=90°, (b) maximum gain difference in planes φ=0°and φ=45°.

Case2: Antenna connected to the polarization circuits (touchstone files from Momentum), with feeding law “C=M= (0.15, 180°)” **(Figure V-6)**. In **Figure V-7.a** and **Figure V-7.b**, the symmetry is still valid between the azimuth planes φ=0°and φ=90° and the realized gain difference (3dB) is 0.5dB more than the “Case1” (due to the losses inside the polarization circuits substrate and at the input of the polarization circuits), also.

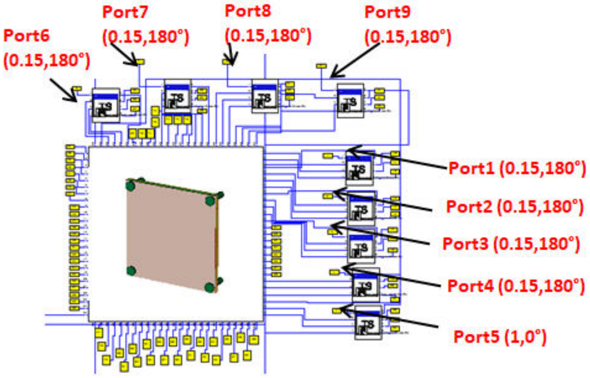

Figure V-6. “Case2” ARMA antenna connected to the polarization circuits fed by Symmetrical Sinc-Circular law “C=M=0.15”.

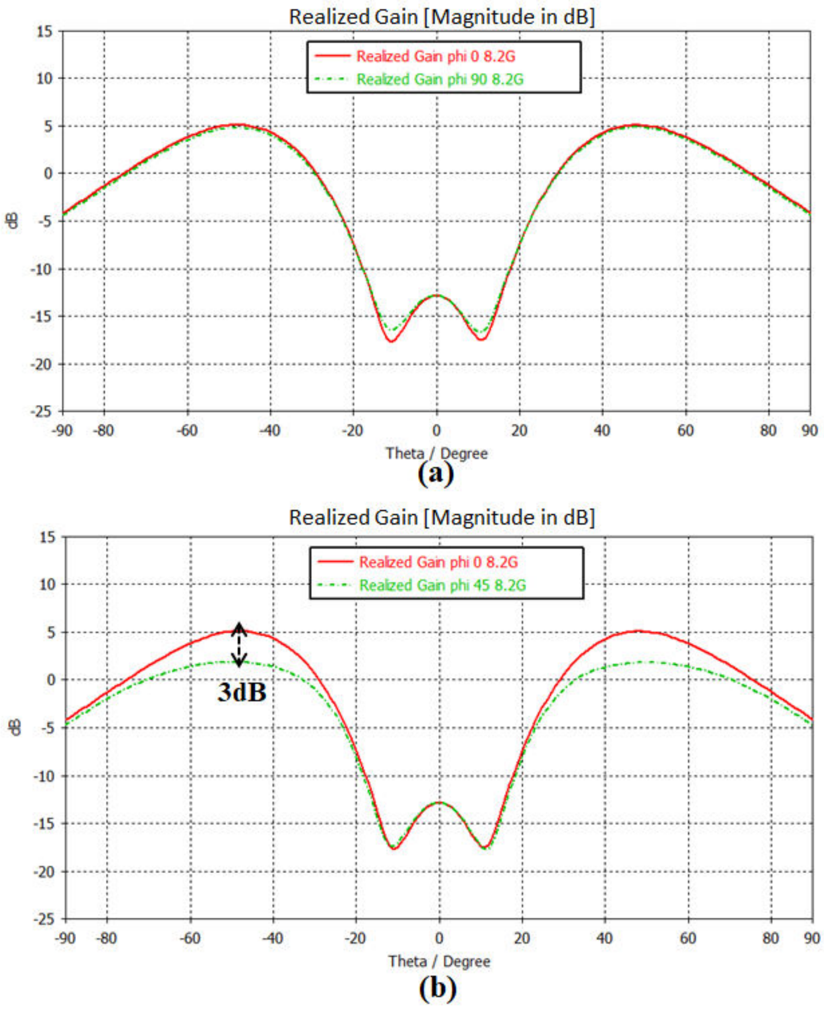

Figure V-7. “Case2” Realized gain f=8.2GHz, (a) symmetrical planes φ=0°and φ=90°, (b) maximum gain difference in planes φ=0°and φ=45°.

Case3: Antenna connected to the polarization circuits (touchstone files from Momentum), with the feeding law the results of the power divider measured; no connection with the power divider but only insert its output weights in CST **(Figure V-8)**. In “Case3” **(Figure V-8)** the scenario is to use the same schematic as “Case2” but the weights used are the weights measured at the outputs of the manufactured power divider; to see the effect of the weights error on the gain pattern. **Figure V-9.a** shows that the symmetry in the azimuth planes φ=0°and φ=90° is attained and **Figure V-9.b** shows that the realized gain difference (3.3dB) is increased by 0.3dB compared to “Case2”.

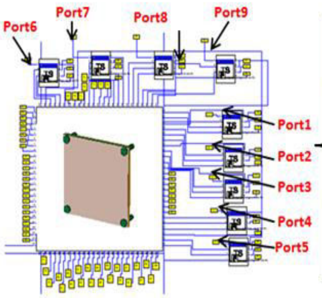

Power divider results	Port1	Port2	Port3	Port4	Port5	Port6	Port7	Port8	Port9
Weight Magnitude	0.154	0.152	0.157	0.148	1	0.148	0.158	0.153	0.155
Weight Phase	180.7°	182.1°	182.3°	179.8°	0°	178.2°	181.4°	180.6°	179.7°

Figure V-8. “Case3” ARMA antenna connected to the polarization circuits fed by outputs of the realized power divider.

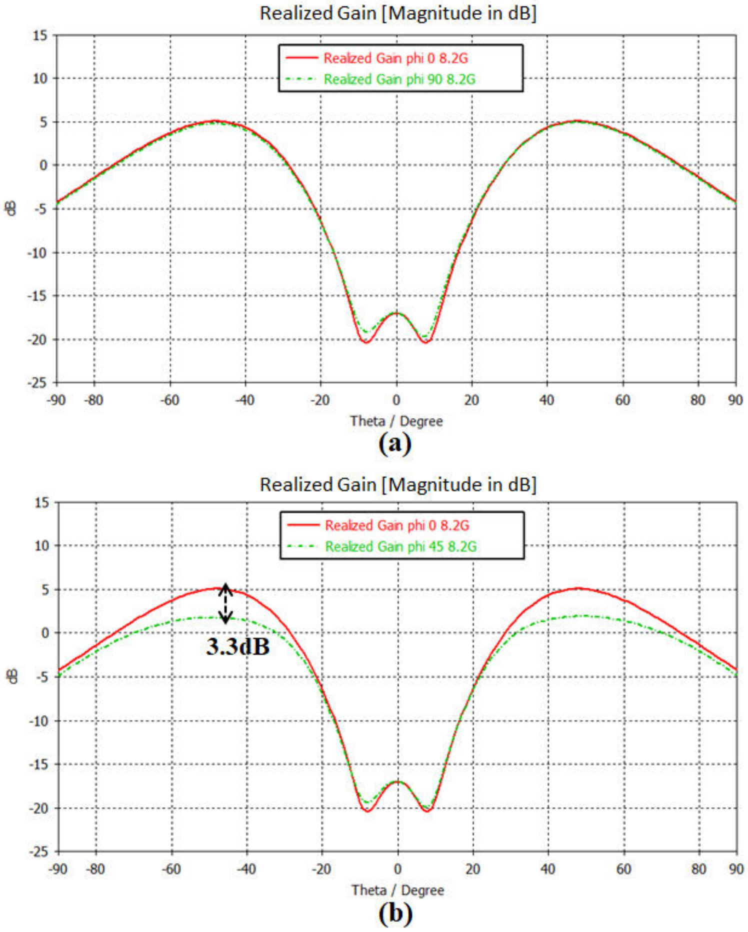

Figure V-9. “Case3” Realized gain f=8.2GHz, (a) symmetrical planes φ=0°and φ=90°, (b) maximum gain difference in planes φ=0°and φ=45°.

Case4: Antenna connected to the polarization circuits (touchstone files from Momentum) and power divider measured file (including all the S-matrix of the measured power divider) **(Figure V-10)**. The problem occurs starting from the connection of the measured power divider file to the polarization circuits and matrix antenna. The dissymmetry in the azimuth planes φ=0°and φ=90° appears with a gain difference of 5dB **(Figure V-11.a)**, it was expected (gain difference) to be more than

“Case3” by [0.5 to 1] dB, due to the losses in the power divider substrate and at the input of the power divider. The gain difference is increased dramatically to attain 7dB **(Figure V-11.b)**.

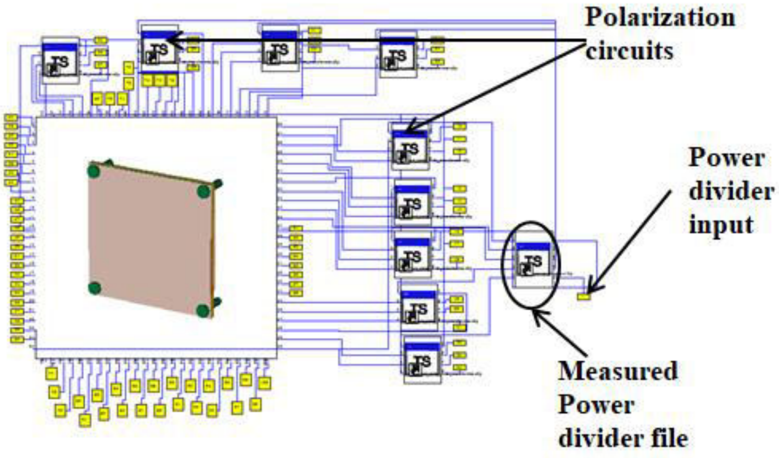

Figure V-10. “Case4” ARMA antenna connected to polarization circuits and measured power divider file.

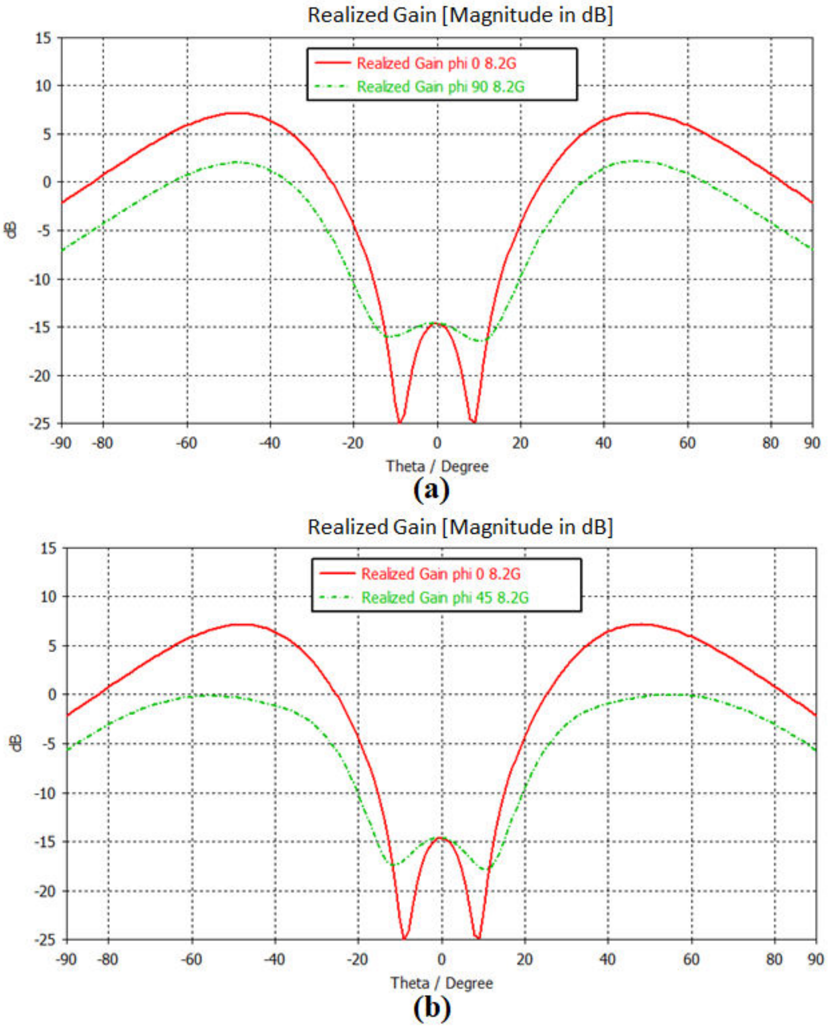

Figure V-11. “Case4” Realized gain f=8.2GHz, (a) symmetrical planes φ=0°and φ=90°, (b) maximum gain difference φ=0°and φ=45°.

From these cases the problem comes after the connectivity between the power divider and the antenna is maintained. The analysis to go in deep inside the problem must study the connectivity problem and the effect of manufactured power divider on the pattern; when placed behind the antenna and connected by cables.

III-2 Power divider Input/output impedances

The one input and nine outputs power divider was built using the classical microstrip lines theory with parallel architecture **(Figure V-12)**. We avoid at the first study the use of the same architecture as the polarization circuit that was implemented using the hybrid couplers. Hybrid couplers insure good stability of its matching impedance and its outputs in a wideband; however we were aware of the power losses that could happen in its 50Ω port since we have to use many of the hybrid couplers to build the power divider.

The power divider designed **(Figure V-12.a)** (input labeled 10 outputs labeled from 1 to 9) started by the input 50Ω microstrip line, then the parallel transmission lines after follow the theory illustrated in **FigureV-12.b**. The aim was to get the feeding law for the isoflux at the outputs of the power divider (magnitude and phase), but the impedance at these outputs ports and the isolation were not taken in account, so we did not master it in this design. The impedance at the power divider input is closed to 50Ω at f=8.2GHz, with a negligible imaginary part ($Z\_in = 50(1.063 - j0.029)$), but the impedance at the output ports is: $Z\_out = 50(0.406 + j0.542)$ at f=8.2GHz. This includes the mismatching between the outputs of the power divider and the polarization circuits that are connected by the cables and the SMA connectors. On the other hand the isolation of these output ports was not good. **Figure V-13.a** shows that the outputs return loss parameters are not well adapted and **Figure V-13.b** shows that they are not isolated.

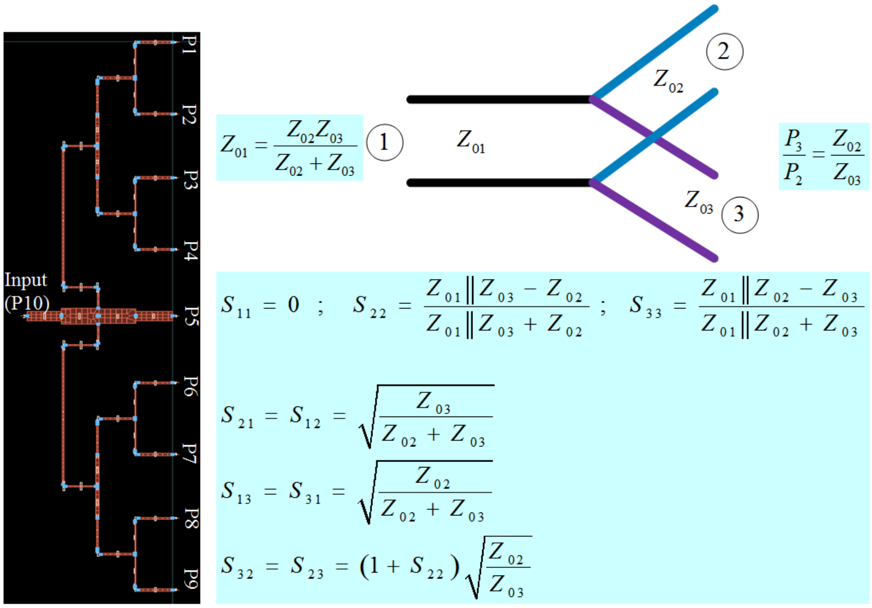

$$Z_{01} = \frac{Z_{02}Z_{03}}{Z_{02}+Z_{03}}$$

$$\frac{P_3}{P_2} = \frac{Z_{02}}{Z_{03}}$$

$$S_{11} = 0 \ ; \quad S_{22} = \frac{Z_{01}\|Z_{03} - Z_{02}}{Z_{01}\|Z_{03} + Z_{02}} \ ; \quad S_{33} = \frac{Z_{01}\|Z_{02} - Z_{03}}{Z_{01}\|Z_{02} + Z_{03}}$$

$$S_{21} = S_{12} = \sqrt{\frac{Z_{03}}{Z_{02} + Z_{03}}}$$

$$S_{13} = S_{31} = \sqrt{\frac{Z_{02}}{Z_{02} + Z_{03}}}$$

$$S_{32} = S_{23} = (1 + S_{22})\sqrt{\frac{Z_{02}}{Z_{03}}}$$

(a) **(b)**

Figure V-12. Manufactured Power divider design and the corresponding equations.

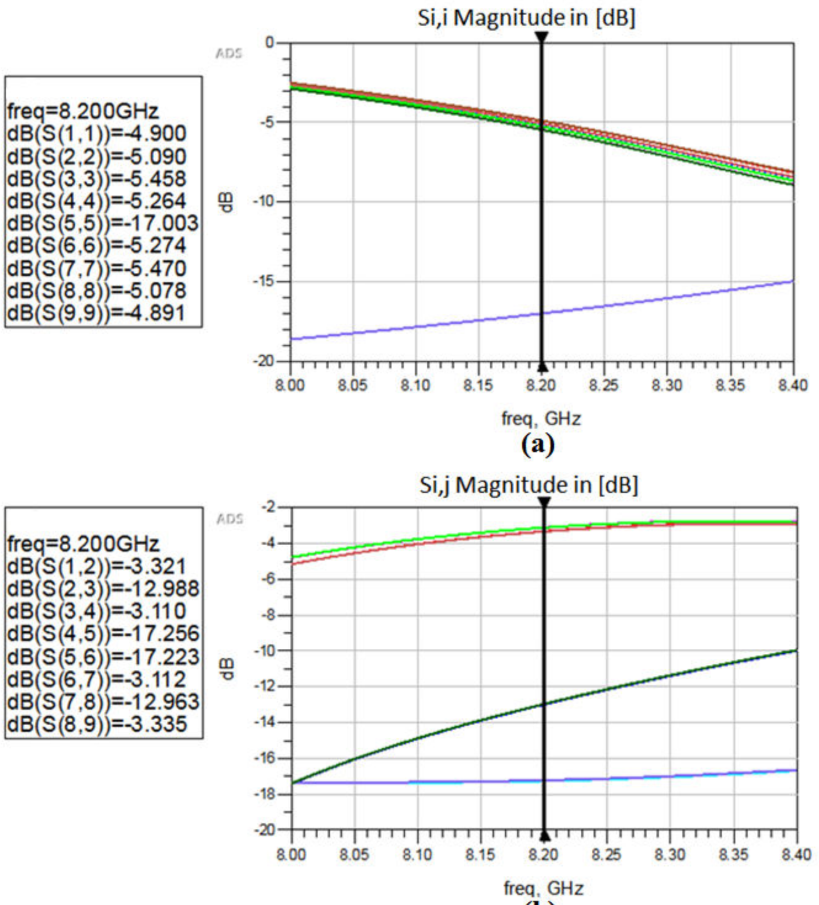

(b)

Figure V-13. Power divider outputs S-parameters, (a) Si,i adaptation, (b) Si,j Couplings.

III-3 Feeding law perturbations

In this paragraph the feeding law modifications and its effect in the gain pattern will be shown; due to the bad adaptation at the outputs lines of the power divider (mismatching between the power divider outputs and the polarization circuits inputs) and due to the bad isolation of the power divider outputs. To see the feeding law modification it necessary to connect the power divider with the polarization circuits, then look for the weights at the outputs of the polarization circuits (**Figure V-14**). In **Figure V-14** the power divider file taken from the measurements is used; measurements inside the metallic box; and all the couplings and return losses of the input and output ports of the manufactured power divider. Polarization circuits are labeled from “C1” to “C9” with the label “C5” corresponds for the polarization circuit file to be connected to the central pixel inside the **ARMA**. For each polarization circuit the four outputs are labeled in red color, for example for “C1” the output ports to be connected to a pixel in the matrix are labeled “1”, “2”, “3” and “4”. Input of the power divider is labeled “64”. The other ports are related to the 50Ω impedances of the hybrid couplers of the polarization circuits.

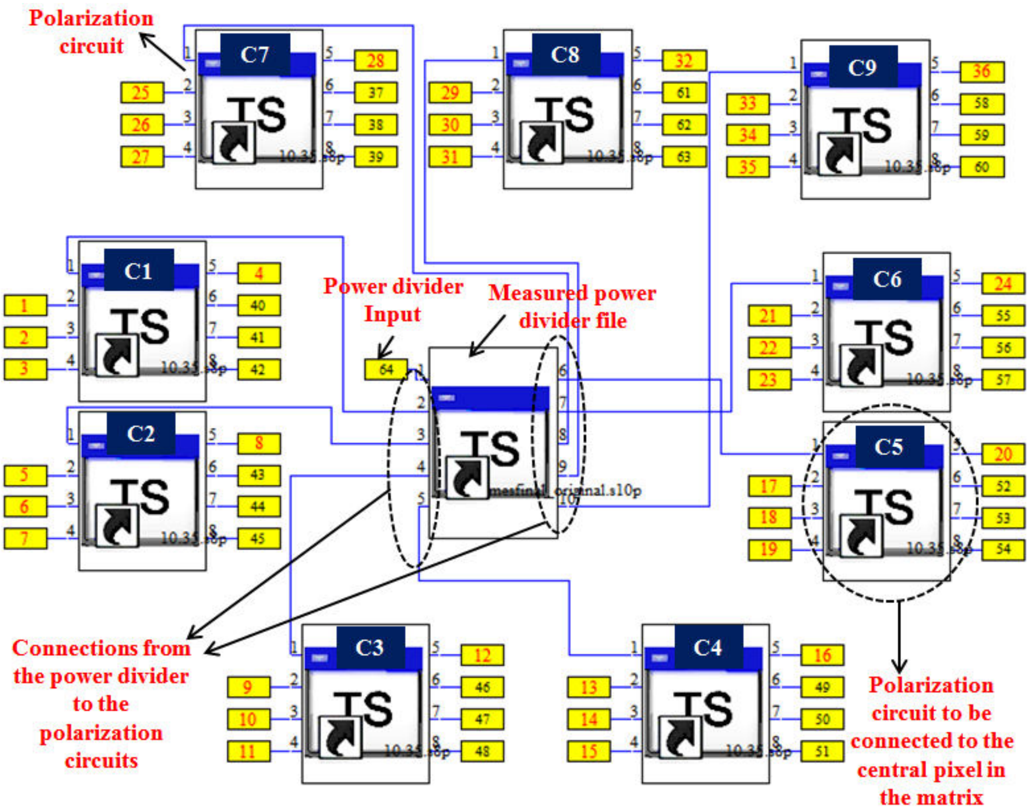

Figure V-14. Manufactured power divider file connected to the polarization circuits.

Consider an example of two sets of results (f=8.2GHz), first are the outputs of “C1” and second are the outputs of “C5”. The S-parameter at each output port of the two circuits considered, are taken with respect to the input of the power divider (labeled “64”in **Figure V-14**); magnitudes in linear and phases in degrees of $S_{64,i}$ where i=1,2,3,4,17,18,19,20 for the “C1” and “C5” **(Figure V-15)** respectively. For the magnitudes of $S_{64,1}$, $S_{64,2}$, $S_{64,3}$ and $S_{64,4}$ (related to “C1”) the weights are approximately equal (0.061, 0.062, 0.062 and 0.062 respectively), meaning that for “C1” we can consider that these magnitudes are equal to their mean value 0.06175. This case of approximately equal magnitudes at each circuit outputs is the same for the other circuits, but the mean magnitudes are not all the same (different values in the other circuits). Now to see the weight given for the pixel connected to “C1” we take the ratio of the magnitude mean of outputs of “C1” and that of “C5”. Then the weight is 0.06175/0.3815=0.161.

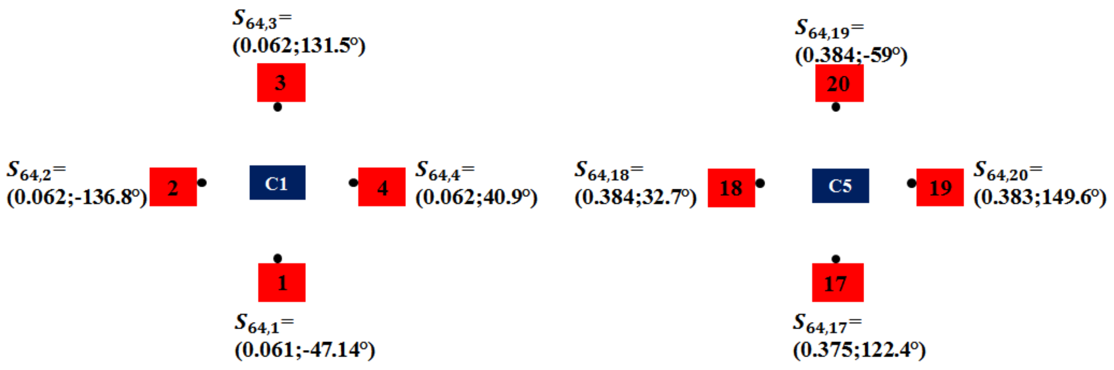

Figure V-15. Output ports of the polarization circuits “C1” and “C5”.

For the phases, are taken with respect to the outputs phases of the central pixel, each phase of the output port in “C1” is calculated taking as reference the corresponding port phase in “C5”. For example in **Figure V-15**: “1” in “C1” has a reference “17” in “C5”, “2” in “C1” has a reference “18” in “C5”, “3” in “C1” has a reference “19” in “C5” and “4” in “C1” has a reference “20” in “C5”. Theoretically according to the desired feeding law the phase difference in each of these cases should be 180° (example: $\text{phase}(1) - \text{phase}(17) = 180°$). Then the phase error is measured according to the 180°.

The weights to be given for the 3x3 activated pixels inside the 5x5 pixels matrix at f=8.2GHz, taking as a reference the central pixel, are given in **Figure V-16.a** with maximum phase errors. Phase errors are given as the following example: calculate first the error between the port phase of “1” and phase of “17”, then the same for (“2”, “18”), (“3”, “19”) and (“4”, “20”). Then take the maximum error of theses phase errors. The magnitudes are not too much deformed (all near to 0.15 desired by the Symmetrical Sync-Circular solution), but the phase include high errors that reaches to +25° in some cases (Pixel.6 in the **Figure V-16.a**). The weights (magnitudes and phases) distributed on the matrix are shown in **Figure V-16.b**. The feeding law deformation is now clear and show also the dissymmetry in the weighting law in the two azimuth planes φ=0° and φ=90°, the realized gain pattern for these planes show also the dissymmetry in **Figure V-17**. Then in this paragraph the feeding law perturbation effect is clearly justified with the corresponding effect in the realized gain pattern.

Pixel no.	Pixel.1	Pixel.2	Pixel.3	Pixel.4	Pixel.5	Pixel.6	Pixel.7	Pixel.8	Pixel.9
Magnitude	0.161	0.151	0.158	0.165	1	0.156	0.169	0.148	0.156
Max phase error	+11°	+5°	+15°	+20°	0	+25°	+14°	+5°	+13°

(a)

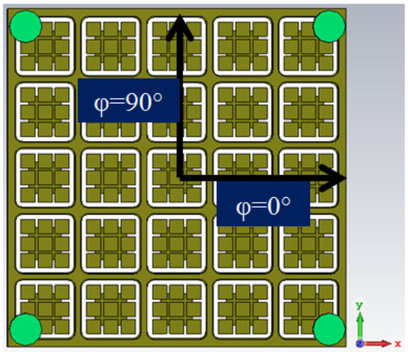

Feeding law					
	1	2	3	4	5
1	0	0	0	0	0
2	0	0.161; 191°	0.151; 185°	0.158; 195°	0
3	0	0.165; 200°	1;0°	0.156; 205°	0
4	0	0.169; 194°	0.148; 185°	0.156; 193°	0
5	0	0	0	0	0

(b)

Figure V-16. Feeding law perturbations due to mismatching between power divider and polarization circuits.

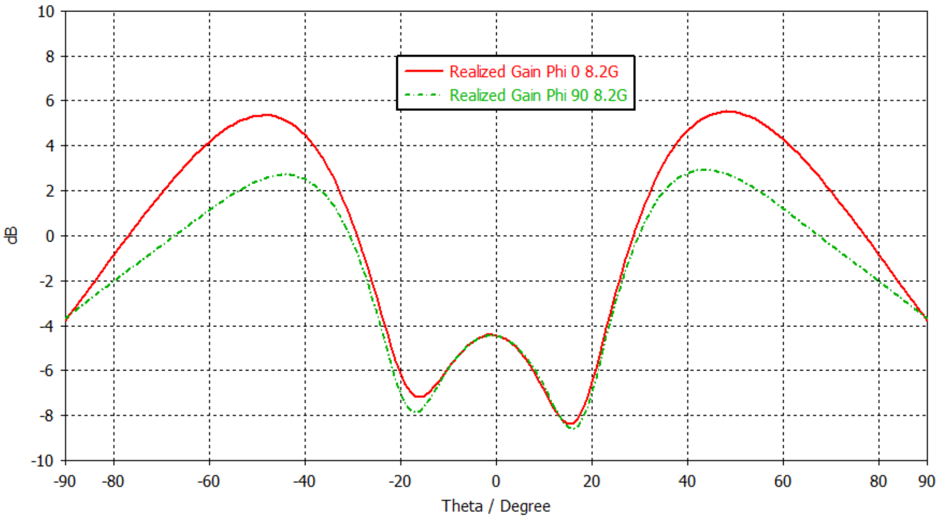

Figure V-17. Realized gain of the matrix with perfect feeding procedure and using the perturbed feeding law.

III-4 Power divider radiation

The mismatching impedance between the outputs of the power divider and the inputs of the polarization circuit has also another effect. The reflected power due to the high reflection coefficients at the outputs of the power divider is radiated by the transmission lines which were expected to do the function of transmission power lines with negligible radiation. But it was not the case. **Figure V-18** shows the radiation of the power divider (Realized gain magnitude in dB) in 3D plot, the realized gain is high according to its designed functionality (reaches 1.59dB). The combination of the measured realized gain ("Case4" in **paragraph III-1**) and the realized gain of the power divider radiation was made in Matlab and presented in **Figure V-19**. Combination is done at the frequency f=8.2GHz in the azimuth planes φ=20°, φ=30°, φ=50°, φ=60°, φ=70° and φ=90°. These results in **Figure V-19** show high deformation in the realized gain pattern of the antenna and that the power divider functionality is not attained as desired due to its electromagnetic radiation.

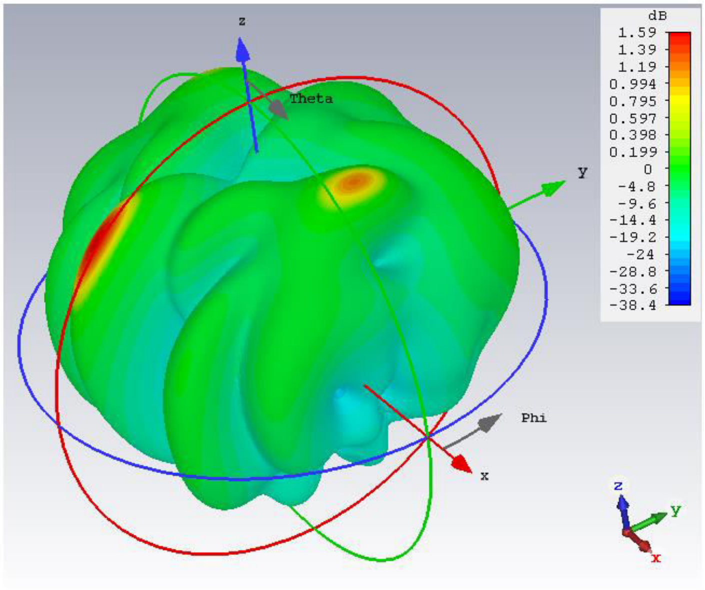

Figure V-18. Realized gain 3D plot pattern of the manufactured power divider radiation.

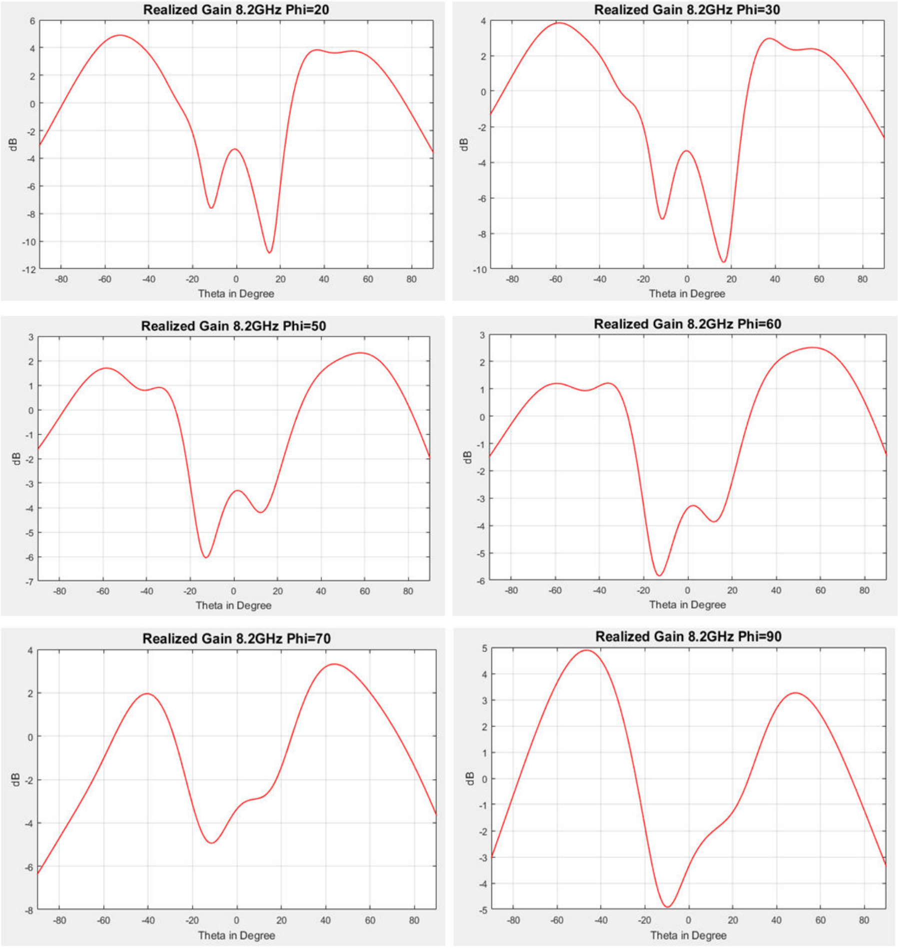

Figure V-19. realized gain of matrix antenna with polarization circuits and power divider files, with the effects of the power divider radiation.

III-5 New power divider solution

III-5.1 New power divider specification

Due to the problems mentioned above on the manufactured power divider, new power divider (printed on substrate of permittivity 2.45, tangent loss 0.002 and thickness 0.78mm) was designed taking in account the following:

1. Impedance at the output ports equals to 50Ω.
2. Output ports isolated.
3. Very low gain for its electromagnetic radiation.
4. Finally the restrictions mentioned previously regarding the dimensions specifications the distance between the ports and the alignment of the output ports on the same side **(Chapter IV paragraph V-1)**.

III-5.2 New power divider design

The first three are the constraints listed above solve the problems of the fabricated power divider and must be attained as possible as near the desired conditions. The new power divider **(Figure V-20)** was designed using a combination of microstrip transmission lines and hybrid couplers, where the dimensions are good according to the specifications (≤13cm), the distance between the output ports (≥13mm) and the output ports are aligned at the same side. In **Figure V-20** hybrid couplers are used at the outputs of the new power divider, this makes it easily to attain the 50Ω without using impedance transformers (at the output terminals). The impedance transformers inside the design are used to maintain always the 50Ω when going from the outputs (labeled "P1" to "P9") back towards the input of the power divider (labeled "P10").

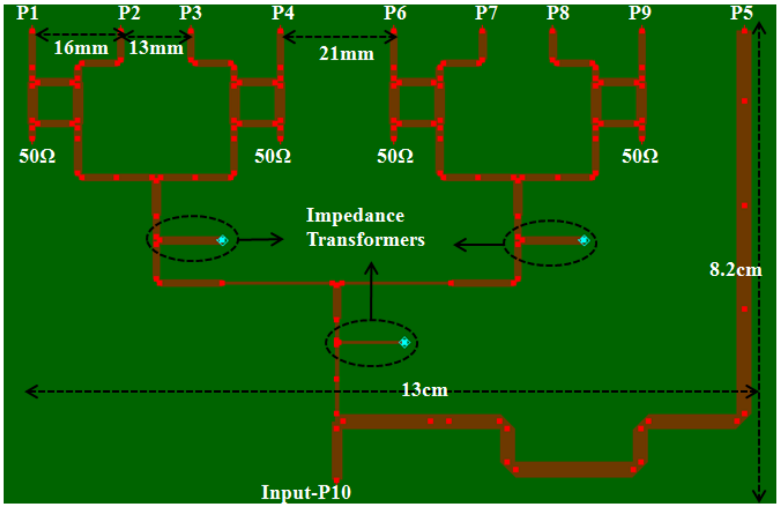

Figure V-20. New power divider design with the hybrid couplers at the output ports.

III-V.2.1 Input-output ports impedance and output weights

$S_{i,i}$ and $S_{i,j}$ parameters at the power divider outputs **(Figure V-21)** show good adaptation and isolations of the ports "P1" to "P9", except for some cases like "P4", "P6" and "P9" are not well adapted. The input "P10" is well adapted as shown in **Figure V-22**. Then the results at the outputs of the power divider at f=8.2GHz in magnitudes (normalized to the magnitude of "P5" to be connected to the central pixel in the matrix antenna) and phases (phase difference with "P5") are listed in **Figure V-23** and distributed on the matrix.

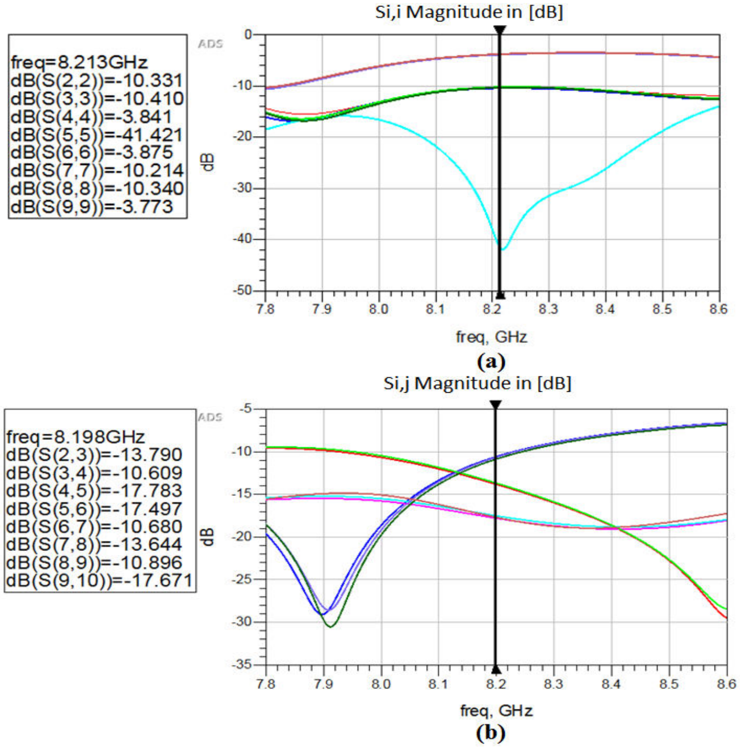

(a)

(b)

Figure V-21. S-parameters of the new power divider output ports, (a) Si,i adaptation, (b) Si,j couplings.

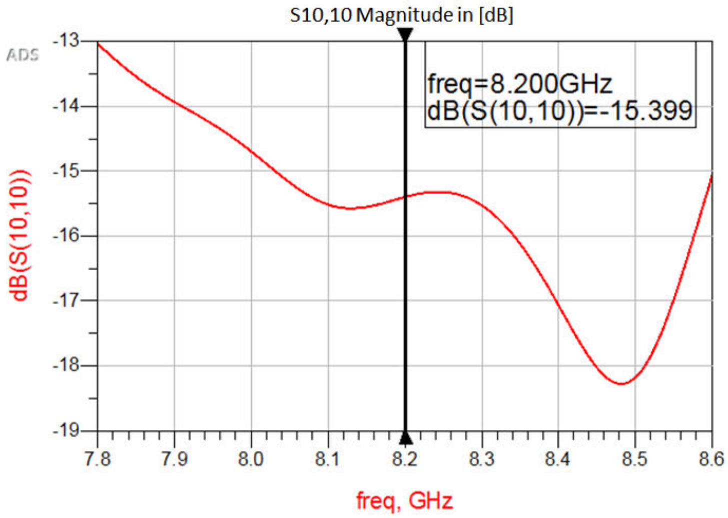

Figure V-22. Adaptation at the input of the new power divider “P10”.

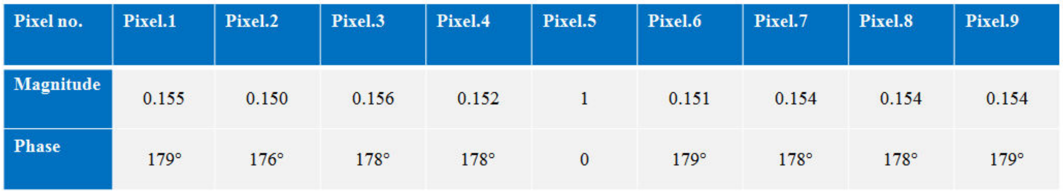

Pixel no.	Pixel.1	Pixel.2	Pixel.3	Pixel.4	Pixel.5	Pixel.6	Pixel.7	Pixel.8	Pixel.9
Magnitude	0.155	0.150	0.156	0.152	1	0.151	0.154	0.154	0.154
Phase	179°	176°	178°	178°	0	179°	178°	178°	179°

(a)

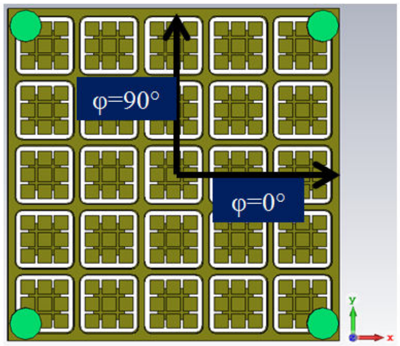

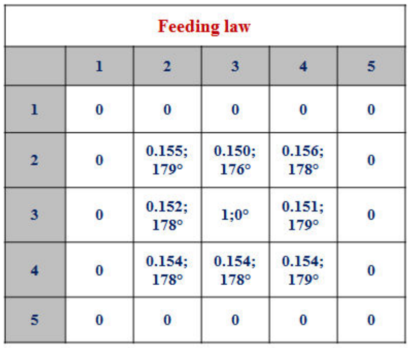

Feeding law

	1	2	3	4	5
1	0	0	0	0	0
2	0	0.155; 179°	0.150; 176°	0.156; 178°	0
3	0	0.152; 178°	1;0°	0.151; 179°	0
4	0	0.154; 178°	0.154; 178°	0.154; 179°	0
5	0	0	0	0	0

(b)

Figure V-23. outputs of the power divider, (a) magnitudes and phases, (b) feeding law distributed on the matrix.

III-5.3 Antenna patterns using the new power divider

The new power divider is connected to the polarization circuits and the matrix antenna in CST, using the files taken from Momentum software (same as “Case4” in **paragraph III-1**), to simulate the whole system. Results of the realized gain and axial ratio patterns at f=8.2GHz are shown in **Figure V-24**. The realized gain of the whole system (Matrix antenna with polarization circuits and power divider) has a maximum difference of 2.9dB between the different azimuth planes, whereas using the fabricated power divider the difference is 7dB (**paragraph III-1**). Also the symmetry of the realized gain between the azimuth planes φ=0° and φ=90° is attained; this was one of the problems as mentioned in **paragraph III-1**. Then this gives a result that the feeding procedure is not deformed after the connectivity is attained between the new power divider and the polarization circuits.

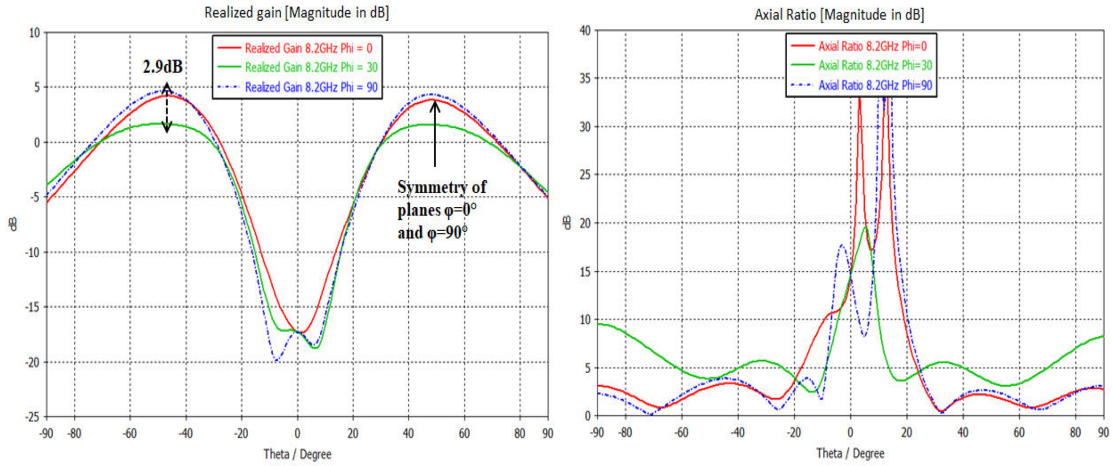

Figure V-24. Realized gain and axial ratio patterns of the matrix with the polarization circuits and the new power divider.

Another test was done to test the problem of the power divider electromagnetic radiation; as done for the fabricated power divider in **paragraph III-4**. **Figure V-25** shows the 3D plot of the realized gain obtained by simulating the new power divider with its metallic enclosure and the connectors in CST. The maximum realized gain is -65dB, obviously this very low gain will have no significant effect on the pattern of the antenna. **Figure V-26** compares the realized gain obtained in **Figure V-24** and the realized gain after adding the effect of the new power divider radiation. Comparisons are done at frequency f=8.2GHz in the azimuth planes φ=0° and φ=30° show no effect for the new power divider radiation; this is the case for all the other azimuth planes.

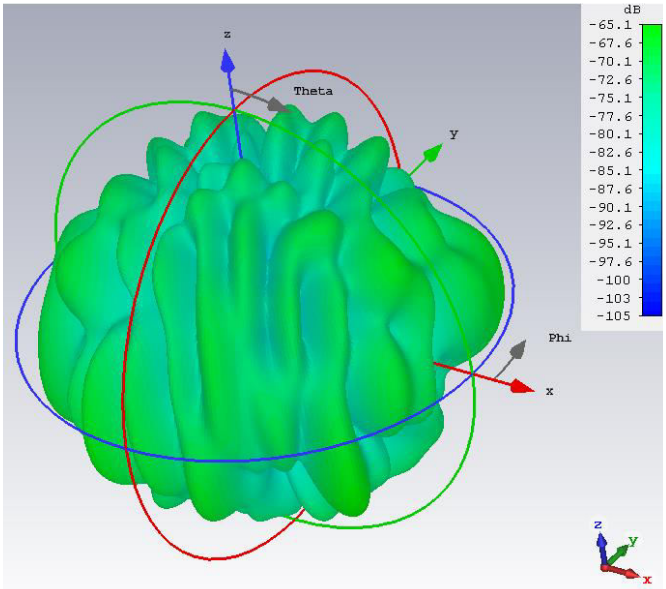

Figure V-25. Realized gain 3D pattern of the new power divider.

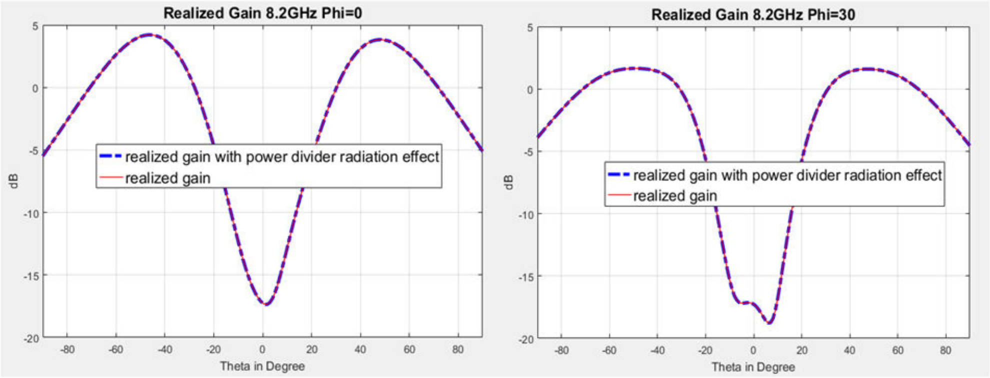

Figure V-26. Comparison of the realized gain pattern of the matrix connected to the polarization circuits and new power divider with and without the power divider radiation effect.

IV. Antenna Geometrical limitations and Cube-Sat support effect

IV-1 Geometrical antenna limitations effects on the gain pattern

In the **Chapters III**, **IV** and **V** the geometrical structure used for the matrix antenna **ARMA** is square (5x5 pixels). The reflections from the edges of the antenna affect the patterns of the antenna and have its contribution in the different azimuth and elevation angles. When the geometry of the antenna is not the same in all the direction as shown in **Figure V-27** then the contribution of the edges effects will not be the same in all the directions (azimuth planes). This limits the homogeneity of the pattern in the different azimuth planes, that is why the results includes gain difference as shown in all the cases of the entire chapter and in some cases in **Chapter IV**. To overcome this problem optimization of the feeding law was done **(Chapter IV paragraph III-2)** to compensate for this dissymmetrical geometrical structure. The optimization aimed to have more homogenous gain pattern in all the azimuth planes even if the edge effects are not the same in all the directions. Results after optimizing the feeding law gives maximum gain difference of 1.1dB **(Chapter IV paragraph III-2)**, that is the best to be obtained using the square geometry of the **ARMA** antenna. Then as a conclusion the considered geometrical Square structure has its limitations and these limitations could be decreased to minimum using other geometrical structures, but we tried to give the best by compensating the dissymmetry and homogeneity of the antenna pattern using the feeding law.

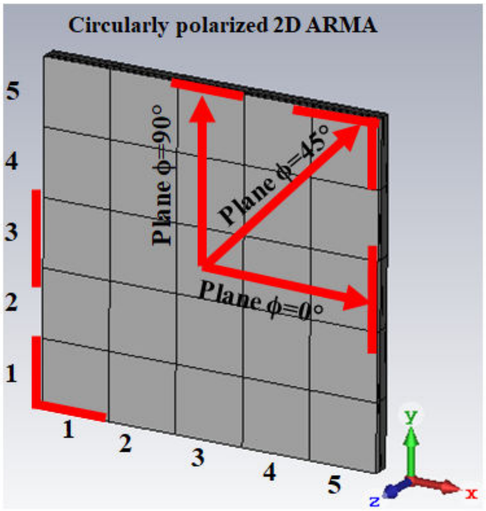

Figure V-27. Geometrical Square ARMA with the examples of different edges in different azimuth planes.

V-2 Cube-Sat support effect

This paragraph studies the effect of the Cube-Sat effect on pattern on the antenna. **Figure V-28.a** shows the manufactured antenna covered by a metallic cube. The power divider behind the antenna exceeds the dimensions of the Cube-Sat. The same dimensions of the power Cube-Sat support and the metallic box of the power divider were designed in CST where the antenna is placed on the top **(Figure V-28.b)**. Simulation at f=8.2GHz was done with the weights are given in the perfect feeding procedure with no errors; using the coaxial cables and the Symmetrical Sinc-Circular solution. The results of the gain and axial ratio patterns with and without the support are compared in the azimuth planes φ=0°, φ=30°, φ=60° and φ=90° (**Figure V-29** and **Figure V-30**). Comparisons show that there is no significant effect for the support of the Cube-Sat and the extra dimensions of the power divider box.

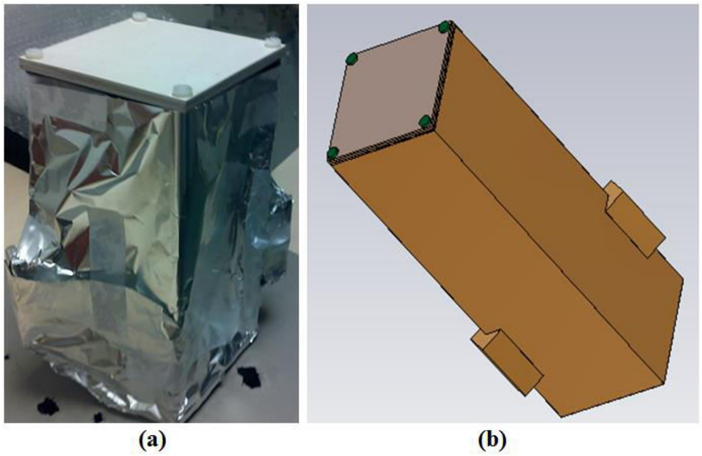
(a) **(b)**

Figure V-28. Antenna with Cube-Sat support and power divider extra dimensions, (a) manufactured, (b) design in CST.

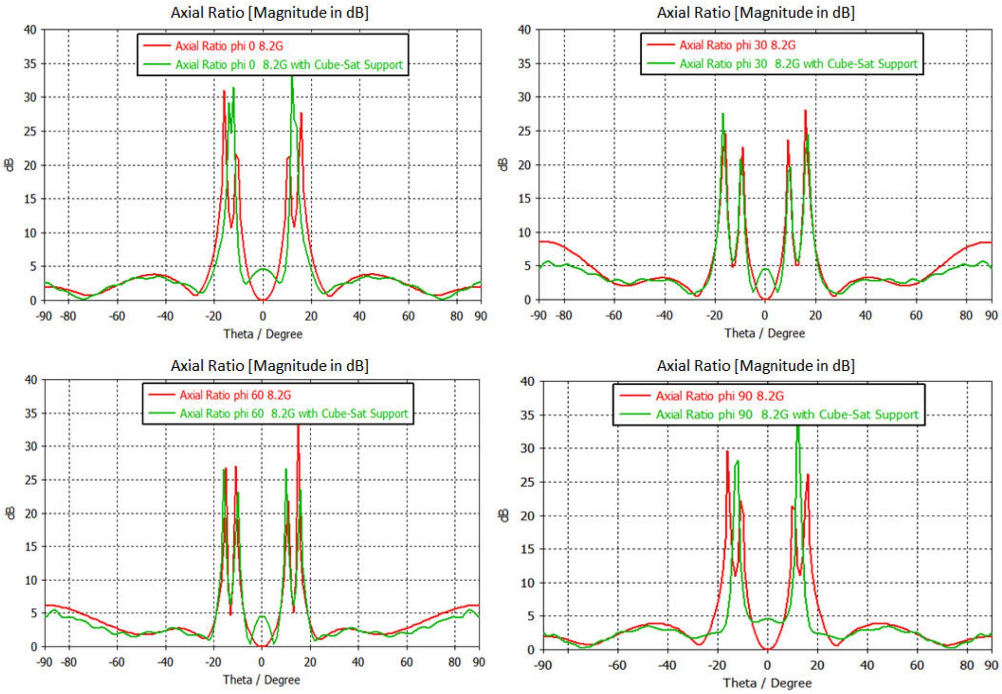

Figure V-29. Realized gain comparison, (a) perfect feeding procedure in CST, (b) adding the effect of the Cube-Sat support.

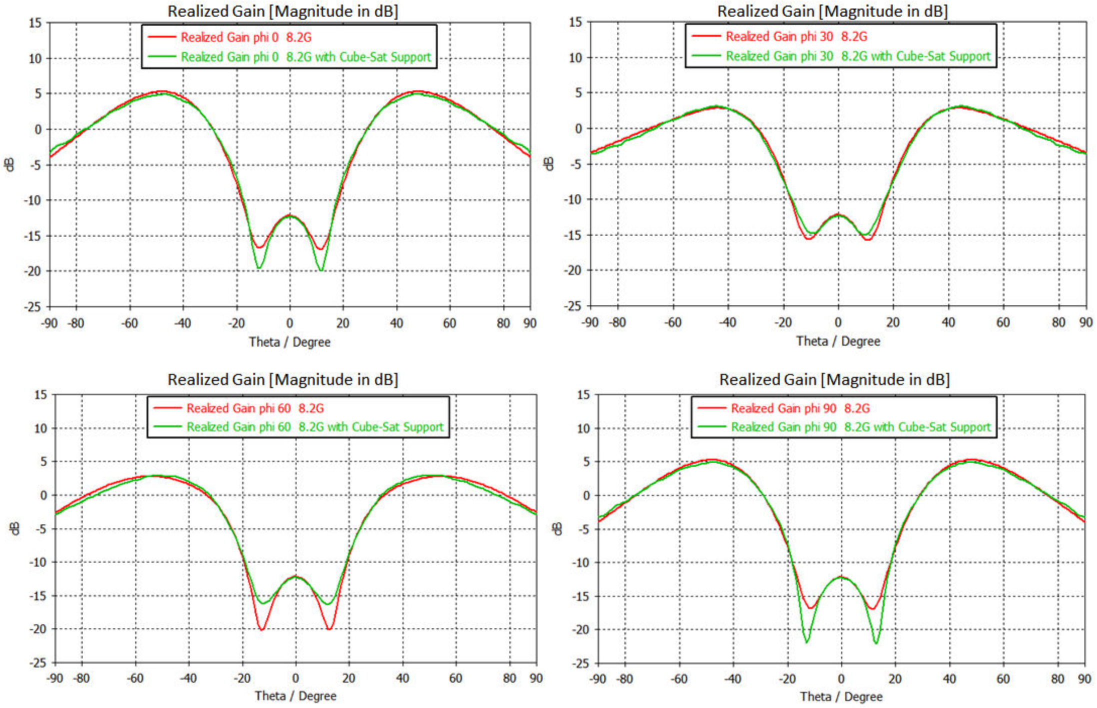

Figure V-30. Realized gain comparison, (a) perfect feeding procedure in CST, (b) adding the effect of the Cube-Sat support.

V. Conclusion

In this chapter the conception problems were discussed and resolved, the limitations of the geometrical structure was explained and the testing of the antenna pattern in the presence of the Cube-Sat support was presented. The understanding of the conception problems needed several tests and simulations that were done and give arise to suggest and give the good solutions. Frequency shift problem could be resolved easily as described in **paragraph II-3**. The study of the power divider conception problem was presented using the necessary simulation step by step to find the exact disadvantages in the designed and manufactured power divider. The main constraints specified after in **paragraph III-5.3** solves the problems and the design of the new power divider verified that. The new power divider solves the undesired effects of the manufactured one; good matching with the polarization circuits, good isolation and negligible electromagnetic radiation. Then the results of the realized gain and axial ratio in **paragraph II-5.3** proves that by presenting the maximum gain difference and the symmetry of the azimuth planes φ=0° and φ=90°. Also the perturbations due to the power divider radiation was checked, where the realized gain pattern show no effect and the symmetry with respect to the elevation angles was attained in each azimuth planes.

New fabrication was not done due to financial problems and due to some perspectives in the work that could be included in the antenna before the manufacturing. In the next there is the general conclusion and the future work and perspectives. Future work mainly regarding the structural design of the whole antenna system that is expected to be compact with an extra layer stacked behind the antenna for the power divider. Connectivity of the power divider will be without cables but using vias between the new power divider outputs and the polarization circuits (this solves many problems mainly the 50Ω at the terminals of the power divider). Matching impedance (power divider and polarization circuits) is not necessary to be 50Ω. Also the limitations of the geometrical structure gives arise to future work on different geometrical designs (circular or hexagonal) of circularly polarized **ARMA**.

VI. Bibliography of Chapter V

[1] Jamil FOUANY, «Nouvelles architectures d’antennes à éléments parasites pour la polarisation circulaire. Application à la conception d’une antenne en bande X pour nano-satellite». XLIM – Département Ondes et Systèmes Associés 2015.

List of Figures

General Conclusion
And Perspectives

This thesis introduces the new approach **ARMA** to the circular polarization designs and applications. The special radiating surface with the uniformity and the quantified sampling procedure is attained, giving the pixel the circular polarization pattern. For the pixel the axial ratio was achieved for a wide elevation angles in between ±90° below 3dB and with a high bandwidth (950MHz, 11.5%). In comparison with the patch antenna the axial ratio is better and the bandwidth is more than the double of the patch bandwidth. The polarization circuits designed were with good performances, where the best obtained using a combination of three hybrid couplers. The stability of the output magnitudes and phases of these circuits gives arise to high circularly polarized bandwidth of more than 800MHz. Using the same polarization circuits with the patch antenna this bandwidth is less than half the **ARMA** bandwidth. The design of the circular polarization circuit was achieved with small dimensions that fit the size of the pixel; designed to work at the central frequency 8.2GHz. Designed pixel has dimensions of 0.5λx0.5λ then the dimensions of the ground plane behind the pixel are 18.29mmx18.29mm, the circuit with the hybrid couplers and the resistors pads are optimized to have small dimensions to be suitable for the limited allowed surface.

Then the study of circularly polarized **ARMA** was given with the best solution first for the circularly polarized pixel; best solution for the circularly polarized pixel (feeding patch with four feeding probes) and the use of the circular polarization circuit (with three hybrid couplers). In **Chapter III** different architectures of **ARMA** and AESA were used for the aim of comparison. The bandwidth comparison of the pixel inside the **ARMA** and the patch antenna inside the ASEA shows the same results as the pixel and patch antenna alone (more than double bandwidth in **ARMA**).

Axial ratio for the scanning beams with the 1D AESA and **ARMA** were compared in small and large scanning elevation angles. In **ARMA** the axial ratio is better especially for the far scanning angle ($\theta \geq 50°$). Comparisons of the two approaches in 1D Isoflux wide beam shows an enhancement of the Isoflux maximum gain position (elevation angles), where in **ARMA** the Isoflux gain pattern is wider by 11°. The 1D Isoflux pattern was extended to 2D Isoflux, for that the 2D circularly polarized **ARMA** was designed and the two feeding law using the Butler matrix technique and the Sinc-Circular was used. Sinc-Circular solution gives better axial ratio and gain patterns regarding the specifications of the CNES (axial ratio below 3dB for $-60° < \theta < 60°$ and maximum Isoflux gain at ±60°).

Study of the Sinc-Circular solution with zero edges (pixels at the peripherals not fed) shows that the gain and axial patterns are the same as these pixels (at peripherals) are fed. But, the physical elimination of the pixels at the peripherals has bad drawbacks on the axial ratio. Then the best solution suggests the activation of the 3x3 matrix inside the 5x5 matrix. This makes it easier for the design of the power divider with one input and nine outputs. Then **Chapter IV** focuses on the CNES requirements and the Isoflux specifications. The feeding law was optimized with different solutions to get wider position for the Isoflux maximum gain and to achieve the homogeneity of the gain pattern in the different azimuthal planes. The maximum Isoflux gain difference was reduced to 1.1dB in the different azimuth planes. The position of the Isoflux maximum gain was attained at ±50° in the different azimuth planes approximately, the required positions by the CNES is ±60°. But the gain pattern achieved has the gain at ±60° less than the maximum gain by no more than 1dB in the different azimuth planes. The axial ratio for the Isoflux pattern obtained less than 3dB in the entire interesting region for the Isoflux.

The second directive mode for the CNES was studied and achieved using the corresponding feeding law. The directive beam has a gain of 14.2dB with an axial ratio less than 3dB in the entire aperture angle. The two beams (Isoflux and directive) were presented together and the resulted pattern for each shows the achievements of the CNES desired specifications. Where the commutation between the two beams is attained at $\theta=\pm 33°$, near to the specified elevation angles =±30°. The axial mode was studied with different patterns: The high gain beam 19dB, the sectorial axial beam that includes the uniformity of 11.4dB around the axial direction, and finally the axial Isoflux beam. These later three beams were not requested by the CNES but studied to give different beam configurations.

The problem of the metallic walls and ground plane connectivity was solved, and matrix antenna with the polarization circuits was fabricated. Measurements of the return loss parameters at the input of the polarization circuits show frequency shift of approximately 400MHz, but still adapted below -10dB with a bandwidth of 800MHz. The frequency shift problem is due to the shift in the true value of the permittivity of the TMM10i and the RO6002 substrates. Characterizations of these substrates were not done before the fabrication due to financial problems. Since, to do the characterizations, we have to buy a large laminate of the TMM10i substrate to make several designs with the stacked layers of the TMM10i and the RO6002. The realization and measurements of the power divider alone show good agreements with the Momentum design results of the outputs (magnitudes and phases).

Problems observed after measurements of the whole antenna are: bad adaptation at the input of the first power divider and perturbations in the Isoflux realized gain and the axial ratio patterns. The origin of the problem was the conception of the power divider design. The mismatching impedance between the power divider output ports and the polarization circuits input ports and the bad isolation of the power divider output ports, had many drawbacks. Drawbacks are the modifications in the feeding law and the electromagnetic radiation effect of the fabricated power divider. The solution suggested was a new power divider with 50Ω impedances at its outputs and good isolation of these output ports. The new power divider was designed in Momentum with the hybrid couplers at the output ports, and then the testing of the power divider with the matrix antenna and the polarization circuits shows good results that maintain the symmetry in the feeding law and then in the Isoflux pattern (in the azimuth planes φ=0° and φ=90°). The maximum gain difference in the azimuth planes φ=0° and φ=45° was near the expected value (2.9dB). Radiation effect of the power divider was very low and has negligible changes in the gain pattern of the antenna. Then the problem of the power divider was solved in the design.

We were not able to make new measurements after the first one; some parts of the antenna were damaged. New fabrication for the antenna and the new power divider to make new measurements was not possible due to the financial problems. The suggested solution of the new power divider and the characterization of the substrates surely will solve the problems and will give the expected good results in the after a new fabrication and measurements in the future.

In the perspectives of this thesis two main works are expected:

First: The design of new geometrical circularly polarized **ARMA** structures (circular or hexagonal shapes see the figure below) to overcome the limitations of the geometrical dissymmetry of the square **ARMA** in the different directions. The square shaped **ARMA** antenna introduces different contributions for the edge effects; this is normally due to the physical structure. We tried to compensate that by the feeding law optimization that partially success but it still a need to have more symmetrical physical structure.

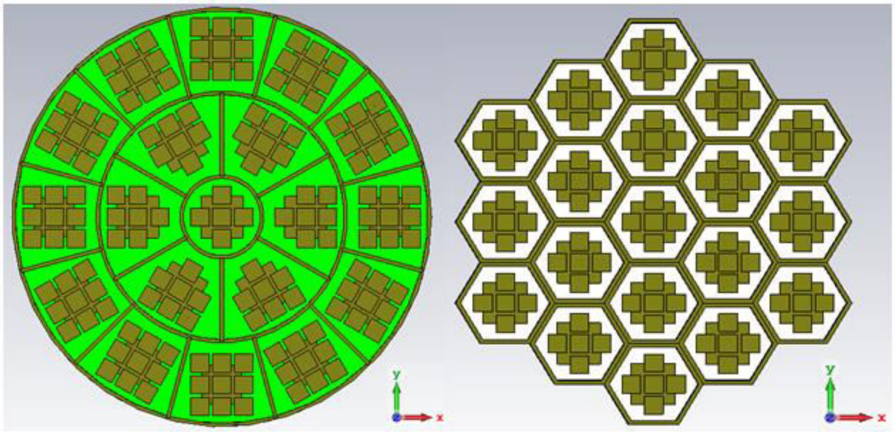

New suggested geometrical shapes for circularly polarized ARMA, circular and hexagonal.

Second: The design of compact form for of the whole antenna system; the matrix with the polarization circuits and the new power divider. In the future we are looking for a stacked solution where the power divider is printed in a layer behind the antenna and connected to the polarization circuits by means of vias and not cables (see the figure below). Then we will have a layer for the FSS, a layer for the patches inside the pixels cavities, a layer for the polarization circuits and finally a layer for the power divider. The advantages of this suggested structure are:

- The more compact structure will have smaller size since no cables in between the power divider and the antenna.
- The connection of the power divider and polarization circuits by vias solves the problem of the 50Ω matching impedance. It will not be necessary to match the output ports of the power divider with 50Ω, but with more options since the commercial cables are not used. Then it will be simpler to achieve good connectivity and matching impedance between the layer of the power divider and the layer of the polarization circuits, but will also introduce new challenges due to the small area reserved behind the antenna.

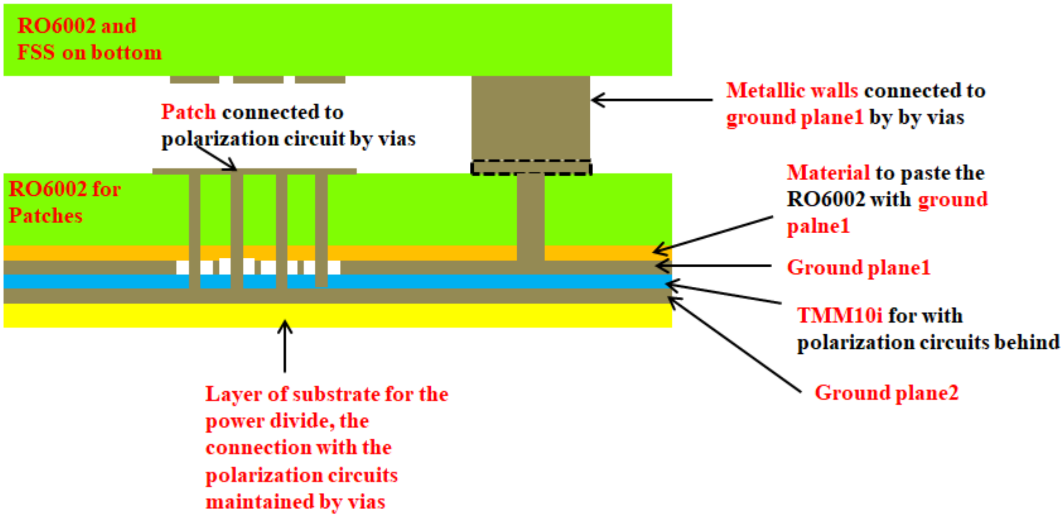

New stacked structure with the new power divider layer proposed (in yellow color) for the future work.

Appendixes

Appendix I

I. EBG Antenna

In general, EBG antenna is constituted as its name indicates from EBG material, which is composed of a periodic assembly of dielectric or metallic elements in one, two or even three directions (**Figure 1**). They are used to control the propagation of electromagnetic waves by frequency filter and spatial filter. In this manuscript, brief materials and their electromagnetic properties, the general structure, the principle of operation and the main electromagnetic characteristics of EBG antennas.

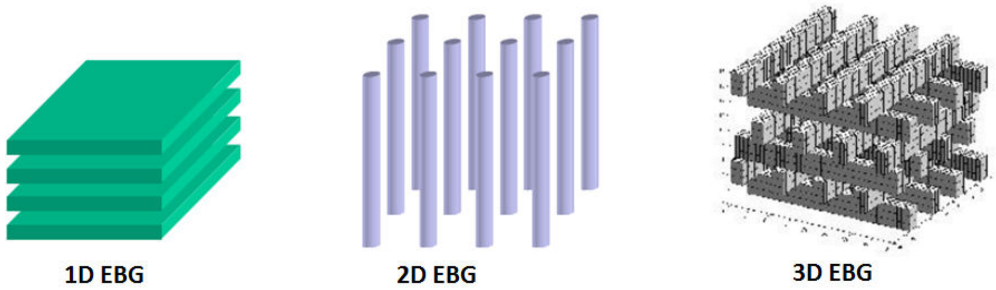

Figure 1: Examples of periodic assembly of EBG materials.

I-1 EBG material

Electromagnetic Band Gap materials commonly referred to as EBG, are the transposition at microwave frequencies of the Photonic Forbidden Band more commonly known as BIP materials. In 1D, this transposition leads to the superposition of several layers of periodic dielectrics spaced by, $\lambda_0/4$, which are illuminated by a wave plane EM. The transmission coefficient of the material under consideration reveals a band of frequency centered around f_0 for which no wave can propagate (a simple Example of a EBG material formed by 3 dielectric plates is shown in **Figure 2**).

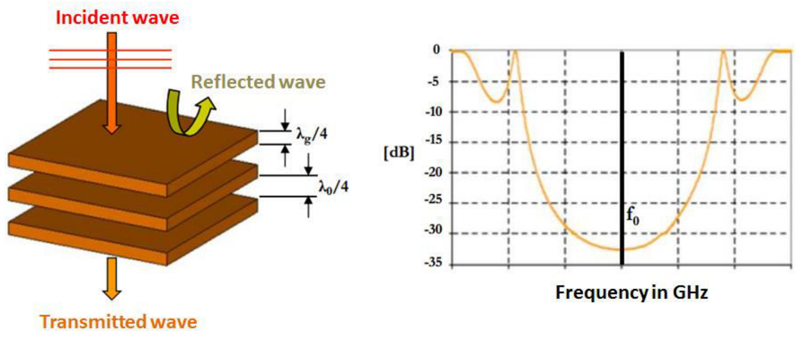

Figure 2: Characterization of EBG material in transmission.

I-2 EBG material defect in periodicity

The characteristics of EBG materials become particularly important when a defect is inserted in the periodicity. **[I-8]** and **[I-9]** show that insertion of a break (defect) in the periodicity of the EBG material, makes it possible to modify its electromagnetic behavior by creating pass band within the band gap enabling the waves to pass through. In the example of **Figure 2**, the defect in the three plates corresponds to a spacing of λ_0 in the middle of the structure is made **(Figure 3)**. The pass band created in the band gap is shown in **Figure 3**. The use of other types of defects would lead to the same principle and it is the nature of the defect which characterizes the permitted band. These results also are applicable to 2D and 3D structures (for example FSS). Frequency characterization highlights a property of the EBG materials: **frequency filtering**.

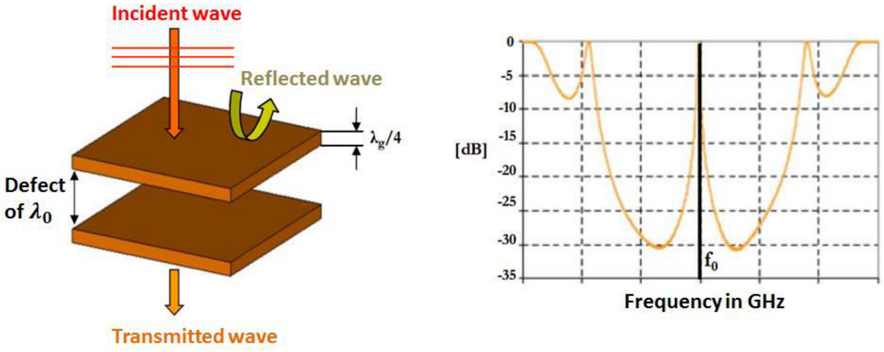

Figure 3: Characterization of EBG material with defect in transmission.

I-3 From EBG material periodicity defect to EBG antenna

I-3.1 General principle and geometrical structure of the EBG antenna

The insertion of an excitation source in the middle of the EBG material in the absence of periodicity of **Figure 3** reveals, in addition to the frequency filtering properties presented previously, the possibility of spatial filtering with two directions of radiation **(Figure 4)**. A bidirectional EBG antenna is thus obtained.

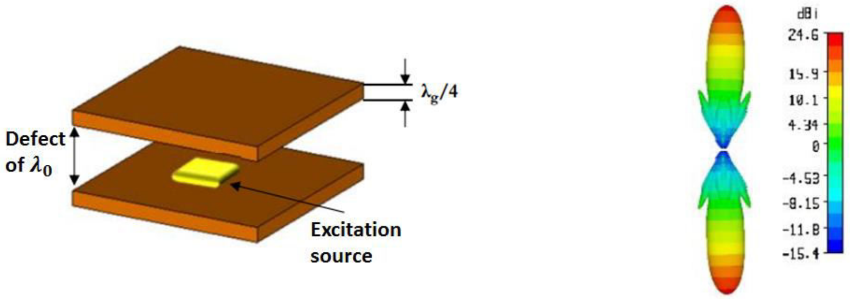

Figure 4: General structure of bi-directional EBG antenna.

The cartography of the tangential electric field of the EBG material with defect at the pass band frequency shows that the field is essentially confined to the defect zone and has a zero in the middle of the defect **(Figure 5)**. According to the image theory we can insert a ground plane at the position of zero fields, without changing the distribution of the field. The height of the resonator created from the defected EBG structure is $\lambda_0/2$ **(Figure 5)** and then the radiation of the antenna becomes unidirectional.

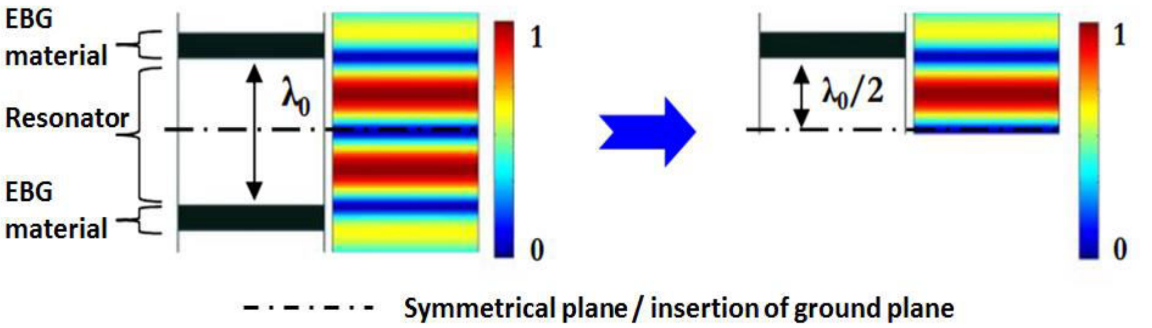

Figure 5: Cartography of the tangential electric field in the EBG material.

The antenna thus obtained is a directive EBG antenna and commonly used simplified examples are shown in **Figure 6**. This antenna is generally composed of:

- Semi-reflective upper wall formed in the simplest case either by a dielectric plate **(Figure 6.a)** or by a frequency selective surface FSS **(Figure 6.b)**.
- Lower wall formed by totally reflected metallic ground plane.
- Resonator located between the upper and lower walls.
- Source to excite the system.

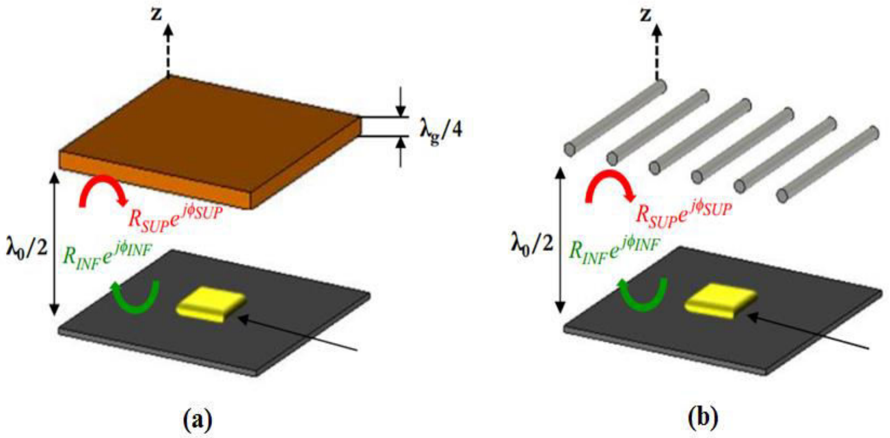

Figure 6. Illustration of two special cases of EBG antenna with two types of upper plates (a) dielectric plate and (b) FSS with metal rods.

I-3.2 Excitation source

In the examples of **Figure 6**, the excitation source is inserted into the cavity and can also be supported by the ground plane of the EBG antenna, but it can be placed also outside the cavity in the z direction. The energy source will resonate between the ground plane and the top wall. In the work of this thesis, the EBG pixel of **ARMA** is excited by a printed solution of patch type. However other types of sources may also be considered (dipoles, slots, monopoles, waveguides, etc.).

I-3.3 Upper wall

The upper wall with partial reflectivity may be, in a simplified version, a dielectric plate or also a metallic FSS as shown in **Figure 6**. Metallic FSS are usually planes structures obtained by the repetition of an elementary pattern of predefined shape. Depending on the form, different reflection properties can be obtained with this type of structure. Upper wall is partially reflective ($R_{sup}e^{j\emptyset_{sup}}$) and the ground plane is totally reflective ($R_{inf}e^{j\emptyset_{inf}} = -1$ with $\emptyset_{inf} = 180°$). The total structure thus forms a 1D resonator in the z direction which acts transversely as a radial guide with evanescent waves. This principle will be detailed in the next paragraphs.

I-3.4 Functionality of the EBG antenna

I-3.4.1 1D resonator along z

The operation of an EBG antenna is based on a frequency structure which is fixed by the longitudinal resonance between the ground plane and the upper wall. This frequency f_0 of the fundamental resonance also corresponds to the frequency of operation of the antenna. It is a function of the height h of the resonator and the coefficient of reflection of the lower and upper walls (R_{sup}, R_{inf}, $\emptyset_{sup}$ and $\emptyset_{inf}$) according to **[Eq.1]**. The reflection coefficient of the walls also influences the quality factor Q which conditions the performance of the structure **[Eq.2]**.

$$f_0 = \frac{c}{2h}\frac{\phi_{SUP}+\phi_{INF}}{2\pi} \qquad \textbf{[Eq.1]}$$

$$Q = \frac{\sqrt{R_{SUP}}}{1-R_{SUP}}\frac{\phi_{SUP}+\phi_{INF}}{2} \qquad \textbf{[Eq.2]}$$

I-3.4.2 Radial and evanescent modes

An EBG antenna acts transversely as a radial evanescent waveguide (direction xy). In the evanescent zone of the EBG mode, the fields decrease exponentially and radially around the source **(Figure II-9.a)** and the energy does not start thus horizontally. This will result in a distribution of the circular field of type Gaussian over the antenna (seen on its upper surface)

(Figure 7). The latter defines the radiating aperture equivalent of the antenna and leads according to **[Eq.1]** and **[Eq.2]** to directional diagrams.

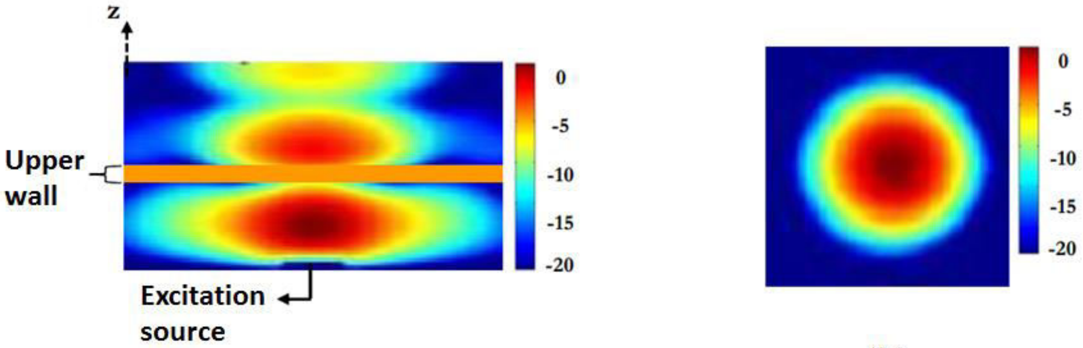

(a) (b)

Figure 7: (a) Repartition of the radial field (vertical cut at the middle), (b) radiation from upper surface view.

I-3.4.3 Frequency behavior in radiation

In terms of radiation, two zones delimited by the cut-off frequency f_0 (f_0 shows the cutoff frequency of the resonator and at the same time the resonant frequency of the antenna) are distinguished **(Figure 8)**. Above f_0, the mode propagates horizontally between the ground plane and the upper wall. Leaky-type wave is obtained, which leads to non-directional diagrams in the axis. On the other hand, for f_0 and below, the radiation patterns are directional in the axial direction. The mode is evanescent transversally and the fields decreasing exponentially and radially around the source **(Figure 7.a)**.

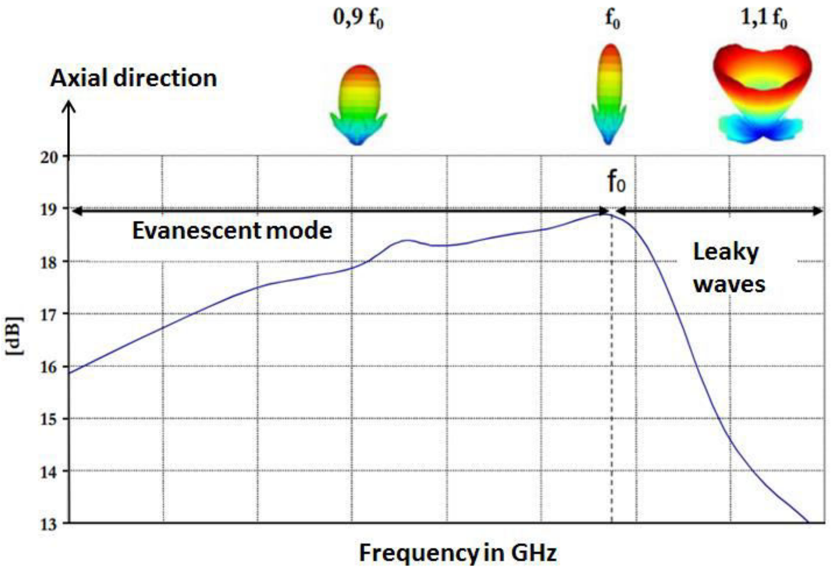

Figure 8: Frequency evolution of the directivity and radiation pattern.

Appendix II

I- Polarization circuit dimensions optimization

The area reserved for the polarization circuit is small (18.29mmx18.29mm). The circuit must include three hybrid couplers, three 50Ω impedance ports with their pads and the connector pad to fix the connector at the input of the polarization circuit. Also the pixels that are not fed are connected to 50Ω impedances; the patch is connected by vias to the pads where the resistors exist (**paragraph V-2.4 Chapter IV**).

I-1 50Ω Resistor pad

Figure 9.a shows the design of a small pad printed on the TMM10i substrate placed on the ground plane with the corresponding necessary simulation ports. The 50Ω impedance is replaced by the 50Ω impedance discrete port in CST and the input is simulated by the waveguide port. Three vias with diameter 0.3mm connect the pad to the ground plane (**Figure 9.b**). The overall size of the pad in **Figure 9.b** is: 2.2mmx1mm.

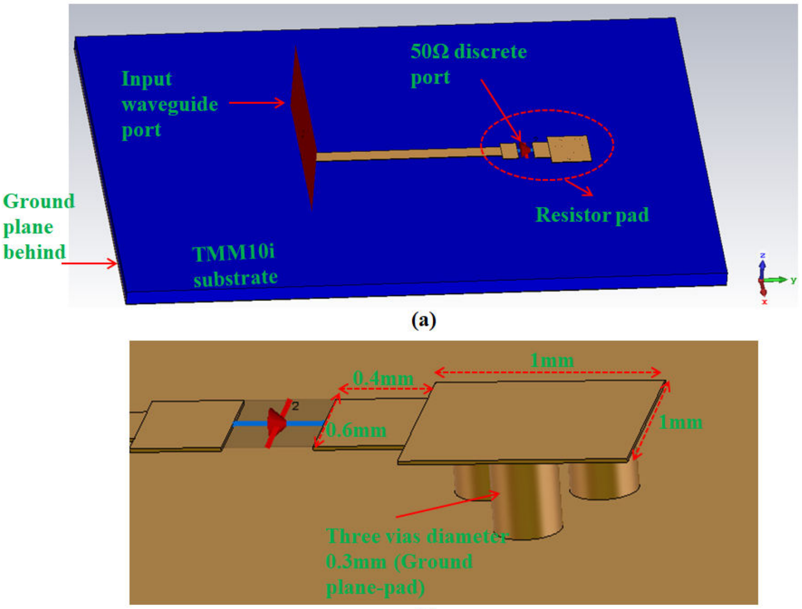

(a)

(b)

Figure 9: 50Ω resistance pad, (a) design in CST with the ports, (b) vias and pad dimensions.

The design is optimized to give a well-adapted return loss parameter at the input waveguide port (**Figure 9.a**). Then for any reflected power inside the power divider, the power is absorbed by the 50Ω resistance and. The S-parameter at the input waveguide port is shown in **Figure 10** with a very good adaptation at a wide bandwidth.

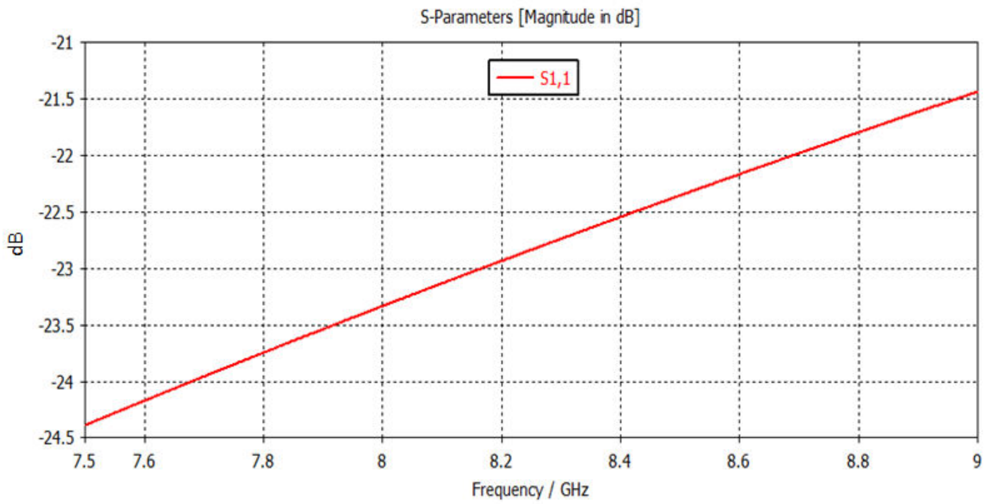

Figure 10: S-parameter at the input of the pad waveguide port.

I-2 Connector pad

The pad for the connector used **(R222.508.000)** has a standard pad to be soldered on. This pad has two transmission lines modes the coplanar microstrip line and the microstrip line. The design in CST of the standard pad shows that using the substrate TMM10i the coplanar transmission line has very small dimensions and this may have bad drawback effects due to the manufacturing error and the soldering of the connector pin on the transmission line. Also the pad dimensions are not efficient to be used in the circuit, since the area allowed to be used is very small as mentioned above. Then a customized pad was designed and optimized in CST to get small dimensions with only on transmission line mode (microstrip line). **Figure 11** shows the pad designed in CST with the connector.

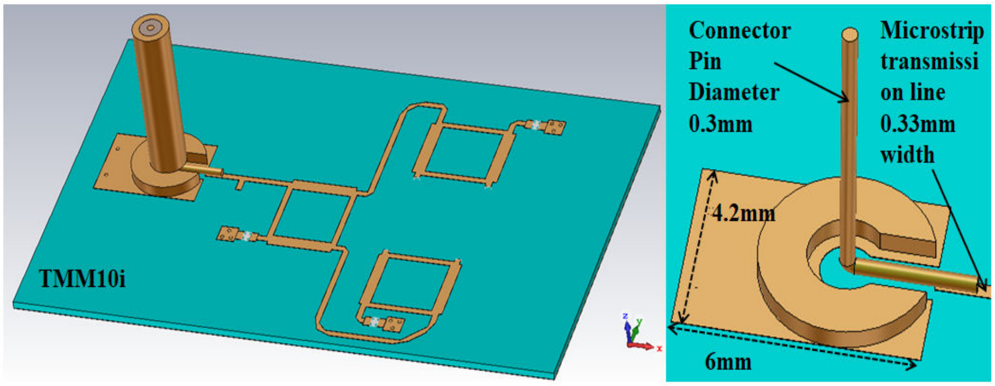

Figure 11: Connector pad customized design in CST.

II- Metallic walls and ground plane connectivity

The connectivity between the ground plane and the metallic walls **(Chapter IV paragraph V-2.4)** in the matrix were not attained directly (no direct contact as described in the pixel concept in **Chapters I**, **II** and **III**). Due to some manufacturing problems described in this connection was achieved using vias **(Chapter IV paragraph V-2.4)**; vias between the ground plane and the metallic walls. **Figure 12** shows the whole antenna with different plots to explain the location of the metallic plates (used to make vias with the ground plane) on the layer of the patches inside the matrix. Then **Figure 13** shows the metallic plates, the metallic walls and the vias connectivity. Optimizations were done with several simulations to get the good values of the periodicity between the vias and the diameter of the vias (periodicity = 3mm and diameter 1.6mm). These optimizations give the values that have no effects on the functionality of the antenna and the EBG cavity of the pixel. Patterns obtained using this structure in CST show no modifications when compared with the antenna in the case of direct metallic walls and ground plane connectivity.

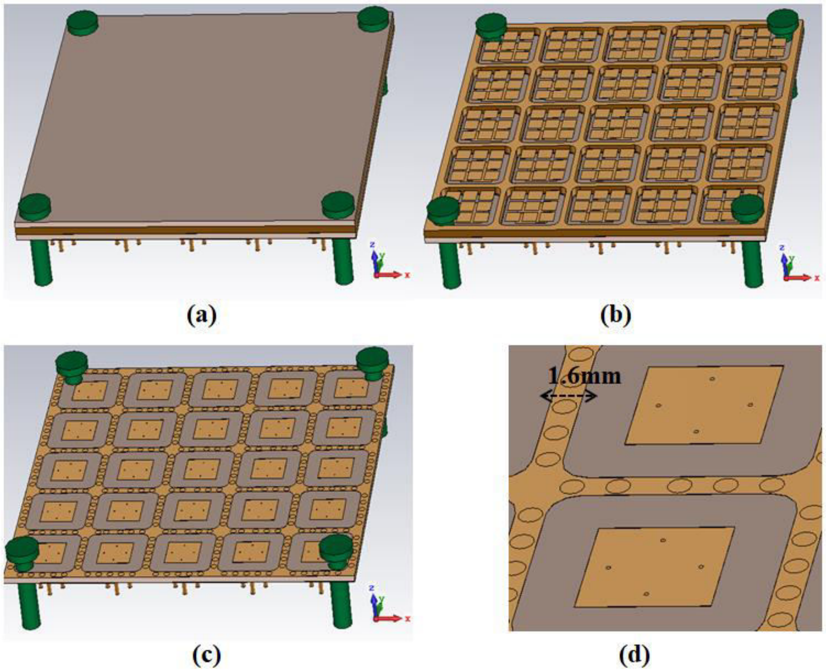

Figure 12: (a) whole antenna structure, (b) antenna without the FSS substrate, (c) shows the patches and patches substrate layer and the metallic plates.

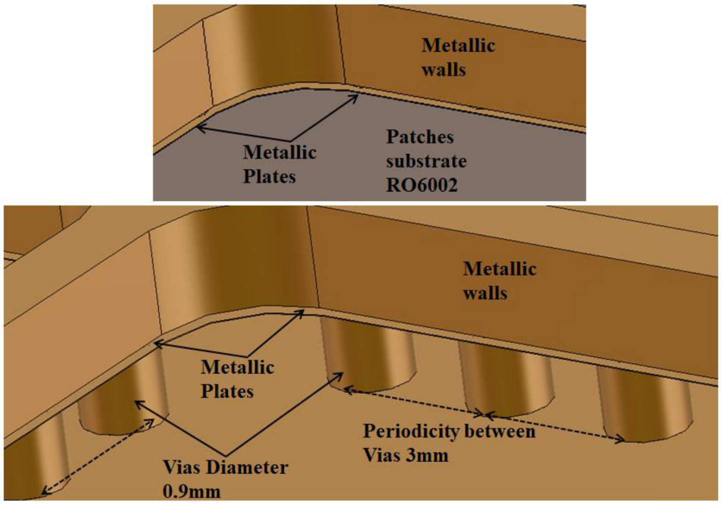

Figure 13: Metallic walls, ground plane, metallic plates and vias connectivity.

III- Possible fabrication errors testing

Many fabrication errors were tested to see their effects before fabrication. In what follows the studied cases. In this paragraph as a reference the matrix with perfect feeding procedure is considered (with the given dimensions and all parameters values used in the design and fabrication). Then the errors are introduced in the antenna and comparison of the corresponding results with the reference results with no errors is done.

III-1 Metallic walls positioning error

The antenna has a stacked form with different layers, the metallic walls as mentioned above is placed on the metallic plates. Then the whole structure (FSS, Patches, circuits and metallic walls) are fixed together by the screws. It is possible that the metallic walls are not perfectly aligned in its position. And then a small shift in its position will occur as shown in **Figure 14**. The error introduced in this positioning is set to its maximum manufacturing possible value that is 0.2mm. Then the simulation of the antenna is done and the patterns results with and without this error are compared. Comparisons are given in **Figure 15** (return loss at the central pixel), **Figure 16** (realized gain pattern and axial ratio pattern f=8.2GHz). Comparisons show that this error has no effect and could be ignored.

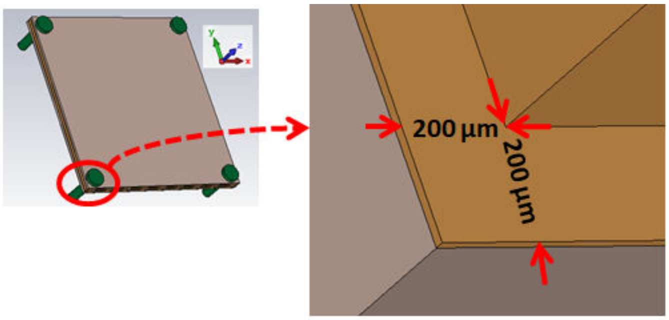

Figure 14: Metallic walls positioning error of 0.2mm.

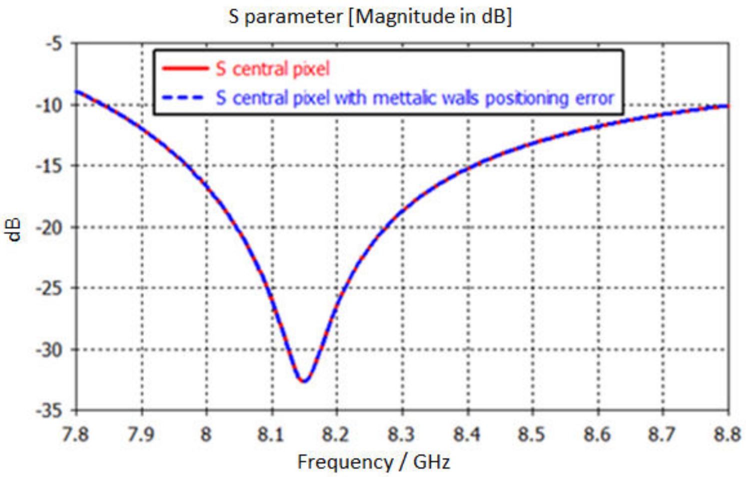

Figure 15: S-parameter central pixel with and without metallic walls positioning errors.

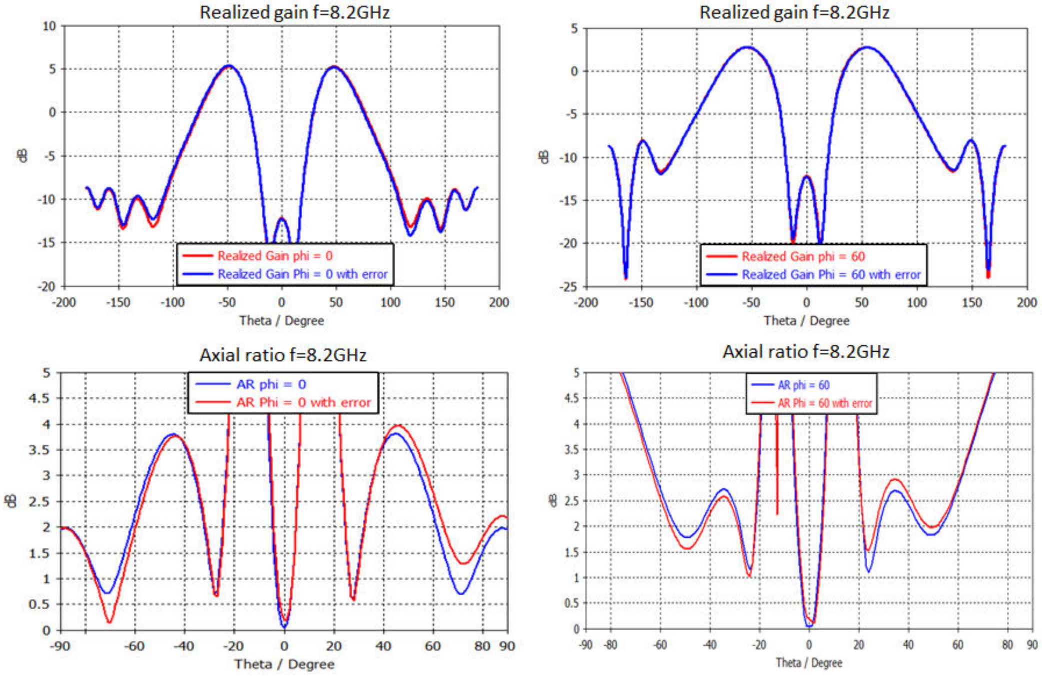

Figure 16: Realized gain and axial ratio patterns f=8.2GHz with and without metallic walls positioning errors.

III-2 Metallic walls height error

Height of the metallic walls used is 2mm, error in the metallic walls manufacturing was tested. **Figure 17** shows the antenna with the considered error. The reference design has metallic height of 2mm, and then this reference is taken to check and compare to it with the results when the errors are introduced. The error in the metallic walls height means an error in the pixel EBG cavity. The S-parameter **(Figure 18)** at the central pixel in the matrix is shifted -25MHz for the metallic height error of +0.2mm and shifted +40MHz for the metallic height error of -0.2mm. Then for the realized gain and axial ratio patterns these errors have no significant effects as shown in **Figure 19**.

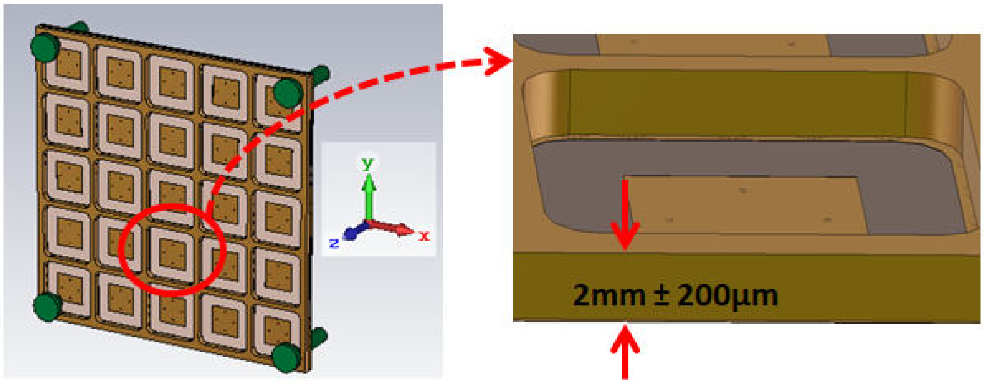

Figure 17: Metallic walls height errors.

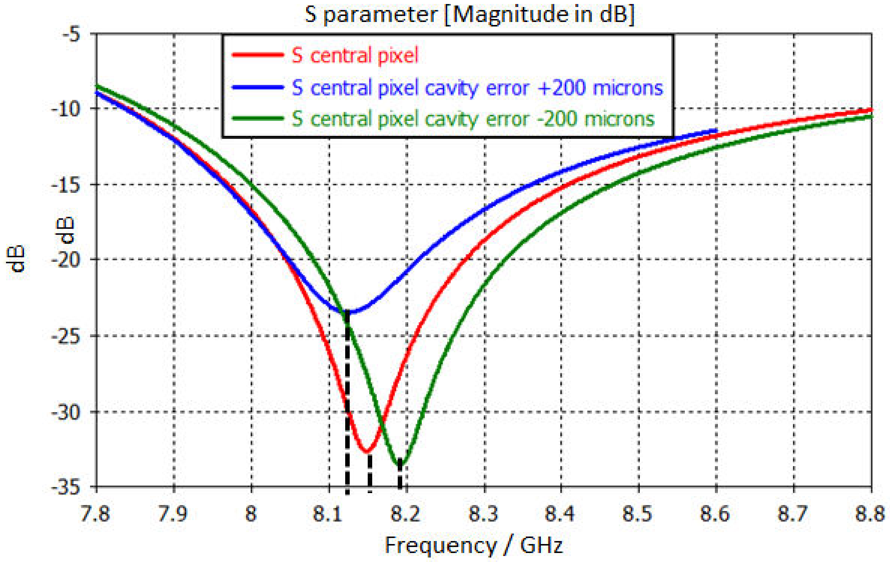

Figure 18: S-parameter shift due to metallic walls height errors.

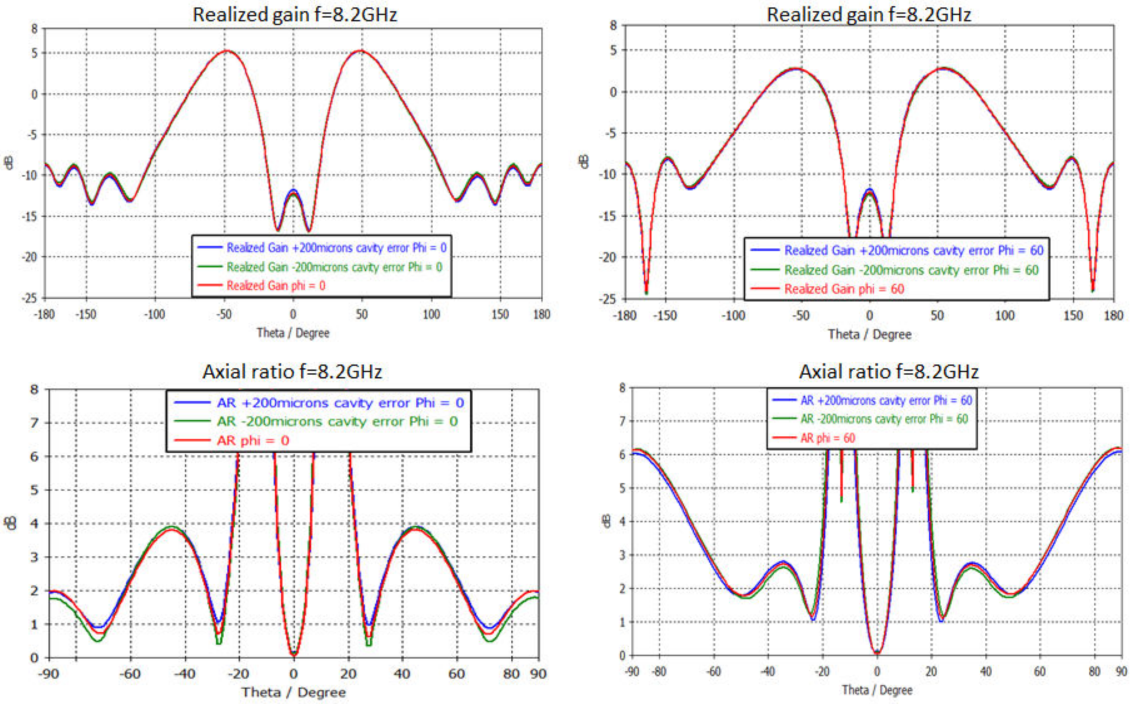

Figure 19: Realized gain and axial ratio patterns with and without metallic walls height errors (pixel cavity errors).

III-3 Polarization circuit lines width errors

The machines used for the manufacturing of the polarization circuits have a precision in drawing the microstrip lines on the substrate. This precision has a maximum error of ±20µm. This error if occur will have the same value in all the lines of the circuit. Then these maximum and minimum errors values were introduced to the circuit design **(Figure 20)** in the Momentum software and the effects on the adaptation at the input of the circuit and the outputs of the circuits were checked. **Figure 21** shows that the adaptation at the input of the circuit has no significant modifications due to this kind of error.

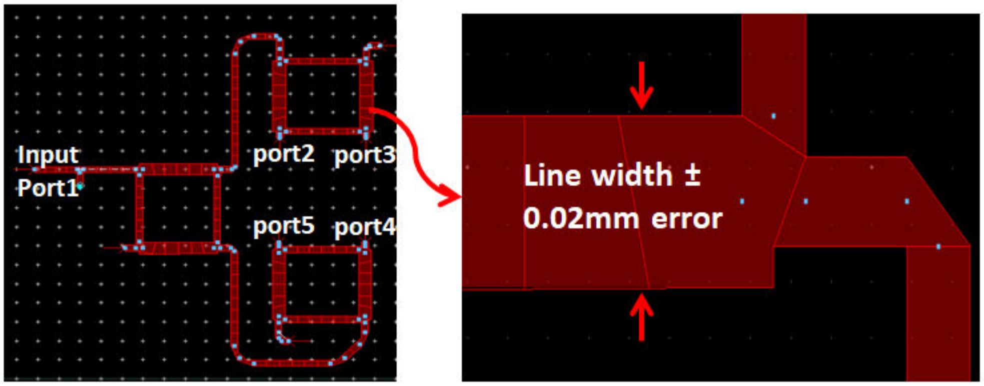

Figure 20: Polarization circuit lines widths errors in Momentum.

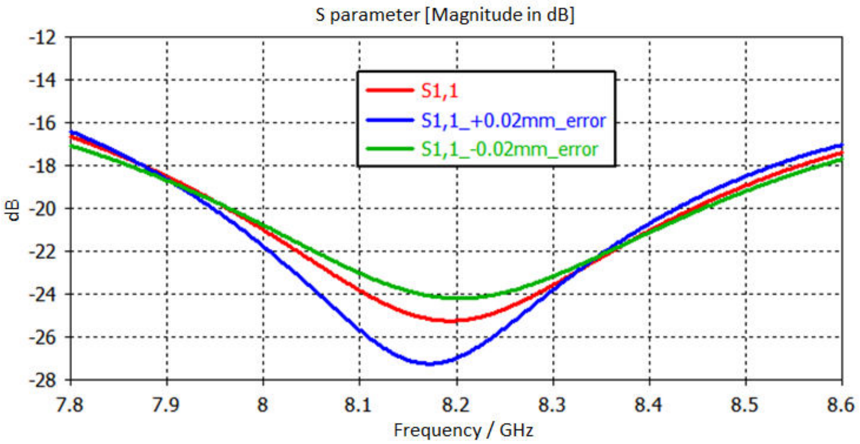

Figure 21: S-parameter at the input of the polarization circuit with and without lines widths errors.

The effects of these errors on the polarization circuit output (labeled 2, 3, 4 and 5 in **Figure 20**) is not very significant. **Figure 22** shows the magnitudes of the S-parameters at the outputs with respect to the input port (labeled 1 in **Figure 20**) ($S_{1,2}$, $S_{1,3}$, $S_{1,4}$ and $S_{1,5}$). Theoretically these magnitudes must be equal however in the design it introduces a maximum difference of 0.2dB at f=8.2GHz. Introducing the lines widths errors make this difference to be 0.4dB (+0.2mm lines errors). This error is not very significant and has no big effect in the axial ratio of the antenna; remind that this circuit was designed to feed the pixel for circular polarization. This is the same case for the phase results after introducing the errors.

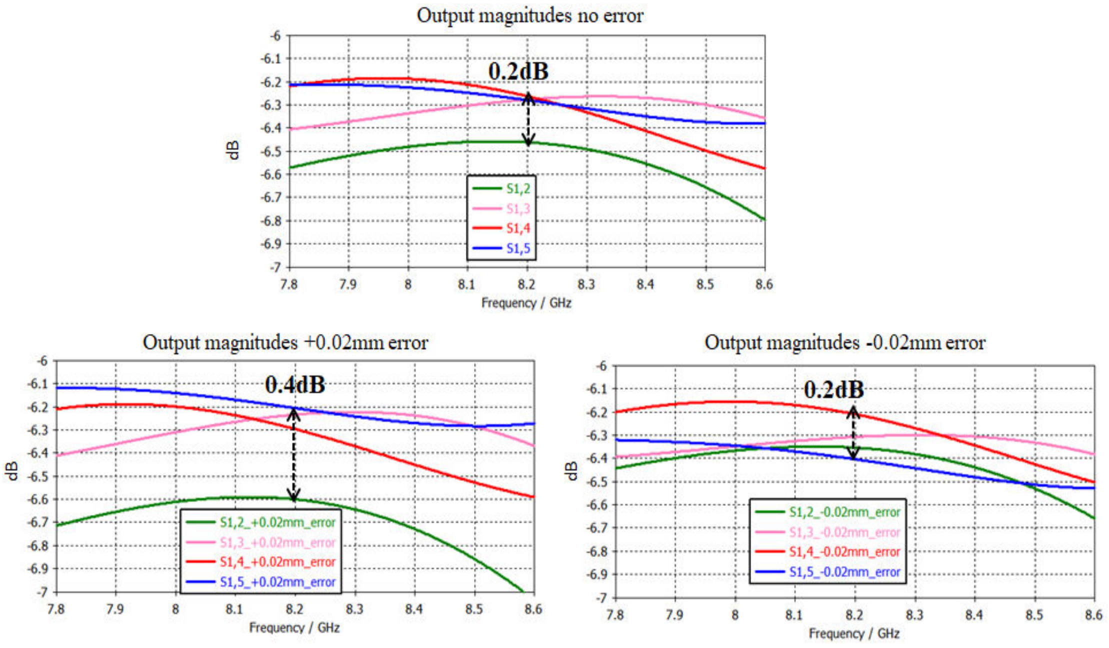

Figure 22: S-parameters magnitude evolution with the error of the lines widths of the polarization circuit.

List of Publications

❖ Journals

«The ARMA Concept: Comparison of AESA and ARMA technologies for agile antenna design».

- **Authors:** Bernard Jecko, Eric Arnaud, Hussein Abou Taam, Ali Siblini.
- **Journal:** Forum of Electromagnetic Research Methods and Application Technologies, Volume 20, Article 2, 2017.
- **Status:** Accepted.

«ARMA Feeding Techniques for Isoflux Coverage from a Micro-Satellite».

- **Authors:** Ali Siblini, Hussein Abou Taam, Bernard Jecko, Mohammad Rammal, Bellion Anthony, Eric Arnaud.
- **Journal:** Advances in Science, Technology and Engineering Systems Journal (ASTESJ 2017).
- **Status:** Accepted.

«ARMA Performances In The Light of Radar Applications».

- **Authors:** Bernard Jecko, Michele Lalande, Joel Andrieu, Eric Arnaud, Hussein Abou Taam, Ali Siblini, Mohammad Majed.
- **Journal:** International Journal of Antennas and Propagation (Hindawi 2017).
- **Status:** Submitted.

❖ International Conferences

«New Agile EBG Matrix Antenna for Space Applications».

- **Authors:** Ali Siblini, Hussein Abou TAAM, Bernard JECKO, Mohammad Rammal.
- **Conference:** Microwave Conference (EuMC), 2016 46th European. IEEE, 2016. p. 874-877.
- **Status:** Accepted.

«Multimode Reconfigurable Nano-Satellite Antenna for PDTM Application».

- **Authors:** Ali Siblini, Bernard JECKO, Eric Arnaud.
- **Conference:** Antennas and Propagation (EUCAP), 2017 11th European Conference on. IEEE, 2017. p. 542-545.
- **Status:** Accepted.

«New Circularly Polarized Matrix Antenna for Space Applications».

- **Authors:** Ali Siblini, Hussein Abou Taam, Bernard JECKO, Mohammad Rammal.
- **Conference:** Wireless testing symposiums London UK 2016.
- **Status:** Accepted.

«Wideband Circularly Polarized Pixel antenna using special EBG Approach».

- **Authors:** Ali Siblini, Hussein Abou Taam, Bernard JECKO, Mohammad Rammal, Bellion Anthony.
- **Conference:** Antennas and Propagation (MECAP), 2016 IEEE Middle East Conference on. IEEE, 2016. p. 1-4..
- **Status:** Accepted.

«Pixel and Patch Comparison Circular Polarization».

- **Authors:** Ali Siblini, Hussein Abou Taam, Bernard JECKO, Mohammad Rammal, Bellion Anthony.
- **Conference:** International Conference on Sensors, Networks, Smart and Emerging Technologies, SENSET Beirut Lebanon September 2017.
- **Status:** Accepted.

«An Agile Electronically Scanned EBG Matrix Antenna for Monitoring Target Activity».

- **Authors:** Taam, H. A, Siblini, A, El Nashef, G. Z, Jecko, B, Arnaud, E, Chevalier, N Rammal, M.
- **Conference:** Microwave Conference (EuMC), 2015 European. IEEE, 2015. p. 1435-1438.
- **Status:** Accepted.

❖ National Conferences

«Matrice Antennaire Planaire Grand Gain Munie Des Pixels Rayonnants À Grandes Dimensions (1.2λ×1.2λ) ».

- **Authors:** Hussein Abou Taam, Ali Siblini, Eric Arnaud, Bernard Jecko, Mohamed Rammal.
- **Conference:** XIXèmes Journées Nationales Microondes 3-4-5 Juin 2015 - Bordeaux.
- **Status:** Accepted.

«Validation Expérimentale d'une Matrice Antennaire Agile Rayonnante pour la Formation de Faisceaux et le Pointage Electronique».

- **Authors:** Hussein Abou Taam, Ali Siblini, Eric Arnaud, Bernard Jecko, Mohamed Rammal.
- **Conference:** XIXèmes Journées Nationales Microondes 3-4-5 Juin 2015 - Bordeaux.
- **Status:** Accepted.

«Système Rayonnant Agile Multifaisceaux (100) à Antennes « Papillon » pour applications RFID indoor».

- **Authors:** Salma AIJA, Salima IDAHMANE, Bernard JECKO, Ali SIBLINI.
- **Conference:** XXèmes Journées Nationales Microondes 16-19 mai 2017 – Saint-Malo.
- **Status:** Accepted.